Fall 2011

Exploration of multi-volumetric hyperpolarized 3Helium MRI: cross-correlation with quantitative MDCT

Ahmed Fathi Halaweish
University of Iowa

EXPLORATION OF MULTI-VOLUMETRIC HYPERPOLARIZED 3HELIUM MRI: CROSS-CORRELATION WITH QUANTITATIVE MDCT

by

Ahmed Fathi Halaweish

An Abstract

Of a thesis submitted in partial fulfillment
of the requirements for the Doctor of
Philosophy degree in Biomedical Engineering
in the Graduate College of
The University of Iowa

December 2011

Thesis Supervisor: Professor Eric A. Hoffman
Professor Edwin J.R. vanBeek

ABSTRACT

Pulmonary ventilation is a complex physiological phenomenon controlling the gas exchange process, through localized physiological responses. Detection of regional changes that occur with the onset of early disease conditions and changes occurring over short time intervals are of increasing importance as imaging is applied to the evaluation of the efficacy and safety associated with surgical and pharmaceutical interventions. Therefore, it is critical to establish and validate the regional sensitivity achievable via imaging modalities relative to the standardized global anatomical and functional assessments obtained through pulmonary function tests (PFT). Hyperpolarized 3Helium (HP ^{3}He) magnetic resonance imaging (MRI) provides metrics associated with the size of the most peripheral airspaces in the lung, free of the use of ionizing radiation. Thus derived measures have been sought as an index of regional changes associated with emphysema in an assessment of smoking associated lung disease. The minimally invasive nature and suitability for longitudinal and pediatric assessments are key advantages in its synergistic and/or surrogate use in probing the underlying function and structure. In this thesis we explore the underlying relationship between the diffusion weighted measurements attainable via HP ^{3}He MRI and lung inflation levels, as well as its ability to assess regional ventilation and the density and flow rate based distribution discrepancies within the lung airspaces.

Evaluation of the diffusion weighted measurements of lung microstructure demonstrated a statistically significant relationship between microstructure expansion and degree of lung inflation at the time of imaging on a regional and global basis, following well recognized alveolar ventilation patterns. Regional ventilation estimates obtained via HP ^{3}He MRI showed significant correlations and near unity slopes with estimates obtained via conventional MDCT in normal never-smoking subjects, with similar gravitationally dependent-nondependent gradients throughout. Coefficient of variation

analysis demonstrated similar regional heterogeneity between the MRI and MDCT based measures. Further assessments of the MRI based ventilation measures against xenon-enhanced MDCT demonstrated an insensitivity to slow and fast ventilating regions, but a superior depiction of ventilation defects. Evaluation of the density and flow rate dependent distribution patterns of helium in a normal airway model via dynamic HP ^{3}He MRI and computational fluid dynamics (CFD), demonstrated an increased preferential distribution in the nondependent airways, irrespective of flow rate.

In combination with the developmental aspects of the presented research, we have validated the ability of HP ^{3}He MRI to assess regional ventilation, via multiple quantitative assessments against conventional based and exogenously enhanced MDCT techniques and extracted the lung inflation level dependencies. Complimented with dynamic imaging and CFD simulations of helium distribution, these results provide insight into future considerations critical to the establishment of the technique as a surrogate to the ionizing radiation based modalities in assessing the regional changes occurring with the onset of early disease conditions.

Abstract Approved: _____
Thesis Supervisor

_____
Title and Department

_____
Date

_____
Thesis Supervisor

_____
Title and Department

_____
Date

EXPLORATION OF MULTI-VOLUMETRIC HYPERPOLARIZED 3HELIUM MRI: CROSS-CORRELATION WITH QUANTITATIVE MDCT

by

Ahmed Fathi Halaweish

A thesis submitted in partial fulfillment
of the requirements for the Doctor of
Philosophy degree in Biomedical Engineering
in the Graduate College of
The University of Iowa

December 2011

Thesis Supervisors: Professor Eric A. Hoffman
Professor Edwin J.R. van Beek

Graduate College
The University of Iowa
Iowa City, Iowa

CERTIFICATE OF APPROVAL

_____

PH.D. THESIS

_____

This is to certify that the Ph.D. thesis of

Ahmed Fathi Halaweish

has been approved by the Examining Committee
for the thesis requirement for the Doctor of Philosophy
degree in Biomedical Engineering at the December 2011 graduation.

Thesis Committee: _____
Eric A. Hoffman, Thesis Supervisor

_____
Edwin J.R. vanBeek, Thesis Supervisor

_____
Joseph M. Reinhardt

_____
Matthias Ochs

_____
Daniel R. Thedens

_____
Edwin L. Dove

_____
John D. Newell

To my father Dr. Fathi T. Halaweish, my mother Dr. Joulan S. ElBarhamtoshi, my brothers Drs. Ihab and Sherif Halaweish, Hossam ‘Basha’ Halaweish and my wife Dina S. Abosheasha …

Nothing tends so much to the advancement of knowledge as the application of a new instrument. The native intellectual powers of men in different times are not so much the causes of the different success of their labours, as the peculiar nature of the means and artificial resources in their possession.

Sir Humphrey Davy

Any intelligent fool can make things bigger and more complex ... It takes a touch of genius - and a lot of courage to move in the opposite direction.

Albert Einstein

ACKNOWLEDGMENTS

I would like to thank my thesis supervisors Drs. Eric A. Hoffman and Edwin J.R. van Beek for their steadfast support, numerous insightful conversations and their belief in my abilities during the early phases of my biomedical engineering career. Their unrelenting encouragement, guidance and assignment of multi-faceted responsibilities, has enabled my growth both scientifically and personally and it has been an honor and an enlightening experience to work with two such renowned scientists.

The academic guidance of Dr. Joseph M. Reinhardt has facilitated an extensive understanding of the materials and methods involved in the medical imaging field, that I am thankful for. Many thanks to Dr. Daniel R. Thedens for his extensive efforts in pulse sequence generation, troubleshooting and scanner operation. I appreciate all late nights spent testing the protocols and the time spent teaching me the ins and outs of the MRI machines. Also, I would like to thank the remainder of my committee members Dr. Edwin L. Dove, Dr. Matthias Ochs and Dr. John D. Newell for their encouragement and guidance throughout this journey.

Thank you to the Polarized Helium Lung Imaging Network (PHeLINet – European Union) for the extensive lung imaging based workshops and facilitating numerous insightful discussions between the hyperpolarized noble gas imaging experts, which provided me with the sufficient knowledge and tool requirements for successful conduction of hyperpolarized ^{3}Helium imaging experiments at the University of Iowa. I would also like to thank Siemens Healthcare for their continuous MRI and MDCT support along with the opportunity to attend several MRI based educational workshops, GE Healthcare for the loan of the ^{3}Helium polarizer, VIDA Diagnostics for their Pulmonary Workstation & Apollo support and Linde Gases for facilitating acquisition of the gaseous supplies. Special thanks to Craig Cornegay of GE Healthcare for his technical expertise and backing of the ^{3}He polarizer.

Similarly, I would like to thank our clinical collaborators Dr. Abhay Divekar – Pediatric Cardiology, Dr. Susan Hanes – Pediatric Cardiology, Dr. William 'Bill' Lynch – Cardio-Thoracic Surgery and Dr. David Stoltz – Internal Medicine (Pulmonary) for the insightful hands-on educational experience. Thank you to the late Dr. Geoffrey Mclennan, for his guidance and the eye opening discussions in relation to the clinical/translational perspective of lung imaging. Thank you to Kim Glynn and Chris Mclenann from the Iowa Institute of Biomedical Imaging (IIBI) for their friendship and support throughout the past few years.

Special thanks to all my colleagues and co-workers in the Department of Radiology's Iowa Comprehensive Lung Imaging Center (I-CLIC) for their complimentary efforts, continued assistance and friendship throughout this journey: Ann M. Thompson – facilities/personnel management (hunting down Dr. Hoffman when needed), Joanie M. Wilson – human subject recruitment, Junfeng Guo – PASS, Nathan E. Burnette – Database/IT, Brian K. Walton– IT (Geek) Support, Heather Baumhauer – Clinical Trials, IND and FDA management, Janice Granroth – Image Analysis support, John H. Morgan – Experimental Setup, Liz Minard – MDCT Scanner Operation & Party Planning Committee Chair, Jered P. Sieren – MDCT/MRI scanner operation and experimental management, Dr. Youbing Yin – CFD & Image Registration, Matthew Fuld – Xe-MDCT and Dragos Vasilescue – Image Processing.

I would also like to thank my friends Mehmed 'Bill' Diken, Tariq 'Toga' ElMeri, Moemen 'Maytag' Zaki, Dennis 'Agent CD' Lambing, Zaid 'Cali' Towfiq, Jered & Jessica Sieren and Ryan & Amber Carda, for their encouragements, their company, the indulgence in insightful multi-faceted intellectual conversations and the numerous distractions they provided away from the graduate life. Special thanks to the staff at the local Javahouse for pharmacological and environmental support.

I am truly indebted to my parents, brothers, extended family and friends in Egypt (Al Mansoura & Meet El Amel) for their never ending love and their continuous

encouragement throughout this scientific endeavour, for without them, none of this would have been possible. Thanks to my mom and dad for continually encouraging me to challenge myself and my surroundings and for teaching me that nothing worthwhile comes easily. Thank you to my brothers Ihab and Sherif for being the best friends a big brother could have and for encouraging me to enjoy my hobbies, no matter how expensive they were. Thanks to Hossam Basha for teaching me patience, for reminding me how important family is and for beating me in every possible gaming console we have ever owned. Special thanks to my best friend, my wife Dina, for accommodating my unusual sleeping patterns, waking me up when I had successfully ignored my alarm clock, providing continuous gastronomical support and for keeping me on track, I love you.

ABSTRACT

Pulmonary ventilation is a complex physiological phenomenon controlling the gas exchange process, through localized physiological responses. Detection of regional changes that occur with the onset of early disease conditions and changes occurring over short time intervals are of increasing importance as imaging is applied to the evaluation of the efficacy and safety associated with surgical and pharmaceutical interventions. Therefore, it is critical to establish and validate the regional sensitivity achievable via imaging modalities relative to the standardized global anatomical and functional assessments obtained through pulmonary function tests (PFT). Hyperpolarized 3Helium (HP ^{3}He) magnetic resonance imaging (MRI) provides metrics associated with the size of the most peripheral airspaces in the lung, free of the use of ionizing radiation. Thus derived measures have been sought as an index of regional changes associated with emphysema in an assessment of smoking associated lung disease. The minimally invasive nature and suitability for longitudinal and pediatric assessments are key advantages in its synergistic and/or surrogate use in probing the underlying function and structure. In this thesis we explore the underlying relationship between the diffusion weighted measurements attainable via HP ^{3}He MRI and lung inflation levels, as well as its ability to assess regional ventilation and the density and flow rate based distribution discrepancies within the lung airspaces.

Evaluation of the diffusion weighted measurements of lung microstructure demonstrated a statistically significant relationship between microstructure expansion and degree of lung inflation at the time of imaging on a regional and global basis, following well recognized alveolar ventilation patterns. Regional ventilation estimates obtained via HP ^{3}He MRI showed significant correlations and near unity slopes with estimates obtained via conventional MDCT in normal never-smoking subjects, with similar gravitationally dependent-nondependent gradients throughout. Coefficient of variation

analysis demonstrated similar regional heterogeneity between the MRI and MDCT based measures. Further assessments of the MRI based ventilation measures against xenon-enhanced MDCT demonstrated an insensitivity to slow and fast ventilating regions, but a superior depiction of ventilation defects. Evaluation of the density and flow rate dependent distribution patterns of helium in a normal airway model via dynamic HP ^{3}He MRI and computational fluid dynamics (CFD), demonstrated an increased preferential distribution in the nondependent airways, irrespective of flow rate.

In combination with the developmental aspects of the presented research, we have validated the ability of HP ^{3}He MRI to assess regional ventilation, via multiple quantitative assessments against conventional based and exogenously enhanced MDCT techniques and extracted the lung inflation level dependencies. Complimented with dynamic imaging and CFD simulations of helium distribution, these results provide insight into future considerations critical to the establishment of the technique as a surrogate to the ionizing radiation based modalities in assessing the regional changes occurring with the onset of early disease conditions.

TABLE OF CONTENTS

LIST OF TABLES

LIST OF FIGURES

CHAPTER 1: MOTIVATION AND AIMS

The complexity of pulmonary ventilation as a physiological process during which gas exchange between the outside environment and internal structures occurs, is reflected in the complexity of the lung's anatomic structure and localized physiologic responses. The human lung is composed of approximately 300M alveoli, up to 23 generations of conducting and respiratory bronchial segments leading to the terminal ascini which represent the smallest gas exchange unit of the lung. (174, 175, 177, 179, 180). This complexity is further complicated by the fact that numerous muscle groups serve to generate transpulmonary pressures serving to bring air into the lung while elastic recoil largely serves to expel gas back out of the lungs. Proper assessment of these physiological events rely on the ability to regionally characterize inflow, outflow and distribution of the gases within the anatomical structures governing the overall functionality of the lungs (alveoli, airways, bronchioles, etc ...) (69, 147, 174, 176). The appearance of ventilation defects or abnormalities within a majority of pulmonary disease conditions suggests the importance of this phenomenon in regulating the overall integrity and function of the lungs. Assessment of these disease conditions suggests the dominance of a ventilation/perfusion imbalance as the driving force in the onset of early disease states (185). Early on, the classifications of ventilation discrepancies were observed to be either restrictive, obstructive and/or diffusion related, demonstrating the intrinsic complexity lung diseases and the onset of their deleterious effects (185). It is therefore critical to establish and develop proper tools and techniques to quantitatively and qualitatively provide serial measurements of the underlying physiology within the clinical setting. The significance of these tools is of considerable interest within the clinical setting to assess suitable treatment plans and pre-operative planning assessments, evaluation of new and targeted therapeutic agents, guide diagnosis of disease progression

and to better understand the pathological processes leading to the onset of these conditions.

The current reliance on Pulmonary Function Testing (PFT) via spirometry provides a static anatomical measurement of lung function dependent upon the characteristic alterations that occur following disease onset (128, 185). However, PFTs lack the regional ability to detect early changes in lung disease prior to the advent of the full deleterious effects. Spirometric measurements, which are dependent on individual subject efforts, only evaluate how the disease has altered the underlying function without any regards to the anatomical and/or pathological pathways taken (128, 185). Chronic obstructive pulmonary diseases (COPD) are a group of slowly progressive diseases characterized by airflow obstruction as a result of airway destruction, pulmonary parenchymal destruction or the combination of both (15, 46). COPD affect more than 5% of the adult population, is the 3rd leading cause of death and the 12th leading cause of morbidity (128). Current literature and spirometric guidelines limit the treatment options of patients suffering from mild to severe COPD, as assessed via spirometry, to pulmonary rehabilitation, long term oxygen supplementation and the use of inhaled bronchodilators, long acting anticholinergics, long acting B-agonists and corticosteroids (12-15). Guidelines set forth by the American College of Physicians (ACP), American College of Chest Physicians (ACCP), American Thoracic Society (ATS) and European respiratory Society (ERS), limit the use of spirometric evaluations to subjects that could possibly benefit from such therapeutic interventions, but clearly state the lack of evidence supporting the use of these spirometry as a clear screening strategy (128). Similarly, evidence suggests that the use of patient reported health history and physical examinations are poor predictors of disease onset, progression and diagnosis and in combination with spirometry, result in unnecessary testing, increased costs and unnecessary disease labeling. A quote from The Lung, written by Comroe et al. states that "*Pulmonary function studies will not tell where a lesion is, what the lesion is, or even*

that a lesion exists if it does not interfere with the function of the lung. Therefore they supplement and do not replace a good history and physical examination, radiological, bacteriological, bronchoscopic and pathological studies" (31). Although comprehension of this reality occurred several decades ago, the current guidelines mainly rely on the use of these global, pathologically inspecific measurements. Therefore, it is becoming critical to develop techniques that are regional, comprehensive, sensitive and disease specific, to evaluate these conditions and improve the overall effectiveness of the treatments administered as a result of disease severity, with the hopes of improving the lifestyle of the affected population and reduce the mortality rates.

The use of medical imaging methodologies to provide quantitative and qualitative visual assessments of pulmonary ventilation and the onset of disease conditions, lends themselves as minimally invasive modes of providing serial measurements of the various disease conditions on a more regional basis. Early attempts to quantitate the interplay between the wide array of variables leading to the onset of disease have relied mainly upon regional density measurements of computed tomography (CT) (67, 70, 130), regional strain assessments via bi-plane x-ray fluoroscopy (73, 77), nitrogen washout curves (36), radioactive aerosol assessments (135) and positron emission tomography (PET) based topographic evaluations via radio-tracer distributions (132, 166). While these diagnostic procedures are successful in providing a clear delineation between the normal and pathological processes occurring within the lungs, they have been criticized for their use of radio-active elements, limited spatial and temporal resolutions and limited longitudinal use, based on the ionizing radiation nature of the techniques. More recently the use of CT has become the current gold standard in assessing regional density changes in normal and disease states (68, 161), leading to a considerable amount of development into the use of stable xenon as an inhaled contrast agent to assess the washin and washout of the gases, along with regional distributions throughout the airspaces (25, 29, 57, 60).

The significant insights provided via this methodology have limited use in longitudinal and pediatric assessments, governed by the radiation based nature of the technique.

The emergence of Magnetic Resonance Imaging (MRI) is a result of the exploratory efforts into the strong magnetic properties of the hydrogen atom and its characteristics within a homogenous magnetic field. Triggering the curiosity of several scientists such as Felix Bloch, Edward Mills Purcell, Sir Peter Mansfield and Paul Lauterbur, brought forth the use of the magnetic properties and characteristics of this simple yet powerful element in acquisition of 2D and 3D images of the human anatomy (1, 37). The strength of the produced magnetic resonance signals relies on the total available magnetization, which is a byproduct of concentration, excess spin density and the volume of the probed element. Albeit the success of MRI in visualizing and providing means of assessing normal and pathological conditions in cardiac, orthopedic and brain applications, the thermal equilibrium polarizations ($\sim 10^{-5}$) available within the lung structures has limited its use as a result of the motion and susceptibility artifacts (2). Recently, several attempts to assess pulmonary structure and function have emerged, relying on the use of exogenous contrast agents such as pure oxygen, fluorine and noble gas isotopes(helium and xenon) , providing means of counteracting the available signal to noise (SNR) limitations of conventional ^{1}H MRI. Most prominently, the emergence of Hyperpolarized Noble gas MRI utilizing 3-Helium (^{3}He) (99, 105) and 129-Xenon (^{129}Xe) (2) as exogenous contrast agents, have counteracted the poor signal intensities and magnetic susceptibility artifacts generated as a result of minimal proton density and numerous air-tissue interfaces. Initially demonstrated via ^{129}Xe, recent interest in the modality has shifted towards the use of ^{3}He, due to its low solubility coefficient, higher gyromagnetic ratio and more efficient means of achieving higher non-equilibrium polarizations (81, 109). At room temperature and atmospheric pressure, these gases exhibit a molar concentration of approximately a few tenths of a percentile to that of H_2O. Therefore to increase the available excess spin density (polarization), considerable

enhancements are achievable through spin exchange optical pumping with intermediary alkali metal (Rubidium – Rb) vapor, during which the continuous polarization of the Rb via absorption of circularly polarized 795nm resonance laser light, results in the transfer of the accumulated angular momentum from the electron spins of the alkali metal vapor to the nucleus of the noble gas, through gas phase collisions (2, 172).

Although initially used in nuclear physics experiments as a neutron mirror (an application still used for detection of radioactive weapons), the technique was introduced into the medical imaging field with remarkable results (22, 42, 43, 84, 99, 102, 169, 170). While being a byproduct of tritium (^{3}He) nuclear decay, this stable, non-toxic, non-radioactive isotope has shed a light into what was considered the black hole of MRI, the lungs (99, 105, 141). The following presented material aims to explore the underlying physiology probed via HP ^{3}He MRI in relation to our previous understanding of lung ventilation, expansion and physiology based on functional Multi-Detector CT (MDCT) methods and the limitations involved. Both developmentally and experimentally, we evaluated the uncertainty revolving around HP ^{3}He MRI and its sensitivity to regional ventilation and expansion changes through the following hypothesis and developmental driven aims.

In Chapter 2, we present a brief and comprehensive introduction into the background and founding principles of MRI, the underlying limitations of the technique with respect to lung imaging and image acquisition and quality considerations. Following which we discuss the background and current perspective revolving around pulmonary physiology with focus on the structural and functional aspects of lung ventilation as understood physiologically and technically. Finally the background review is wrapped up with a comprehensive technical overview of HP ^{3}He MRI, along with several other MRI based lung imaging techniques utilized in probing both lung structure and function.

In order to successfully conduct HP ^{3}He MRI experiments at the University of Iowa Hospitals and Clinics (UIHC), we needed to become familiar with the proper

operating procedures of the equipment utilized, develop adequate pulse sequence protocols and perform comprehensive testing of the tools to validate proper operating conditions and generation of structural and functional information (*Aim 1*). Chapter 3 discusses the developmental and testing phases of the HP ^{3}He MRI program at the UIHC, including polarizer training, maintenance and fine-tuning, along with pulse sequence testing and preliminary animal experiments. Given the unit-less nature of HP ^{3}He MRI images, the need arose for the creation of a custom graphical user interface (GUI) to facilitate the reconstruction and analysis of the acquired HP ^{3}He MRI static ventilation and diffusion weighted datasets and facilitate the multi-modality assessments against the generated MDCT based measures (*Aim 2*). Chapter 4 discusses the aforementioned GUI and the components included within for the reconstruction, segmentation, visualization and analysis of the collected imaging data and the different means of interpreting the acquired datasets and its effect upon ones understanding of the data. Chapter 5 (*Aim 3*) discusses the development of a simple yet effective method for the standardization of lung volumes in MRI imaging sessions via exploitation of PFT and slow vital capacity ($_{S}$VC) measurements, to study the effects of varying lung inflation levels upon the underlying function observed. Initial results, testing and final considerations are discussed. Furthermore, to aid the quantitative and qualitative comparisons between HP ^{3}He MRI and the MDCT functional estimates of lung ventilation, unification of image spaces is required (*Aim 4*). Chapter 6 concludes the developmental aspect of the presented research, as we discuss the development of a flexible image registration work-flow based on the Insight Toolkit (ITK) libraries and functionality of the various components within, along with testing results on multi-modality and multi-volumetric functional and structural datasets.

HP ^{3}He MRI has several unique functional measures that are of interest, one specific measure the Apparent Diffusion Coefficient (ADC) probes the underlying airways and microstructure through exploiting the diffusive nature of ^{3}He. The present

literature has shown the dependence of this functional measure on many variables including but not limited to subject position and degree of lung damage (asthma and COPD, alpha-1-antitrypsin (A1AT) deficiency) with respect to normal lung findings (4, 39, 44, 83). Minimal advancements have been made to evaluate the suitability of the method for assessing differences between longer time intervals where lung compliance is most likely to change or between subjects at very different lung volumes. Because of the non-linear characteristics of the pressure-volume curves of the lung, we believe it to be important that the lung be imaged at the same vital capacity (VC) across time and between subjects, if this technique is to be utilized in longitudinal assessments of disease heterogeneity. In Chapter 7 (*Aim 5*), we evaluate the dependency of the ADC methodology upon variability in lung inflation levels based on subject specific VC. We hypothesize that the variability of ADC values based on anatomical location (dependent – nondependent, left – right, apical – basal, whole) will follow similar ventilation patterns as demonstrated by Millic-Emili et al. (106, 107), where degree of ventilation varied with lung expansion as a function of inspiratory initiation.

The underlying sensitivity of HP ^{3}He MRI to changes in ventilation and its ability to extract this functional biomarker has been minimally evaluated throughout the years. In chapter 8 (*Aim 6*), we evaluate the ability to extract regional ventilation and expansion information from ADC and Static Ventilation HP ^{3}He MRI images, via correlating the findings to changes in regional mean lung density (MLD) and local air volume (AVC) as determined from mass preserving matching of functional residual capacity (FRC) and total lung capacity (TLC) MDCT scans. The mass preserving matching of the MDCT scans allows a prospective analysis of the regional ventilation and expansion changes observed between the two lung inflation levels (187), were we hypothesize that the ADC and static ventilation changes at TLC or possibly between FRC and TLC will provide similar insights. More recently, studies in our laboratory have demonstrated the ability to extract regional ventilation information from MDCT based measures utilizing xenon as

an inspiratory contrast agent, xenon-enhanced MDCT (Xe-MDCT). The method has shown great sensitivity in evaluating regional ventilation and the differentiation between slow and fast ventilating regions in both animal and human subjects alike. The ability to differentiate between normal-never smoker subjects and smokers has also been demonstrated with great sensitivity. In chapter 9 (*Aim 7*), we aim to evaluate the similarities and differences between HP ^{3}He MRI and Xe-MDCT, where we hypothesize that HP ^{3}He MRI assessment of ventilation will reflect CT assessment of ventilation (Xe-MDCT) except in slow ventilating regions defined by CT, while HP ^{3}He MRI assessment of ventilation will demonstrate ventilation voids better than Xe-MDCT. The use of exogenous contrast agents such as helium, xenon, fluorine and krypton in generating sufficient SNR or contrast to facilitate lung function assessments is becoming increasing popular within the medical imaging community. Although xenon and krypton have been used in Nuclear Medicine imaging, these require radioactive isotopes to be used and spatial resolution remains inferior to that of CT (113, 120, 156-158). Albeit the success of these attempts in probing the underlying structure and function, density based differences in distribution with respect to air have not been fully evaluated to establish the similarities and trends with respect our known physiological understanding of ventilation distribution. Therefore in Chapter 10 (*Aim 8*), we explore the anatomical and gravitational dependence of ^{3}He distribution in a rapid prototyped normal airway model, via HP ^{3}He Dynamic MRI and Computational Fluid Dynamics (CFD) modeling, to assess the similarities and trends with respect to our physiological understanding of air distribution.

The importance of this work lies within its non-invasive nature of probing the limitations of HP ^{3}He MRI in evaluating regional ventilation and expansion changes and has significant implications for the advancement of the technique as a clinical research tool and/or a surrogate for available techniques. In combination with the developmental aspects of the presented work, the validation of the regional sensitivity revolving around

the HP ^{3}He MRI methodology against the current MDCT based measures presents a simple and effective pipeline to extract and validate the capabilities of a given technique on an intra or inter modality basis.

CHAPTER 2: BACKGROUND

2.1 Magnetic Resonance Imaging (MRI)

Medical Imaging techniques such as Multi-Detector Computed Tomography (MDCT), Ultrasonography, Single Photon Emission Computed Tomography (SPECT) and PET have become increasingly sophisticated since their first documented medical use. Scientists and engineers all over the world have dedicated many years of research into developing what is now, state of the art systems, allowing for real time diagnosis and assessment of anatomical structures. One area of research that has risen up from all these efforts is functional imaging of the anatomical organs and structures through the use of these advanced imaging techniques. The usefulness of functional imaging is obvious, shining a light into the overall functionality of the various organs, physiological mechanisms within the human body and the changes occurring during and following the onset of pathological conditions (45, 170).

Although the aforementioned imaging techniques have proven their power and value in assessing anatomical structures and physiological states, their main drawback has been the use of ionizing radiation, single plane acquisitions and the use of radio-active isotopes. As the name implies, ionizing radiation has the ability to ionize any atom or molecule in its path, thus creating a hazard to the overall health of the human population undergoing such procedures and limiting the overall achievable results (74, 104). Other drawbacks of these imaging modalities include the confinement to single plane imaging, limited spatial and temporal resolutions and limited longitudinal and pediatric assessments. Over the past several years, regulations regarding the allowable radiation doses have been getting stricter, starting with the European Union with the United States not far behind.

One imaging modality that has overcome the ionizing radiation and radio-active aerosol limitations that have hindered the development of MDCT and nuclear medicine

techniques is Magnetic Resonance Imaging (MRI). MRI is based on the use of magnetic fields to align the environmental magnetic moments apparent within hydrogen (^{1}H) molecules in the body, resulting in an overall macroscopic and measureable net magnetization. Being that the human body is composed of approximately 75% H_2O, this natural occurring magnetic moment serves as an excellent doorway to imaging the soft tissue and organs of the body, with superior resolutions compared to MDCT and nuclear medicine techniques (45, 170, 178). The use of MRI in clinical settings is a very appealing option, as it requires no ionizing radiation and there are no known side effects to prolonged and/or longitudinal magnetic field exposure. MRI is far from perfect as it requires long examinations times on the order of 1-2 hours for imaging organs and structures and the inability to image air filled spaces, specifically the lungs. This inability to image air filled spaces does not come as a surprise as the amounts of ^{1}H atoms present are minimal in comparison with compact tissue throughout the body. The numerous tissue-air interfaces apparent throughout the lung, serve as an obstacle limiting the overall available net magnetization for imaging, through the introduction of susceptibility artifacts. Even with such limitations on pulmonary imaging, MRI has been successfully utilized in gadolinium based vascular assessments (7, 55, 58), thoracic cavity volume and diaphragmatic measurements, along with multi-modality cancer screenings and treatment planning (19, 125-127). Recent advancements in magnetic gradients, pulse sequence design and radio-frequency (RF) coil designs have given further impetus to the development of imaging the pulmonary airspaces via inhaled exogenous contrast agents such as oxygen (O_2), Helium (^{3}He), Xenon (^{129}Xe) and Fluorine (^{19}F). Upon inhalation, these gaseous agents fill up the airspaces facilitating assessment of the pulmonary structures, respiratory dynamics and perfusion parameters between these airspaces and the pulmonary vasculature (80, 81).

2.1.1 MRI Basics and Physics

MRI is only applicable to atomic nuclei that have an odd number of nucleons, resulting in a magnetic moment, which describes the direction and magnitude of the bipolar electric field induced by the rotation of the charged particle (angular momentum) (1). The simplest of all nuclei is hydrogen, with its single proton, high abundance, mobility and concentration, resulting in a more sensitive detection and evaluation of the molecular level environment, exceeding that of PET by several orders of magnitude. In an external magnetic field, the magnetic moments of a specimen under evaluation are oriented along the field in two states, parallel and anti-parallel, each with different energies. This energy difference can be described as a function of the gyro magnetic ratio of the nuclei (γ), Plank's constant ($\hbar$) and the strength of the field (B_o).

$$E = \gamma.\hbar.B_o$$

The population of each energy level follows the Boltzman statistic, where the lower energy states tend to have a larger occupational capacity, resulting in a measureable net macroscopic magnetization (Figure 1)(1, 75, 178).

At thermal equilibrium, this macroscopic net magnetization can be further distorted utilizing a radio-frequency (RF) pulse with energy equal to that of the energy difference between the parallel and anti-parallel states,

$$E_{Diff}=\hbar.w_o$$

where w_o is the resonance frequency of the spin system under evaluation. The additional energy gained is dissipated as a function of T_1 and T_2 relaxation times, where T_1 is the longitudinal (spin-lattice) relaxation time, as a result of coupling of the specimen to the microenvironment and T_2 is the transverse (spin-spin) relaxation time, due to coupling of the spins within the specimen to themselves (Figure 2). In normal biological tissues, the ranges of T_1 and T_2 relaxation are are 100-2000 ms and 10-1000 ms respectively.

Additionally, the magnetic field inhomogeneities contribute to the overall energy dissipation, through the T_2^* relaxation time (1, 75, 178).

Untouched, this measureable macroscopic magnetization is an arbitrary value, with no spatial information. To facilitate the generation and reconstruction of an image with spatial information representative of the specimen, additional spatial-varying magnetic fields can be added along the three main spatial coordinates (antero-posterior, dorso-ventral and left-right axis), with an overall field strength several orders of magnitude smaller than the main magnetic field B_o. This additional spatially varying energy application, results in a different net magnetic field for each element (voxel) within the specimens, leading to different resonance frequencies based on spatial location (1, 75).

To add to the overall complexity of an MR experiment, several key components are required, the most important of which are a strong homogenous magnetic field, gradients coils and transmit and receive coils. The two main methods of generating the strong magnetic fields are through the use of a superconducting magnet or a permanent magnet, the latter of which is more commonly used, due to the high cost and availability of the material for the permanent magnets. Permanent magnets are made of NdBFe, a magnetic material characterized by its non-linear response to an externally applied magnetic field (hysteresis curve), such that increasing the field strength of the aforementioned field, increases the material's magnetization. A saturation point is eventually reached, where all the magnetic domains of the material are aligned (maximal field strength). These types of magnets require no maintenance following the removal of the external field, as they maintain their magnetization as a result of the high remanance fields within. As the desired field strength of these permanent magnets increases, as does the weight and overall cost, thus permanent magnets have been limited to field strengths ranging between 0.3-0.4 T (tesla). As the name implies, superconducting magnets are based on the concept of superconductivity, where a material losses all its resistance at a

certain transitional temperature. The most common materials are niobium-titanium (NbTi) and niobium-tin (Nb_3Sn), with transitional temperatures around -270 $^{\circ}$C and 263 $^{\circ}$C, which are achieved through the use of liquid helium cooling. To ensure safety of all individuals working around the MRI magnets, shielding of the facilities is required to decrease/eliminate the stray magnetic fields of the magnet. This is achieved through passive or active shielding, where passive shielding utilizes iron to confine the stray field lines to the inside of the facility, while active shield utilizes a second set of wire loops around the magnet to create a magnetic field in the opposite direction of the main one, thus eliminating the stray fields (1, 178).

Gradients are generally placed between the imaging volumes and the magnet, thus reducing the overall bore diameters to approximately 60 cm. These imaging gradients are conceptually similar to the main magnetic fields, where current through a loop of wire generates a magnetic field. Now if we were to add another coil of wire, with current in a counter propagating direction and a certain distance away from the first, the resultant magnetic fields cancel each other at the iso-center of this distance and increase linearly as we move away from the iso-center, thus creating our varying magnetic fields for imaging. Finally, RF coils can be split into two categories, either transmit (Tx) or receive (Rx). The Tx coils are utilized to excite the spin system through the use of an RF pulse. Through the use of a frequency synthesizer oscillating at the larmor frequency of the specimens, the output is then modulated by a pulse shaper to take on the form of an RF pulse, thus resulting in spin system excitation. In order to receive the resultant weak echoes induced, the RX coil must amplify the signal (close to coil, to avoid external signal interference) and demodulate it to remove the unwanted larmor frequency components to be left with the low frequency components as a result of the varying gradient fields applied. The signal is then passed through an analog to digital (ADC) converter and sent to the image reconstruction computers to extract the spatial information of the acquired signals (150, 178).

2.1.2 Spatial Encoding and Pulse Sequences

Spatial encoding of the induced signals is achieved almost entirely through the use of the spatially varying gradients. Superimposing the main magnetic field (B_o) with these gradients generates a spatially dependent variation in the larmor frequency of the desired spins, resulting in selective region excitation and position encoding within. Selective excitation of a slab of interest is achieved by superimposing the magnetic field with a gradient that varies perpendicularly to it, in the case of axial acquisitions, this would be the gradient in the z-direction (G_z). Application of an RF pulse tuned to the frequency bandwidth of this slab results in excitation of the spins within, following which spatial encoding can be applied. This is achieved by frequency and phase encoding of the spin system. For simplicity purposes, let's assume an axial acquisition, with the z-direction gradient representing the slice-selective gradient, while the x and y-direction gradients representing the frequency and phase encoding ones respectively. Turning on the phase encoding gradients induces a spatially varying phase shift, dependent upon magnitude and duration of the gradient, such that each line (y-direction) throughout the imaged slab has a unique phase shift. Furthermore, turning on the frequency encoding gradients induces similar effects upon the underlying spins, such that their precession speeds are spatially dependent as well. The combination of these three encoding mechanisms and the application of a two dimensional Fourier Transform (2D FT) (x- and y-direction) upon the acquired signal allows for proper voxel identification (150, 178).

Readout of the excited spins is achieved only when the magnetization vector of the excited spin system is rotated into the transverse plane of the field (due to RF pulse) such that the vector is perpendicular with the gradients. Prior to excitation, the magnetization vector is referred to as the longitudinal magnetization (M_z), representing the sum of all magnetization available within the specimen placed inside the magnetic field. While the vector flipped into the transverse plane is referred to as the transverse magnetization (M_{xy}). The flexible nature of MRI lies within the ability to achieve

different combinations of excitation and contrast manipulation through the use of the slice-selective, frequency and phase encoding gradients. This combination is referred to as a pulse sequence. Conventional imaging pulse sequences, such as Spin Echo (SE) and Inversion Recovery (IR) rely on the use of multiple RF pulses for the excitation and refocusing of the spins into the transverse plane. Once this is achieved, repetition of the procedure is only allowed following complete recovery of the magnetization to the longitudinal plane (pre-excitation) (1, 75, 178).

More recently, advancements in gradient hardware and partial excitation of the longitudinal magnetization into the transverse plane through the use of smaller flip angles (α), than the conventional 90º ones, has shined a light into faster acquisitions, improved SNR, while maintaining identical spatial resolutions as achieved with conventional imaging pulse sequences. Fast Low Angle Shot (FLASH) and Fast Imaging with Steady Precession (FISP) are two pulse sequences from the gradient Echo (GRE) family of sequences that have allowed for such achievements (Figure 3). Both sequences operate under identical principles, but vary in their contrast manipulation characteristics (1).

2.1.3 Image Quality Considerations

Image quality is assessed by the signal to noise ratio (SNR), which is a measure of single corruption via noise. In MRI, noise factors include magnetic field inhomogeneities, patient based sources such as motion causing artifacts and image acquisition and reconstruction parameters. The image acquisition and reconstruction are of upmost importance as control of these parameters is much more feasible than the aforementioned ones. These parameters include magnetic field strength, field of view (FOV), number of acquisitions, slice thickness, inter-slice gap and receiver bandwidth to name a few. More often than not, the optimal slice thickness is defined as the thinnest one possible, but in MRI, the amount of noise increases (SNR↓) as a function of decreasing slice thickness. On the other hand, increasing the slice thickness results in numerous partial volume

artifacts, thus careful consideration must be taken to minimize the these deleterious effects. Although not ideal, these effects can be partially counteracted via increasing the number of planar acquisitions and or repetition times, at the cost of increased overall acquisition times. Due to the non-rectangular excitation profiles applied via the slice selective gradients, the inter-slice gaps play an important role in determining overall quality of the images. The lack of inter-slice spacing between the adjacently acquired slices results in cross-excitation between the slices, leading to saturation of the signals within and decreases in SNR. Receiver bandwidth relates to the range of frequencies collected on the receiver end, which is directly related to acquisition speed and noise, such that a wide bandwidth allows for a much faster acquisition with the introduction of more noise artifacts, while a narrower one results in SNR improvements at the cost of increased motion artifacts and slower acquisition times. Spatial resolution is one of the more important quality factors to consider in the overall acquisition process as it is a measure of how clearly one can distinguish structures with imaged volume. The relationship between the FOV and acquisition matrix (FOV / Matrix) is the main determining factor of pixel size. The complex interplay between these factors, results in trade-offs between SNR, acquisition times and spatial resolution. Another method of increasing the overall SNR is the use of higher magnetic fields. The number of protons that align with the main magnetic field increases as a function of increasing magnetic field, resulting in improved SNR. Due to other limiting factors such as safety concerns and application needs, as well as the inability to change the field with the push of a button, minimal consideration is usually given to the strength of the field (1, 75, 178).

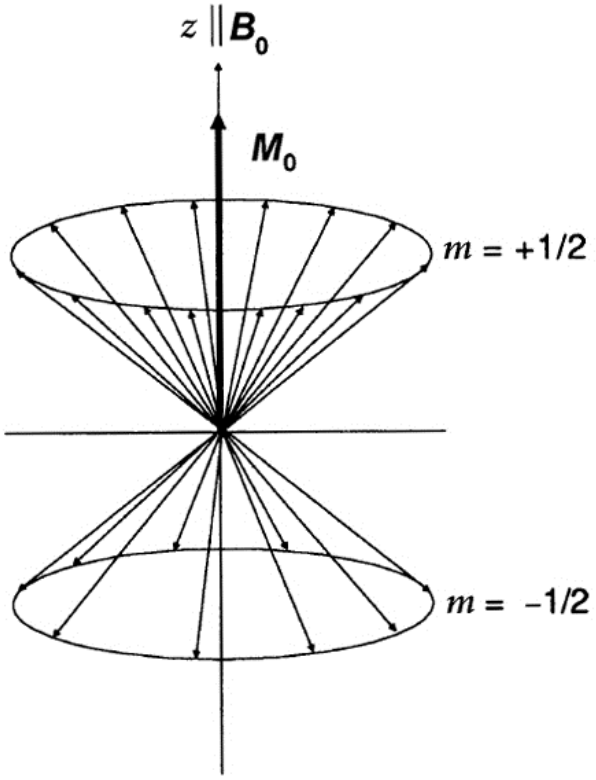

Figure 1. The origin of the macroscopic (net) magnetization of the nuclear spins within an external magnetic field, follows the Boltzman statistic, stating that a slightly larger number of spins will fall on the lower (m=+1/2) energy level parallel to the B0 field, in relation to the higher energy level (m=-1/2), or anti-parallel to the B0 field (1).

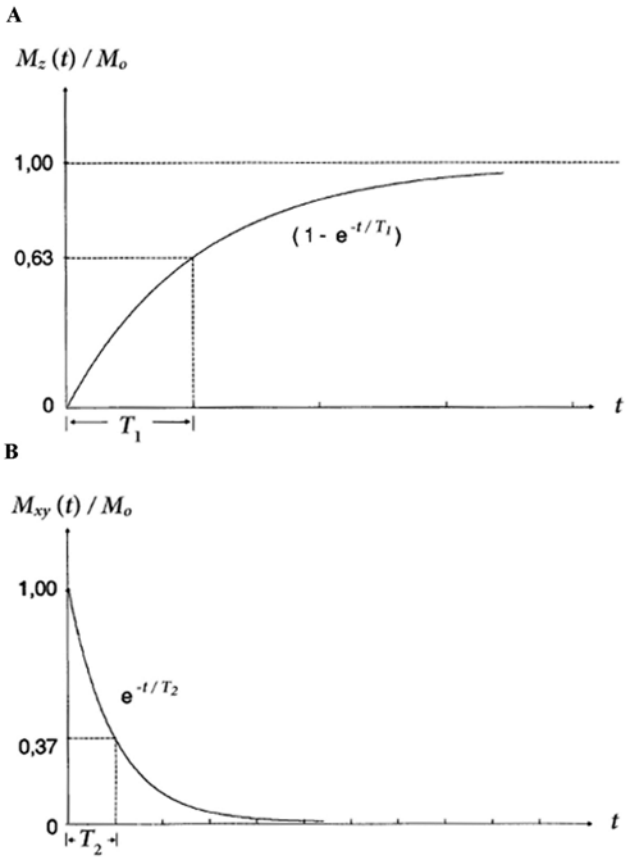

Figure 2. Graphical representation of longitudinal (A) and transverse (B) magnetization relaxation, following excitation by a 90º pulse. T_1 represents the time required for the longitudinal magnetization to reach 63% of its pre excitation equilibrium value, while T_2 is the time required for the transverse magnetization to reach 37% of its post excitation equilibrium (1).

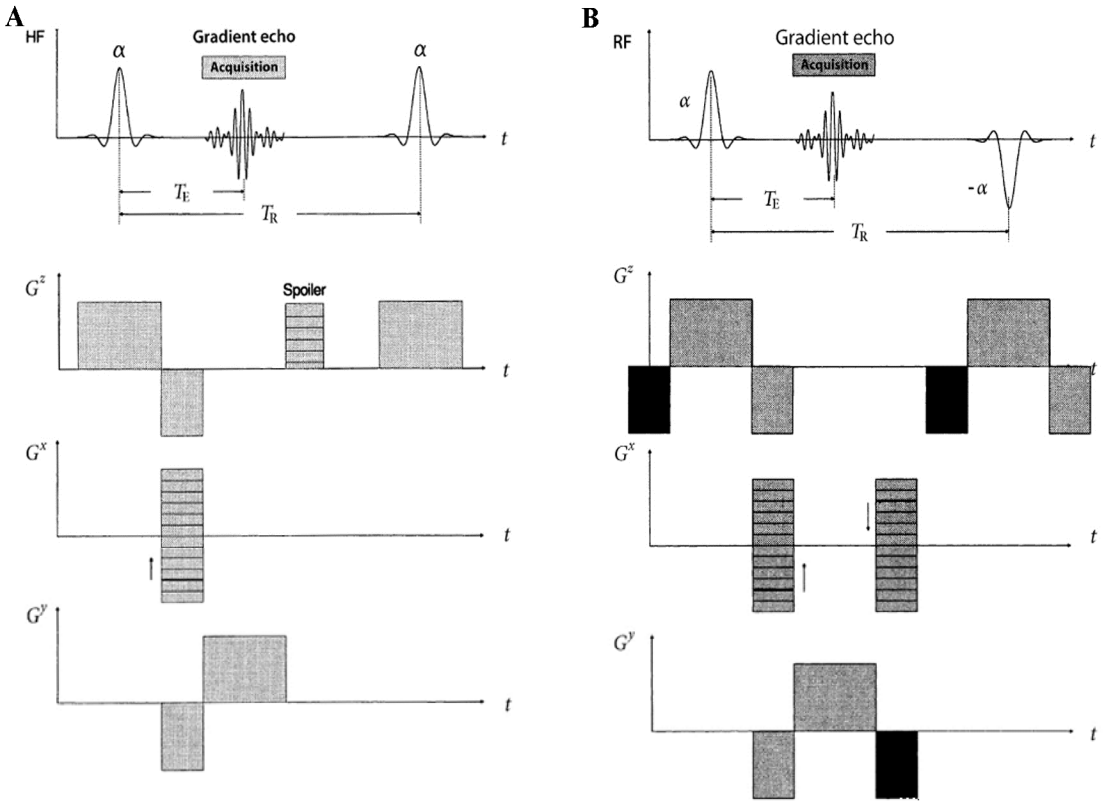

Figure 3. Gradient echo (GRE) based Fast Low Angle Shot (FLASH) Gradient schematic (A) and trueFISP gradient schematics (B). The main differences in acquisition between the two GRE based sequences revolve around the destruction of the remainder transverse magnetization following each acquisition in the FLASH and refocusing of it in the trueFISP (1).

2.2 Pulmonary Physiology

2.2.1 Structure and Function

The lung is compromised of approximately 300 million alveoli, generating up to 6 liters of volume and 85m^2 of surface area for gas exchange. The most important element in the gas exchange process is the blood gas interface, which allows diffusion of oxygen (O_2) and carbon dioxide (CO_2) between the blood and the alveoli based on a high to low gradient. Governed by Fick's diffusion law, the amount of gas moving across the interface is proportional to the area and inversely proportional to the thickness, thus the alveoli are wrapped in capillaries to increase the efficiency of the gas exchange process. Air reaches the alveoli via a series of branching airways and airspaces which are divided into two zones based on their unique features, the conducting zone and the transitional (respiratory) zone. As the name implies, conduction (bulk flow) is the main driving force of gas flow through the conducting zone which encompasses levels 1-16, starting with the trachea at the uppermost level and further dividing into main, lobar and segmental branches and ending at the terminal bronchioles. The terminal bronchioles are considered to be the smallest airways without alveolar lining and are the closest to the gas exchange regions. The transitional (respiratory) zone is compromised of the respiratory bronchioles, alveolar ducts and sacs and encompasses levels 17-23. The respiratory bronchioles are partially lined with alveoli, while the alveolar ducts are completely lined. Airflow through these branches is a multi-faceted process, initiated by diaphragmatic and intercostal muscle contractions, leading to the descent of the diaphragm and movement of the intercostals muscles, thus increasing the cross-sectional area of the thoracic cavity. As mentioned previously, bulk flow is the main process by which gas flows through the conducting zone, distal to which gas flows via diffusion, due to increases in cross-sectional area and slower velocities throughout. The elasticity of the lung allows it to return to its pre-inspiratory volume. Given that the lung is the largest surface area

exposed to a hostile environment, several mechanism are available for eliminating inhaled particles such as mucous, cilia in the conducting airways (which can be paralyzed by toxins) and macrophages in the alveoli (91, 179, 180).

Similar to the airways the blood vessels are a series of branching tubes starting with the pulmonary arteries and leading to the capillaries and returning to the pulmonary veins. Initially the arteries and veins run close together, but at the lobar levels, they separate, while the arteries follow the bronchi. The capillaries form a dense network on the alveolar walls, generating an almost continuous sheet facilitating efficient gas exchange (91, 92, 179, 181).

2.2.2 Ventilation

Ventilation is a process by which the lungs exchange gases between the outside air (relative to body) and alveolar compartments, where gas flow is driven by the apparent gradient between the outside atmospheric pressures and that within the lungs (atmospheric pressure > alveolar pressure during inspiration and vice versa for expiration) (179). Respiratory movements regulating ventilation are controlled by afferent nervous stimulation, either through chemical stimuli and/or the vagus nerve. The excess of O_2 and/or the excess CO_2 within the inspiratory volumes, leads to the increased respiratory center activity, resulting in increased respiration efforts. Slight changes in overall alveolar CO2 concentration can double alveolar ventilation during rest (179, 180).

Attempts to quantitate the regional distribution ventilation nitrogen washout curve technique (36), regional density changes observed in CT (67, 70), regional strain measurements obtained via bi-plane x-ray fluoroscopy (73, 77), as well as the distribution of radio-active 133Xenon gas following inhalation (135, 136), have paved the way for future methods and needs in this emerging field (68). Lung scintigraphy using macro-aggregates of albumin can facilitate the detection of pulmonary emboli (96, 97), while the use of radio-active tracer gases such as ^{15}O (O_2 isotope), ^{13}N (nitrogen radio-isotope) and ^{133}Xe (xenon isotope) can provide the means for a topographic evaluation of lung

ventilation. Although ideal, the technique suffers from a few shortcomings which include high cost of the nitrogen and oxygen isotopes utilized, along with their short half-lives, but more notably its gross estimation of lung ventilation (135, 136). PET complemented with the use of inhaled radio-active tracer gases such as ^{19}Ne (neon isotope) and ^{13}N can measure regional ventilation, by means of its minimal invasiveness, low radiation exposure to subject and the administration of a single dose to acquire the data (113, 131, 132, 166). The main disadvantage of the use of PET was purely physics based, as the resolution of the extracted functional maps were dependent upon the distance traveled by each positron before annihilation through its collision with an electron, which produces the pair of gamma waves used in detection and localization of the phenomenon. Furthermore, the inhalation of fluorescent microspheres (FMS) can also provide a relatively regional evaluation of pulmonary ventilation using distribution of microspheres in each analyzed lung segment. This technique proved flawed as the use of large volume elements in analysis biased the data based on the convective movement of the gases throughout, where as the actual deposition of the micron-based aerosol particles is strictly based on gravitational effects and their inertial impact, far from relating to alveolar ventilation (133, 134, 164). More recently, the introduction of Dual Energy (DE) CT, has shown promise into simplistic lung ventilation assessments of both normal and abnormal subjects alike, with exceptional spatial resolutions, through the use of xenon as a contrast agent (24, 25, 56, 57). Following a similar trend as the Xe-MDCT methodologies developed within our laboratories, ventilation assessments via DECT can be carried out in a single or multi-breath fashion (24, 56).

2.3 Imaging Techniques

2.3.1 Hyperpolarized ^{3}Helium MRI

Hyperpolarized Noble gas imaging has established itself as one of the most complex, yet effective pulmonary MRI techniques available. Hyperpolarization of the noble gases, dose preparation, gas transportation, storage and administration, the non-renewable nature of the signal and the need for a broadband RF amplification system are some of the factors creating the overall complexity involved with these methods. ^{3}He is an inert, stable, non-toxic isotope of ^{4}He that is a byproduct of nuclear tritium decay. Although being a byproduct of nuclear waste decay sounds extremely unpleasing, the ^{3}He atom is stable, with no adverse side effects upon administration other than slight dryness of contacted surfaces. Major advantages of ^{3}He include its small molecular size, thus making it lighter than air and easier to breath (especially helpful in diseased pulmonary states), its confinement to the airspaces due to a low solubility coefficient in water molecules and long T_1 relaxation times as a result of the non-existence of any electrical field gradients or magnetic moment production by the electrons in the filled orbitals (90). The inherent complexities involved, in combination with the additional costs involved with the technique have limited the advancement of the HP ^{3}He MRI methodology to a few centers spread throughout North America and Europe. Additionally, recent political agendas pertaining to the use of ^{3}He as means for weapons detection, have created a huge bottleneck in gas supplies (84), hindering the advancements achievable throughout the past year and resulting in a global wide renewed interest in ^{129}Xe, due to its natural abundance.

2.3.1.1 Hyperpolarization, Storage and Administration

Hyperpolarization is the process of increasing the overall angular momentum of nuclear and electron spins of an atom above its thermal equilibrium state through the use

of externally applied energy, which is performed entirely outside the MR magnetic fields. The need for this increase in angular momentum makes up for the low density of the gas, when compared with its liquid rival water, which is achieved through the use of circularly polarized laser light, a process defined as optical pumping (OP). Currently there are two different techniques widely used for optical pumping; spin-exchange (SEOP), which is suitable for both ^{3}He and ^{129}Xe and metastability-exchange (MEOP), which is only suitable for ^{3}He (20). SEOP is achieved by optically pumping an intermediary alkali metal vapor, followed by spin exchange between the alkali vapor and the noble gas (Figure 4). This process is successful only for noble gases with quantum spins equal to one-half (I = ½), because of their stability and longer longitudinal relaxation times (T_1), involved with loss of the angular momentum. The noble gas is first pressurized (10 bar) into a glass chamber, containing trace amounts of an alkali metal (ex. Rubidium) and nitrogen and surrounded by a low magnetic field. Heating of the chamber creates a dense vapor of the alkali metal, allowing absorption of the circularly polarized laser light (30-140 Watts) spectrum being shined into the chamber (78, 90). The resonant laser is tuned such that its spectrum is that of the electron spins of the alkali metal vapor (Rb = 794.8 nm), thus allowing an efficient transfer of the angular momentum of the laser photons to the electron spins of the atoms (172). Through random hyperfine collisions between the excited state alkali metal atoms and the noble gas atoms, this angular momentum is partially transferred to the nuclear spins of the noble gas, with an efficiency of approximately 0.1-1% for ^{3}He and 4% for ^{129}Xe. Given the weak state of these hyperfine interactions, polarization times in excess of 10 hrs are required to reach polarization levels of +20% for a one liter batch of ^{3}He and 1 hr for a half liter batch of ^{129}Xe up to 5% (171, 172). In MEOP, the process of nuclear spin hyperpolarization is conducted directly between the circularly polarized laser light and the noble gas atoms (^{3}He only). The resonant laser light spectrum is thus tuned to the frequency of ^{3}He (1083 nm), which in return excites the electron spins of the ^{3}He atoms and through a series of hyperfine

interactions between the excited state and ground state ^{3}He atoms, this polarization is transferred to the nuclear spins (Figure 4). This process is advantageous in the fact that there is no need for an intermediary substance to transfer the polarization. A major concern with this technique is the need for powerful laser diodes to polarize the helium atoms in an unpressurized state, which have recently become commercially available. Also due to the low pressures needed for polarization, only small amounts of ^{3}He are polarized per run, thus requiring the need for compression and storage of the already polarized batches to accumulate large enough doses for dispensing (78, 90).

The efficiency of the polarization step in SEOP largely depends on the density of the alkali metal vapor, integrity of the glass chamber and spectrum of the laser light. Following completion of the polarization process, the chamber is cooled to room temperature, to allow the alkali metal to return to its solid state, eliminating its gaseous presence within the dispensed polarized gas. In the case of MEOP the gas is compressed and stored. The hyperpolarized doses of noble gas are then dispensed into Tedlar® plastic bags, equipped with medical grade Tygon® tubing. The Tedlar bags are free from any paramagnetic impurities to minimize the relaxation rate of the hyperpolarized noble gas, while the Tygon tubing is efficient for administration of the gas doses to the subjects with minimal obstruction. During transportation, the hyperpolarized noble gases are shielded via a homogenous magnetic field (0.1 - 0.5 *mT*), to reduce the effects of the various inhomogeneous external magnetic fields along the path (compressors, elevators, pumps, etc ...) between the polarizer apparatus and the MRI magnet. Administration of the doses can be either directly from the Tedlar plastic bags or through an MRI compatible ventilation system with non-metallic valves and compression scheme. The latter is suitable for small scale animal experiments, where control of tidal volume and breath-holds is difficult (78, 79, 90).

Volumes of administered breath-hold doses have generally been (300-500ml) hyperpolarized noble gas and (500-700ml) medical nitrogen. Given that most polarizers

available to research community can only produce one liter at a time, the available gas must be rationed to allow for multiple imaging sessions. Nitrogen is a biologically inert molecule, thus not interacting with the hyperpolarized noble gas molecules to decrease the apparent signal. Its use serves the function of a filler agent to achieve desired tidal volumes. A major obstacle in repeatability of imaging sessions is the need for an accurate dose delivery of the administered volumes in order to achieve equal tidal volumes and thoracic pressures. The tidal volume of the patient must be monitored accurately alongside the maximum pressures achieved during a breath-hold, to allow for proper quantification and evaluation of resultant datasets (170).

^{3}He and differ from ^{1}H in properties: they will both precess at entirely different frequencies (Larmor frequency – dependent upon externally applied magnetic field) once introduced into an external magnetic field [4]. Therefore, MR scanners must be equipped with broadband capable RF transmitters, receivers and amplifiers, to allow proper conduction of the imaging protocols. This intrinsic difference also necessitates the need for a completely different Tx-Rx RF coil arrays that are specifically tuned to the frequency of the tracer noble gas. This frequency varies as a function of the magnetic field strength, thus for different magnetic fields, different coils are required (109).

2.3.1.2 Static Ventilation Imaging

Unlike normal MR imaging, the signal obtainable from hyperpolarized ^{3}He doses is non-renewable, thus meaning that a single 90º flip angle will completely quench all available non-equilibrium polarization (net magnetization) within a medium. Therefore the need for low flip angle pulse sequences with careful considerations of sequence parameters is a must when performing any noble gas imaging. For the purpose of static 2D and 3D ventilation imaging, FLASH GRE sequences have been utilized widely, almost becoming the gold standard for such imaging techniques. In these sequences the flip angle value ranges between 2º-10º, allowing proper rationing of the available

magnetization. In static ventilation imaging, the acquired series of images is of the spin density of the gas itself during a breath-hold, resulting in a positive-linear relationship between the acquired signals and amount of helium within. One limitation of this procedure is the inability to evaluate and assess blocked and restricted lung regions, due to the absence of the tracer gas. Ventilation maps obtained are unit-less quantifications of the overall ventilation distribution throughout the lungs. There are no measureable physiological parameters involved, but the maps can be utilized as a screening tool for determining integrity and severity of damage. Evaluation of the acquired ventilation maps is dependent upon criterion set by the evaluators, such as homogeneity of gas distribution, number and size of defects and SNR (45, 170).

A typical imaging protocol would consist of the acquisition of approximately 6-8 coronal images in the supine position, requiring a breath-hold of approximately 10-12 seconds, with spatial resolutions far better than obtainable with nuclear medicine techniques (~2mm). Although the ventilation maps are unit-less and provide no direct physiological information, their usefulness has been demonstrated in assessing total lung volumes with great correlations with PFTs (45). Static ventilation of normal volunteers appears to have a homogenous gas distribution throughout the images with minimal to no ventilation defects (Figure 5) (79, 165). These minor defects are expected due to the awkward positioning of the subject along with the weight of the lungs pushing down on the posterior regions. On the other hand, ventilation maps acquired of asthmatic subjects, showed multiple ventilation defects alongside low SNR and an inhomogeneous gas distribution. The ventilation defects found in asthmatic patients are mostly due to inflamed and restricted airways, limiting or completely obstructing the flow of helium. The increase of the ventilation defects found in these asthmatic subjects, correlated well with decreased values of spirometry obtained prior to imaging. In a couple of asthmatic subjects, bronchodilators were administered via inhalation and a second imaging series was conducted a few days following the original scans. In these subjects, the ventilation

maps showed no ventilation defects and a more homogenous gas distribution throughout the images, thus showing the usefulness of such a simple and quick technique in follow-ups of drug administration and disease progress (5, 81).

2.3.1.3 Apparent Diffusion Coefficient (ADC)

The ^{3}He ADC technique is a mean of evaluating and probing the lung microstructure, connecting pores and pathways, leading to an inclusive assessment of the integrity and size of such structures through the exploitation of the high diffusive nature of ^{3}He. The diffusion rate (D) of free ^{3}He at room temperature is approximately 1.8 cm^2/s, while that of dilute ^{3}He in nitrogen is ~ 0.8 cm^2/s (33). Diffusion as used in this context doesn't refer to the crossing of the alveolar-capillary membrane via chemical gradients, but rather displacement according to Brownian Laws of random motion. According to Brownian Laws, the root mean square (*rms*) atomic displacement of helium along a single axis during a given observation time (t) is

$$\sqrt{2\,Dt}$$

resulting in an overall displacement of 0.7-0.8 mm for dilute ^{3}He. The use of dilute ^{3}He is the most reasonable estimate, as during any given ^{3}He examination, a dose of approximately 300-500 ml of ^{3}He is administered for a total lung volume ranging between 5-6 liters, creating a very dilute mixture. This displacement estimate can be observed in the larger sized airways (trachea, primary bronchi), due to their larger dimensions, creating an obstacle free zone during a given observation time. The smaller size of the alveoli (radius ≈ 0.08mm) alongside their walls, alveolar ducts, sacs and connecting bronchioles all act together as obstacles restricting the path of displacement, creating a smaller measureable D which is referred to as the ADC (Figure 6)(16, 110, 146).

The diffusion of ^{3}He is easily quantified via the *Stejskal-Tanner* pulsed gradient field setup, where a set of specialized bi-polar gradients are incorporated into the startup

of an MRI sequence (most likely a FLASH sequence) (27, 51). The bi-polar gradients are a set of linearly changing gradient fields (equal magnitude, different polarity) along a given direction, inducing an overall phase shift proportional to amount of displacement taking place throughout the duration of the gradients (Figure 6). This displacement is probed on a pixel-by-pixel basis, where the net phase shift given within a single pixel acts to decrease the overall available signal. The amount of diffusion sensitization of the bi-polar gradient fields is determined by their b-value. This value is proportional to the gyromagnetic ratio of ^{3}He, ramp-up and ramp-down times of the gradient fields, total duration and delay between positive and negative lobes. In order to quantify the measured displacement a baseline (reference image) must be acquired to evaluate against; therefore a typical examination would involve the acquisition of two images, where the first image has zero diffusion sensitization ($b=0$) and the second some quantifiable amount of diffusion sensitization ($b>0$). One must take into consideration the non-renewable nature of the available polarization, and thus b-values utilized in experiments must be small to ration the amount of signal available. This diffusion is then mathematically quantified with the *Stejskal-Tanner* diffusion equation

$$S_1 = S_0.e^{-(b.ADC)}$$

where S_1 is the signal intensity of the non-diffusion weighted image, S_o is the signal intensity of the diffusion weighted image, b is the amount of diffusion sensitization and D is the calculated diffusion rate (27). Diffusion maps are then created from these calculated values on a pixel-by-pixel basis, through a simple solution of the given equation. This large free diffusivity observed is a result of two intrinsic properties of the ^{3}He molecule itself, 1) the small atomic mass relates to a high thermal velocity, allowing the traversal of relatively long distances within a few milliseconds, along with 2) a small diameter, leading to an even smaller cross-sectional area, thus minimizing the effects of collisions with the lung walls and other gas molecules (33, 146).

ADC maps of normal healthy volunteers have shown to be homogenous and uniform, illustrating the overall integrity of the lung structures and airspaces, which is expected in an intact lung. On the other hand, the opposite was found true for emphysema subjects, where the ADC maps were non-uniform and contained larger diffusion values (18, 41, 81, 146, 160). This non-uniformity of the ADC values correlates well with the nature of the disease, where the degree and location of destruction varies throughout the lung. Reported ADC values in normals range between 0.17 cm^2/s and 0.24 cm^2/s with a mean of 0.2 cm^2/s, a factor of four smaller than that of the dilute helium, revealing the overall restricted nature of the traversed environment (33, 41). Morbach et al. reported average ADC values of 0.18 cm^2/s and 0.27 cm^2/s for normals and emphysema patients respectively. The reproducibility of the technique was also demonstrated on a global and ROI basis with accuracy of 2% and 6% respectively, demonstrating the overall feasibility of the technique. Due to gravitational effects on the human body, the lower most regions of the lungs are considered dependent regions, whereas the upper most regions are considered non-dependent (110). During a given ^3He examination, the subject is placed supine inside the bore of the magnet, thus changing the gravitationally affected regions from cranio-caudal to antero-posterior for the dependent – nondependent regions respectively. This gravitational gradient is observed, where ADC values of the most posterior regions are lower than those of the anterior regions. This is possibly explained by the compression of the lung tissue in the posterior regions of the lung, due to the effects of gravity and the weight of the lungs and heart (81). Aside from quantification of disease severity, ADC has also been utilized in evaluating lung volume reduction surgery (LVRS) patients. The surgery itself improves the respiratory dynamics, elastic recoil and chest wall function, by removal of non-functional lung regions (ex. severe emphysema), which in turn improves the overall functionality of the intact regions. ADC maps obtained post-LVRS showed significant changes in the overall diffusion distribution

throughout the lung, in comparison with pre-LVRS maps, illustrating improved function of possibly restricted or compressed lung regions (33).

In the past, only invasive techniques such as microscopy or micro-CT of lung lobes were available to evaluate the intrinsic properties of the lung microstructure. The achievable results demonstrated by the ^{3}He ADC technique have shined a light into a new non-invasive radiation free measure of evaluating lung microstructure, with excellent depiction of structural integrity and degrees of destruction. Although ADC measurements have set a new standard in pulmonary evaluation, it suffers from a few drawbacks. First, the high cost and complexity involved with polarization, storage and administration of the noble gas doses, scanner time costs and the need for a broadband capable scanner and specialized RF coil for transmission and reception of ^{3}He signals, pose a limitation towards clinical acceptance, as most centers will not have the ability to afford and maintain such costs and requirements, along with the specialized personnel required to conduct the procedures. Second, in order to accurately and efficiently assess the achievable results and statistical coherence of the technique, all imaging parameters must be maintained throughout, such that the tidal volumes, breath-hold pressures and imaging planes are identical from one subject to another. Although not impossible, this perfection requirement along with the added complexity of the procedure, overshadow the excellent visualization and assessment achievable via this technique. Last but not least, the clinical relevance of utilizing ^{3}He in the evaluation of the airspaces might not be optimal in detecting early micro-structural changes. This does not come as a surprise due to the naturally small size of the ^{3}He atoms, resulting in a differentiation between free and restricted diffusion in geometries much larger in size than the alveoli under investigation. Thus the utilization of a larger atom which would differentiate between free and restricted diffusions on the order of the alveolar dimensions would be of great relevance.

2.3.2 Hyperpolarized ^{129}Xenon Imaging

Hyperpolarized ^{3}He has been the preference of many researchers and scientist in gas-phase measurements of functional and structural pulmonary parameters, partially due to the larger gyromagnetic ratio and less complex optical pumping techniques, thus achieving an overall larger polarization level which leads to higher signal intensities and better resolutions. Although the higher signal advantage of ^{3}He over ^{129}Xe prompts this biased selection, the intrinsic characteristics of ^{129}Xe gas make it suitable in probing different pulmonary function characteristics than achievable by ^{3}He. More recently, the increasing costs of raw ^{3}He gas and improvements in the overall design and process of the polarization equipment have sparked a new interest in this modality (65). Upon inhalation of the xenon gas, a small fraction is absorbed into the moist parenchyma tissue, which then further diffuses into the capillary circulation, a process that is continually attempting to reach equilibration of concentrations in the airspaces, tissue and blood. Given the high sensitivity to its surroundings, hyperpolarized ^{129}Xe is observed as three different resonant frequencies arising from the three different compartments (airspaces, parenchyma and blood) (Figure 7). The difference in frequencies between the gas and dissolved phase ^{129}Xe is large enough to allow acquisition of both within a single rapid measurement with no complications. This unique intrinsic characteristic of ^{129}Xe has allowed quantification of pulmonary pO_2, low resolution static ventilation images, diffusion capacity of the lungs and surface-to-volume ratio of the alveolar-capillary membrane, the latter two which were not achievable with ^{3}He (121, 138, 139).

Until recently, the low achievable polarization (5-7%) levels of ^{129}Xe have crippled its imaging power and applications. This low level of polarization is a direct result of the depolarizing effect experienced by the optically pumped rubidium atoms before they have a chance to polarize the ^{129}Xe nuclear spins, due to their low photon efficiency. A new scheme of SEOP ^{129}Xe polarization, involving a combination of low xenon partial pressures, higher velocity gas flows and longer polarization chambers, has

created a more efficient optical pumping solution to the depolarizing effect experienced by the rubidium atoms, achieving polarization rates of up to 50%. This advancement in production will essentially improve the overall achievable image quality and possibly improve knowledge regarding the diagnostic power of ^{129}Xe (121).

A major limitation and drawback involved with the use of xenon gas is its anesthetic nature. Prior to its use in CT and MR imaging procedures, xenon found its niche as a general anesthetic. It has been shown that inhalation of high concentrations of this gas have lead to side effects such as euphoria, breathing difficulties as expect with a heavier molecule, and loss of consciousness (35). Therefore administered doses are limited to tidal volume mixtures of at least 21% oxygen and no more than 70% ^{129}Xe, while maintaining the alveolar xenon concentrations well below 35% (lower limit of anesthetic effect). In most circumstances, this is not an issue as most procedures are conducted in one or two breath-holds, with minimal to no adverse events (119, 138). On the other hand, given the low achievable signal improvements over thermal equilibrium along with the dose concentration limitations, the use of this technique in an attempt to produce superior image quality to its opponent will be somewhat of a challenging task.

2.3.2.1 Chemical Shift Imaging (CSI)

The first observations of the unique phases of hyperpolarized ^{129}Xe were achieved via chemical shift spectroscopy. In layman terms, a spectroscopic evaluation of a given volume produces a resultant spectrum of all frequencies apparent within. One would consider the accidental case where proton frequencies appear in this spectrum and possibly ruin or lower the quality of the data, but given the different precession frequencies, RF coils utilized in all hyperpolarized noble gas imaging are tuned specifically to the molecule's larmor frequency eliminating the possibility of acquiring false frequencies. The key factor in this method is the recognition that the unique phases

appear at different peaks in the acquired spectrum, allowing a simple and effective temporal evaluation of their progress (112).

By taking advantage of the never ending battle of concentration equilibration between the gas and dissolved phase ^{129}Xe and the employment of multiple free induction decay (FID) acquisitions over the time of an imaging protocol, this spectrum along with its variations are extracted. In a given acquired spectrum, the zero-reference frequency is that of gas-phase hyperpolarized ^{129}Xe @ 0 ppm, while the dissolved phase hyperpolarized ^{129}Xe is shifted approximately 200 ppm away from the reference (Figure 7). This shifted frequency gives rise to two peaks, relating to the tissue and blood accumulations, the latter of which is minimal as the circulatory system is continuously renewing the supply of blood in any given region (112, 138).

2.3.2.1 Alveolar Surface Area measurements (S_A/V_{gas})

As the major function of the lung is exchange of O_2 and CO_2, the ability to regionally and globally quantify the available surface-area-to-volume ratios for this exchange to take place, can provide an insight into the progression of pathological conditions affecting the alveolar and parenchymal integrity. There are numerous techniques for acquiring this parameter such as stereology, μCT and confocal microscopy, all of which are highly invasive and destructive, limiting its applicability in human subjects. A solution to this dilemma is the temporal spectroscopic evaluation of the different ^{129}Xe phases, which has given rise to a minimally invasive procedure for acquiring the surface-area-to-volume ratios of the porous nature of the pulmonary structures (21).

The use of Chemical Shift Saturation Recovery (CSSR) imaging has made this acquisition possible, through the monitoring of the polarization transfer rates between the gaseous phase hyperpolarized ^{129}Xe in the airspaces and the dissolved phase in the solid tissue. This is accomplished by completely saturating (quenching) the available signal of

dissolved ^{129}Xe in the tissue, via a frequency selective pulse, followed by the measurement of its recovery through transfer of polarized molecules from the airspace pores to the tissue. The preliminary quenching results in an initial baseline condition of polarized ^{129}Xe in the gas space and un-polarized ^{129}Xe in the tissue space (21, 121).Through the fitting of a 1D diffusion equation (Fick's 2nd Law), which states that the rate of change of a concentration in a volume element within a diffusion field is proportional to the rate of change at that point in the field, information regarding the thickness of the alveolar-capillary membrane, blood volume and perfusion rates can be extracted. The general pulse sequence architecture utilized in these acquisitions starts out by initially sampling the available ^{129}Xe polarization levels via a small flip angle as to not destroy all available polarization. Once an initial amplitude value is determined, a series of selective saturation pulses are applied at the frequency (≈ 200 ppm away from reference) of the dissolved phase ^{129}Xe, to completely destroy any available signal, allowing for a clean starting slate. Following the selective saturation of the dissolved state signal, a delay period is introduced to allow diffusion to take place. Finally, another frequency selective RF pulse is applied to the dissolved phase ^{129}Xe signal, not to completely eliminate its appearance, but rather to excite the available spins and observe its recovery. The repetition of this procedure allows temporal evaluation of peak times and magnitudes. This temporal assessment of diffusion progression through monitoring the appearance of the blood spectral peak has assisted in determining the overall thickness of the parenchymal layer (21).

The inter-pulse delay between selective saturation and excitation of the dissolved ^{129}Xe spins plays an important role in determining the thickness value calculated. Throughout the lungs, the different tissue layers all have different thicknesses, leading to different diffusion times, affecting the appearance of peaks in those compartments. Therefore, careful selection of the delay time between these pulses, determines the level of tissue thickness evaluation achievable. Although the idea is conceptually pleasing,

minimal results have been presented in human subjects verifying the validity or sensitivity of the technique. Most of the work has been conducted on porous materials that exhibit similar characteristic sizes as the alveoli, along with some small number of human studies, the latter which has not been compared with gold standard measurements obtainable via standard histology measurements in animals and excised lungs (21, 121).

2.3.2.3 Xenon Transfer Contrast (XTC)

The unique dissolved phase imaging of hyperpolarized ^{129}Xe is not only limited to spectroscopic procedures, but can also be extended to probe the lung physiology along with diffusion capacity. XTC is the indirect evaluation of the dissolved phase signal via the monitoring of the gas phase signal attenuation. A typical procedure consists of two separate breath-hold acquisitions via 2D FLASH sequences, referred to as a control and XTC experiment. In each one of these breath-holds two separate images are acquired, with approximately 40 frequency selective RF pulses in between the acquisition of the first and second image. In the control experiment, the selective preparatory RF pulses are applied at an off resonance frequency of approximately -200 ppm (*mirrored location on other side of the 0 ppm reference*), serving as the control condition. Since the RF pulses are only applied at this off resonance frequency, leaving the dissolved and gas phase frequencies un-touched, the resultant image represents the recovery of the gas phase signal following T_1 depolarization effects experienced by the applied RF pulses along with loss of hyperpolarized ^{129}Xe atoms due to the blood circulation. In the XTC experiment, the same two images are acquired, except for the frequency selective RF pulses are applied at the resonance frequency of the dissolved-phase ^{129}Xe. This preparatory saturation of the dissolved-phase signal creates a map illustrating recovery of the available signal in the tissue following the exchange with the gas-phase signal. By correcting the XTC experiment for the observable T_1 depolarizing effects obtained in the control experiment, a regional map representing the exchange between the airspaces and

tissue is obtained (138, 139). This map represents the overall integrity of the exchange process within the lungs and can be used to assess the morphological changes apparent during disease onset. This double breath-hold evaluation technique is not very efficient, due to the need for accurate monitoring of the administered tidal volumes along with airspace pressures following breath-holds, creating complexities during the post processing of the data.

Patz et al. have proposed a single breath technique (SB XTC) to acquire a series of three images representing the control and exchange images. The first acquired image is a simple static ventilation image to be utilized as the baseline. The second image in the series is acquired following the application of the same sequence of preparatory RF pulses at the off resonance frequency of -200 ppm. This difference in acquisition creates an observable change in signal intensities between the first and second images primarily due to the T_1 depolarizing effects of the RF pulses and dipolar interactions with molecular oxygen. The third and final image is acquired following the application of a sequence of RF pulses centered at the frequency of the dissolved phase signal. Now the observed difference between the second and third images is due to the previously mentioned depolarizing effects along with exchange between the gas and tissue compartments of the lung. A simple subtraction between the first and second images allows quantification of the T_1 decay due to the molecular oxygen interactions and applied RF pulses, while another subtraction between the second and third images creates a gas exchange efficiency map representing the evaluated lungs. Analysis of the maps yields a very simple observation: higher values are related to increased gas exchange, while lower values represent a decreased gas exchange, which has been demonstrated and evaluated in a number of human subjects (Figure 8) (121).

2.3.2.4 Intra-Pulmonary pO_2

As mentioned previously, hyperpolarized noble gas atoms are sensitive to the regionally varying intrapulmonary pO_2 due to the depolarizing effects experienced from the dipolar interactions with the molecular oxygen in the airspaces. This observation can also be utilized in ^{129}Xe imaging to create representative maps of regionally and temporally varying oxygen partial pressures. A pO_2 map can easily be calculated from the images acquired via the SB-XTC experiment. It was previously shown that the attenuation of a single RF pulse can be easily calculated and corrected for thus the application of RF corrections upon the second image in the acquisition pipeline facilitates the generation of a pO_2 map of the examined lungs. It seems almost straightforward, but one can't forget the complexities that were involved with acquiring these three images in the SB-XTC experiment (121).

The representative pO_2 maps demonstrate the previously mentioned gravity dependent ventilation and perfusion effects, resulting in higher pO2 values at the apex descending towards the base. This observation is self-explanatory as the ventilation and perfusion of the lung structures are much higher in the basal portions, resulting in more efficient transport of the molecular oxygen out of the airspaces, creating lower partial pressures and vice versa for the apex. One would expect to see this same gradient in the XTC gas transport maps, but in reality the gradient in completely flipped. Since the gas transport maps represent the regional efficiency of the gas transport, the higher values in the maps represent an increase in gas exchange leading to a decrease in the regionally available oxygen, thus creating a lower pO_2, while lower values in the maps represent a decrease in gas exchange, which demonstrates minimal removal of the available oxygen and therefore an increased pO_2 (121).

Although the complex interactions observed upon administration of ^{129}Xe have given rise to previously un-achievable diagnostic parameters, minimal experience and lack of proper understanding of measured parameters are major obstacles in the road

towards clinical acceptance. In the case of pO_2 maps, ^{3}He remains advantageous, as the solubility of ^{3}He in its surrounding is almost non-existent, reducing the overall needed for offsetting computations and preparatory procedures.

2.3.3 ^{9}Flourine Imaging

Available as a naturally abundant stable isotope of 6-Fluorine (^{6}F), ^{6}F is an excellent MR sensitive molecule as it possesses a spin quantum number of one half (I = ½), which allows it to be susceptible to the externally applied magnetic fields of the scanner. Albeit its recent development and introduction to the MR imaging community, ^{19}F containing liquids have been utilized in liquid ventilation for many years, due to its relatively low solubility in blood and high solubility in oxygen. Attempts have been made in the past to quantitatively image the lungs with these liquids, resulting in images with poor SNR and minimal spatial resolution (89).

Recently the focus has turned away from these ^{19}F containing liquids, towards the use of fluorinated gases in pulmonary assessment. The basis of imaging the lungs using ^{19}F in an acceptable fashion (i.e. minimal scans times, patient comfort), consists of choosing a gaseous molecule that possesses rapid relaxation properties and large a number of atoms per molecule, to allow multiple signal acquisitions (averages), providing large attainable signals. Sulfur Hexafluoride (SF_6), Tetrafluoromethane (CF_4) and Hexafluoroethane (C_2F_6) have meet these criteria as they posses very short relaxation properties along with being non-toxic and insoluble in the pulmonary airspaces and circulation. All these compounds contain ^{19}F, which is a large molecule containing a large number of atoms, allowing for maximal signal generation at thermally equilibrated conditions. The rapid relaxation properties possessed by these compounds allows for rapid repetition of the scanner RF pulses, acquiring multiple signal averages to make up for the low spin density available upon inhalation (145). The use of these inert compounds removes the need for complex polarization transfer processes as in

hyperpolarized noble gas imaging at the cost of inferior SNR and compressed timing constraints of the molecule relaxation properties, resulting in a small finite window to quantitatively assess the gas distribution through static and diffusion measurements (123). Initial testing of the concept in randomly selected ROIs of a phantom containing SF6 gas, produced extremely pleasing results, as the signal intensities within these ROIs was significantly higher than those acquired from a background ROI. It was also demonstrated that large flip angles can be utilized in the pulse sequence schematics, as the changes in the maximum achievable signals within the evaluated ROIs were minimal. The ability to utilize a larger flip angle than that of hyperpolarized noble gas imaging facilitates the incorporation of a larger number of gas spins into the measureable transverse plane magnetization, creating a substantially larger signal than that of the thermal equilibrium conditions (123, 145).

Schreiber et al. have performed static 2D (coronal and axial), 3D and wash-in and wash-out experiments using SF6 in in-vivo porcine lungs with acceptable results, through the use of a FLASH pulse sequence and a large number of signal averages. The static ventilation images showed a very homogeneous gas distribution throughout the airspaces, while maintaining the ability to distinguish structures such as the heart contour lines, trachea and mainstem bronchi. The gas distribution illustrated confinement to the airspaces only, thus verifying the overall concept of minimal solubility in the blood. The dynamic wash-in and wash-out measurements were the first of their kind using an inert fluorinated gas, proving the viability of dynamic and quantitative measurements are possible. The acquired dynamic curves illustrated a typical behavior of an inert, insoluble gas, where signal intensities reached 80% of the maximum projected values within the second SF6 breath-hold. Also, there were no quantifiable differences between the left and right lung signal –time curves (145). Perez-Sanchez et al. have acquired ADC maps of SF_6 in rat lungs through the use of a spiral-radial pulse sequence developed in their laboratory, with the incorporation of bi-polar sinusoidal gradients for diffusion tagging

along the slice select direction. The ADC maps acquired presented values in the range of $1.87x10^{-8}$ m^2/s – $8.58x10^{-6}$ m^2/s, with a mean of $2.22x10^{-6}$ m^2/s. Although the results obtained have no immediate meaning as to the overall integrity of the pulmonary structures and require a more complex evaluation, the study has proven that invivo ADC maps of the pulmonary airspaces can be acquired with reasonable SNR and acquisition times. A major concern in these diffusion measurements is the large size of the molecules that acts as a limitation to the overall diffusivity of the gas, thus possibly limiting the overall usefulness (123). Wolf et al. have shown that sub-second 2D acquisitions and 3D volumes of in-vivo porcine lungs with acceptable SNR can be obtained utilizing C_2F_6, due to the relatively long longitudinal relaxation of the compound. Analysis of the 2D images demonstrated reasonable visualization of the trachea, mainstem bronchi and heart contours, relatively homogeneous gas distributions along with image quality improvements with respiratory gating rather than through normal end-tidal scanning (182).

All these preliminary results have proven the concept and ability in obtaining static 2D, 3D volumetric datasets, dynamic wash-in wash-out and diffusion measurements for quantitative assessment of the pulmonary integrity, but lack a useful insight into the nature of the environment they are evaluating. Being that diffusion and dynamic measurements are the first of its kind in this field of imaging, more detailed results are needed to fully evaluate and understand these parameters and to further enhance the image quality. The concept of utilizing a gas that requires no optical pumping processes for signal generation, cheaper, non-toxic and insoluble in the blood and airspaces might seem very promising, but limited SNR, highly advanced gradient hardware for fast ramp up and down of the extra fields, limit the overall usefulness of this technique in a clinical setting as not all scanners have such high demanding hardware requirements and image quality is a major concern when evaluating these images in hopes of assessing certain pathological conditions.

2.3.4 Oxygen-Enhanced Imaging

A paramagnetic material is one that possesses a small positive susceptibility to magnetic fields, such that it is slightly attracted but does not retain any magnetic properties upon removal of the magnetic field. This paramagnetic effect arises from the presence of unpaired electrons and the re-alignment of their orbitals during application and removal of the magnetic field. Due to the presence of some unpaired electrons in the oxygen orbitals, oxygen is considered a paramagnetic substance and this property of the gas is the main concept behind oxygen enhanced MRI.

The suitability of oxygen is primarily based on its weak paramagnetic property, promoting longitudinal relaxation of nearby protons in an MR setting, its natural abundance and low effective cost. Partial pressures of oxygen in room air and 100% oxygen mixtures are very different, due to the different concentrations of the gas in each mixture. This pressure difference is magnified inside the lung airspaces due to the large surface area of the lung, thus amplifying the reduction in longitudinal relaxation (T_1) of the nearby protons. The assessment of this process in itself is what makes oxygen enhanced ventilation imaging feasible, as it determines the lifetime of the available net magnetization. Seeing that the main purpose of the lung is gas exchange, primarily oxygen and carbon dioxide (CO_2), upon inhalation of oxygen mixtures, the oxygen either diffuses across the blood gas membrane to be carried away by the blood to the rest of the body or dissolves in surrounding parenchymal tissue, creating paramagnetic regions within or surrounding the lung, allowing for the visualization of lung parenchyma and blood volume leaving the lungs. The ability to efficiently quantify this reduction in T_1 relaxation in-vivo is already complicated by low proton density of the lung, dephasing and washout effects of the pulmonary blood flow and the various air-tissue interfaces creating a very short phase coherence (short T_2) within the lung, all of which limit the available signal and pulse sequence considerations (63, 64, 116, 152).

As the images acquired are considered T_1 dependent, the most suitable pulse sequence considerations are those of the inversion-recovery (IR) family and specifically ones that are fast (to maximize signal gain from the short T_2 lungs) and efficient. IR sequences with the incorporation of fast spin echo acquisition have gained popularity in this field of imaging specifically turbo spin echo (TSE). IR Half Fourier Single Shot Spin Echo (HASTE) and other sequences with similar parameters such as short inter-echo spacing and centrically-reordered phase encoding steps have shown great results in acquisition of oxygen-enhanced images (118). The short inter-echo spacing allows for acquisition of the signal from the lungs, with minimal dephasing of the signal, the centric phase encoding steps allows for maximal gain in SNR (116, 118) and the IR concept itself is optimal for acquisition of T_1 or T_2 contrast based images. These pulse sequences are very similar in contrast to the conventional spin echo (SE) family, except for enhancement of desired contrast within a volume and the appearance of bright fatty tissues, which can be modulated through the use of saturation regions placed around the thorax (64).

In order to evaluate the difference apparent from the paramagnetic effect of oxygen, the imaging protocol consists of two primary acquisitions, baseline and contrast enhanced images. The baseline images are those acquired during the breathing of normal room air mixtures (21% O_2) and the contrast enhanced images are those taken following the inhalation of 100% O_2 mixtures. Following the acquisitions, the images are post processed and evaluated through the subtraction of the image series and definition of relative pixel and/or ROI enhancements as follows.

$$\frac{\left| SI_{\text{100\% Oxygen Inhalation}} - SI_{\text{Average of Baseline Images before Inhalation}} \right|}{SI_{\text{Average of Baseline Images before Inhalation}}}$$

where SI is the signal intensity at the difference acquisition states. An important factor during the contrast enhanced series is to verify that the O_2 concentrations within the lung

are close to 100%, requiring multiple breaths in order to achieve an equilibrated concentration within. In order to obtain maximal SNR and resolution of the depicted anatomy, the inversion time (T_I) of the pulse sequence must be determined such that apparent contrast is T_1 dependent. This is accomplished through the application of multiple 180º IR pulses with various inversion times to deduce this value prior to proceeding with the imaging protocol (Figure 9).

Hatabu et al. have observed enhancement of lung parenchyma associated with the pulmonary veins and not the arteries in nine healthy volunteers. These results showed a decrease in overall T_1 values between baseline and contrast enhanced images, thus proving the overall paramagnetic effect of inhaled molecular oxygen at higher concentrations. Excellent correlation (r = 0.997) was found between the observed T_1 enhancement and recorded arterial partial pressures of oxygen (PaO_2) in an in-vivo porcine lung. As the partial pressure of oxygen in the arterial blood (P_aO_2)supply is very closely related to that of the pulmonary venous flow and thus the oxygen partial pressures in the pulmonary capillary beds, the linear relationship apparent between P_aO_2 and the observable reductions in T_1, provide a mean for quantitative and qualitative assessment of regional pulmonary ventilation and O_2 transfer. A dynamic imaging series of wash-in and wash-out values were also acquired to evaluate the integrity of the lungs. Upon evaluation, the wash-in values of the lung were different from the wash-out values, which might be due to the removal of oxygen from the ROIs via the pulmonary blood flow (64).

Chen et al. produced static ventilation scans of five healthy subjects consistently and observed clear delineation of ventilation defects in an anesthetized pig following placement of an endobronchial blocker in a primary bronchus. Ohno et al. produced dynamic ventilation scans of seven normal volunteers and ten emphysematous volunteers, without any adverse side effects such as chest pain, nausea, dyspnea, headache and dizziness. In the normal population studied, the relative enhancement was observed to be strong and homogenous, whereas in the emphysematous population, the

enhancement was weak and heterogeneous. Results obtained correlated well with spirometry based diffusion capacity measurements obtained prior to the imaging protocol. In the emphysema volunteers, the decrease in relative enhancement is possibly due to the decreased diffusion of molecular oxygen in the capillary beds due to blockages or tissue destruction (26). In an attempt to verify the T_1 dependence on magnetic field strength and its effect on acquired oxygen enhanced images, Stock et al. acquired ventilation images of eight non-smokers. Results showed higher SNR with a higher magnetic field of 1.5T compared to the lower end 0.2T. This is primarily due to the dependence of the T_1 values on the magnetic field strengths, as the magnetic field increases so does the overall longitudinal relaxation of the volume and thus producing a longer period of time for signal acquisition with minimal loss and noise corruption (152, 153).

The enhancement ability of the O_2 imaging technique in visualizing pulmonary ventilation and O_2 transfer is undeniable, as results have shown, but lacks sufficient resolution needed for a more in-depth evaluation. This technique has produced a non-invasive, relatively cheap and simple acquisition of the aforementioned parameters, overcoming the complex imaging requirements of other imaging methods such as hyperpolarized noble gas and ^{19}F imaging, but as the presented results have shown, major improvements are needed in image quality and relative quantification of normal and diseased baselines.

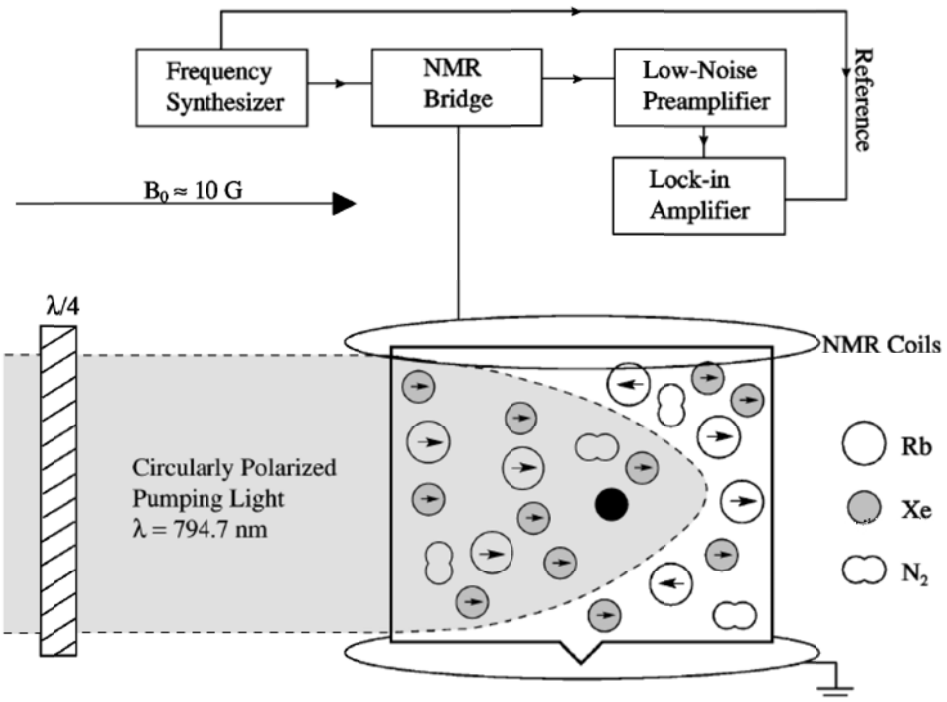

Figure 4. SEOP experimental setup, demonstrating the different components involved such as the glass cell, NMR coils, circularly polarized laser light and application of a small external magnetic field. Inclusion of nitrogen within the glass cell acts as a buffering agent, while the rubidium is the main component facilitating the spin exchange process within the glass cell, as it acts as an intermediary agent between the laser light and noble gas (172).

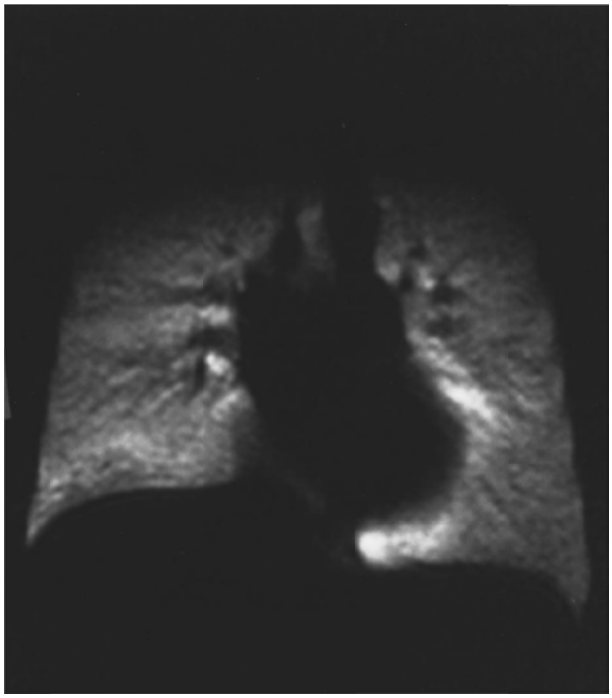

Figure 5. First acquired HP ^{3}He MRI static ventilation image of a normal volunteer (99).

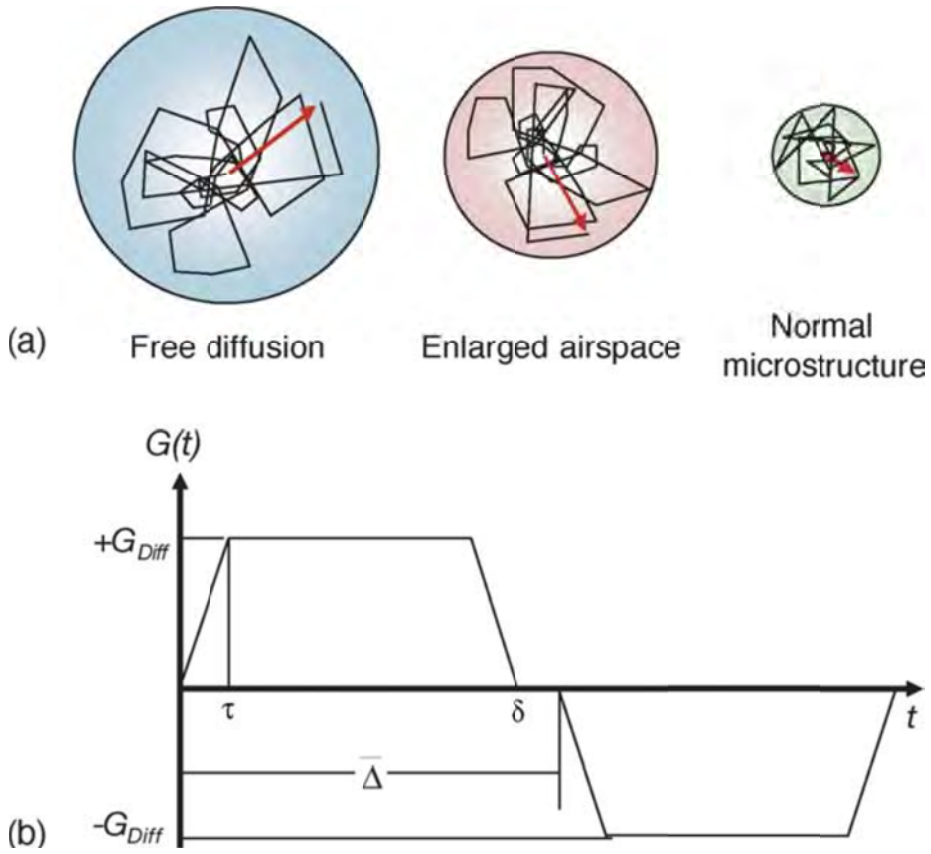

Figure 6. Demonstration of random molecular brownian motion and the dependent interplay between the structure size and overall resultant diffusion (a). To facilitate proper acquisitions and diffusion sensitization, the use of bipolar gradients (b) is incorporated in the applied pulse sequences. (146)

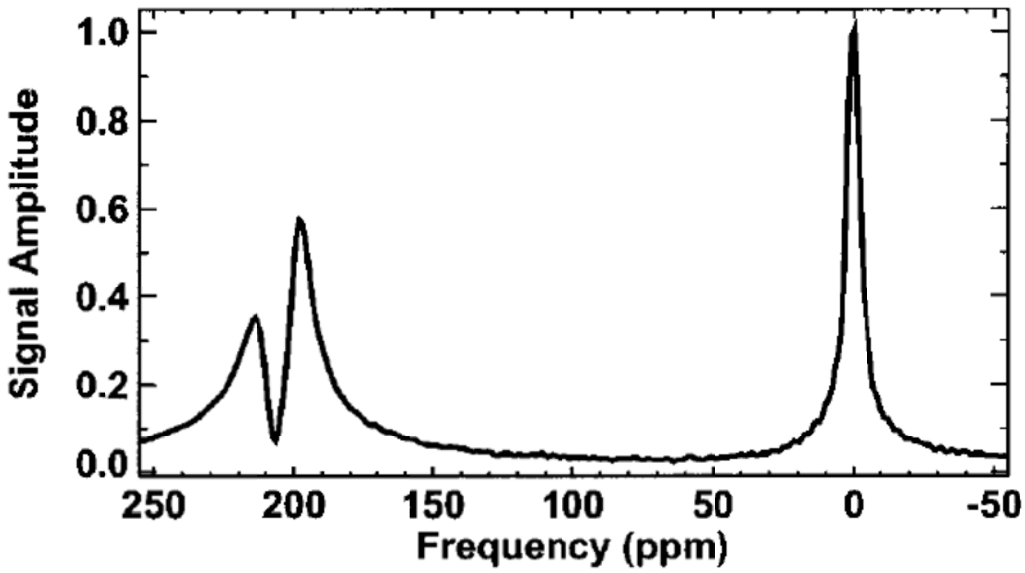

Figure 7. Nuclear magnetic resonance (NMR) spectrum of ^{129}Xe in a dog lung, demonstrating the gaseous phase (0 ppm) and dissolved tissue (197 ppm) and blood phases (212 ppm) of the ^{129}Xe upon administration (138)

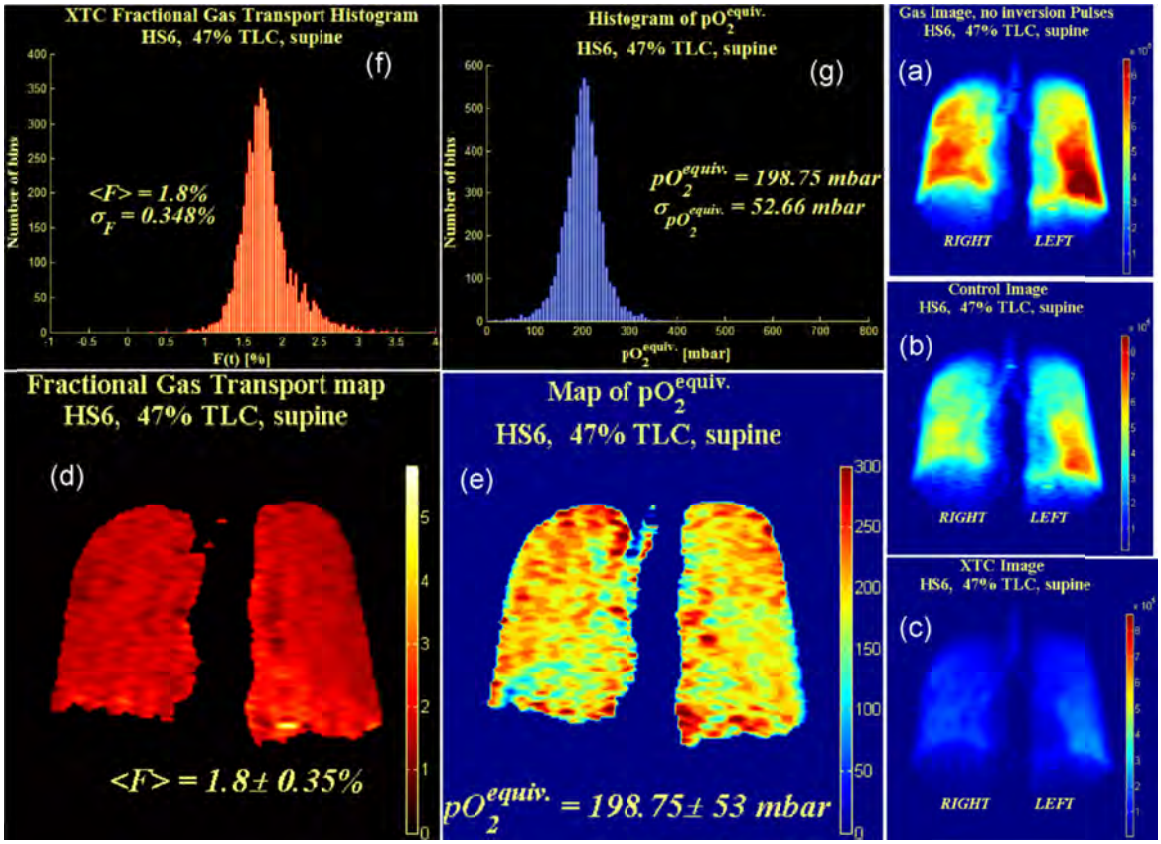

Figure 8. Single Breath Xenon Transfer Contrast (XTC) acquisition following administration of a one liter 86% enhanced 129Xe bolus. Ventilation (a), control (b) and XTC sensitization (c) images are representative of a typical XTC imaging protocol. Fractional gas transport (d) and pO2 map (e) along with their respective histograms (f) and (e) demonstrate the homogeneity of distribution at a 50% inflation level. (121)

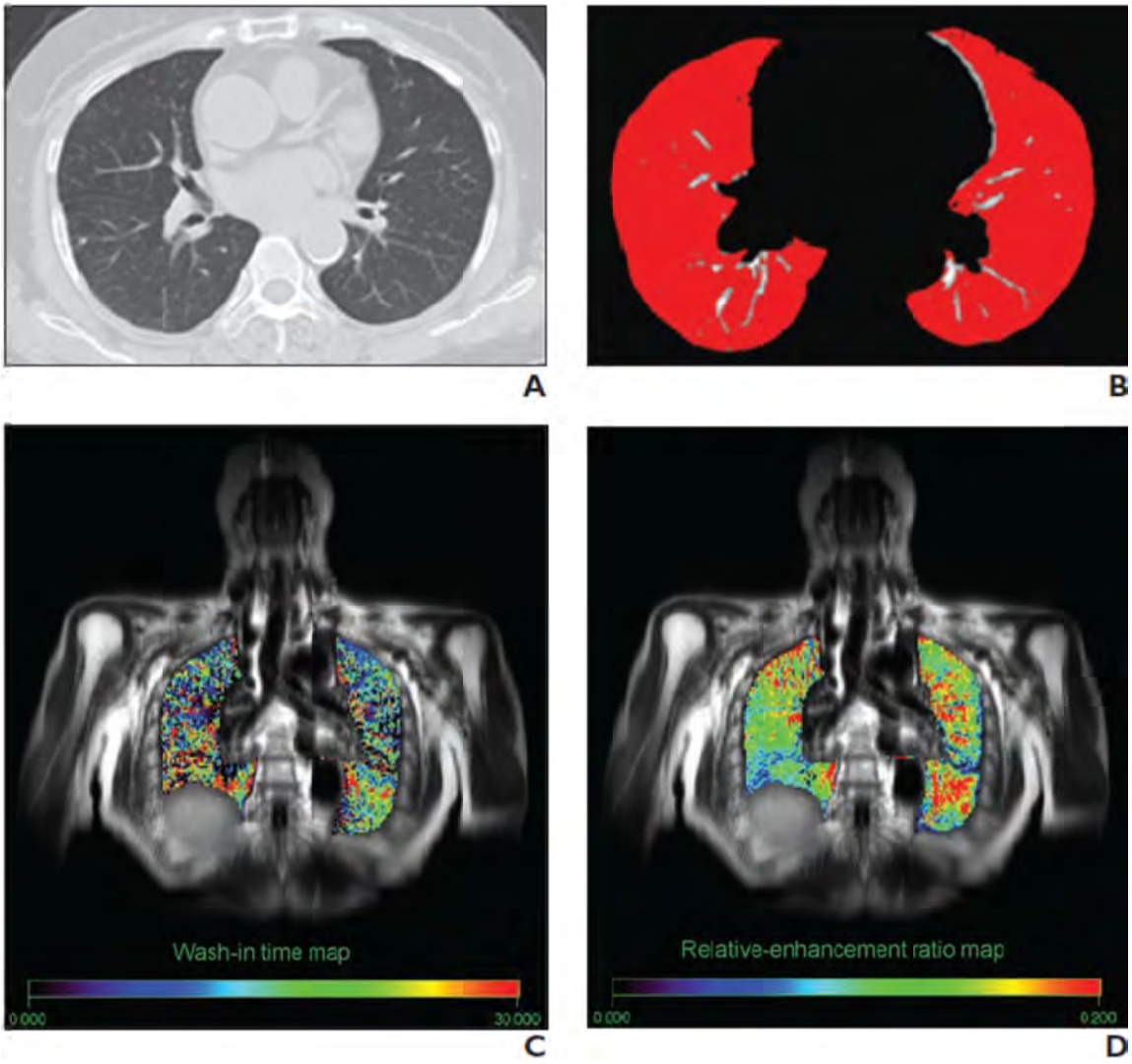

Figure 9. Oxygen enhanced MRI wash-in time (C) and relative enhancement (D) maps of a normal never-smoking subject, demonstrating a homogenous distribution of enhancement and varying wash-in times throughout both lungs and in agreement with the minimal difference in attenuation observed in the MDCT acquisitions (a and b).(117)

CHAPTER 3: ESTABLISHING HP 3HELIUM @ THE UNIVERSITY OF IOWA

Successful implementation of the HP ^{3}He Imaging technique is dependent upon many factors as presented in Chapter 2, including but not limited to gas polarization, dose dispensing and administration, pulse sequence development and proper training of the individuals involved, the most important of which is the gas polarizer. Installation of the helium polarizer and calibration station was carried out with the assistance of a GE Healthcare (Amersham Healthcare) engineer at the University of Iowa Hospitals and Clinics (UIHC). Given the complex nature of the polarization process and sensitivity of the components within, comprehensive testing and evaluation of the functionality must be conducted following transport of the polarizer from one location to another to ensure proper operating conditions. Therefore several spin-up and spin-down runs were carried out to test the functionality of all the different components as well as train several individuals within our laboratory on the proper operating procedures.

The main components of the polarizer include two 30W lasers to provide sufficient energy for the polarization process, helm-holtz coils to isolate the polarization process and allow exponential increase of the polarization levels, glass cell and oven compartment to hold the solid state rubidium / helium mix and heat up the rubidium respectively, nitrogen gas supply to act a buffer gas and a vacuum pump to eliminate all excess unwanted gases (Figure 10). Prior to each run of the polarizer, several pump and purge maneuvers are carried out with nitrogen gas to ensure elimination of all unwanted gases, including oxygen, which is deleterious to the overall polarization process. Following which the polarization process is initiated through the use of a LabVIEW program to monitor the free induction decay (FID) signal of the polarization process as well as the polarization levels and baseline transmission of the laser diodes. The efficiency of the polarization process is dependent upon the pureness of gas within the

glass cell, oven temperature controlling the density of rubidium vapor and laser currents and voltages affecting the overall baseline transmission. The simplest of which is controlling the purity of the gases within the glass cell, which is achieved via the pump and purge processes carried out prior to initiation of the polarization. In order to maximize the density of the rubidium vapor within the glass cell and transmission power of the laser diodes to optimize the polarization, the oven temperature (160-170 ºC) and laser diode settings were adjusted and several spin up runs were performed. Following recording of the polarization levels, the optimal temperature was set at 167 C which produced the highest polarization levels (Figure 11, Figure 12). Adjustment of the laser diode current settings controls the output power of the diode, while adjustment of the diode temperature facilitates fine tuning of the desired wavelengths. This procedure was repeated several more times throughout the duration of the experiments to fine tune the polarizer settings, which significantly improved the efficiency of the polarization process, producing mean polarizations on the order of 38%, compared to 32 and 35 %.

During the early stages of the HP ^{3}He project, the only multi-nuclear capable MRI scanner was based at a remote outpatient clinic, which housed a Siemens Magnetom 1.5T scanner. This limited testing and scanning times to after-hours in order to not interfere with normal patient scheduling. Prior to initiation of human subject imaging, pulse sequence development and testing were carried out on a ^{3}He phantom (Figure 13). The end result of which, was validation of the pulse sequence operation and that it was indeed tuned to the proper larmor frequency, with the desired frequency and phase encoding steps. Figure 14 illustrates the first acquired HP ^{3}He images at the University of Iowa. As mentioned in Chapter 2, proper rationing of the helium signal is of upmost importance, thus a GRE based FLASH sequence was implemented. Given the expense factor associated with the 3Helium gas, this step was crucial in minimizing operating costs during the testing phases. Once the pulse sequences where deemed operational, several imaging sessions were conducted on actual ^{3}He doses (300ml 3He + 700ml Nitrogen) in

Tedlar bags (Figure 15, Figure 16). Given the location of the helium polarizer (UIHC Campus), all helium doses were transported via MITI transporters (Figure 17), equipped with glass cells (similar to those in the polarizer – excluding the rubidium) housed within battery powered external magnetic fields to ensure sufficient T_1 durations, thus maintaining polarization levels during transport with minimal loss.

As a proof of concept, two animal studies were scheduled and conducted to test out the functionality of the HP ^{3}He static ventilation and ADC sequence. Although transportation of the helium doses from the University of Iowa campus to the remote outpatient clinic was feasible, the requirement for a portable pump and purge station arose to ensure the purity of the delivered doses and minimize the oxygen concentrations when dispensing. Through the use of several Swagelok fittings, valves and copper tubing, a wheeled cart was fitted with a vacuum pump and nitrogen tank regulator to allow the conduction of the pump and purge maneuvers onsite and maximize the imaging potential of the transported ^{3}He batches (Figure 17). A few hours prior to the scheduled imaging times, the animals were administered 0.5 cc of pre-anesthetic (Ketamine 75 mg/ml /Xylazine 25 mg/ml) and transported to our surgical suite in the basement of the UIHC. Maintenance of anesthesia during the surgical procedures was achieved through the use of isoflourane administered via nose cone, while maintenance of anesthesia during animal transport and imaging sessions was achieved through the use of Pentobarbitol and Pancronium. Arterial and venous cut-downs were performed, to facilitate blood pressure monitoring and administration of drugs respectively, while a tracheostomy was performed to minimize dead-space. Once stable (normal heart rate, blood pressure and oxygen saturation levels), the animal was transported from the UIHC campus to the remote outpatient clinic for imaging. Artificial ventilation during the transport was achieved through the use of a battery powered ventilator system, while ventilation during the imaging session was achieved through the use of an MR compatible ventilator. All imaging breath-holds were performed without the ventilator, where the animal was

disconnected and allowed to reach FRC, following which the ^{3}He dose was administered manually reaching a lung volume of FRC + 1 Liter (Figure 18). Similarly, a rubberized pig lung phantom was utilized on several different occasions to test out pulse sequence operation and functionality of the imaging protocol (Figure 19). Table 1 illustrates the finalized pulse sequence parameters of both the conventional proton and hyperpolarized ^{3}He imaging sessions.

All animal and human imaging sessions were carried out following acquisition of a physicians IND under the supervision of Dr. Edwin J.R. vanBeek. Organization and execution of the imaging followed strict regulations in compliance with our institutional's Investigational Review Board (IRB) and Animal Care Committee.

Figure 10. GE Healthcare ^{3}He SEOP Polarizer (left) and glass cell containing solid state rubidium (upper right). A sample Tedlar Bag fitted with ¼" Tygon tubing, utilized in administering the 3He doses is shown on the bottom right of the figure.

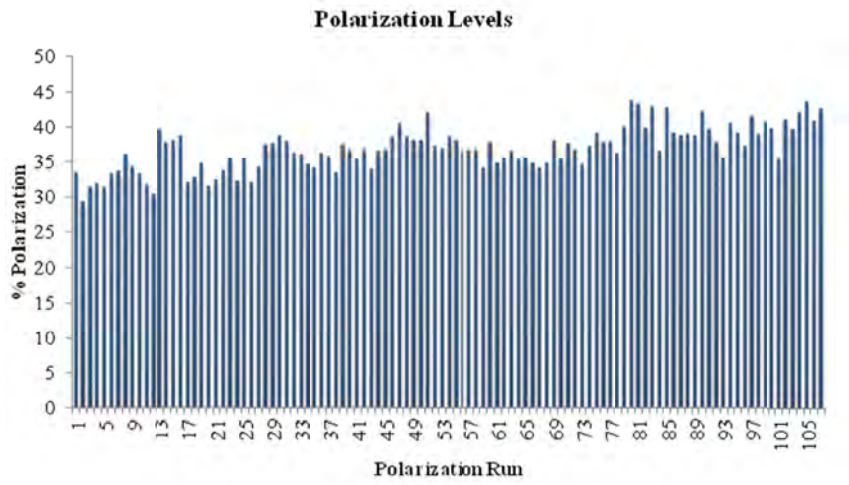

Figure 11. Recorded polarization levels of all Spin-Up runs performed to date (μ = 36.77 ± 3.12 %). Considerable improvements were achieved following adjustment of oven temperatures and laser diode settings.

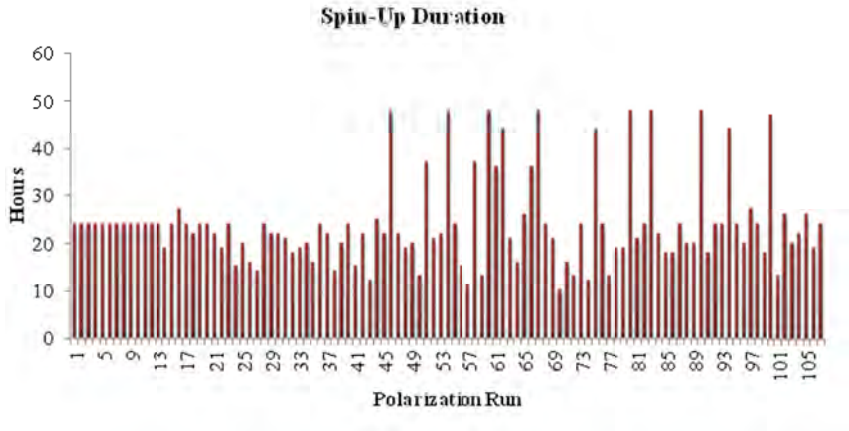

Figure 12. Recorded Spin-Up durations for all performed Spin-Ups. The duration of the polarization process has minimal to no-effect upon the end resultant polarization (μ = 23.95 ± 9.18 hrs).

Figure 13. ^{3}He phantom (right) utilized in calibrating and adjusting pulse sequence parameters. Two cylindrical compartments are centered within the phantom and filled with non-polarized ^{3}He. Visualization of the ^{3}He compartments requires the implementation of multiple averages during the acquisition due to the non-polarized nature of the residing gas. Its usefulness is demonstrated in ensuring proper tuning of the pulse sequence parameters to the ^{3}He frequency. The vest like ^{3}He coil utilized throughout all imaging sessions is shown on the left.

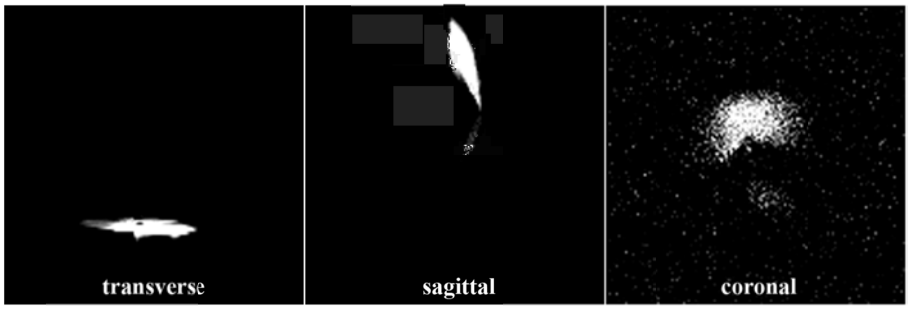

Figure 14. First Acquired HP ^{3}He Images of Tedlar Bag Filled with HP 3He. It can be clearly seen that optimization of the protocol was needed, as the signal was almost quenched by the third (last) acquisition.

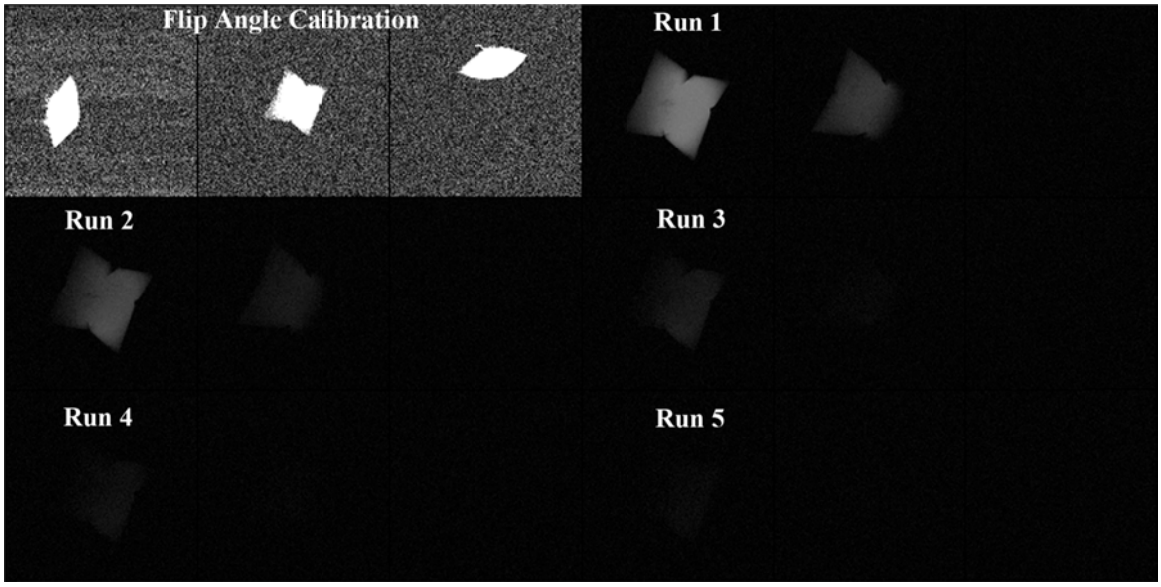

Figure 15. Results of preliminary pulse sequence testing and calibration. Initial images were utilized to properly calculate the desired flip angle, while the following acquisitions tested the rationing of the available signal. Decrease in signal intensities and disappearance of the Tedlar bag are due to the improper setting of the flip angles and field of view of imaging respectively.

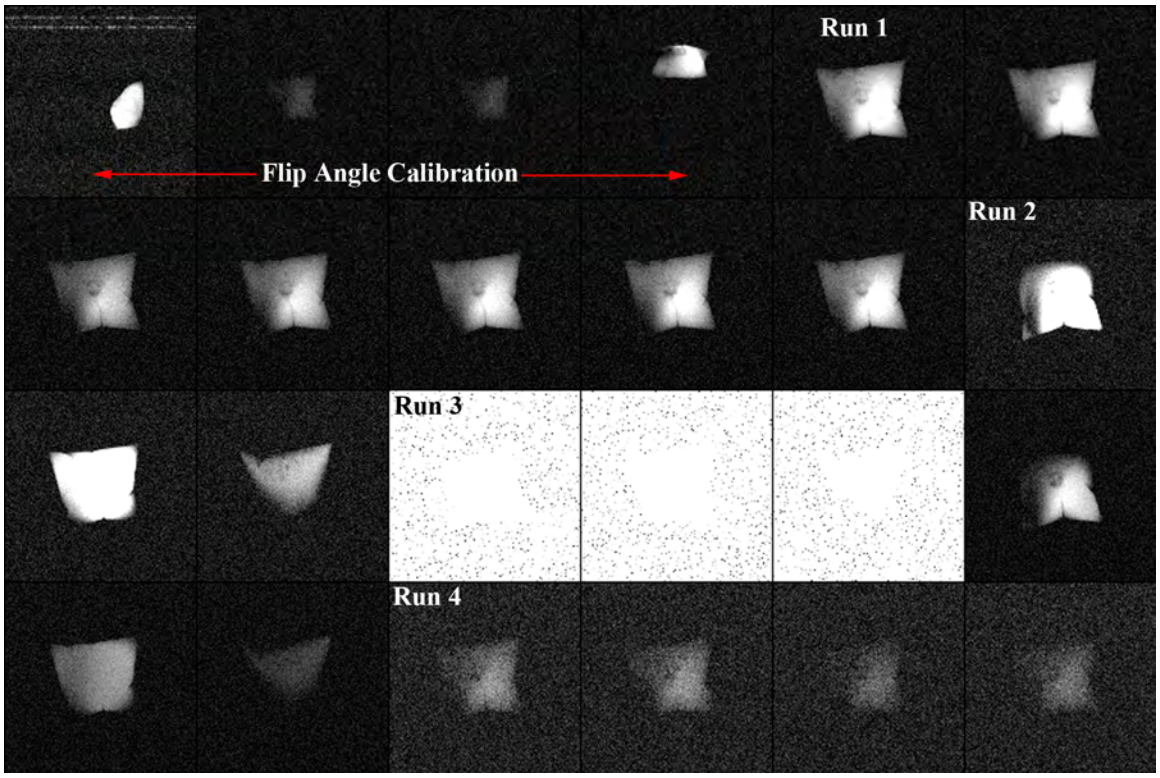

Figure 16. Results of flip angle testing sessions following significant modifications and adjustments to the pulse sequences. It can be clearly observed that proper setting of the flip angle values play a crucial role in the quality of images acquired. Improvements in pulse sequence adjustments and overall acquisition are demonstrated from previous imaging sessions.

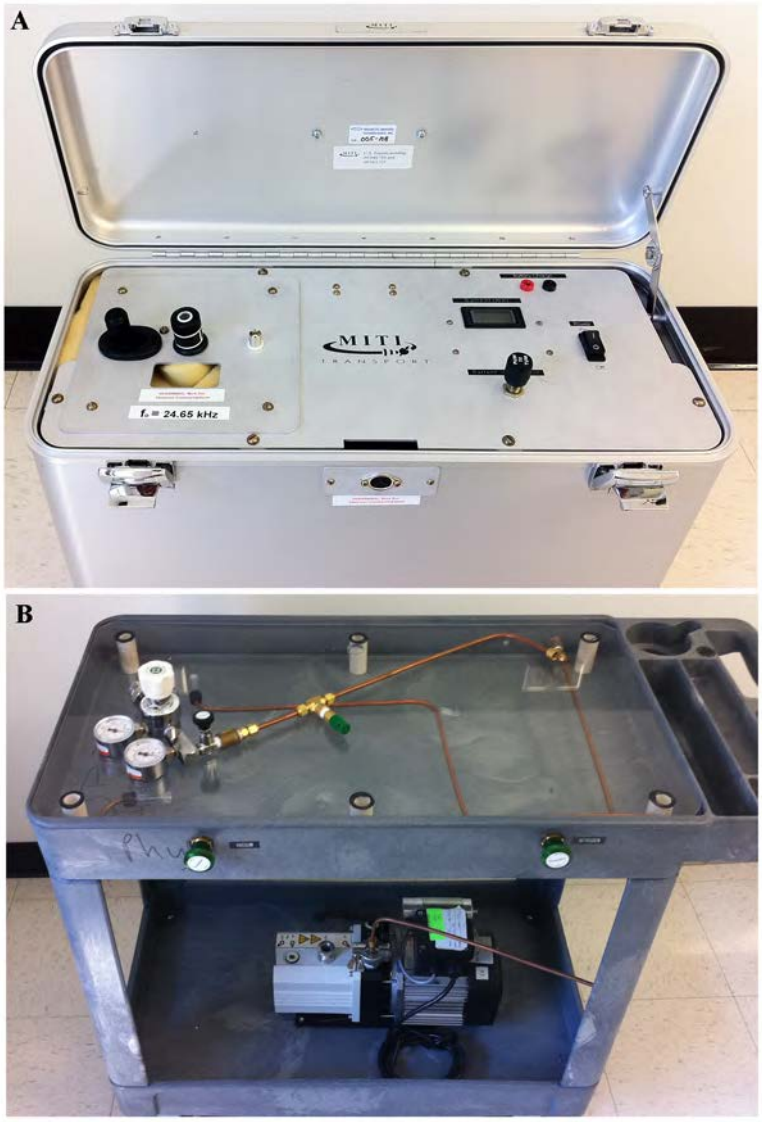

Figure 17. MITI ^{3}He Transporter (A), equipped with a battery powered external magnetic field to shield the helium doses from external interferences. Use of the transporters was limited to the testing phases of the experimentation (phantom and animal), due to the unavailability of FDA approval for human use. The Portable Pump and Purge station (B), with nitrogen connection and regulator was utilized in eliminating unwanted gases from the administered ^{3}He doses. A nitrogen tank was housed onsite to provide means of obtaining large quantities of the buffer gas

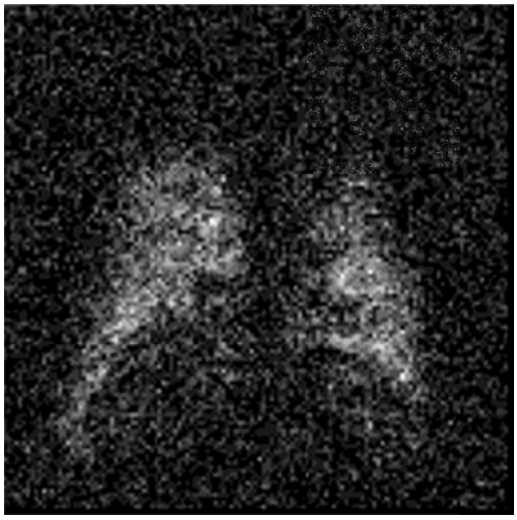

Figure 18. Sample Coronal Result of proof of concept animal (sheep) experiments.

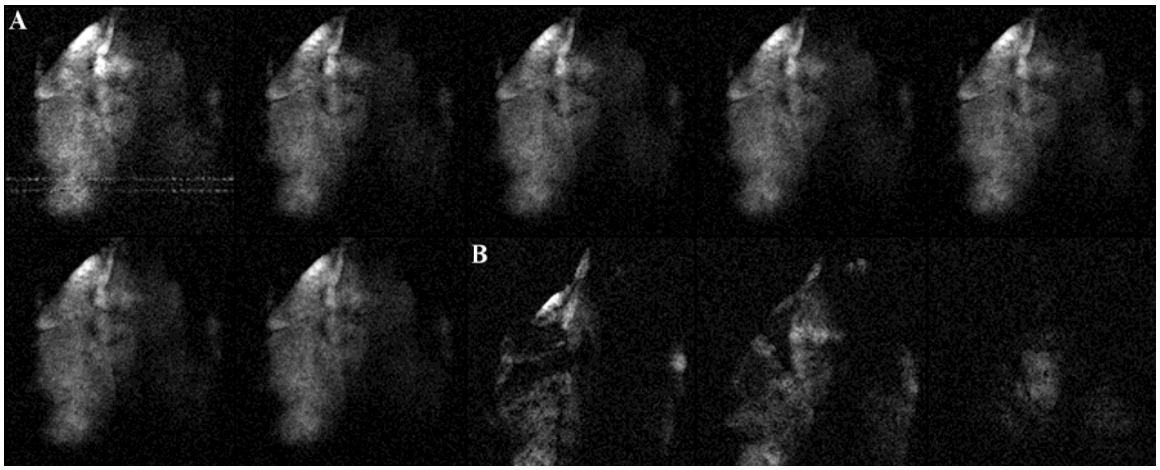

Figure 19. HP ^{3}He testing on rubberized pig lung (*eNasco, Fort Atkinson, WI*).

Table 1. Proton (^{1}H) and Hyperpolarized ^{3}Helium Pulse Sequence Parameters

Parameters	2D FLASH	3D FISP
nucleus	^{3}He	^{1}H
frequency (MHz)	48.4676	63.6235
acquisition matrix	128 x 128	256 x 140
T_R *(repitition) (ms)*	86	413.78
T_E *(echo) (ms)*	6.92	1.16
slices	6 (repeated)	60
slice thickness (mm)	15	5 - 7.2

CHAPTER 4: IMAGE PROCESSING

Qualitative assessment of structure and function of the underlying anatomy has been the stronghold of MRI in both the clinical and research environments. Direct visualization and evaluation of these parameters is easily achieved through the use of the reconstructed DICOM files, represented as unit-less voxels throughout due to the complicated nature of the acquisitions. Furthermore, these acquired intensities are usually adjusted to suit the visualization needs of the physicians and radiologist alike. In the case of qualitative assessments, the need arises to adjust the reconstruction protocols either directly on the scanner or in the post-processing of the data to achieve the desired results. Proper evaluation of HP ^{3}He data relies on the actual intensities acquired, representing the inherent spin density, rather than the adjusted intensities. Limitations in reconstruction protocols, computational cost and availability, limit these procedures to offsite post processing, where programming tools such as MATLAB (*Mathworks Inc., Natick, MA*) and C++ can be utilized to achieve the proper results required for analysis. Given the exceptional ability of MATLAB in performing matrix manipulations, the availability of numerous predefined functions as well as the flexibility of the programming environment, all HP ^{3}He image processing scripts were written utilizing the numerous predefined functions available.

The image processing aspect of the presented work is divided into two portions, pre-processing of the datasets to generate desired functional maps and post-processing to facilitate the cross-comparison between the multi-modal functional maps of lung ventilation and expansion, following image registration. *All written MATLAB scripts have been properly commented and documented to facilitate ease of use and manipulation for future users and researchers.*

4.1 HP ^{3}He Analysis Script

4.1.1 Methods

The main purpose of this script was to semi-automatically reconstruct, segment and analyze acquired HP ^{3}He datasets (*Aim 1c*). The script was divided into separate modules and written in the form of functions to minimize computational and debugging times and allow flexibility in construction of the script for future users. First the raw-data file is fed into the script utilizing the *uigetfile* command and reconstructed by rastering through the header information until the first line of actual data is reached. 2D images are then reconstructed according to the phase encoding (row) ordering of the acquisitions and placed into a stack (3D matrix) according to z-axis encoding ordering. To eliminate any erroneous intensities due to noise or other external factors, a three step filtering procedure is applied. First all negative valued intensities are removed, via acquiring the absolute values of each pixel. Following which, a 20 x 20 pixel region placed at the top left corner of each image is averaged to estimate the mean (μ_{noise}) and standard deviation (σ_{noise}) of the background noise. Utilizing the generated noise mask, the dataset is then filtered to remove all pixel intensities within 2-3 standard deviations of the μ_{noise}. To finalize the filter, a 3x3 moving average window is implemented to further eliminate any underlying inconsistencies across the image intensities.

Segmentation and left-right separation of the lung field of view (FOV) is then achieved through manual segmentation utilizing the *roipoly* command. The script has the ability to read in an externally generated mask file, by setting the proper flags prior to running the script. Similarly, the script has a built in function that allows manual segmentation of the trachea and major airways, to allow for easy removal of these structures during analysis if needed. In the case of an ADC assessment, the acquired stack is represented as a pair wise acquisition of baseline and diffusion weighted images, thus a single mask for each pair is sufficient. Calculation of ADC values is then carried out

through a pixel-by-pixel calculation according to the Stejskal-Tanner diffusion equation defined in Chapter 2: The generated lung masks along with the noise masks are incorporated into the processing pipeline to limit the calculation to valid pixels only. Generated functional ADC maps and their representative histogram distributions are visualized following the ADC calculation of each pair of images to allow for qualitative assessment of the underlying distribution prior to proceeding to the next step. Finally, the data is split along the antero-posterior axis to establish gravitationally dependent and non-dependent regions in both left and right lungs and the mean, standard deviation and coefficient of variation (COV) values of each region are saved to an excel file. The final resultant ADC maps are then saved as float valued analyze volumes for future processing and comparisons. In the case of a ventilation assessment, the procedure is identical to the ADC pipeline up through the manual segmentation. Following which, the dataset is mean normalized according to either slice or whole dataset means and then saved as a float-valued analyze volume, for future fractional ventilation assessment and comparisons. All generated variables and image sets within the MATLAB workspace are then saved to file, to eliminate/minimize the need for future re-evaluations.

Generation of analyze/nifti datasets from the resultant calculated HP ^{3}He volumes is achieved through the use of the *Tools for Nifti and Analyze image for MATLAB* package written by Jimmy Shen, available on the MATLAB File-exchange server. This package facilitates the generation of analyze file headers and manual editing of spatial parameters, as well as saving the header information along with the image data to generate an analyze/nifty volume compatible with all external image processing programs, such as Slicer3D (72, 124), ITK-Snap (189) and Fiji .

4.1.2 Results

The current version of the script *ADC_ICLIC_v3* is fully functional and compatible with all HP ^{3}He datasets generated at the UIHC. In cases where ^{3}He

polarization levels are subpar (<25%), minimal fine tuning of the noise masking parameters is needed due to the poor quality of the images leading to misclassification of image data as background noise. Figure 20 illustrates the resultant of the script at different stages throughout the processing pipeline. Figure 21 and Figure 22 illustrate a reconstructed static ventilation volume and calculated ADC maps respectively of a normal never-smoking subject. Background removal was accomplished through the use of the manually generated masks. All generated workspace variables and analyze volumes associated with any specific volume and/or subject are placed in a user defined directory (user prompted for directory path during execution of script). Re-evaluation of datasets is easily accomplished by dragging the saved workspace variables file into the MATLAB environment, while analyze volumes can be visualized through the use of the *load_nii* command.

4.2 Cross-Comparison MATLAB GUI

4.2.1 Methods

Given the multi-modal nature of the acquisitions and the need for proper cross-comparison tools between the generated MRI and MDCT functional datasets, the main purpose of this GUI was to facilitate these calculations post-registration of the datasets. The GUI generation process was initiated through the use of the *guide* command, creating a blank GUI template and an m-file to include all respective functions and callbacks. The properties of each component (push buttons, plotting axes, pull-down menus, etc …) and their respective callbacks functions were edited utilizing the *property inspector*. Following organization of the components in their proper locations and editing of their parameters, the generated m-file was further edited to tie together all the different components and generate their respective functions upon execution. The execution of the GUI is split into four portions: 1. *Data Import*, 2. *Left/Right anatomical split*, 3. *Definition of analysis parameters* and 4. *Data analysis and Visualization*. The only pre-

execution requirements of the GUI are 1.*the placement of all datasets to be analyzed into a single directory to facilitate the search process*, 2. *proper alignment of all datasets (ex. RPI) and* 3. *Removal of all background information*. A screen shot of the final GUI is illustrated in Figure 23.

Prior to starting the cross-comparison process, the user must define the input directory, containing all the analyze datasets and output directory, for placement of resultant analyze volumes and excel spreadsheets, by pressing the *Select Input Directory* and *Select Output Directory* respectively. Definition of all analysis and anatomical split criteria, located in the *Anatomical Split and Analysis* section, can be found in Table 2. These criteria must be selected prior to loading the data, by pressing on the radio-buttons next to each and defining the number of desired gradient segments, by entering the number of segments into the text box labeled *Segments*. The data is then loaded into MATLAB by pressing the Load Data button, where each dataset is assigned to a *struct*, to hold all dimensional information, anatomical split criteria and filenames, for ease of access throughout the cross-comparison process.

Once the data is loaded, the user may proceed to the Left-Right splitting process, to define the left and right lung boundaries. To minimize memory requirements, improve computational speeds and eliminate the need for loading a mask for each dataset, the left-right splitting procedure is carried out manually by defining the most central column of each dataset that best approximates a proper left-right split. For each dataset, the GUI displays four equidistant slices, allowing the user to utilize the data cursor at the top of the GUI to determine the centermost column achieving this split in all views. Once the column value is determined, the user must input the value into the *Right-Left Splitter* text box and press the *Set Left-Right* Button. The process is then repeated for all datasets until the last dataset is reached, which is signified by the availability of the *Analyze* button (previously grayed out). Pressing the Analyze button, initiates the calculation process, where each dataset passes through the same pipeline, until all datasets have been

analyzed according to the user defined criteria. The completion of the cross-comparison process is signified by the availability of the *Update Plot* functionality, where the user has the option to select a dataset and its respective analysis result to visualize in the plotting axis within the GUI.

The calculation of the lung profiles is carried out by replacing all intensities within a given row, by the sum of all intensities within that row. Left-Right splitting is achieved through the use of the user defined left-right split value, limiting all left lung calculations to pixels on the right of the split value and all right lung calculations to pixels on the left of the split value. With regards to the gradient calculations, all pixels within each segment are replaced by the mean of all pixel intensities located within the segment. The segments are defined by dividing the lung height within each slice by the number of desired lung segments and utilizing the resultant segment widths to define the boundary conditions of each segment.

4.2.2 Results

The current version of the GUI (version 2) is fully functional and compatible with all HP 3Helium and MDCT based datasets generated from our laboratory. Occasionally, the number of datasets to be analyzed must be split into different runs, to reduce computational cost introduced with larger file sizes (MDCT datasets in specific). This issue is avoided by utilizing a computer with sufficient memory capacity, to hold the multiple copies of each dataset generated throughout the comparison process. This is only applicable to the MDCT based datasets, due to their larger file sizes with respect to their MRI counterparts. Figure 24 and Figure 25 illustrate analysis results of a HP 3Helium static ventilation dataset, from a normal never smoking subject, demonstrating the profile and gradient analysis performed within the GUI.

Multi-modality comparisons require, multiple measures of comparison to extract the maximal amount of information possible, with respect to similarities and differences

of the techniques evaluated, thus having the ability to define such measures is a crucial aspect of the success of the comparison. Statistical analysis of the similarities and differences can be easily achieved through the use of the statistical functions of Microsoft Excel or through importing of the generated excel spreadsheets into statistical processing programs such as CRAN (*v2.9.2*) and PASW (*v18, SPSS Inc., Chicago, IL*). Several scripts have already been written to perform student t-tests and analysis of variance (ANOVA) comparisons in CRAN.

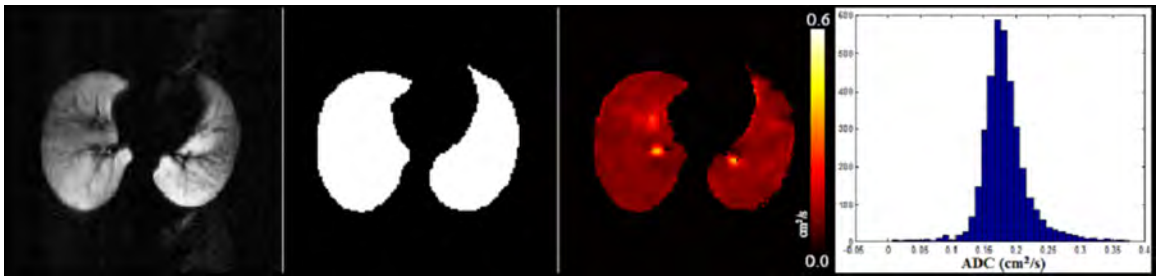

Figure 20. Resultant of ^{3}He MATLAB script, illustrating sample reconstructed ^{3}He image (left), manually generated mask, calculated ADC map and corresponding histogram distribution of ADC values (right).

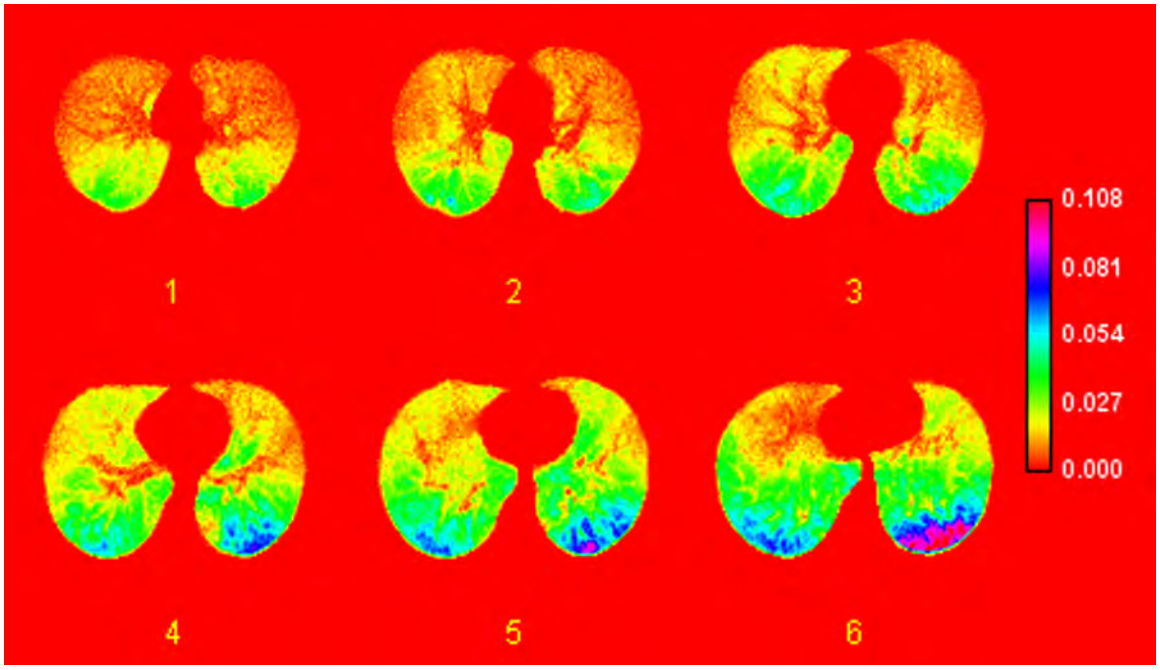

Figure 21. Montage of reconstructed HP ^{3}He static ventilation dataset encompassing the apical-basal lung coverage.

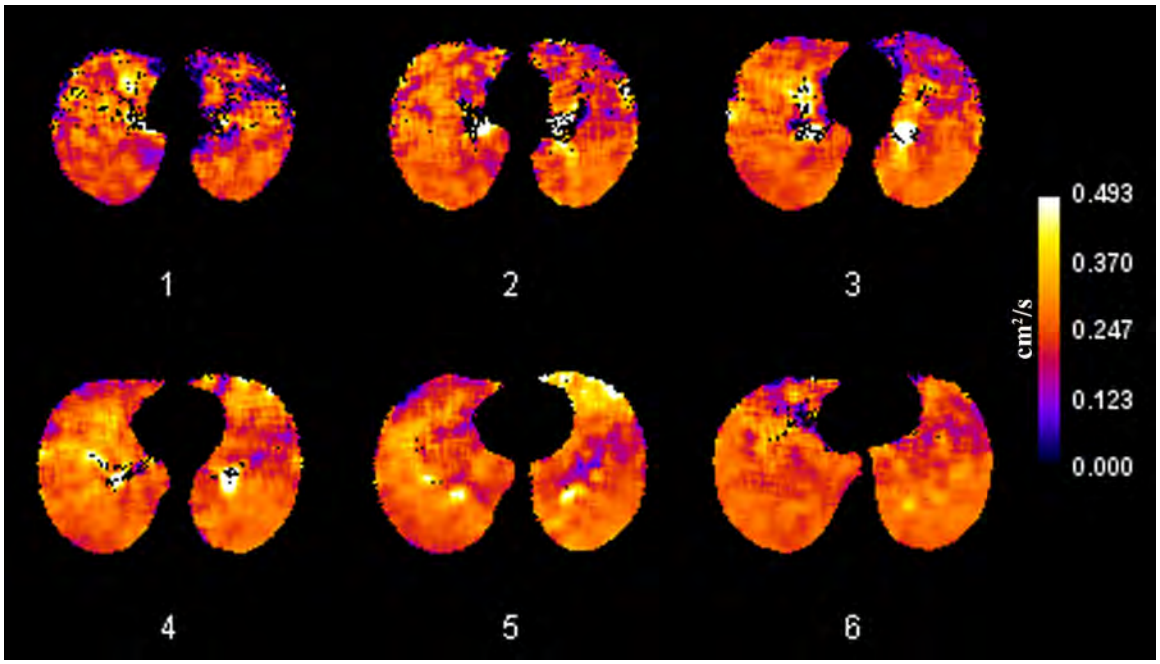

Figure 22. Montage of calculated ADC maps (same subject as in Figure 21) encompassing the apical-basal lung coverage.

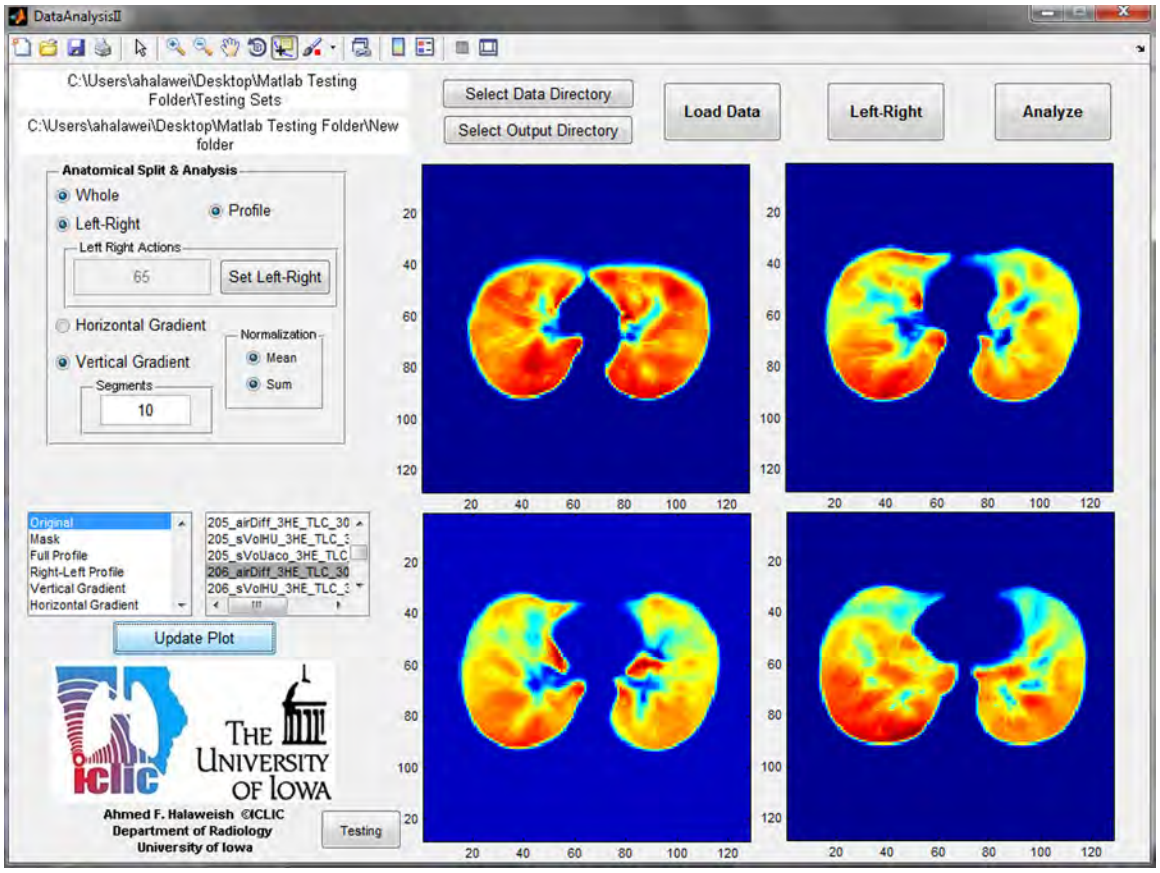

Figure 23. Screen shot of Cross-Comparison GUI, illustrating the different analysis criteria available, along with overall organization and structure of the GUI.

Table 2. Anatomical splitting and analysis criteria of Cross-Comparison GUI

Analysis Criterion	**Definition**
Whole	Whole Lung analysis **without** differentiation between left and right lungs
Left-Right	Whole Lung analysis **with** differentiation between left and right lungs
Profile	Generation of lung profile measurements via mean row intensities
Gradient	
Horizontal	Splitting along the left-right axis (user defined # of segments)
Vertical	Splitting along the antero-posterior axis (user defined # of segments)
Normalization	
Mean	Normalization via the mean lung intensity values
Sum	Normalization via the sum of lung intensity values

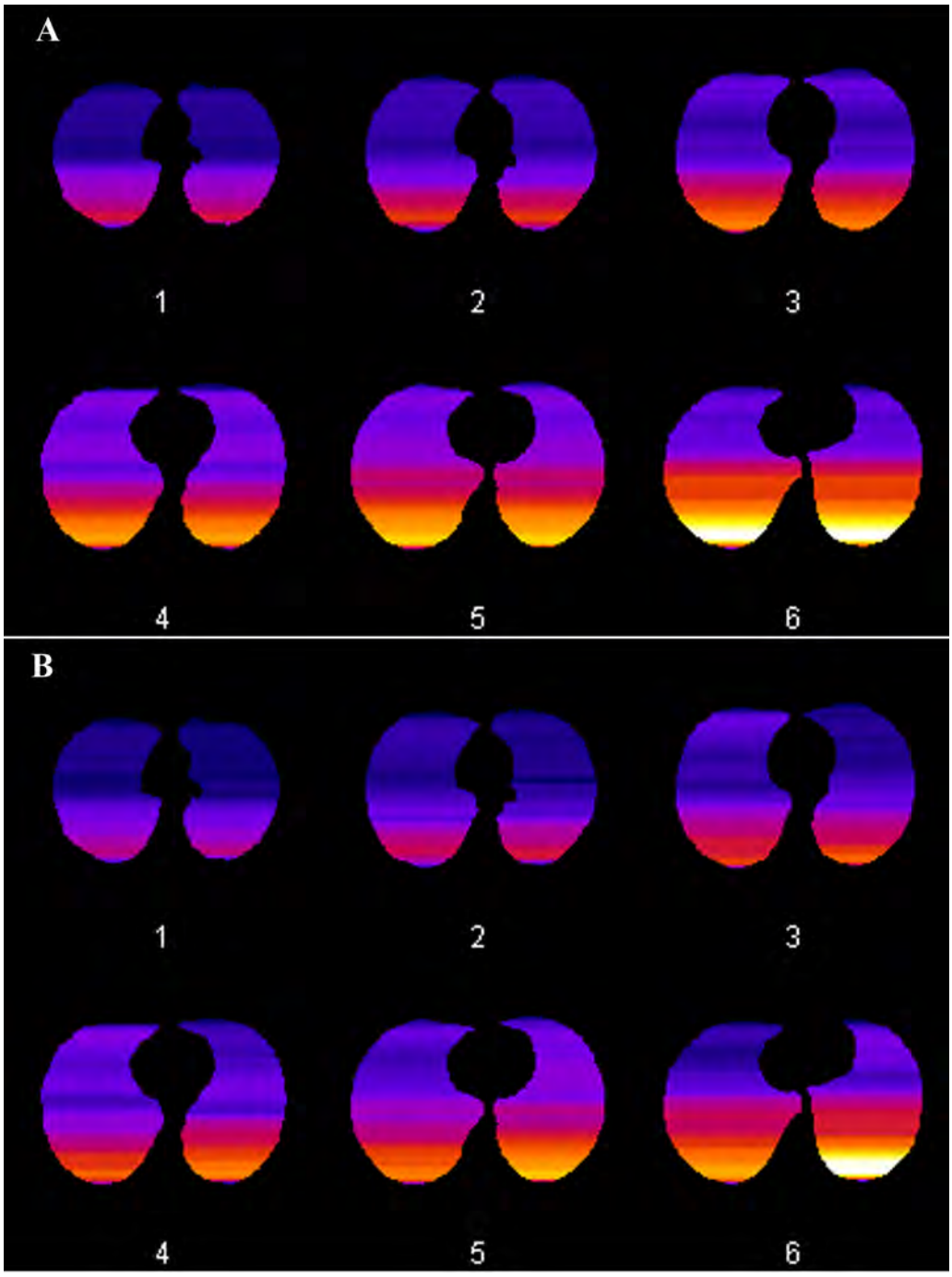

Figure 24. Whole lung (A) and Left-Right split (B) profile results of a static ventilation dataset from a normal never-smoking subject. Clear differences are observed between the profiles of each, illustrating the need for multiple measures of comparison.

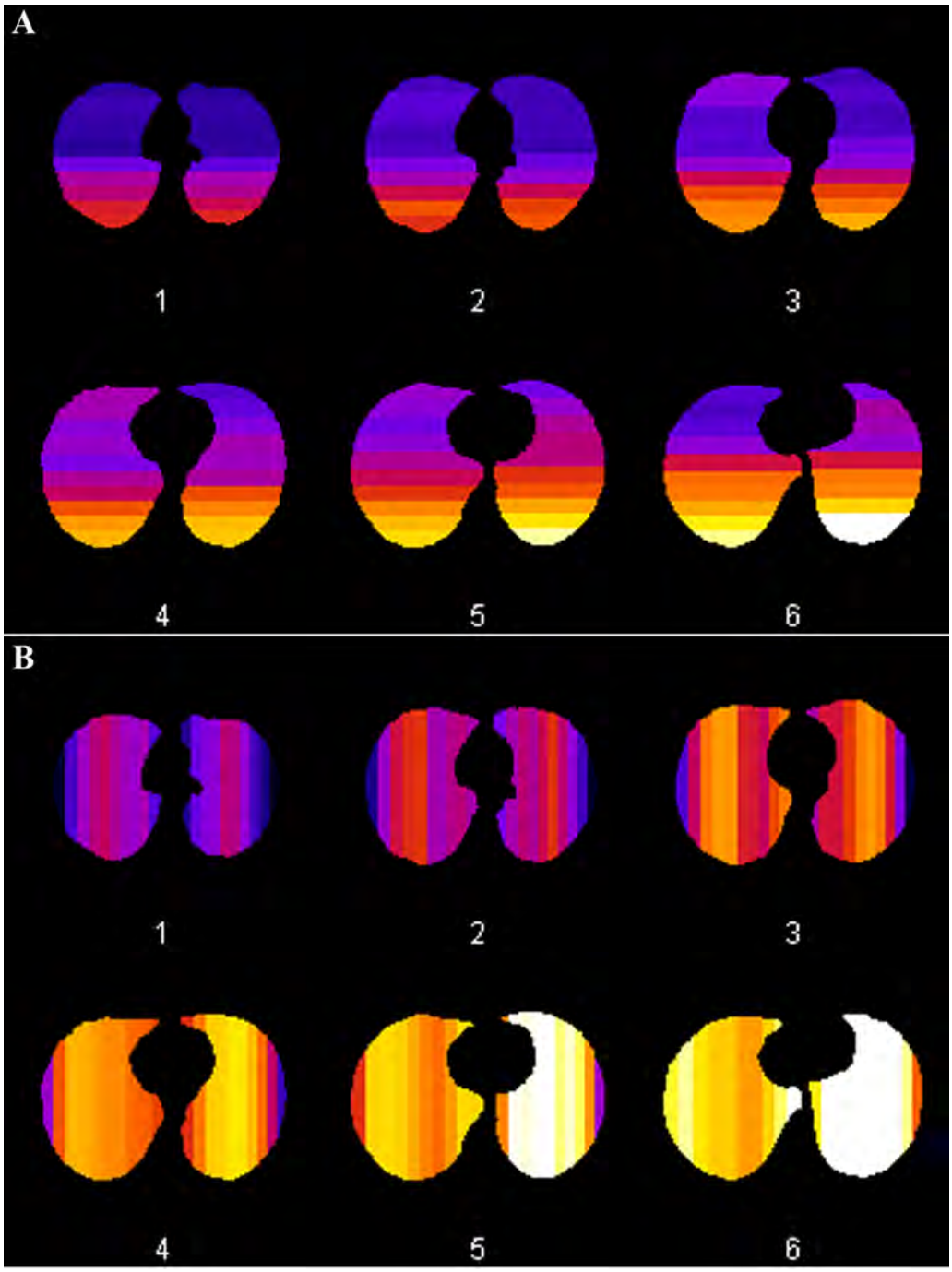

Figure 25. Vertical (A) and Horizontal (B) Gradient GUI results of a static ventilation dataset, from a normal never-smoking subject.

CHAPTER 5: STANDARDIZATION OF LUNG INFLATION LEVELS

The standardization of lung volume measurements has been a crucial driving factor in early and ongoing attempts to characterize and quantify lung physiology and pathological severity (173). This is of upmost importance in all aspects of the lung physiology, as lung inflation plays in a key role in the overall cardio-respiratory response of the individuals under analysis (108, 173). In order to accurately assess these changes via an imaging methodology, standardization and control of the imaged lung inflation levels must be taken into account, as shown by the non-linear response of the pressure volume curves. In addition, if a multi-modal imaging assessment is desired for either correlation and/or synergistic assessments, standardization of the lung inflation levels between the imaging modalities is needed to establish a common physiological and structural background between the imaging modalities. Although further processing of the data is required to establish a pixel-by-pixel or regional assessment pipeline between the modalities via image registration (Chapter 6), ensuring identical physiological and structural states remains the most important key controlling the precision and accuracy of these assessments.

Given the proposed multi-modal assessment of lung ventilation and expansion in the presented work, we aimed to devise a system for the proper control of lung inflation levels between the MDCT and MRI based imaging sessions, via exploitation of lung volume measurements acquired through PFTs and slow vital capacity (sVC) measurements acquired in the supine position (Figure 26). The magnetic nature of MR imaging creates a bottleneck with respect to the materials and equipment to be utilized and albeit the availability of complex equipment to attain both active and dynamic mechanical ventilation, it was our aim to achieve proper lung inflation control utilizing a minimalistic approach.

5.1 Methods

Conventional mechanical ventilation is based on either a pressure or volume based methodology of breath termination. During pressure controlled mechanical ventilation, the termination of the breath is determined by setting upper (peak inspiratory pressure – PIP) and lower pressure limits to control both the inspiratory and expiratory phases. In the case of volume controlled mechanical ventilation, an inspiratory volume is set, such that once this volume is inspired, the breath is terminated and the expiratory phase is initiated. Either mode of ventilation is adjusted accordingly for each subject, given the differences introduced by gender, weight, height and underlying pathological conditions (148, 149). Given the fact that each subject in the presented work undergoes a series of slow vital capacity maneuvers in the supine position, along with the determination of their respective lung volumes from PFTs, the optimal solution for standardizing lung inflation levels during the imaging sessions was determined to be a volume based method, where control is achieved by only allowing subjects to inspire a pre-determined volume based on their respective vital capacities.

Utilizing a bite-down mouth piece rather than a full face mask, a simple device was constructed utilizing several readily available 1” tubing sections and tubing connectors (Figure 27). At the end of the volume control device are two breathing ports, an expiratory port and inspiratory port. Once the subjects are positioned in the scanner, they are asked to bite down on the mouth piece and ensure that their lips create a proper seal around the outer edges of the mouth piece. Free breathing is initiated through the use of the expiratory port, while a large 7-8 liter inspiratory volume Tedlar bag is connected to the inspiratory port. The large inspiratory volume Tedlar bag is utilized to hold the predetermined volume of air required to reach the desired lung inflation levels. This bag is closed to the patient during the free breathing phase of the setup. A bacterial filter and an MR compatible spirometer are placed in line between the mouthpiece and breathing ports for elimination of any harmful bacteria and calculation of delivered volumes

respectively. The incorporation of the MRI compatible spirometer was only implemented during the testing phases of the design process, but was eliminated once the accuracy of the device was evaluated.

In order to accurately control the desired breath-hold volumes during the imaging sessions, proper control of the inspiratory volumes within the inspiratory volume Tedlar bag must be achieved. This was accomplished through the use of a calibrated Hans Rudolph (*Hans Rudolph Inc, Shawnee, KS*) syringe, allowing precise determination of the volumes within. Another limiting factor to the accuracy of the control mechanism and resultant breath-hold is the initiation point of each breath-hold (107). Given the variability of each subject's degree of comfort and effort throughout the imaging sessions, any variability in the initiation of the breath-holds and inspiration of the inspiratory volumes could result in a completely different end inspiratory volume. Therefore several subjects (n=5) outside of the imaged cohort were studied to establish the protocol. They were repeatedly instructed to perform several breathing maneuvers in the supine position on the scanner table while connected to a spirometer, following determination of their respective vital capacities. The breathing maneuvers were structured similar to a VC maneuver, such that the calculation of their pseudo vital capacities was based on either an FRC-TLC volume or the conventional RV-TLC volume. These maneuvers were randomly repeated six times for the FRC and RV pseudo VC measurements, facilitating assessments of the subjects' consistency in reaching their respective RV or FRC volumes.

During conventional MDCT imaging of the lungs, subjects are required to keep their hands positioned over their heads, to minimize unnecessary radiation exposure and eliminate density artifacts in the lung field of view. This is easily accomplished due to the larger bore size and minimal depths of these scanners with respect to their MRI equivalents. Due to the larger bore depths of the MRI scanners and longer duration times of the imaging sessions, keeping the subject's arms above their heads is an unachievable

goal and would result in extreme discomfort of the subjects. Therefore several subjects (n=4) outside of the imaged cohort were evaluated to determine differences in VC measurements based on arm positioning, such that several VC maneuvers were carried out with either their arms next to them or above their heads.

Finally, to assess the accuracy of the designed volume control device, the lung field of view was segmented in several MRI and MDCT scans acquired at identical inflation levels and whole lung volume measurements were preformed to establish end inspiratory breatholds. The total lung volumes of the MRI scans were compared against the VC measurements obtained prior to the initiation of the imaging sessions and the whole lung volume measurements of the MDCT based scans. Manual segmentation of the MRI scans was accomplished through the use of the segmentation editor plugin in Fiji (71) and/or ITKSNAP (189). Total lung volume measurements were calculated in ITKSNAP, based on the volume of the generated lung masks.

5.2 Results

Analysis of the pseudo VC lung volume measurements illustrated that subjects 1-3 were able to reach the same lung volumes during the RV breathing maneuvers with better consistency and accuracy than the during the FRC maneuvers (Figure 28). Subject 4 was able to reach the same lung volume with similar consistency regardless of the breathing maneuvers, while subject 5 had similar inaccuracies in reaching the same lung volume during both types of breathing maneuvers. Subjects 1-3 are normal never smokers, with average active lifestyles, while subjects 4 and 5 were an athlete and an asthmatic respectively. The differences in reaching the same lung volume was analyzed for each breathing maneuver for all subjects utilizing paired t-tests, which illustrated a significant difference ($P<0.001$) between the breathing maneuvers in reaching the same lung volume measurements, for subjects 1-3 only. The results of subjects 4 and 5 are not surprising, as athletes have the ability to regulate their breathing patterns and efforts far

more consistently than the average population (59, 144). In the case of asthmatics, air-trapping and airway reactivity can play a significant role in determining the ability of the subject to reach a certain lung volume consistently (183, 184), thus introducing the inaccuracies observed during the testing. Based on the collected data, RV was chosen to be the initiating point for all maneuvers, where control of lung inflation levels in reaching a desired lung volume was needed. Similarly, assessment of the VC measurements obtained from four subjects with varying arm positioning, yielded no differences in the recorded lung volume measurements, further eliminating a possible contributing factor to the accuracy and consistency of the designed breathing protocol (Table 4).

Repeated VC measurements (Table 4) obtained from two subjects outside the imaged cohort, while varying arm positioning (arms up vs. arms down), demonstrated minimal differences between all three maneuvers independent of arm positioning, with mean VC of 4.874 liters and 3.745 liters in the arms down position and 4.835 liters and 3.714 liters in the arms up position for subject I and II respectively. Mean differences between all three maneuvers conducted for single arm positioning were 1.32% and 3.16% in the arms down position and 1.41% and 2.80% in the arms up position for subject I and II respectively. This data demonstrated minimal differences in VC measurements, with respect to varying arm positioning.

Several factors such as lung recruitment, breathing resistance and comfort levels and the results of the pseudo VC measurements were taken into consideration when design the optimal breathing protocol for the MR imaging sessions. At the beginning of each imaging session, the entire protocol is explained in detail to the subjects to familiarize themselves with the type of breathing maneuvers required of them. Once the subjects are placed supine on the scanner table and fitted with all the required physiological monitoring and imaging coils (HP ^{3}He), they are then instructed to undergo a series of breathing maneuvers similar to what they would perform during an actual breathhold, to familiarize themselves with the remainder of the protocol.

The desired lung volumes for all breathholds is then calculated based on the subjects' previously obtained sVC measurements and the volume air required to reach the desired lung inflation levels is calculated based on the following equation,

$$V_{Imaging} = (I_{Desired}/100)*VC$$

where $V_{Imaging}$ is the volume of air required to reach the desired lung inflation levels, $I_{Desired}$ is the desired inflation level (0-100%) and VC is the sVC of the subject. Once the subjects are comfortable and the MRI technician has loaded the imaging protocols, baseline vitals are recorded and the large inspiratory volume Tedlar bag is prefilled with the pre-calculated volume of air and connected to the breathing circuit. Subjects are instructed to breath normally for a few breaths, prior to initiating a couple of breathing maneuvers from RV to TLC in attempts to recruit the lung and establish a baseline for all breathholds. At end expiration, consecutive blocking of the free breathing port and opening of the inspiratory Tedlar bag terminates the free breathing and allows subjects to inspire the contents of the bag respectively, ensuring minimal inaccuracies. Subjects are then instructed to perform a breathhold following complete inspiration of the contents within. The initial breathing maneuvers are identical for both a ^{1}H and HP ^{3}He MRI scans, except for the pre-calculated volume of air within the inspiratory Tedlar bag. In the case of a 3Helium scan, the volume of air required to reach the desired inflation level is 1 liter less than its calculated ^{1}H counterpart, to account for top up with the 1 liter ^{3}He doses, such that once the subject has inspired the entire contents of the inspiratory Tedlar bag, they are instructed to hold their breath, release the mouthpiece, breath in from the ^{3}He Tedlar bag and then hold their breath for the duration of the imaging, thus reaching the same lung inflation level.

The accuracy of the proposed breathing protocol and breathing circuit was evaluated via calculation of total lung volumes from of the ^{1}H MRI datasets (Figure 30) and compared against those of the MDCT datasets and the sVC measurements obtained.

A sample localizer utilized in placement of the imaging FOV facilitating apical-basal lung coverage within the acquired datasets is presented in Figure 29. Proper volume control of the localizers is one of the most crucial steps in establishing similar apical-basal coverage within all the acquired datasets on a subject per subjects basis. TLC and FRC volumetric scans were segmented for six subjects. Total lung volume measurements, desired VC and percent differences are represented in Table 5. Comparison of the total lung volume measurements (calculated as the sum of all voxels within the lung mask field of view), illustrated a mean difference of 5.25% in lung volume when comparing the MRI and MDCT datasets. Total lung volume differences can be attributed to either the partial volume effects observed due to the larger proton MRI slices, with respect to the MDCT ones, and/or differences due to subject specific VC. Issues affecting the overall matching of lung inflation levels between the MRI and MDCT datasets, arise mainly due to a small subject specific VC and are only an issue during the acquisition of the lower lung inflation level (20% VC) scans. Subjects I and VI are perfect examples of this issue, where the desired %VCs to match the MRI datasets to their MDCT equivalents were 15% and 21% respectively, while the actual %VC was much larger. As mentioned previously, all desired %VC and volumes are calculated prior to initiating the imaging sessions. If the volume required to reach a 20% inflation level based on the subjects' VC measurements is less than 1 liter (minimum allowable volume based on the administered ^{3}He boluses), preferential matching of the proton and ^{3}He MRI datasets is carried out, rather than matching the desired %VC of the MDCT scan, accounting for some of the differences observed during the total lung volume measurements.

5.3 Discussion

To date 43 subjects (32 normal never-smokers, 8 normal smokers and 3 COPD) have been recruited and imaged utilizing the designed breathing circuit and protocol.

Proper instruction of the subjects as well as their adherence to the breathing protocol are crucial to the success in achieving the desired lung inflation levels, following complete inspiration of the volumes within the inspiratory and ^{3}He Tedlar bags is inspired. In the case of the inability of the subject to fully inspire the pre-calculated volumes (air and/or helium), the error in reaching the desired lung volume was calculated as the remaining volume within the Tedlar bags. Throughout all the imaging sessions, only several subjects were not able to fully inspire these pre-calculated volumes, therefore special care must be taken during all aspects of the breathing circuit preparation and breathing protocol instructions, to eliminate any erroneous measurements. The variability revolving around VC measurements with varying arm positioning was eliminated as demonstrated by the data in Table 4, thus facilitating the placement of the arms at the sides of the subjects during MRI imaging rather than extending their arms above their heads for the duration of the imaging sessions. The radiation based nature of MDCT and artifacts introduced due to appearance of the arms within the imaging FOV, necessitate the extension of the arms in the over head position. The short acquisition times involved in acquiring a full volumetric dataset (~5 seconds) and the small bore depths minimize the discomfort involved, while allowing the subjects to rest their arms at their side in-between acquisitions. In the case of the MRI acquisitions, long scanning times and deeper bores eliminate the ability of the subjects to extend their arms in the over head position due to heightened discomfort levels if maintained for prolonged periods of time.

Due to inability of several subjects (n=6) to comply with the breathing protocols and the initiation of breathholds in several others (n=5) from FRC rather than RV, these subjects were removed from the cohort of subject datasets suitable for MRI and MDCT matching. Compliance failures included the inability of subjects to either reach the desired inflation level, determined by the volume of residual gas in the inspiratory bag, or failure to maintain the breath-hold for the duration of the imaging. The majority of these failures occurred during the lower lung volume breathholds, where increasing levels of

CO_2 and minimal O_2 concentrations play a big role in initiating the drive to commence inspiration. Albeit the errors produced due to incomplete inspiration of the inspiratory volumes required to reach the desired lung inflation levels and subject compliance issues, we believe these differences to be minimal with regards to assessing the underlying physiological and/or pathological conditions. This is supported by analysis of the shape of the pressure volume curve, where is can be clearly observed that small changes in volume produce even smaller changes in pressure and vice versa (61).

A major limiting factor to the overall success and accuracy of the generated lung masks and their respective total lung volume measurements is the dependency upon the ability of a given user to distinguish between the actual lung tissue and surrounding areas of artifact and/or similar intensities (bone). Given the minimal proton density available in the lungs, pre-processing of the datasets is required to achieve a sufficient amount of contrast between the lungs and their surroundings to facilitate their segmentation. Different methods have been tested to establish a more defined method to increase border contrast. The most successful solutions (temporary actions performed on the datasets to facilitate the segmentation) have been either contrast manipulations to increase the intensity of the pixels within the datasets (shifting the histogram towards the higher end of the grayscale spectrum) or complete inversion of the image intensities, allowing the lungs to appear brighter than some of the surround tissues.

The presented breathing protocol and breathing circuit design have facilitated accurate control over lung inflation levels, given proper compliance of the subjects. Based on several factors such as the nature of the imaging sessions, administration of HP ^{3}He doses, the increasing cost of raw ^{3}He gas and the limitation in available HP ^{3}He gas per session, we believe this to be an ideal compromise between accurate control of lung inflation levels, elimination of any electrical components that could potentially affect the overall polarization levels and proper rationing of the available HP 3Helium doses. As demonstrated the accuracy achievable via this protocol is very high, with minimal error

margins, but is dependent upon the ability of the investigator to distinguish between the lung field of view and the surrounding tissues. Ideally the presented protocol would be applied to both MRI and MDCT imaging sessions alike, eliminating the difference in %VC matching due to small subject specific VCs.

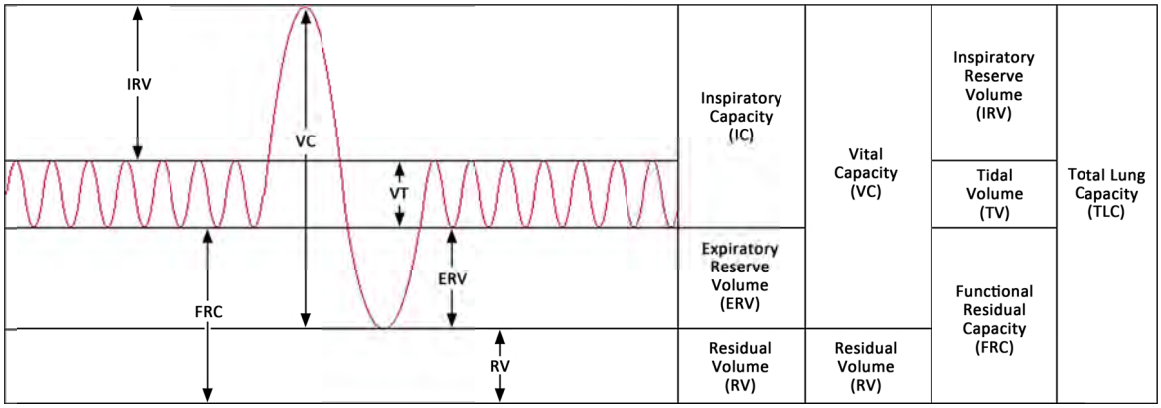

Figure 26. Illustration of lung volumes calculated during the pulmonary function testing procedures. The calculation of VC volumes for each subject is crucial for the standardization of lung volumes and the inflation levels probed between subjects.

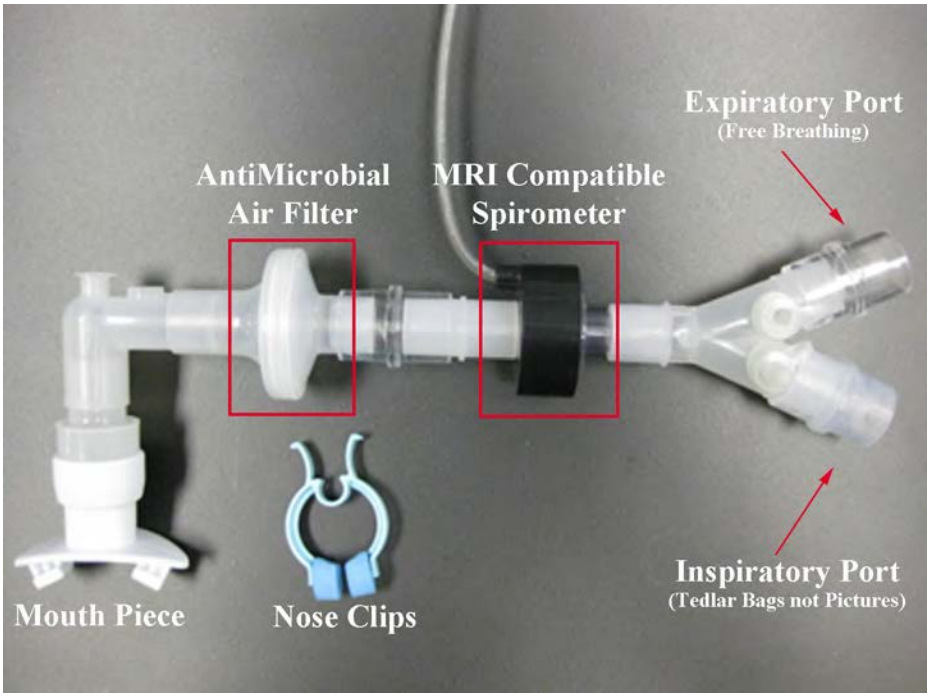

Figure 27. Volume control apparatus for the standardization of lung inflation levels during imaging sessions. The MRI compatible spirometer was only utilized during the testing phases of the design process of both the device and breathing protocol.

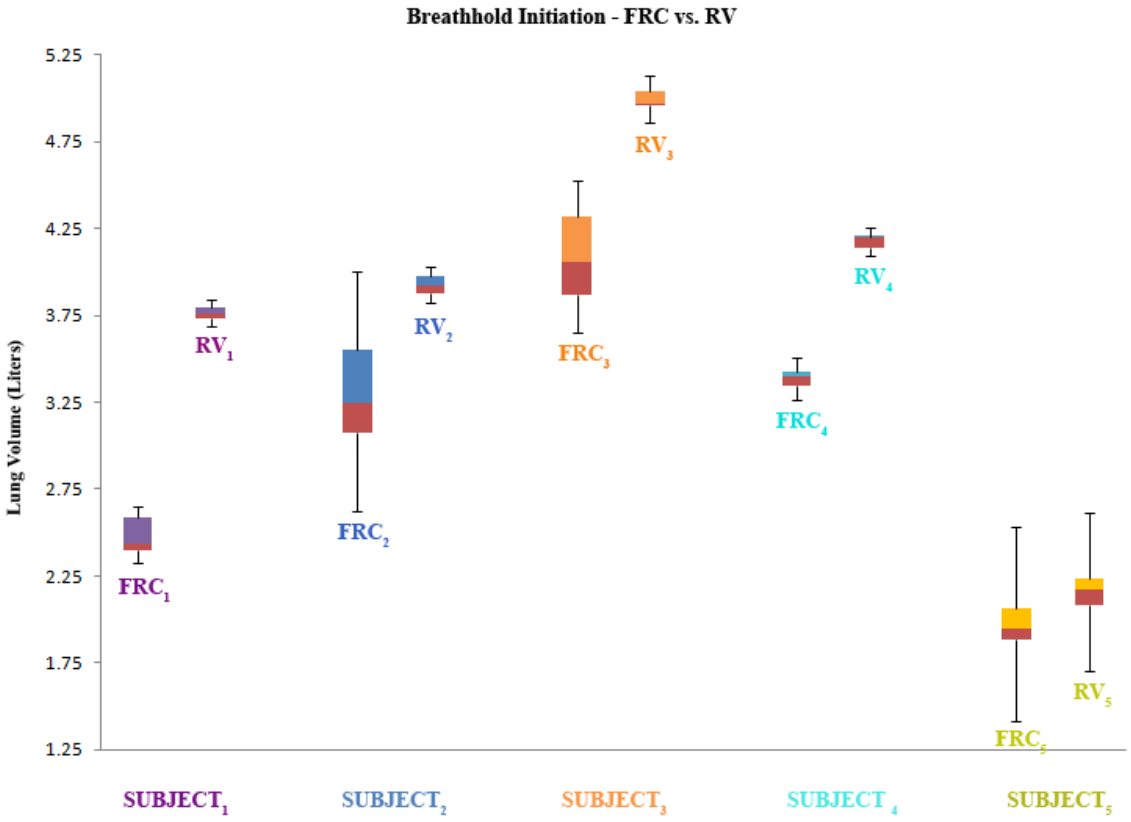

Figure 28. Boxplot representation of breathhold initiation variability in five subjects. Breathing maneuvers were structured to determine repeatability of reaching either FRC or RV. It can be been that RV was reached with better consistency than FRC for Subjects 1-3. Differences in the results of subjects 4 and 5 are possibly due to the fact that subject 4 is an athlete, while subject 5 is an asthmatic.

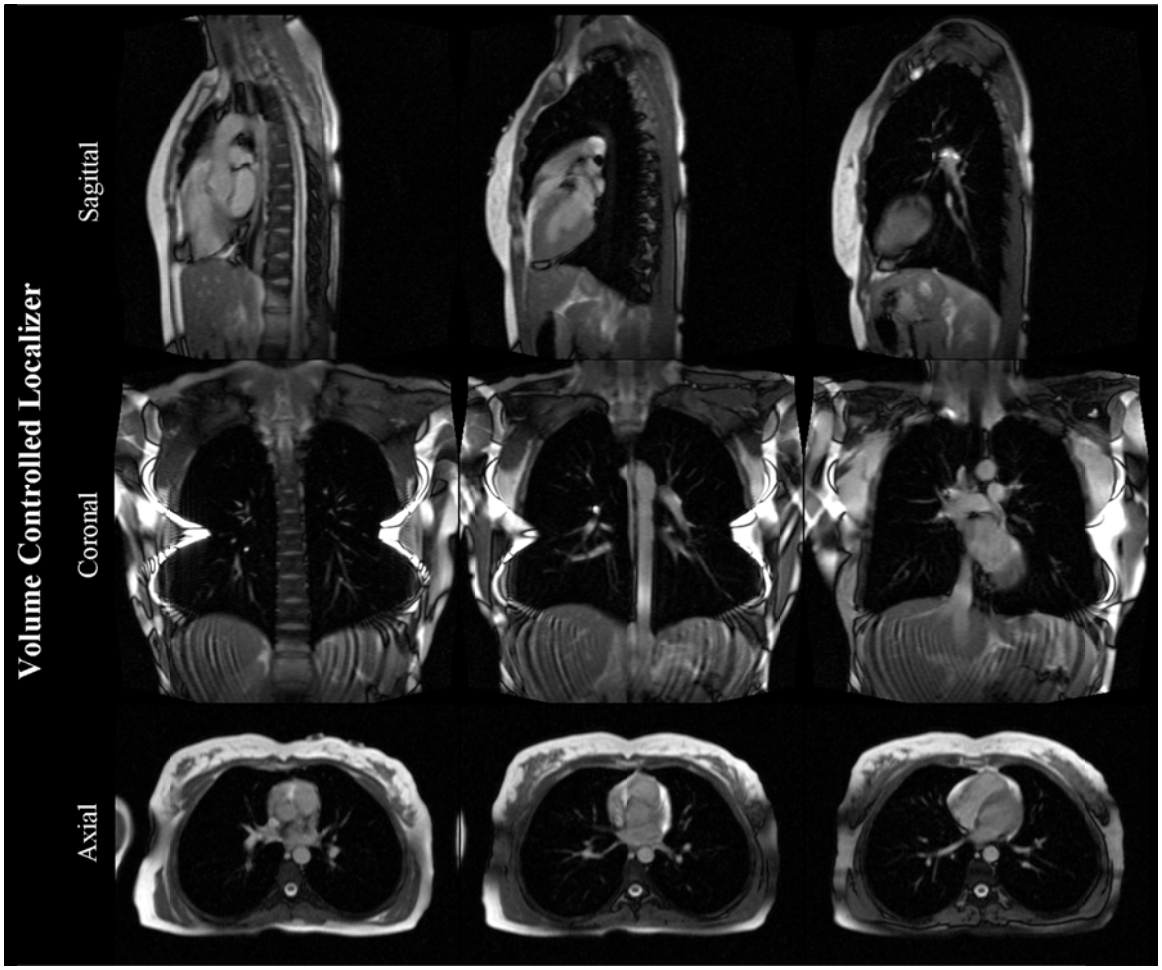

Figure 29. Sample volume controlled localizer. Equidistantly spaced excitations are applied to generate a rough estimate of lung coverage, sufficient for proper FOV placement for the HP ^{3}He and ^{1}H volumetric scans.

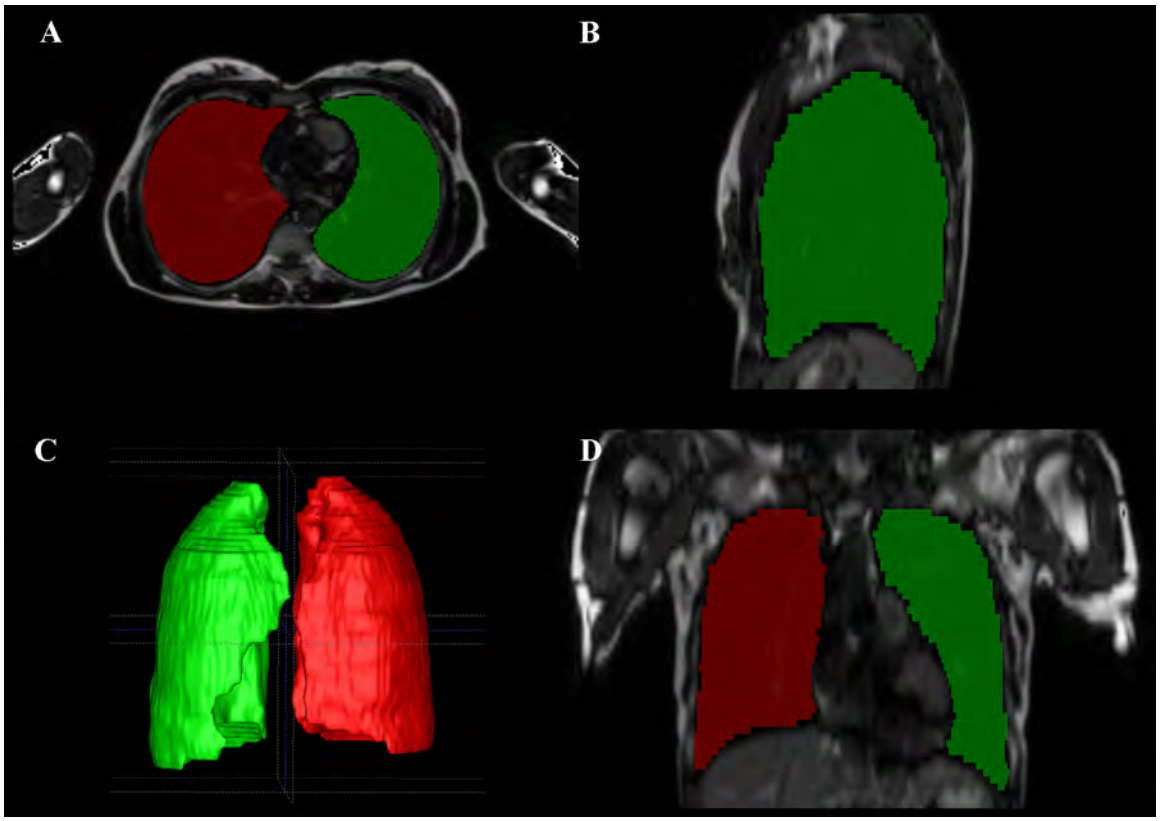

Figure 30. Visual representation of a manually segmented proton MRI TLC (100% VC) lung scan (A - Axial, B - Sagittal, C - Coronal). It can observed that appropriate coverage of the lungs is achieved, along with proper left (green)-right (red) separation. 3D rendering of the lung volumes along with assessment of the resultant masks, illustrates the inherent partial volume artifact due to the large slice thickness of the MRI scans.

Table 3. Average percentage differences in reaching FRC and RV for all 5 subjects tested.

	Subjects				
	1	**2**	**3**	**4***	**5****
FRC	5.18	9.40	6.64	1.93	8.74
RV	1.04	1.59	1.25	1.26	7.96

Average FRC and RV volumes (liters) for subjects 1-5 were 2.49±0.16, 3.24±0.38, 4.07±0.32, 3.39±0.09, 1.89±0.25 and 3.76±0.05, 3.93±0.08, 4.98±0.08, 4.18±0.07, 2.13±0.24 respectively.

* Athlete ** Asthmatic

Table 4. Dependency of VC measurements upon arm positioning.

	Attempts	**Subject I**	**Subject II**
	1	4.971	3.923
Arms Down (at sides)	***2***	4.861	3.728
	3	4.791	3.584
	1	4.855	3.87
Arms Up (over head)	***2***	4.918	3.708
	3	4.733	3.563

*Mean VC measurements for subjects I and II were 4.874±0.091 and 3.745±0.170 liters respectively in the arms down position, while mean VC measurements during the arms up position were 4.835±0.094 and 3.714±0.1535 for subjects I and II respectively.

Table 5. TLC and FRC total lung volume measurements of six subjects

Subject	Scan	VC (L)	RV (L)	Desired %VC		Volume (L)		Diff (L)	Diff (%)
				MRI	CT	MRI	CT		
I **	FRC	3.51	1.84	28	21	2.274	2.61	0.336	12.87
	TLC			100	99	4.334	4.426	0.092	2.08
II	FRC	4.34	3.29	23	20		3.043	3.043	
	TLC			102	103	6.47	6.553	0.083	1.27
III	FRC	2.985	2.52	34	20	3.281	3.269	0.012	0.37
	TLC			87	85	5.35	5.346	0.004	0.07
IV	FRC	3.6593	2.26		20	2.607	2.671	0.064	2.40
	TLC				102	5.29	5.65	0.36	6.37
V	FRC	4.6932	2.35	21	20	2.994	3.007	0.013	0.43
	TLC			92	98	6.303	6.397	0.094	1.47
VI	FRC	2.288	1.65		15	2.728	2.189	0.539	24.62
	TLC				96	3.789	4.025	0.236	5.86

*Average percent difference between MRI and MDCT scans was 5.27±7.46 %, while the average volume difference was 166±176 ml.

**Normal Smoking Subject

CHAPTER 6: IMAGE REGISTRATION

Synergistic applications of medical imaging in assessment of structure and function can lead to complimentary advances in the visualization of the underlying anatomy and physiology. The nature of acquisition and process involved varies from density and magnetic based approaches as demonstrated by MDCT and MRI respectively, to molecular based approaches as demonstrated by SPECT and PET. This multi-modal approach to medical imaging must be gauged with caution due to the varying image spaces of the underlying acquisitions and variability in position and volume of the imaged structures. With the increasing use of medical imaging in both clinical and research settings in diagnosis, planning, treatment and disease progression, it is becoming ever so important to correct for these differences in acquisitions, prior to establishing any correspondences between them.

Unification of the image spaces and elimination of the volume and position based differences can be accomplished via image registration, where the application of rigid and non-rigid transformation models enables spatial mapping of the corresponding voxels (34, 66, 98). Correspondence is defined as either structural or functional, such as pre and post evaluation of treatment response or atlas based assessments of functional variability respectively (34, 66). Image registration is not an end in itself, but rather a mean to add value and facilitate the use of images from different modalities, that without, would have been deemed useless. Image registration has been utilized in the creation of structural and functional based atlases (155), spatial normalization (8, 87, 88), assessment of differences between normal and disease conditions (114, 163), radiotherapy (30), organ deformation (53) and pre and post procedure evaluations (38, 137, 140), demonstrating its versatility and application potential.

Image registration is composed of four components, a similarity metric to determine the extent of match achieved between two volumes, a transformation model to

specify the path by which a source image is deformed to match another, an optimization metric to maximize the similarity criterion and an interpolation algorithm to apply the resultant deformation (34, 66, 98). The similarity metric can be categorized into geometrical or intensity based approaches. Geometric based approaches involve the use of identifiable anatomical elements, functionally important landmarks, curves, surfaces and point landmarks to match a pair of image sets, given that these structures can be easily identified in both. Intensity based approaches rely on the metric's ability to statistically or mathematically match intensity patterns in each set of images, followed by continual adjustment of the transformation model until an optimal solution is reached. The main underlying assumption driving this approach is that the images will be most similar at the correct registration. Algorithms based on information-theoretic knowledge such as mutual information and squared differences of correlation coefficients, intensity and flow patterns, are a few examples of intensity based similarity metrics. These types of metrics are ideal solutions for multi-modality applications where the intensity patterns observed in the image sets are different (34, 66).

The transformation model defines/controls the path of deformation between the source (moving) and target (fixed) image sets of interest, as well as interpolates in the areas that lack usable image information. The most popular transformation models include Rigid, Affine and BSpline, where the latter are generally classified under non-linear deformations, while rigid is classified as a linear deformation. The rigid transform involves rotations and translations, represented by 3 parameters each, one for each dimension (3D space), while the affine transform incorporates the same functionality of the rigid transform, in addition to shearing and scaling, also represented by 3 parameters each. Pixels within the moving image are represented as vectors that are acted upon by the parameters of the transform, mapping its placement into the fixed image space. BSpline transforms utilize equidistantly spaced control points within the image space to globally deform the underlying space to match the target space. The control points work

in such a manner, that if deformed, all pixels within the neighborhood of the point are also deformed. These control points are defined locally, such that the deformations are representative of local and not global information. In such non-linear cases, as with the BSpline transform, a major disadvantage is the appearance of fold-over artifacts or excessive deformations, which can be overcome by setting limitations to degree of deformation achievable with such methods(34, 66, 98, 187).

The main driving force of each registration problem is the optimizer, guiding the similarity metric and transformation to an optimal and reliable solution, by either minimizing or maximizing the similarity criterion. During the registration, the current transformation model of each iteration is utilized to estimate the similarity measure, which is then utilized by the optimizer in generating another similarity measure estimate that will guide the registration along the proper path of convergence. Proper understanding of the task at hand and image space features is required for appropriate optimizer selection, otherwise local minima and maxima can profoundly affect the results, leading to incorrect local optimization. The final component of the registration is the interpolator, which can be thought of as a convolution process. Given the low probability of exact alignment between the fixed and moving image voxels, the interpolator is utilized to estimate the exact intensity value for each corresponding voxel, based on a neighborhood criterion. Interpolation algorithms include nearest neighbor, linear, BSpline and windowed sinc, where the higher dimensionality of the algorithms is directly proportional to the level of approximation achieved (98).

Several software packages dedicated to inter and intra-modality image registration are currently available on multiple computing platforms, such as Slicer3D, Elastix, BrainsFIT and MATLAB. Given the complex nature of the acquisitions at hand and the need for a more personalized/flexible approach to the registration aspect of the presented work (Figure 31), such software packages would require multiple registration steps and manipulations to reach the optimal solution. Therefore, a comprehensive registration

script was written in C++ utilizing the Insight ToolKit (98, 124)libraries to facilitate the registration of the HP 3Helium datasets to their MDCT based counterparts (98). The main objective of the script was to register the desired datasets in a manner, minimizing the need for manipulation of the underlying code to achieve the desired results.

6.1 Methods

The implementation of the script was created to include rigid, affine and a multi-resolution and multi-grid BSpline capabilities to facilitate the testing and implementation of the all the possible registration pipelines required through the presented work (Figure 31). Given the numerous image data formats available to the medical imaging community, such as Analyze, Nifti and Nrrd, the registration script was written as a template, utilizing the image dimension and image type (short, long, unisghed char, char, etc …) as the template variables. This facilitates the implementation of the registration script on all accepted image types, without having the need to recompile the script for each application. Rather than requiring a large number of flags during the execution process or having to recompile the code due to hard coded parameters, all registration parameters (Table 6) are consolidated into a single pre-organized *.txt* file which is fed in as a matrix allowing for the initiation and implementation of the image registration process according to the desired pipeline. Through the use of the MetaCommand (*Kitware*) option, command line parsing was implemented to execute the registration script with the desired parameters, including fixed and moving images, fixed and moving masks (optional), desired prefix and suffix of the output datasets, the registration variables file and image type.

The registration procedure starts by reading in the fixed and moving image datasets and masks (optional) and casting them to the proper image type as defined in the command line arguments. Following which the image datasets are smoothed (optional) utilizing an edge preserving smoothing function (Curvature Anisotropic Diffusion) to

eliminate noise and smooth image intensities. Once the pre-processing of the image data is complete, the multi-resolution image pyramid levels are setup, according to the desired number of resolution levels throughout the registration pipeline. Choice of optimizer (Regular Step Gradient descent - RSGD or Limited-Memory Broyden–Fletcher–Goldfarb–Shannon - LBFGSB), Metric (Mean Squares or Mutual Information) and Interpolator (Linear, BSpline, Windowed Sinc) are carried out through the use of the proper flags from the supplied registration variable file, prior to initialization of the registration process. An optional flag was created to allow output of the transformation and deformed volumes following the completion of each major component, facilitating a more thorough evaluation of the registration process. The implementation of the rigid and affine registrations is relatively straightforward, and is carried out on single resolution single level basis, requiring the definition of only one resolution level for execution, along with other parameters such as number of histogram bins, number of iterations, optimizer precision and image sampling percentage. In the case of the BSpline registration, a schedule of resolution levels along with their desired grid levels is required to execute the registration, along with the aforementioned parameters.

Image dimension re-sampling is an important step in the image registration process and is generally carried out via the generated transformation model and a re-sampling filter, applied to the image dataset under analysis. In some cases, it is beneficial to re-sample the imaging datasets prior to feeding them into the registration pipeline to achieve more fine tuned results and/or to minimize computation time. Therefore, an image resampling script was written utilizing the *itk:ResampleImageFilter* to upsample or downsample acceptable image type datasets to a desired resolution level (98). Similar to the registration script, the resampling script was also templated over image type and command line parsing was utilized to feed the appropriate parameters into the script which included input and output image filenames, x-y-z coordinate resampling factors,

interpolation method (linear, BSpline or windowed sinc), image type and resampling method (desired image size or reduction factor).

Utilizing the *itk:WarpImageFilter*, another script was written to resample and deform any given dataset via a supplied deformation field, which is generally the final result of the registration process (98). This standalone deformation script is very useful in cases where the resultant deformation generated from the registration is required to place similar datasets into the same image space and size. Therefore, rather than re-running the registration with the same exact parameters, feeding the script with the desired deformation field and input images, results in the resampling and deformation of the input image according to the field. Command line parsing was utilized to supply the proper initialization parameters into the script, which included input image, output image and deformation field filenames, interpolation method (linear, BSpline, windowed sinc) and image type.

The most important image registration pipeline required to facilitate the multi-modality aspect of lung ventilation assessment throughout the presented work is the registration of the HP ^{3}He MRI datasets to their respective MDCT based counterparts. This along with ^{1}H MRI – conventional MDCT and ^{1}H MRI – ^{1}H MRI registrations are tested and evaluated to establish the extent of the written script in achieving proper matching of the underlying anatomical structures and similarly providing technical insight into the advantages and disadvantages of each registration problem. *All written ITK based scripts have been properly commented and documented to facilitate ease of use and manipulation for future users and researchers. Testing was performed on a hyperthreaded quad-core Linux platform, running Opensuse with 16 Gb of memory. All registration code was written utilizing the latest available version of ITK v3.20.0.*

6.2 Results

Verification of the functionality of the registration script components was carried via testing each component separately and in combination with the remainder of the script. All components performed exceptionally well in relation to other established image registration programs (3D Slicer). The registration script has been compiled and run on both Windows and Linux machines alike, producing identical registration results without any complications. The performance of the registration script during some of the tested registrations can be observed in Table 7.

Testing of the ^{1}H MRI – conventional MDCT volumetric data registration task on FRC and TLC datasets, was carried out in a multi-resolution and multi-grid fashion, while varying the sampling percentages of the registration components, the resolution of the MDCT datasets, number of BSpline grids, resolution of the BSpline grids and image resolutions during each of the main registration components (rigid, affine and BSpline). Given the superior resolution of the conventional MDCT volumetric datasets with respect to their ^{1}H MRI equivalent, the MDCT datasets were set as the moving images, while the MRI ones were set as the fixed (reference image). Utilizing the re-sampling script, two-fold and four-fold spatially resampled MDCT datasets were generated to test the limitations of the registration and ability to produce accurate results while minimizing run time of the scripts. Regardless of the resolution of the applied BSpline grid (8x8x8, 16x16x16 or 32x32x32), the deformed results were insufficient to achieve proper matching of the underlying anatomy (Figure 32). It can be observed that the applied deformation did not achieve proper matching of the lung borders, regardless of anatomical position (apical-basal). Similarly, the use of the 128x128 resampled MDCT datasets was quickly ruled out as a possible viable resolution level, due to the extremely deformed nature of the registration results (Figure 33). It can be observed that not only was the lung field of view excessively deformed, but anatomical structures including the spine and ribs were as well. The difference in acquisition and contrast generation between

the MRI and MDCT volumetric datasets, results in the later achieving better resolutions (~0.5 mm) along the z-axis, with respect to those achieved during the MRI acquisitions (~5 mm). This results in approximately a ten-fold difference in number of slices available within the MDCT datasets, covering the same z-axis length as the MRI datasets. Registration results of down-sampled z-axis MDCT datasets resulted in similarly deformed results as those presented in Figure 33, regardless of the spatial and grid resolution of the moving images and BSpline grids respectively. The effect of sampling percentage of the moving and fixed images during the registration was similarly tested by varying the value between 5% and 50%, under a single, double and triple grid applications, with no improvements in overall alignment or deformation of the resultant datasets (Figure 34). Figure 35 demonstrates the improved performance of the affine registration with increased sampling percentages. Increasing sampling percentages also increases overall processing time, due to the larger amount of data handled by the optimizer and metric during the registration process. Regardless of this increase in processing time the convergence criterion is reached with less iterations which is a more desirable effect than processing time improvements. Performance of the registration script during a 3-grid BSpline registration is visualized in Figure 36, illustrating the convergence of the metric criterion during the application of the final BSpline grid, further validating the use of a 3-grid BSpline scheme in the proposed ^{1}H MRI – MDCT registration problem. Proper matching of the MDCT and MRI volumetric datasets was achieved utilizing the full resolution fixed MRI datasets and a 256x256 spatially downsampled moving MDCT, in combination with 30% sample percentage and the application of two BSpline grids with varying grid resolutions (8x8x8 and16x16x16). The nature of the rigid and affine transformations in applying translations, rotations, stretch and shear to the datasets does not necessitate the use of the full resolution versions, thus spatially downsampled versions of both datasets were utilized during this process. Improvements in overall lung border alignment and apical and diaphragm regional

alignments were achieved following these parameters (Figure 37), when compared to those achieved during single BSpline grid registrations with varying grid resolutions and the use of the 128x128 spatially downsampled MDCT datasets.

Although these alignment enhancements improved the overall image matching of lung field of view between the MRI and MDCT datasets, improper alignment of the surrounding structures, seen as over rotation of the spine and ribs, eliminates the use of these results in quantitative assessments. Further improvements in lung FOV and anatomical structural alignment between the FRC MRI and MDCT datasets was achieved utilizing a three gridded BSpline, with 50% sampling percentages and full resolution MRI and MDCT datasets throughout all registration procedures (Figure 38). Analysis of the difference images between the fixed and final deformed image datasets, illustrates minimal differences in alignment along some portions of the heart borders and within the diaphragm region (Figure 39). Proper TLC matching between the MRI and MDCT datasets was also achieved utilizing identical parameters, as those implemented for the FRC datasets (Figure 40).

With respect to the ^{1}H MRI – ^{1}H MRI image matching between FRC and TLC datasets, similar testing utilizing varying levels of image resolution, BSpline grid resolutions and sampling percentages was implemented, while alternating between the TLC and FRC as fixed and moving images. Regardless of the parameters implemented during the registration process, or fixed and moving image selections, excessive deformation of the lung FOV and surrounding structures was observed in all final deformed volumes (Figure 41). Slightly less deformations of the lung FOV and surrounding structures were achieved by setting the FRC and TLC datasets as the fixed and moving images respectively, utilizing a two grid BSpline scheme (16x16x16 and 32x32x32), when compared to a three grid BSpline scheme with the incorporation of an initial 8x8x8 gridded BSpline.

In the aforementioned registration problems with regards to ^{1}H MRI – ^{1}H MRI and ^{1}H MRI – MDCT image registration, the inclusion of the surrounding anatomical structures within the imaging FOV is crucial factor in facilitating the overall success of reaching accurately deformed final volumes. The lack of these structures within the HP ^{3}He MRI datasets, prompted us to follow a rigid + affine only registration scheme, utilizing the generated masks as ground truth for the proper matching of the FOV within the datasets. The use of spatially downsampled (128x128) MDCT datasets as the moving images, while the HP ^{3}He MRI images were set as the fixed images, produced excellent image matching between the datasets sufficient for proper quantitative and qualitative assessment of the underlying structure and function (Figure 42). Initial testing was performed utilizing the full resolution MDCT datasets and varying single BSpline grid resolutions, but due to the larger number of z-axis slices within the MDCT datasets with respect to the MRI datasets (MRI – 6, MDCT ~ 500-600), the image registration script failed to achieve proper matching between the two, either through mismatching of the slices or excessive deformation of the MDCT slices. Optimal registration parameters for the tested image pairs can be seen in Table 8.

6.3 Discussion

The tested registration script has demonstrated its ability in facilitating both quantitative and qualitative assessments of the underlying structure and function in common between the ^{1}H MRI – MDCT and HP ^{3}He MRI – MDCT image pairs through appropriate matching of the lung FOVs. In combination with the resampling and deformation scripts, all registrations and deformations can be applied utilizing a single script, rather than utilizing many different registrations and concatenating the results, utilizing the end result of one registration as the input for the next and so forth. The flexibility of the registration script is demonstrated in its ability to modify the registration parameters, through the use of the supplied registration parameters file, eliminating the

need to recompile the code following each change. Similarly, in combination with bash scripts, multiple runs of the registration are achievable in parallel or in successive order.

Extensive testing of the registration script has demonstrated its functionality and repeatable nature of the produced results. The most problematic areas throughout all the image registration efforts of the ^{1}H MRI – MDCT image pairs tend to fall around the heart and diaphragm borders. All the registrations utilize the supplied image masks as the defining limitations of the applied transformations. Given the difficulties involved with proper segmentation of these areas within the MRI datasets, due to motion artifacts and over and/or under segmentation of these regions within the masks, regional mismatches could arise due to the inability of the registration to achieve a proper match between the datasets. Similarly, the appearance of bone structures near the lung FOV, introduces susceptibility artifacts that could possibly lead to the same effects as observed with the heart and diaphragm borders. Improvements in the overall ^{1}H MRI mask generation process to incorporate a more automated approach, rather than the user biased manual segmentation approach utilized could improve the end result of the image registrations within these regions. Similarly, improvements in overall pulse sequence design to enhance the resolution of the acquired MRI datasets and eliminate these artifacts could be very beneficial. Given the current state of these tools and the overall difficulties in volume control and mask generation, the registration script has demonstrated an exceptional ability in matching the lung FOVs in both ^{1}H MRI and HP ^{3}He MRI cases.

In terms of the ^{1}H MRI FRC to ^{1}H MRI TLC image matching, the use of the conventional image information based metrics is not a proper tool in guiding the overall registration between the two datasets. This process could possibly benefit from a more normalized, mass preserving metric, such as the SSTVD metric proposed by Yin et al. (187) applied to MDCT volumetric datasets. Slight modifications to the metric along with proper definition of true tissue and air intensities are some of the modifications to both the metric and image acquisition tools to facilitate the use of this metric in achieving a

proper match between the datasets, while minimizing structural deformation inside and outside the lung FOV.

Further improvements to the registration script include the implementation of a user defined series of landmarks, to guide a landmark based registration and the use of these landmarks as boundary conditions for the applied registrations. The use of these landmarks could serve as another convergence criterion, limiting the excessive nature of the applied deformations, while maximizing the overall deformation potential of the lung FOV. The ability of the registration script to output the transform and deformed images following the completion of the rigid, affine and BSpline components has served as a great tool in assessing the overall success of the applied registration and has facilitated a more robust approach in determining the proper parameters. Rather than outputting the deformation field and deformed volumes following the final BSpline application only, inclusion of intermediate BSpline deformation field outputs following each BSpline implementation will allow for a more detailed assessment of the intermediate deformations applied. The introduction of ITK v4 to the medical imaging community promises with it the implementation of several new filters and segmentation capabilities. One filter for example, the *itk::MaskImageFilter*, takes an input image and its respective mask and performs a background removal process, which was previously performed either through the use of external image processing tools or a pixel-by-pixel based code segment. The implementation of such improvements along with the addition of a Slicer3D execution model compatible xml script, have the potential to enhance the overall ability and outcomes achievable via the registration script and facilitate a more user friendly approach to running the scripts through the use of Slicer3D as a GUI.

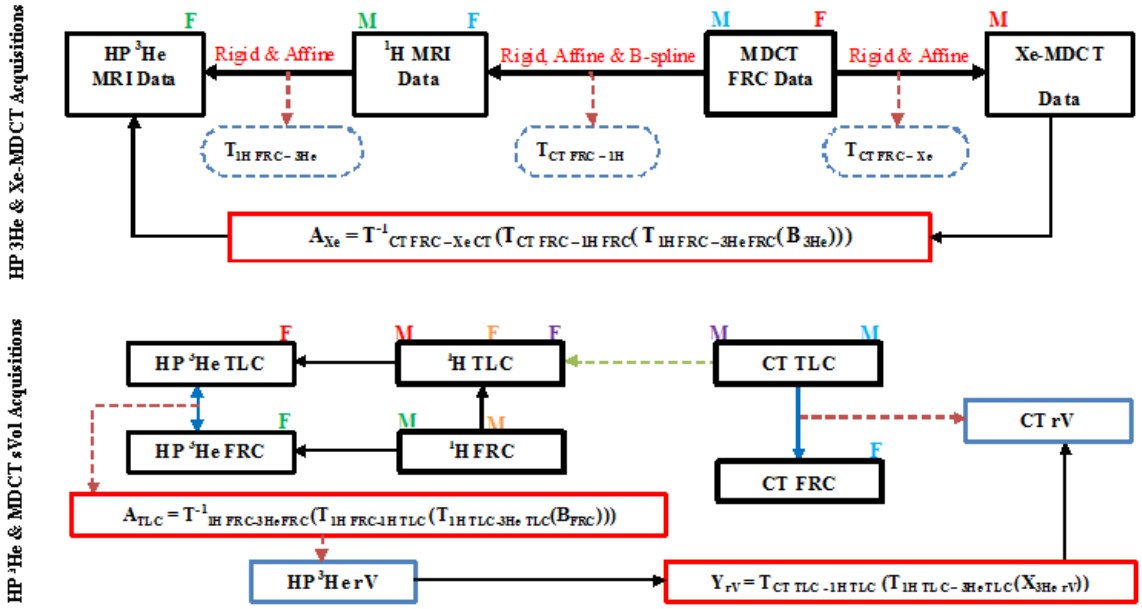

Figure 31. Pipeline demonstrating all possible image registration requirements to facilitate proper multi-modal assessments of the MRI and MDCT based functional estimates of regional ventilation and expansion. Moving and fixed image selections are represented by M and F throughout the pipeline.

Table 6. Rigid-Affine-BSpline (RAB) Registration Parameters

FLAG	**TYPE**	**FLAG**	**TYPE**
Smoothing	*Bool*	Rigid Histogram Bins	*Integer*
Smoothing Time Step	*Float*	Rigid Sample Percentage	*Float*
Smoothing Iterations	*Integer*	Rigid Iterations	*Integer*
Smoothing Filter Conductance	*Float*	Rigid Precision	*Float*
Intermediate Output	*Bool*	Affine	*Bool*
Intermediate Transform	*Bool*	Affine Iterations	*Integer*
Image Pyramid Levels	*Integer*	Affine Precision	*Float*
Optimizer Choice	*Bool*	Affine Sample Percentage	*Float*
Interpolator Choice	*Integer*	Bspline	*Bool*
Metric Choice	*Bool*	Bspline Sampling Percentage	*Float*
MI Use PDF Derivatives	*Bool*	Bspline Registrations	*Integer*
MI Use Bspline Weights Caching	*Bool*	Bspline Iterations	*Integer*
Rigid	*Bool*	Bspline Histogram Bins	*Integer*
Center of Mass	*Bool*	LBFGSB Evaluations	*Integer*
Rigid Resolution Level	*Integer*	LBFGSB Corrections	*Integer*

Table 7. Registration performance during several testing and final result implementations.

		Rigid	Affine	BSpline^{8}	BSpline^{16}	BSpline^{32}	BSpline^{64}	Total Time
^{1}Grid	*Iterations*	9.0	26.0	134.0				89.2
	Time (sec)	20.1	31.1	38.0				
^{2}Grid	*Iterations*	9.0	26.0		165.0			91.5
	Time (sec)	20.7	31.6		39.2			
^{3}Grid	*Iterations*	9.0	26.0			152.0		105.5
	Time (sec)	25.3	37.0			43.1		
^{3}Grid$_{256\ 5\%\ 200}$ FRC	*Iterations*	22.0	58.0	15.0	100.0	17.0		519.4
	Time (sec)	2.9	135.4	80.9	141.4	158.8		
^{3}Grid$_{256\ 5\%\ 200}$ TLC	*Iterations*	5.0	14.0	34.0	100.0	100.0		535.8
	Time (sec)	4.6	45.0	130.0	171.8	184.4		
^{3}Grid$_{256\ 30\%\ 200}$ TLC	*Iterations*	13.0	27.0	100.0	100.0	100.0		2910.2
	Time (sec)	44.5	96.1	926.7	924.4	918.5		
^{3}Grid$_{256\ 30\%\ 200}$ FRC	*Iterations*	40.0	51.0	100.0	100.0	100.0		3041.2
	Time (sec)	130.4	172.7	921.2	922.7	894.1		
^{3}Grid$_{\text{ORIG 30\% FULL}}$ TLC	*Iterations*	17.0	16.0	63.0	100.0	100.0		2858.1
	Time (sec)	68.6	87.3	849.8	918.6	933.8		
^{3}Grid$_{\text{ORIG 30\% FULL}}$ FRC	*Iterations*	25.0	18.0	100.0	100.0	100.0		3175.9
	Time (sec)	129.3	93.0	998.5	1003.7	951.5		

Table 7 Continued

^{3}Grid$_{256\ 30\%\ 200}$ FRC ^{1}H	*Iterations*	8.0	57.0	100.0	100.0	100.0		338.3
	Time (sec)	3.4	44.9	96.2	96.8	97.0		
^{3}Grid$_{256\ 30\%\ 200}$ TLC ^{1}H	*Iterations*	11.0	26.0	100.0	100.0	100.0		321.9
	Time (sec)	3.3	32.0	96.6	96.1	93.8		
^{2}Grid$_{256\ 30\%\ 200}$ FRC ^{1}H	*Iterations*	22.0	57.0	100.0	100.0			318.3
	Time (sec)	6.1	83.5	113.3	115.4			
^{3}Grid $_{ORIG\ 30\%}$ TLC	*Iterations*	18.0	17.0	250.0	176.0	250.0		8395.1
	Time (sec)	63.7	70.2	2073.1	2779.0	3409.2		
^{4}Grid $_{ORIG\ 30\%}$ TLC	*Iterations*	18.0	17.0	250.0	176.0	250.0	250.0	15556.8
	Time (sec)	87.6	85.8	3573.6	4061.2	3894.5	3854.2	
^{3}Grid $_{ORIG\ 30\%\ UCHAR}$ TLC	*Iterations*	16.0	11.0	117.0	250.0	134.0		5138.4
	Time (sec)	62.2	54.8	1469.9	1771.6	1779.9		
^{4}Grid $_{ORIG\ 30\%\ UCHAR}$ TLC	*Iterations*	16.0	11.0	117.0	250.0	134.0	196.0	7075.1
	Time (sec)	67.1	56.9	1473.5	1777.8	1805.3	1894.7	
***^{3}Grid $_{ORIG\ 30\%\ UCHAR}$ TLC**	*Iterations*	25.0	50.0	65.0	250.0	250.0		4510.7
	Time (sec)	80.2	131.9	995.4	1561.1	1742.2		
***^{4}Grid $_{ORIG\ 30\%\ UCHAR}$ TLC**	*Iterations*	25.0	50.0	65.0	250.0	250.0	250.0	12366.3
	Time (sec)	148.2	277.1	2539.4	3103.7	3251.5	3046.5	

The values inserted between the # of Grids and volumes are the resolution, sampling percentage and number of z-axis slices.

** Different Subject*

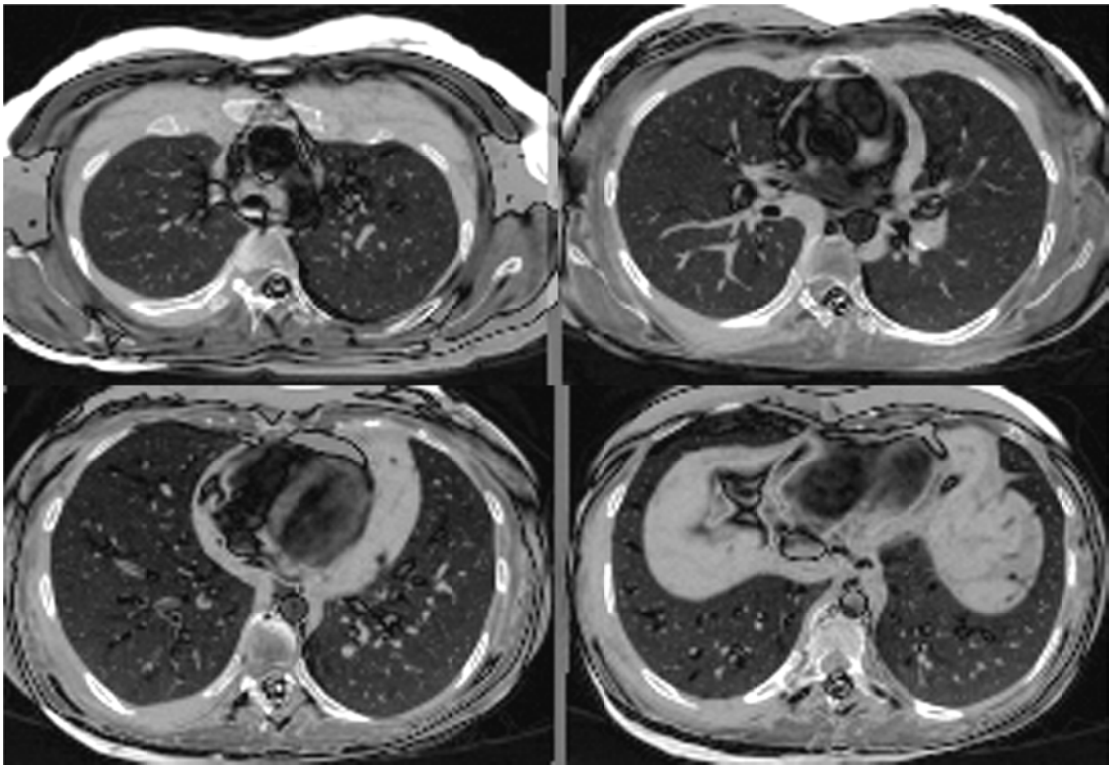

Figure 32. Difference between final deformed MDCT volume (dark lung region) and the fixed MRI volume (light gray lung region) as result of a Single-Grid BSpline registration. Similar results were obtained regardless of the grid resolution.

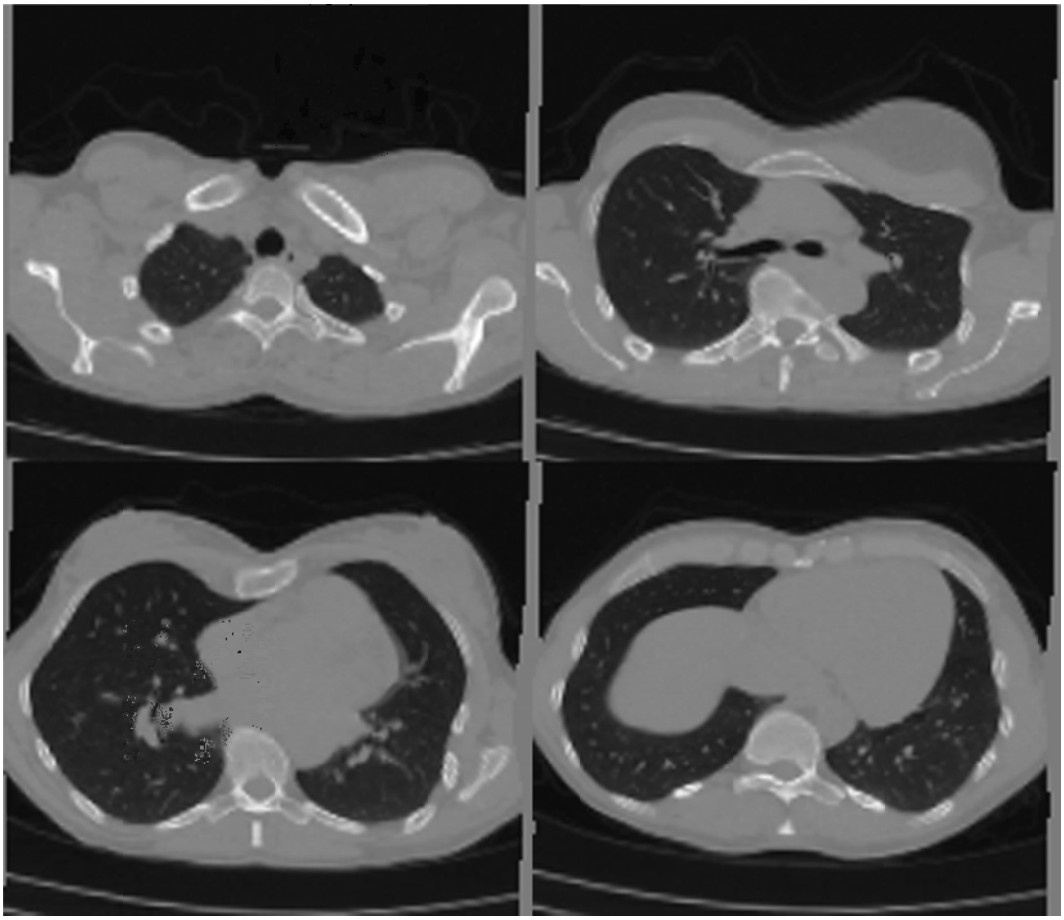

Figure 33. Excessive Deformation of the Moving Image (registration output) as a result of spatially resampling the original images from 512x512 matrix to a 128x128 matrix.

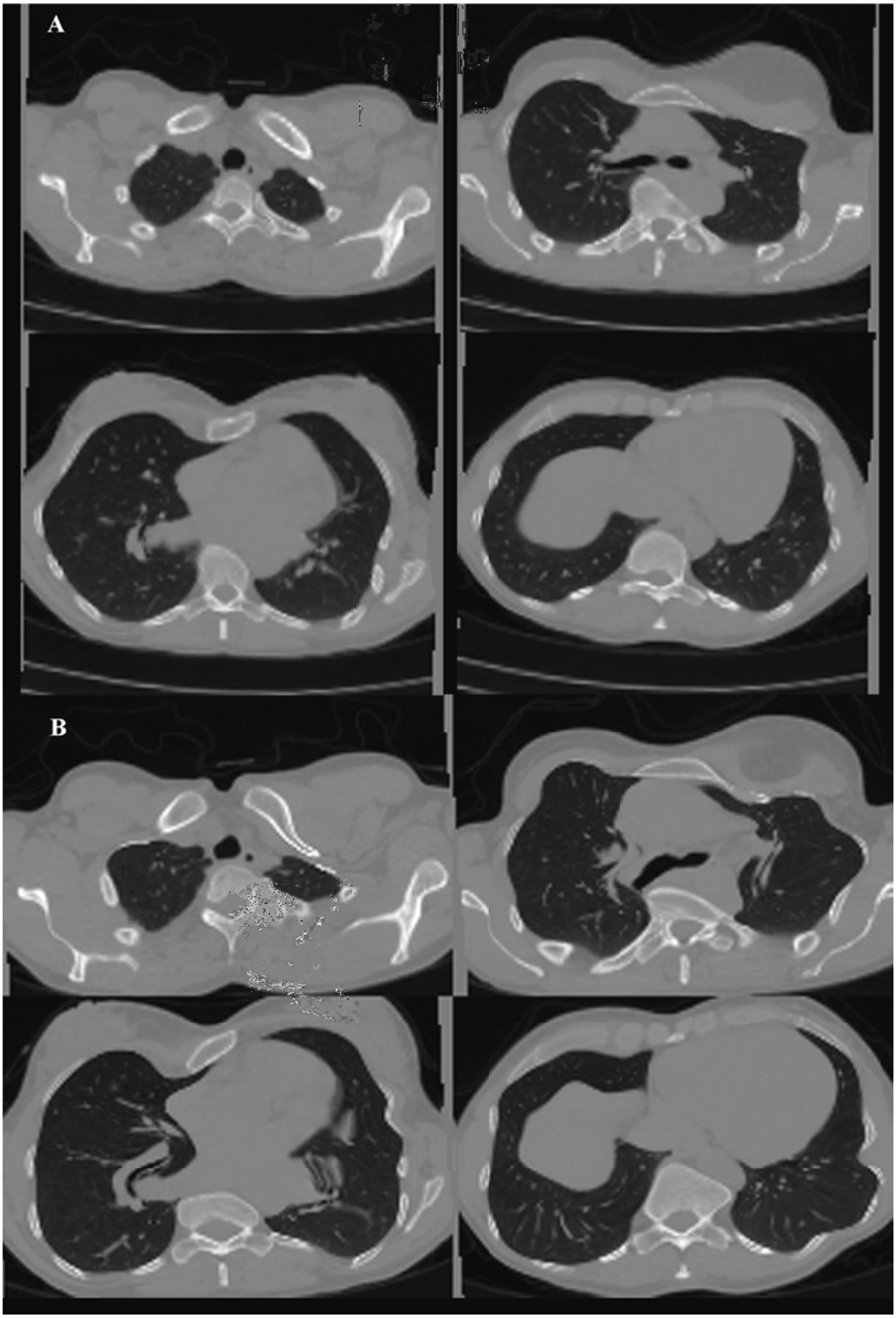

Figure 34. Excessive deformation of the lung field of view along with surrounding anatomical structures is observed regardless of sampling percentage of the registration implemented in a 3 Grid BSpline Registration.

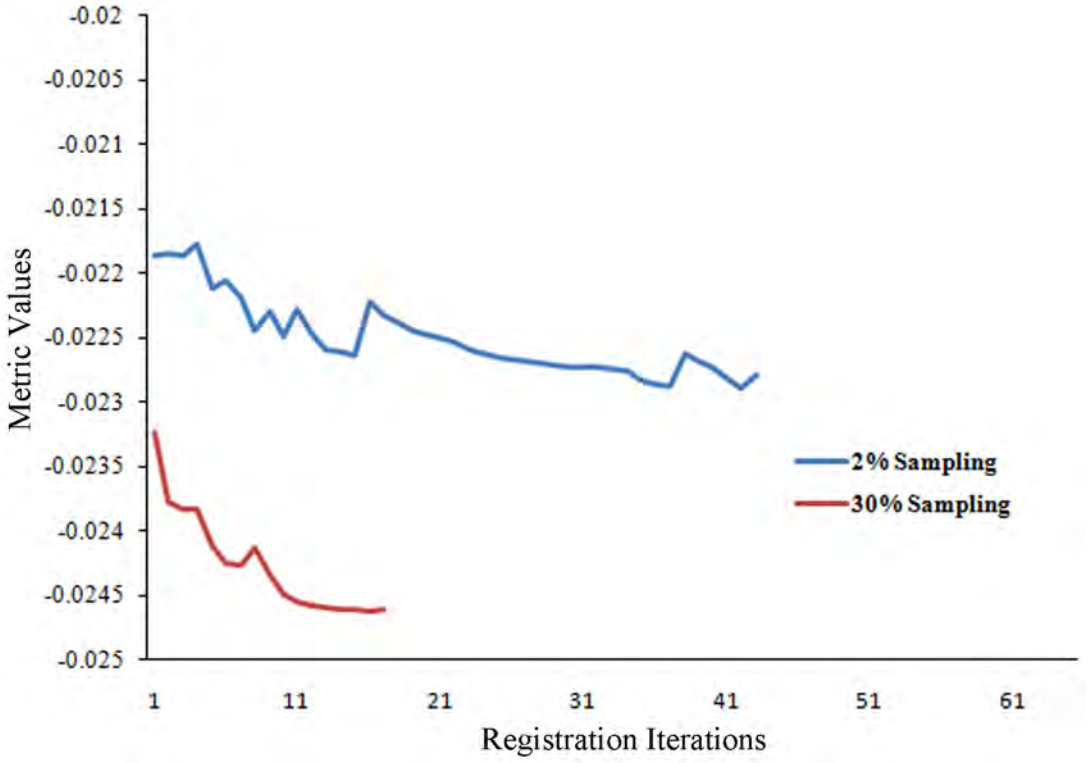

Figure 35. Improved performance of the registration during the Affine Transform implementation is achieved via increasing the sampling percentage of the registration. The convergence criterion is reached with less iterations, thus improving the overall performance of the registration in achieving a proper fit.

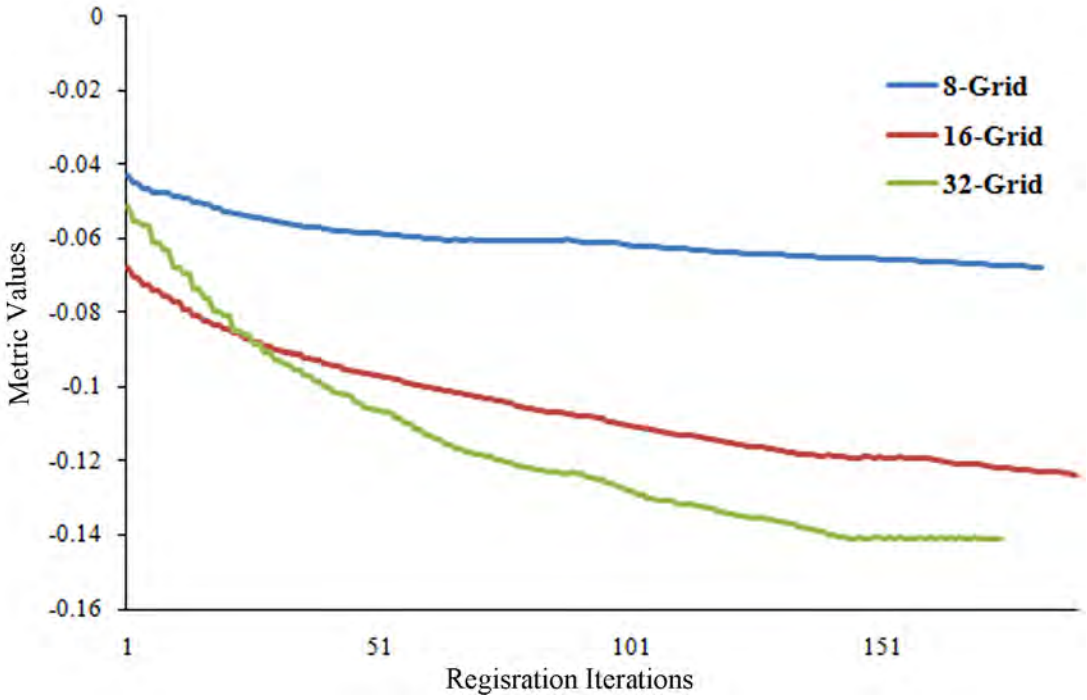

Figure 36. Analysis of the gridded BSpline registration illustrates that a 3 gridded BSpline is required to achieve convergence of the metric values as assessed by the optimizer. It can be observed that convergence is only achieved during the final grid (32) applied during the registration run.

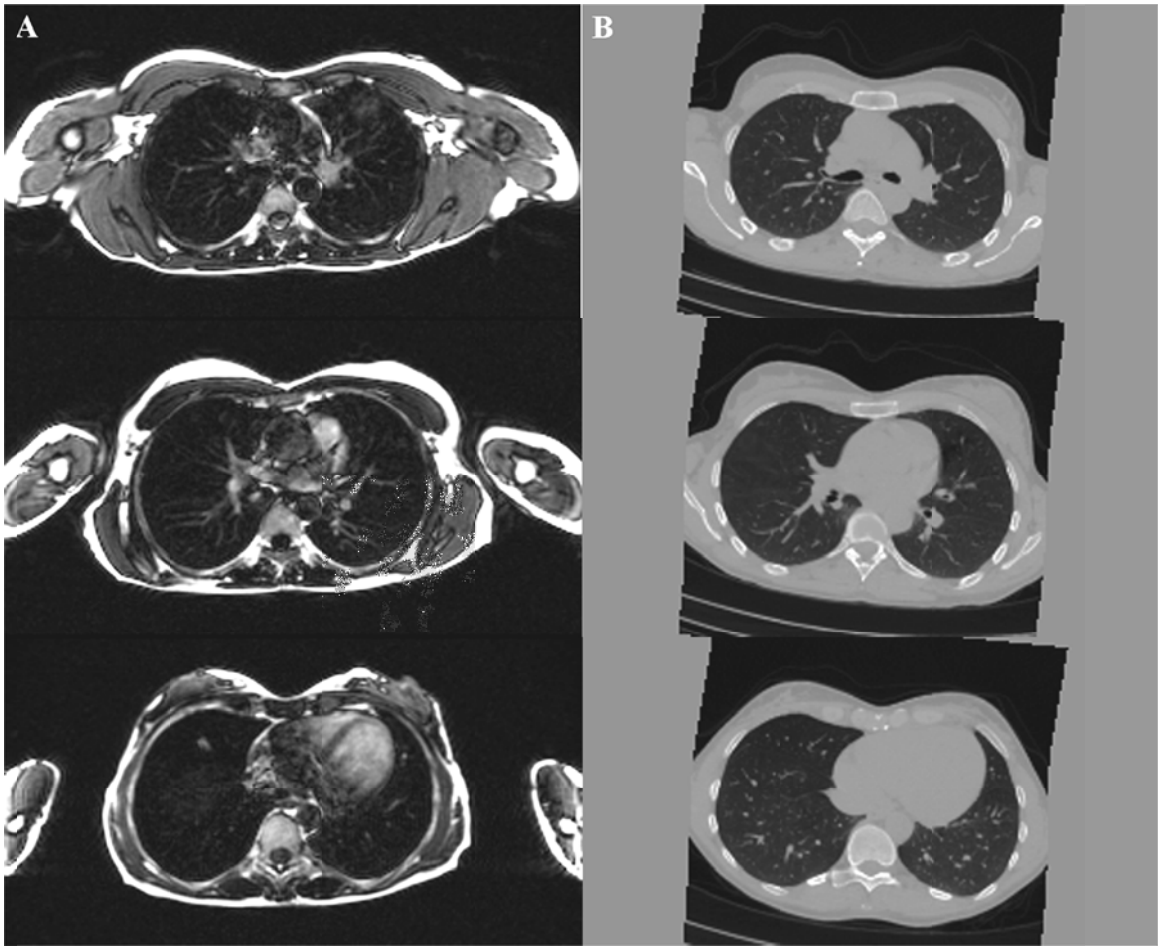

Figure 37. Improvements in matching FRC MRI and MDCT volumetric datasets with respect to those previously presented in Figure 33, Figure 34 and Figure 35 were achieved utilizing 30% sampling percentages and application of a two grid BSpline registration scheme (8x8x8 and 16x16x16) to the full resolution fixed MRI datasets and spatially (256x256) downsampled moving MDCT images. Albeit proper lung FOV matching, over rotation of the surrounding anatomical structures is apparent.

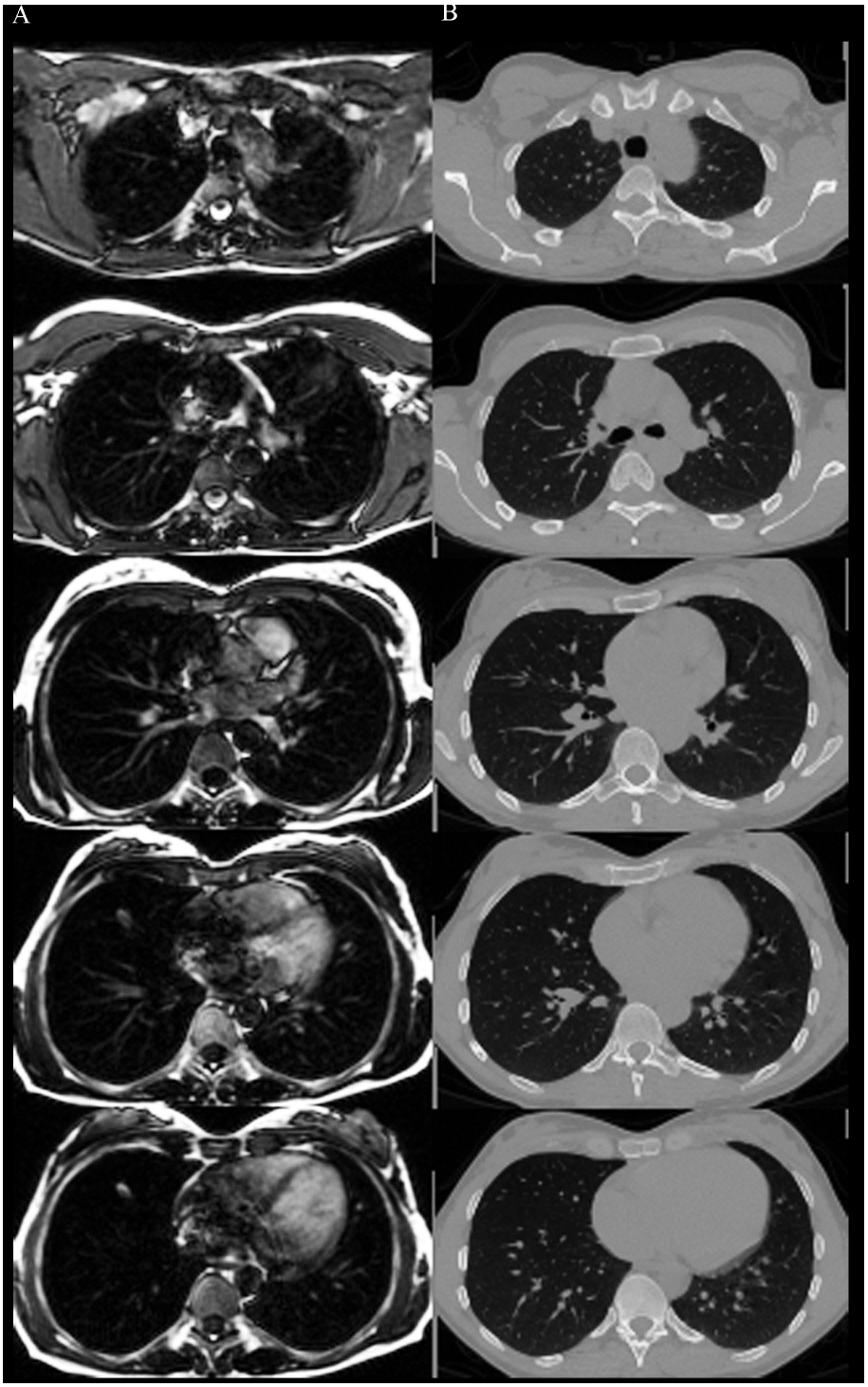

Figure 38. Final results of FRC MRI and MDCT matching illustrate improvements in lung FOV alignment, along with proper alignment of the surrounding anatomical structures.

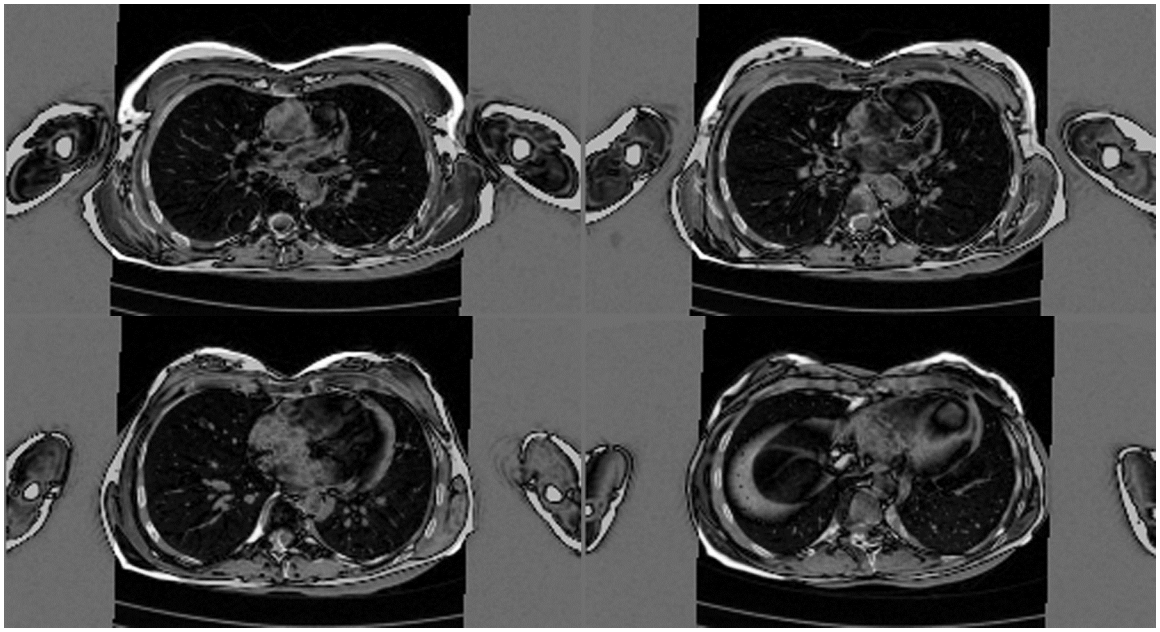

Figure 39. Difference between fixed MRI FRC dataset and resultant deformed moving MDCT dataset, illustrates significant improvements in overall lung FOV and anatomical structure alignments between both datasets. Minimal differences are observed around the heart borders and within the diaphragmatic regions of the datasets.

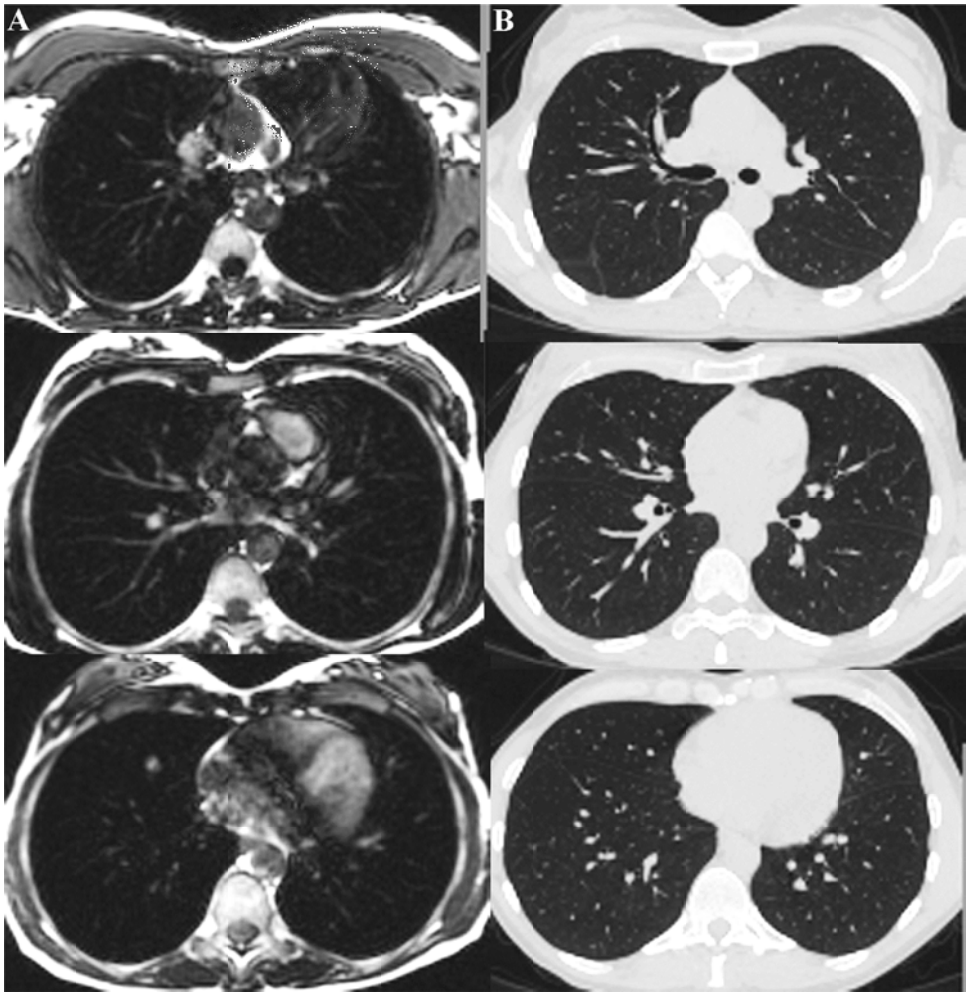

Figure 40. Alignment of TLC MRI and MDCT datasets utilizing a three grid BSpline (8x8x8, 16x16x16 and 32x32x32) scheme, along with 50% sampling percentages and the full resolution images.

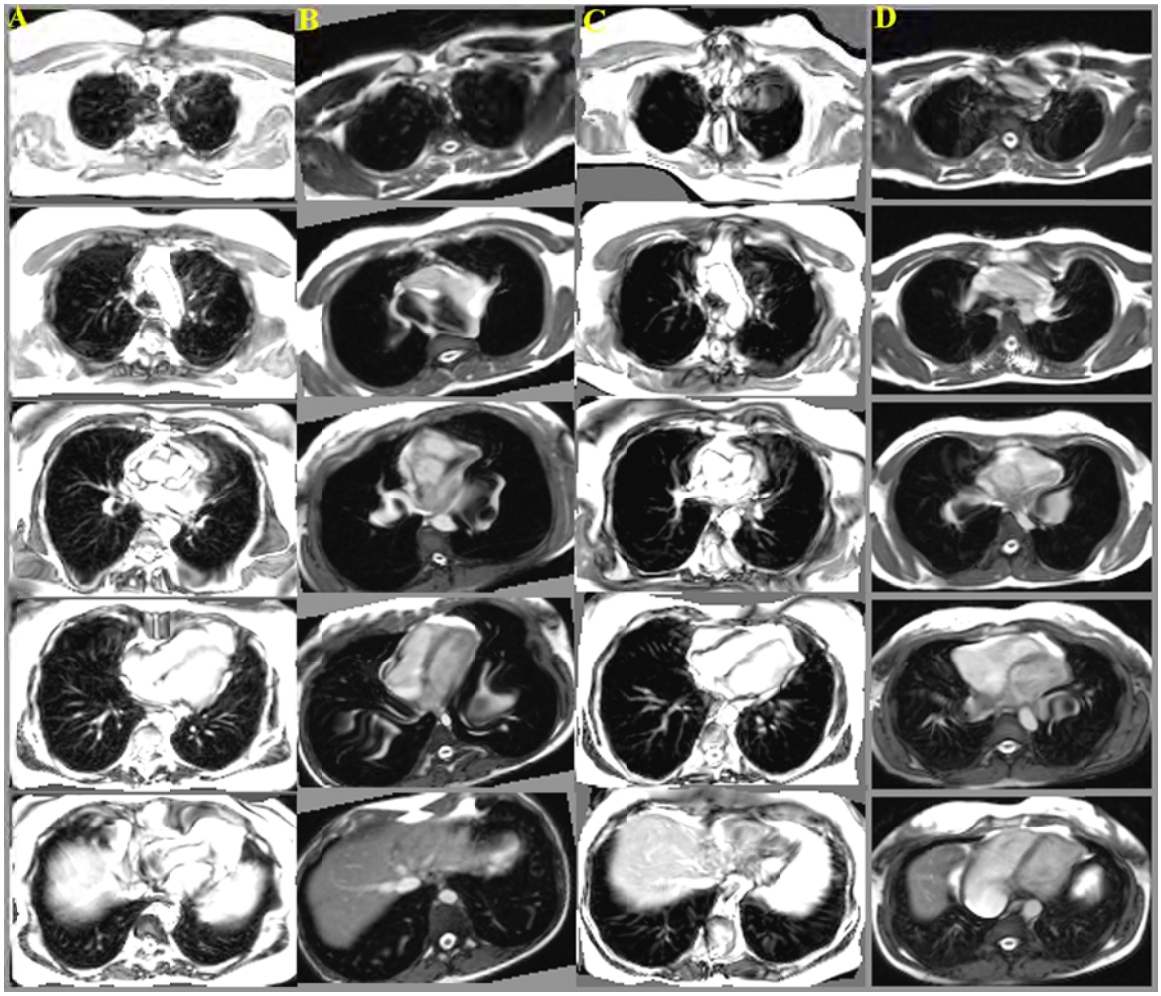

Figure 41. ^{1}H MRI – ^{1}H MRI FRC and TLC image matching results of two subjects. The use of FRC and TLC as moving and fixed volumes respectively resulted in the application of excessively deformed transformations (AandB) in two subjects, while the use of TLC and FRC as moving and fixed images respectively, produced significant improvements in overall deformation in one subject () and not the other (B).

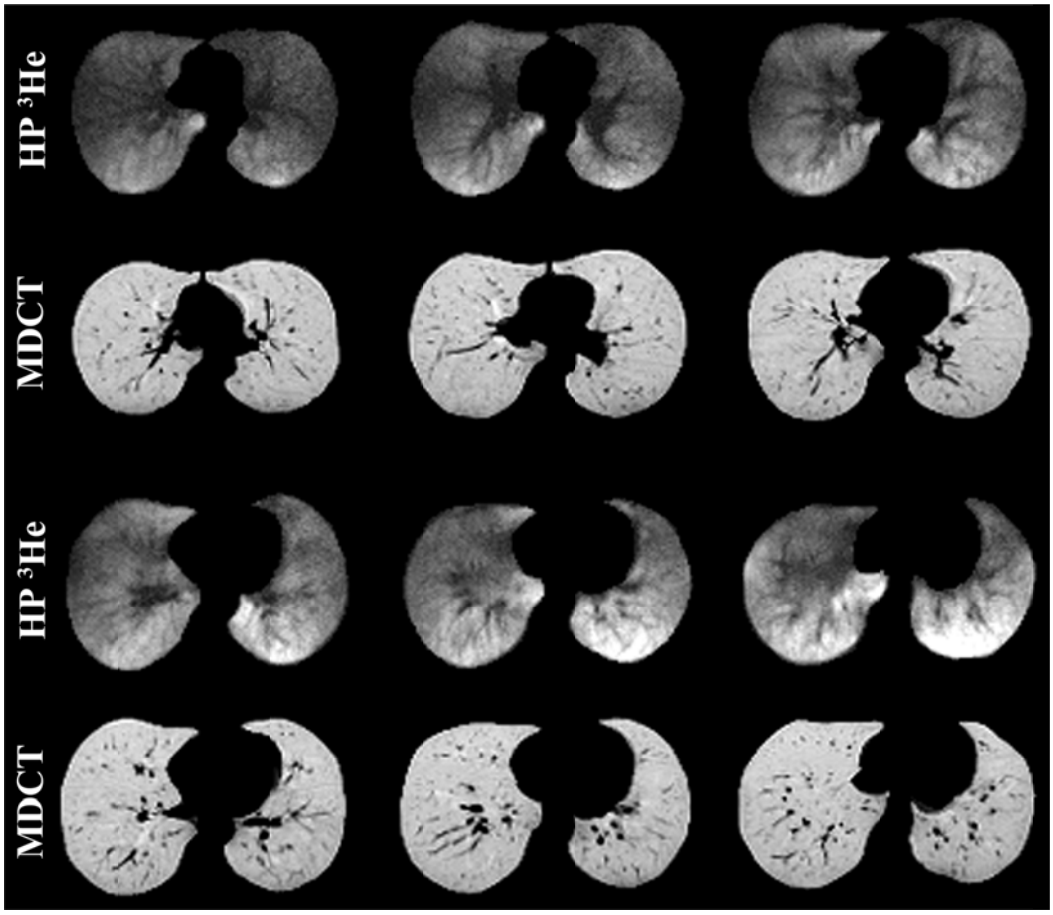

Figure 42. HP ^{3}He MRI and MDCT lung FOV alignment, utilizing a rigid + affine registration scheme. Assessment of the lung borders and vessels yield an almost perfect matching of the lungs between the two datasets.

Table 8. Optimal Registration parameters for proper matching of ^{1}H MRI - MDCT TLC and FRC image pairs and HP ^{3}He MRI – MDCT TLC and FRC image pairs.

	MRI - $MDCT_{FRC}$	**MRI - $MDCT_{TLC}$**	**HP ^{3}He MRI - $MDCT_{FRC\ and\ TLC}$**
Fixed Image Resolution	FULL	FULL	FULL
Moving Image Resolution	FULL or 256x256x200	FULL	128x128x50
Fixed Image Mask	Yes	Yes	Yes
Moving Image Mask	Yes	Yes	Yes
Sample Percentage	50%	50%	10%
Rigid Initialization	Center of Mass	Center of Mass	Center of Mass
Rigid Precision	0.0001	0.0001	0.01
Affine Precision	0.0001	0.0001	0.01
BSPline Precision	0.0000001	0.0000001	N/A
Histogram Bins	128	128	128
$BSpline_{8x8x8}$	Yes	Yes	No
$BSpline_{16x16x16}$	Yes	Yes	No
$BSpline_{32x32x32}$	Optional	Yes	No

CHAPTER 7: VOLUME-CONTROLLED HYPERPOLARIZED ^{3}HE ADC MEASUREMENTS AS A FUNCTION OF LUNG INFLATION LEVELS IN NORMAL NEVER-SMOKING HUMAN SUBJECTS

Hyperpolarized ^{3}Helium (HP ^{3}He) noble gas magnetic resonance imaging (MRI) has emerged as a complex, yet non-invasive imaging method for the assessment of regional pulmonary structure and function, free of the use of ionizing radiation (45, 80). Because of the inherent radiation free nature of this imaging modality, there is a considerable interest in applying this technique to study multiple measures at a given encounter or across multiple encounters. Differences across time, such as a change in lung density as an index of COPD progression can be small (11, 154) and on the order of 2 Hounsfield Units (HU) per year. Thus it is critical to understand how lung volume during scanning affects the measures of the HP ^{3}He apparent diffusion coefficient (ADC) values. ^{3}He is an inert, stable, non-toxic isotope of helium, which is formed as a byproduct of nuclear tritium decay (24, 29, 121, 129, 142) and is confined to the airspaces due to a low solubility coefficient in water, unlike the lipid soluble xenon (Xe) gas and has relatively long T_1 relaxation times (33, 45, 78). Diffusion-weighted ^{3}He MRI allows for evaluation and probing of the peripheral air spaces at the level of the conducting airways and acini, leading to an assessment of the integrity and size of such structures through the exploitation of the highly diffusive nature of ^{3}He (33). Diffusion in this context refers to the gas displacement according to Brownian motion, which can be quantified using dedicated MR sequences as previously described (33, 45, 80, 146). ADC maps of fully inflated lungs of normal healthy volunteers are relatively homogenous and this uniformity is a hallmark of the normal lung (33). ADC maps in patients with emphysema and other lung diseases have been shown to be non-uniform and contained larger diffusion values (18, 48, 80, 146). This non-uniformity of the ADC values correlates well with the onset and progression of the disease, where the degree and

location of destruction varies throughout the lung (143, 167). However it remains unclear as the sensitivity of the ADC measure over a one year time period relative to normal airspace changes occurring with changes in lung volume. Reported ADC values in normal volunteers range between 0.17 cm^2/s and 0.24 cm^2/s with a mean of 0.2 cm^2/s, a factor of four smaller than that of the dilute helium, demonstrating regional containment of ^3He by the lung's microstructure (41, 110, 111). It is felt that the wide range of ADC values in normal subjects may, in part be due to inconsistencies regarding lung volumes at which imaging has been performed, given the lack of lung volume standardization between groups. (110)

Although pilot studies have evaluated the progression of disease in a small cohort of subjects (40, 83, 151) , minimal advancements have been made to evaluate the suitability of the method for assessing differences between longer time intervals where lung compliance is most likely to change or between subjects at very different lung volumes. Because of the non-linear characteristics of the pressure-volume curves of the lung, it would seem to be critical for the lung to be imaged at the same percent of the vital capacity (VC) for longitudinal and between subject comparisons.

Lung inflation at levels below total lung capacity have been shown to be heterogeneous and highly influenced by body posture (67, 70, 106, 107). Diaz et al. have demonstrated sensitivity of ADC to small (6-8%) changes in lung volume (40). The work presented in this paper evaluates the dependence of ADC measurements on lung inflation levels at carefully controlled lung volumes between 20% and 100% of the VC and to compare the volume dependent changes in ADC vs. MDCT based measures. We propose that lung volume as a percent vital capacity rather than as a function of liters above FRC may be a more meaningful standardization.

7.1 Materials and Methods

This study was approved by our Institutional Review Board, complied with HIPAA (Health Insurance Portability Accountability Act) policies and informed consent was obtained for all subjects. Administration of ^{3}He was carried out in accordance with our physicians IND under the supervision of Dr. Edwin J.R. vanBeek.

Subject Population. Twenty-two normal never-smoking subjects between the ages of 23 and 70 were recruited and imaged at functional residual capacity (FRC), total lung capacity (TLC) and a volume midway between the two. All subjects underwent pulmonary function testing (PFT) to verify that they were indeed normal (FEV_1 and FVC > 80% predicted, FEV_1/FVC > 0.7). Given that the PFT was performed in the seated position and imaging in the supine position, all subjects further underwent 3-4 slow vital capacity (sVC) maneuvers in the supine position on the scanner table for proper determination of lung volumes.

Imaging. All Imaging was performed on a clinical, broadband capable, Siemens Avanto 1.5T MR scanner (Siemens, Erlangen, Germany). A flexible, vest-like coil specifically tuned to the Larmor frequency of ^{3}He (48.4676 MHz) was utilized to transmit and receive RF (radio frequency) pulses for the imaging (Clinical MRI Solutions, Milwaukee, USA). Physiological monitoring consisted of ECG (heart rate), non-invasive blood pressure (NBP) and pulse-oximetry (SPO_2). Imaging breath-holds were conducted at three lung volumes (20%, 60% and 100% VC), where each volume required a proton localizer and a HP ^{3}He scan totaling to six volume-controlled breath-holds during a given session.

^{3}He scans were acquired via a 2D FLASH sequence, modified to include a set of bipolar gradients for diffusion sensitization (T_R 86 ms, T_E 6.92 ms, 128 x 128 acquisition matrix, 7º flip angle, six baseline and diffusion weighted 15 mm thick slices, 7.5 mm inter-slice spacing, and 2.5 x 2.5 mm pixels) over the course of a 15 second breath-hold.

The imaging field of view (FOV) was set to approximate the same positioning of the ADC maps with respect to the apical-basal lung coverage for all acquired lung volumes.

Polarization and Doses. ^{3}He was polarized through spin exchange optical pumping (SEOP) using a GE Healthcare polarizer (GE Healthcare, Princeton, USA), generating 1 liter at polarization levels between 38-42%. Doses were transported via rapid transfer between the polarizer and MR scanner. The administered doses consisted of approximately 300 ml ^{3}He and 700 ml of medical grade Nitrogen in a 1 liter Tedlar bag fitted with ½" inner diameter (ID) Tygon tubing, allowing for the conduction of three ^{3}He breath-hold maneuvers per subject with minimal resistance.

Volume Control. The desired lung inflation levels were achieved through the use of a single 7-8 liter Tedlar bag connected to a mouth piece, pre-filled with the desired inflation volume (%VC) of air, thus acting an inspiratory reserve. A bacterial filter and an MR compatible spirometer were placed in line between the mouthpiece and Tedlar bag for elimination of any harmful bacteria and calculation of delivered volumes respectively. In the case of a proton localizer, the Tedlar bag used to deliver an inspiratory volume needed to achieve a given %VC, was filled with a volume of room air to achieve the desired lung inflation level (20%, 60% or 100% VC; 20% approximates FRC and 100% VC is by definition , TLC). Subjects performed a series of breathing maneuvers with expiration down to residual volume (RV) and at the last expiration instructed to completely inspire the volume within the inspiratory bag and hold their breath for the duration of the scan. In the case of a ^{3}He scan, the volume within the inspiratory bag required to reach the proper inflation level was one liter less to allow top up with the ^{3}He doses. Once the volume within the inspiratory bag was completely inspired, the subjects were instructed to hold their breath, release the mouthpiece and then complete the inspiratory process by inspiring the 1 liter ^{3}He dose. With 3 breathholds in each of the 22 subjects a total of 66 breathhold maneuvers were evaluated utilizing our volume control methods.

Image Analysis. All analyses were carried out via automated in-house scripts written in MATLAB (Mathworks Inc., Natick, MA). Gravitationally dependent (posterior) and non-dependent (anterior) regions were determined by dividing the lung along the antero-posterior axis, while apical and basal regions were determined by splitting the acquired images along the superior-inferior (apical-basal) axis, such that the first three slices represented the apical regions, while the last three represented the basal ones. Given the unitless nature of the acquired signals and the dependence upon the actual intensities collected, rather than the scaled intensities visualized on the scanner, all calculations were based on the reconstructed raw data slices instead of their dicom equivalents. Assuming a mono-exponential model of diffusion, ADC calculations were achieved on a pixel-by-pixel basis according to the following equation:

$$S_1 = S_0.e^{-(b.ADC)}$$

where b represents the bipolar gradients utilized to induce diffusion sensitization, expressed as a function of gradient duration, duration of time between gradients and gyromagnetic ratio of the spin system, while S_0 and S_1 are the signals of the baseline (b=0) and diffusion (b=1.15) weighted images respectively. Evaluation of the generated diffusion maps was carried out by thresholding to exclude pixels with intensities less than three times the standard deviation of the background noise, where background noise was calculated as the mean of a 20 x 20 pixel region placed at the top right corner of each pair of images. Manual segmentation was performed on all slices to ensure proper determination of the lung field of view and to eliminate the influence of the trachea and major airways from the evaluated regions. Resultant maps encompassed the apical-basal lung extent through six separate diffusion maps, starting at the apices and ending directly above the diaphragm. The process is illustrated in Chapter 4: Image Processing.

MDCT Comparisons. Retrospective analysis of a separate cohort of 50 normal never-smoker subjects with matching 20% and 100% VC scans was used to compare

aeration and ADC. Degree of aeration was estimated via MLD (mean lung density) using an in house software package PASS (Pulmonary Analysis Software Suite). MLD is defined as the mean Hounsfield Unit (HU) of all voxels encompassing the z-coverage for each lung respectively. Preprocessing steps in PASS included semi-automatic lung segmentation and left-right lung separation. All imaging was performed on either a Siemens Somatom Sensation 16 or 64 (Siemens Medical Systems, Erlangen, Germany), with 120 kV, 100 mAs and 1 mm slice thickness.

Statistical Analysis. Mean ADC values of left and right lungs, dependent and non-dependent regions and whole lung slices were extracted from the evaluated diffusion maps via MATLAB and examined via one-way analysis of variance (ANOVA) and two-sided paired t-tests in PASW Statistics (Version 18, SPSS, Inc., 2009, Chicago, IL, www.spss.com) and R (CRAN v2.9.2). Similarly, left-right differences in MLD were evaluated via two-sided paired t-tests. Results were considered statistically significant when the probability of making a type I error (false positive) was less than 5% ($p<0.05$).

7.2 Results

Lung Volume and Breath-hold Verification. Post-inspiration lung volumes were verified by performing manual lung segmentation of corresponding proton MRI scans in four test subjects utilizing a measure of total lung volume, defined as the sum of all voxel volumes within the lung mask. These segmentation based volumes were then compared to the desired lung volume measured as a percentage of VC and were found to be within 5-7% of the target inflation levels.

ADC vs. Lung Volume. In 12% (8) of the 66 breathholds, there was a study failure because of multiple causes including failure of subject to remain apneic during the scanning or failure to comply with breathing instructions. As a result of these failures, six subjects were excluded from the study. The main analysis inclusion criterion was the successful completion of all three lung inflation level breath-holds, to facilitate an

unbiased assessment of the ADC differences observed as a function of varying lung inflation levels. Therefore, analysis was limited to 16 of the 22 subjects. No adverse side effects or unexpected physiological changes of clinical consequence were observed. An expected decrease in oxygen saturation levels was observed following the 20% VC scans (5-8% drop) in most subjects. ANOVA illustrated statistically significant differences in mean ADC values between lung inflation levels with 2 degrees of freedom ($p<0.001$), apical-basal lung coverage with 5 degrees of freedom ($p<0.01$) and with respect to anatomical position (left, right, dependent and non-dependent) with 6 degrees of freedom ($p<0.001$).

ADC variability between the defined anatomical positions, evaluated with paired t-tests is summarized in Table 10Table 10. Whole lung mean ADC values were significantly smaller at 20% VC when compared to 60% and 100% VC (P=0.0109 and P=0.00002 respectively; Figure 44). In addition, the values at 60% VC were significantly smaller when compared to 100% VC (P=0.00001). Right lung mean ADC values were consistently greater than those of the left lung for all inspiratory volumes ($0.0031 < P < 0.0001$). Furthermore, gravitationally dependent regions had significantly smaller mean ADC values compared to non-dependent regions at the 20% and 60% VC volumes (Figure 45), where at 100% VC this difference was not observed signifying a more homogenous distribution of lung expansion in line with previous reports (28, 67, 70). A statistically significant difference (P=0.02) in mean ADC values was observed for the 20% VC volumes between apical and basal lung regions, however differences between the 60% and 100% VC volumes were not significant.

Left-Right MDCT Analysis. Retrospective analysis of MLD of the 50 normal never-smoker subjects (Figure 46) illustrated a significant difference between the degree of aeration of left and right lungs at 20% VC (P=0.00001). Differences at the 100% VC volumes were not significant (P=0.2493).

7.3 Discussion

ADC values significantly increase with increasing lung inflation levels, while differences between the different gravitational lung regions decreases (Figure 47), due to a trend toward more uniform alveolar expansion at higher inflations. Evaluation of the airspace ventilation differences between FRC and TLC illustrate an increased ^{3}He delivery to the dependent regions at TLC when compared to FRC, confirming the observable expansion increases in the gravitationally dependent regions (Figure 48). ADC values throughout both lungs become more homogenous at 100% VC. This is in agreement with Chevalier et al. (28), who observed that the lung is fully expanded at TLC via bi-planar x-ray and implanted metallic markers.

Although some subjects had difficulties adhering to the breathing protocol, recent experiences in our laboratory with normal-smokers and subjects with COPD (Chronic Obstructive Pulmonary Disease) has shown that these issues can be minimized with proper coaching and sufficient rest periods between breathing maneuvers.

Milic-Emili et al. (107) showed that the relationship between regional lung expansion with respect to overall lung expansion is non-uniform, where the non-dependent lung regions were relatively more expanded than their dependent counterparts at all lung inflation levels except at 100%VC. This was achieved by evaluating both regional and total lung volumes across the vertical distance of the lung, with deviations from the line of identity representing inhomogeneities. Furthermore, for lung inflation levels between 20% and 100% VC (FRC and TLC), the dependent lung regions received a larger proportion of the inspired volume with respect to non-dependent regions. This relationship is reversed for lung inflation levels between 0% and 20% VC (RV and FRC), where non-dependent lung regions received a higher proportion of the inspired volume (106, 107).

The differences between gravitationally dependent and non-dependent mean ADC values as a function of lung inflation levels is consistent with the observations of

Hoffman (67, 70) in supine anesthetized canines, who observed a dependent to non-dependent gradient in CT lung air content, which diminished with increasing lung inflation levels. Furthermore, using proton MRI, Hatabu et al. (62) illustrated a greater relative proton density in posterior (dependent) regions in normal subjects in the supine position.

In agreement with the ADC-based observations, MLD of the left lung (by MDCT) was smaller than the right at 20% VC and approximately equal at 100% VC, suggesting a reduced expansion of peripheral air spaces in the left vs. right lung at the low lung volume. Using CT imaging, Hoffman et al. (67, 70) demonstrated that support of the heart by the lung may serve to alter regional lung expansion at low lung volumes and thus the distribution of an inspired gas; this support is altered with body posture. The left-right differences are small; however, when one is following disease progression longitudinally, the changes are small. Thus care needs to be taken to assure similar lung volume and posture so as not to confound measurements of pathology with differences due to varying lung volumes. Albert et al. (3) have also demonstrated that a shift in body posture alters compression of the lung by the heart and this postural effect has been confirmed by Fichele et al. (47, 48) using ADC as a tool. It is likely that the left-right lung differences found in our study at 20%VC are an index of the variable effect of the heart on the lung. Similarly, CFD simulations have suggested increased flow patterns in the right lung airway geometries with respect to the left equivalents, in a normal airway model, along with higher particle depositions within the left lung geometries, possibly due difference in airway geometries between the two main branches, with respect to the trachea (86).

Several longitudinal assessments of lung disease have been performed in COPD patients, illustrating a significant but small change over a one year interval (extrapolated from a 3 year study) (11, 44, 154). Because of such small changes, considerable statistical manipulations and relatively large numbers of subjects were required to show these

progressions. In this study we present a lung volume approach which can maximize the sensitivity of the ADC protocol to detect yearly disease progression.

In summary, the agreement of the presented results with the prior understanding of regional differences in lung expansion, lung density measures, regional ventilation and anatomical orientation strengthens the hypothesis that HP ^{3}He ADC measures alveolar size. As illustrated, volumetric control of lung inflation levels is crucial to the HP ^{3}He ADC methodology if it is to be utilized in monitoring subjects and disease progression over time and similar care should be taken into consideration for functional imaging protocols utilizing exogenous contrast agents in imaging lung function and structure. Depending on the desired assessment, careful consideration of the underlying regional mechanics and expansion factors should be taken into account with respect to the choice of lung inflation levels during the imaging sessions. Careful consideration of the lung inflation levels during all MRI based lung structure and function assessments through the use of exogenous and endogenous contrast agents, must be integrated into scanning protocols if imaging is to offer an outcome measure which reduces the time period to evaluate new interventions, compared with the current reliance on pulmonary function tests.

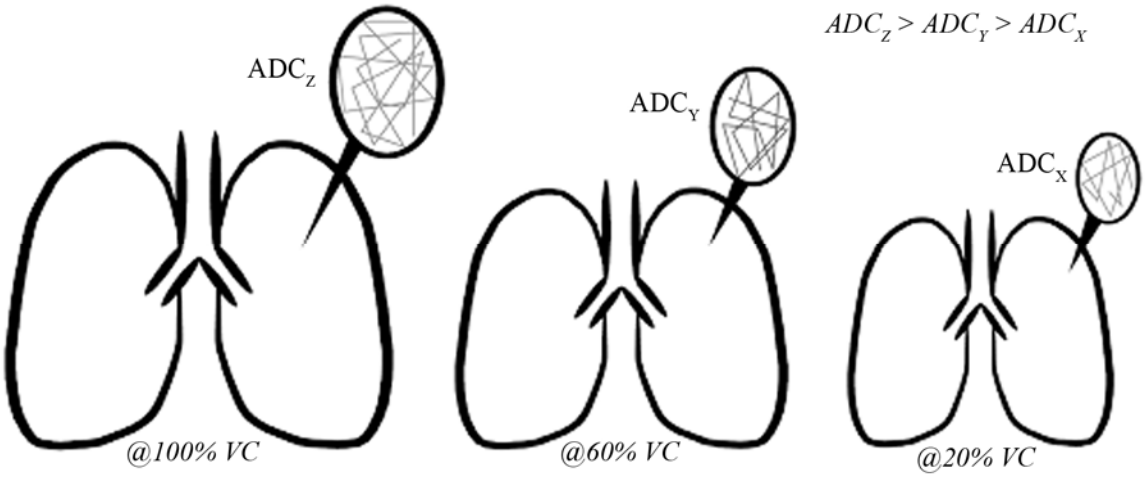

Figure 43. Visual illustration of ADC changes as a function of underlying lung inflation levels. Similar to increases in measurable ADC values with disease onset, we hypothesize a similar structural relationship between the measureable diffusion and the inflation levels at which they are probed.

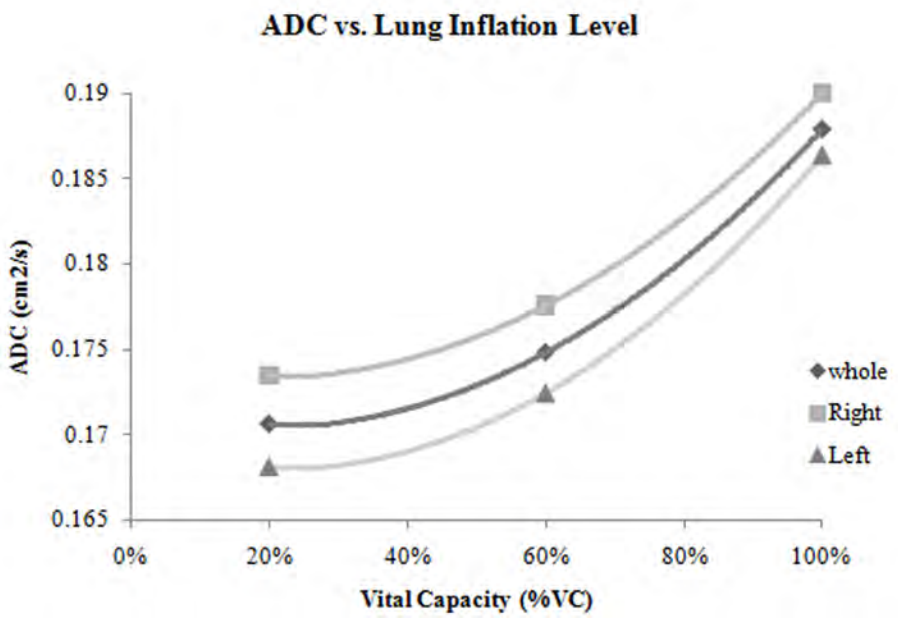

Figure 44. Mean ADC values of whole, left and right lungs, as a function of percent VC, demonstrate a trend towards higher ADC values as lung volume increases. Overall mean ADC values of the right lung are significantly higher than those of the left lung.

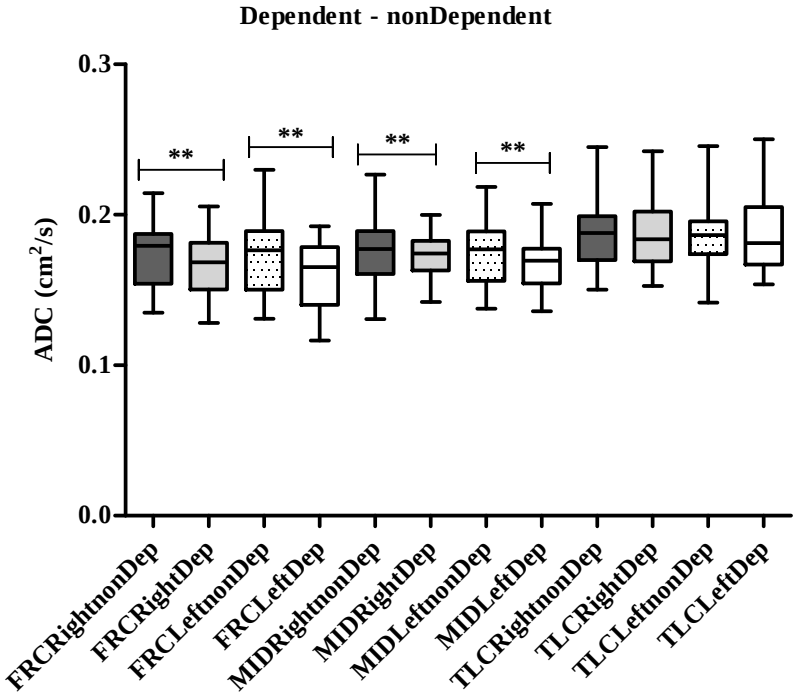

Figure 45. ADC values as a function of anatomical position and percent VC of the imaged cohort. The observed gradients are prominent and statistically significant at the lower inflation levels and disappear completely at the larger inflation level. This follows previous literature where homogeneity of air distribution and inflation throughout the lungs as a function of CT lung density was observed at larger lung volumes only and not at lower ones.

*** Significant difference between mean of groups*

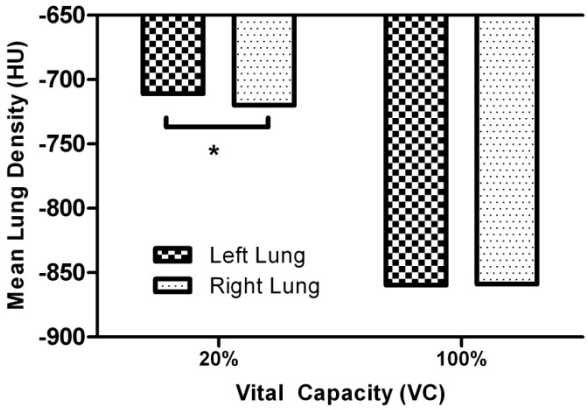

Figure 46. Mean Lung Density (MLD) at 20% and 100%VC of left and right lungs. Significant differences in MLD between left and right lungs were observed at 20% VC (-711.42 ± 53.36 , -720.27 ± 48.81) and not at 100% VC (-859.34 ± 21.69 , -858.6 ± 19.34) (P=0.00001 and P = 0.2493 respectively). Increased MLD of the left lung correlates with the smaller ADC values at 20%VC.

* Significant difference between mean of groups

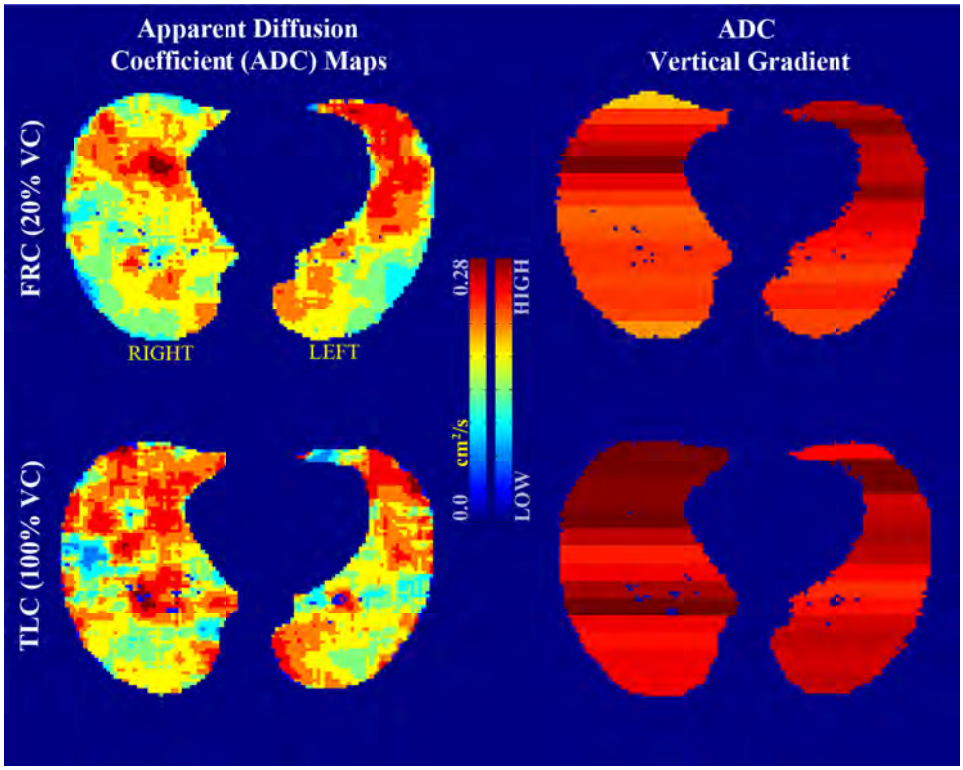

Figure 47. ADC (k-means clustered) and vertical gradient maps at 20%VC (top) and 100%VC (bottom) of the same subject at similar anatomical locations. Increased expansion of the dependent regions is clearly observed in both the clustered and vertical gradient maps of the TLC volume with respect to the FRC one, demonstrating a more homogenous distribution and expansion throughout (refer to Figure 45) (FRC COV = 0.31, TLC COV = 0.24).(ADC scale 0 – 0.28 cm^2/s)

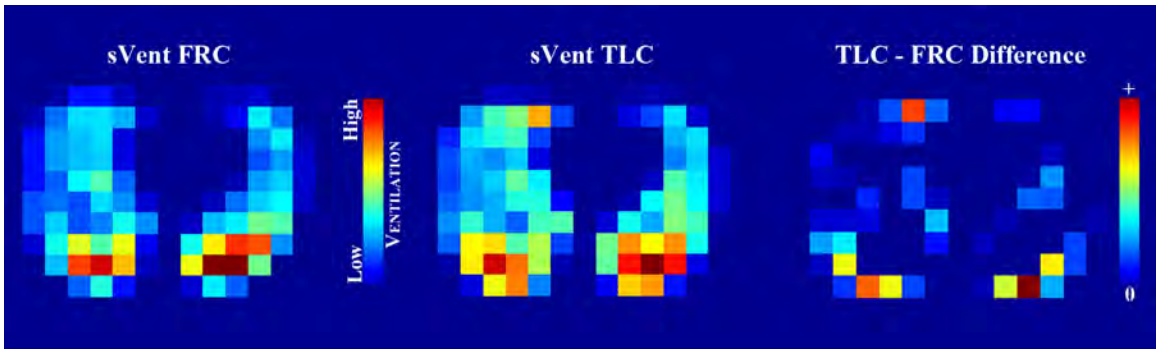

Figure 48. Airspace ventilation of a normal never-smoking subject at 20% (~FRC) and 100% (TLC) of the %VC. Distribution differences between the volumes illustrate increased ^{3}He delivery to the dependent regions. The observable increases in ^{3}He delivery coincide with the elimination of the gravitationally dependent ADC gradients in the larger lung volumes, via increased expansion of the dependent lung regions.

Table 9. Demographic characteristics of imaged normal-never smoker (NVS) population.

Subject	Gender	Age	Weight	Height
1	F	48	77.5	162.7
2	M	30	78	171.2
3	M	27	77.3	174.9
4	M	29	99.7	176.9
5	F	43	57.4	158.4
6	F	35	81.2	163
7	F	60	80.1	165.2
8	M	70	102.8	179.3
9	M	49	93.4	171.5
10	F	41	65.3	153.5
11	M	57	86.1	179.7
12	F	41	65.1	173.9
13	M	33	90.5	179.8
14	F	30	56.7	162.8
15	M	23	63.5	171.6
16	F	56	69.4	153.7

Mean age, weight and height are 44.2 ± 10.1, 69.1±9.7, 161.7±6.6 and 39.7±16.9, 86.4±13.0, 175.6±3.8 for females and males respectively. No Adverse side effects were observed for any of the imaged population, including subjects that were not in the analysis.

Table 10. Regional differences in mean ADC values as a function of anatomical location and %VC.

Volumes (%VC)	P	Dep vs. non-Dep	P
20% - 60%	*0.0109*	**20% Right**	*0.00001*
60% - 100%	*0.00001*	**20% Left**	*0.00001*
20% - 100%	*0.00002*	**60% Right**	*0.143**
Left-Right Differences		**60% Left**	*0.00002*
20%	*0.00001*	**100% Right**	*0.1404**
60%	*0.00003*	**100% Left**	*0.2915**
100%	*0.00031*		

Heterogeneity of mean ADC values decreases between the gravitationally dependent and non-dependent regions as lung inflation levels increase. Differences were considered statistically significant if $P<0.05$.

**Differences are not significant*

CHAPTER 8: QUANTITATIVE VALIDATION OF HYPERPOLARIZED 3HELIUM MAGNETIC RESONANCE IMAGING IN ASSESSING REGIONAL VENTILATION: CORRELATION WITH MDCT BASED AIR VOLUME CHANGE (AVC) MEASUREMENTS

The increasing prevalence of lung diseases such as COPD has been an important driving factor in the development of lung imaging techniques in attempts to non-invasively assess the normal physiological and pathological conditions of the lungs. COPD is a group of slowly progressive diseases characterized by airway and parenchymal destruction and is the 3rd leading cause of death in adults (128). Conventionally assessed via pulmonary function testing (PFT), the lack of regional sensitivity to disease heterogeneity and the resultant global perspective have been major drawbacks in the use of this technique in properly assessing severity of these pathological conditions (23, 82, 128).

The emerging heterogeneities apparent at imaging during both normal and pathological conditions with resultant surgical and non-surgical interventions have yielded the notion that quantitative (regional) analysis of pulmonary ventilation is essential in order to improve classification of subjects and to make prognostic predictions of outcome (12, 13). The quantitative analysis of lung function is not a new concept as attempts to quantitate the regional distribution of pulmonary ventilation via the nitrogen washout curve technique (36, 135, 136), regional density changes observed in computed tomography (CT) (67, 68, 161), regional strain measurements obtained via bi-plane x-ray fluoroscopy (68), as well as the distribution of radio-active gases, such as ^{133}Xe (135), have paved the way for future methods and needs in this field.

Multi-Detector CT (MDCT) has been a prominent player and the standard tool for lung imaging, through the use of both exogenous and endogenous contrast agents. The use of single and multiple-breath applications of xenon gas in MDCT has given new

insight into the dynamics and distribution of gas during ventilation with great spatial resolution (24, 29, 68). Similarly, the use of regional volume changes and fractional air content assessed by Hounsfield Units (HU), between varying inflation levels has provided a less invasive and similarly effective assessment of regional ventilation, compared to its multi-breath xenon-enhanced counterpart (52, 68{Yin, 2009 #32, 187).

The versatility of MRI in assessing different nuclei and complimentary use of these nuclei as exogenous contrast agents has facilitated means for minimally invasive assessments of lung function and structure, overcoming the traditional handicap introduced due to minimal proton density and high susceptibility artifacts (9, 170). The usefulness and importance of MRI as a lung imaging tool is further demonstrated by its lack of ionizing radiation, thus enabling minimally invasive longitudinal and pediatric assessments. Hyperpolarized (HP) noble gas imaging through the use of 129-Xenon (^{129}Xe) and 3-Helium (^{3}He) as inhaled contrast agents have been extensively utilized in the assessment and visualization of the airways, alveolar spaces, respiratory dynamics and lung ventilation in both animal models and humans (65, 80, 81, 101, 121, 122, 138, 139, 167). Although the techniques are similar, the use of the inert, stable, non radioactive ^{3}He gained more popularity as the research tool of choice, partially due to the higher signal to noise (SNR) ratios achievable and its confinement within the airspaces (109). However, recent advancements in polarization of ^{129}Xe and improvements in post processing of the acquired datasets have provided new and complimentary advancements in the visualization of both lung function and structure. This complimented with the decreasing supply and increasing costs of ^{3}He have eliminated the bias and increased the popularity of hyperpolarized ^{129}Xe as a viable tool in imaging the lungs.

To validate the ability and sensitivity of HP ^{3}He MRI in assessing regional ventilation, we compared ventilation estimates obtained from MDCT based local volume changes, with those obtained via HP ^{3}He MRI. We hypothesize that HP ^{3}He MRI would correlate with the overall distribution and gravitationally induced gradients, thus

establishing the technique as a validated surrogate to its ionizing radiation based counterparts. Furthermore, given the difference in density of the gaseous contrast agent utilized in both modalities, we hypothesize the exaggeration of ventral regional ventilation estimates in the HP ^{3}He MRI datasets, with respect to their MDCT counterparts. We believe this to be the first actual assessment of the regional sensitivity achievable with HP ^{3}He MRI in relation to MDCT based estimates of ventilation.

8.1 Materials and Methods

This study was approved by our Institutional Review Board, complied with HIPAA (Health Insurance Portability Accountability Act) policies and informed consent was obtained for all subjects. All imaging was carried out under FDA approval, with careful consideration of subject safety. Administration of ^{3}He was carried out in accordance with our physicians IND under the supervision of Dr. Edwin J.R. vanBeek.

Subject Population. Nine healthy normal never-smoking subjects between the ages of 26 and 48 were recruited and imaged. All subjects underwent pulmonary function testing (PFT) in the seated position to verify that they were indeed normal (FEV_1 and FVC > 80% predicted, FEV_1/FVC > 0.7), according to the American Thoracic Society guidelines. All subjects further underwent 3-4 vital capacity (VC) maneuvers in the supine position on the scanner table for proper determination of respective lung volumes. Vital capacity measurements were utilized throughout both MRI and MDCT imaging sessions to ensure identical lung volumes during the breathholds and anatomical coverage of the underlying structure and function. Physiological monitoring consisted of ECG (heart rate), non-invasive blood pressure (NBP) and pulse-oximetry (SPO_2) during all imaging sessions.

^{3}He Imaging. MRI was performed on a clinical, broadband capable, Siemens Avanto 1.5T scanner (Siemens, Erlangen, Germany), utilizing a flexible, vest-like coil specifically tuned to the Larmor frequency of ^{3}He (48.4676 MHz) to transmit and receive

RF (radio frequency) pulses for imaging (Clinical MRI Solutions, Milwaukee, USA). Volume controlled proton localizers and HP ^{3}He static ventilation (sVent) scans were acquired for each subject at 100% of their respective VC.

A 2D gradient echo FLASH (Fast Low Angle Shot) sequence, (TR/TE = 86 msec / 6.92 msec, flip angle = 7, bandwidth = 260 Hz/pixel, matrix size = 128 x 128 mm, pixels = 2.5 x 2.5 mm, slice thickness = 15mm, interslice spacing = ~7.5 mm, number of slices = 6, duration of acquisition = 10-15 sec) was used for HP ^{3}He imaging, while proton localizers where acquired via a modified 2D trueFISP sequence (imaging frequency = 63.6235 MHz, TR/TE = 591.5 msec / 1.05 msec, flip angle = 57, bandwidth = 1132 Hz/pixel, matrix size = 384 x 384 mm, pixels = 1.04 x 1.04 mm, slice thickness = 6 mm, interslice spacing = ~18 mm, number of slices = 6, duration of acquisition = 8 sec). The imaging field of view (FOV) was set to approximate the apical-basal lung coverage for each subject, evenly distributing the acquired slices throughout, starting at the apex and ending directly above the diaphragm.

^{3}He was polarized on site through spin exchange optical pumping (SEOP) using a GE Healthcare polarizer (GE Healthcare, Princeton, USA), generating 1 liter at polarization levels between 38-42%. Doses were transported via rapid transfer between the polarizer and MR scanner. The administered doses consisted of approximately 300 ml ^{3}He and 700 ml of medical grade Nitrogen in a 1 liter Tedlar bag fitted with ½” inner diameter Tygon tubing, allowing for the conduction of the ^{3}He breath-hold maneuver with minimal resistance.

Desired lung inflation levels were achieved via the use of a 7-8 liter Tedlar bag, pre-filled with the desired inflation volume (%VC) of air based on the subjects’ VC measurement, serving as an inspiratory volume. Volume control of localizers was accomplished via instructing the subjects to perform several breathing maneuvers with expiration to residual volume (RV) and at the last expiration, inspire the volume within the inspiratory Tedlar bag. The process of volume control of the ^{3}He scans was identical

except for the calculation of the air volume within the inspiratory Tedlar bag, which was one liter less to allow top up with the one liter ^{3}He dose. A mouthpiece, bacterial filter and MR compatible spirometer were placed inline with the inspiratory Tedlar bag, to assist subjects in performing the breathholds, eliminate any harmful bacteria and calculate delivered volumes respectively.

MDCT Imaging. Volume controlled spiral MDCT scans were acquired at approximately 20% and 100% VC for each subject on either a Siemens Somatom 64 or Definition FLASH (Siemens, Erlangen, Germany) (rotation time = 0.5 sec, collimation = 128 (64) X 0.6 mm, kV = 120, effective mAs = 110 – 160, pitch = 1.0, matrix size = 512 x 512, slice thickness = 0.75 mm, interval = 0.5 mm, number of slices = 500 – 600,scan time = < 10sec, care-dose = Off, reconstruction kernel = B35). Volume control at the MDCT scanner was achieved through the use of a spirometer in line with a pneumatically activated balloon occlusion valve. Real time monitoring of lung volumes was achieved by utilizing the spirometer readings as input to a LabVIEW program, to plot the inspiratory and expiratory phases of the respiratory maneuvers as a percent of vital capacity, such that once the desired inflation was reached, the balloon occlusion valve could be inflated for the duration of the scanning to eliminate leaks and ensure proper lung volumes throughout. Subjects were imaged in the supine position with a mouthpiece connected to the volume control device and were instructed to perform several breathing maneuvers similar to those performed during the MRI imaging sessions and at end expiration breath in to the desired inflation level and perform a breath-hold.

Data Processing. ^{3}He datasets were processed via an in-house script and graphical user interface written in MATLAB (*Mathworks Inc., Natick, MA*). All ^{3}He ventilation calculations were based on the reconstructed raw data slices, due to the unitless nature of the acquired signals and the dependence upon the actual signal intensities acquired. Preprocessing of the ventilation maps included noise threshholding, excluding pixels with intensities less than three times the standard deviation of the background noise, where

background noise was calculated as the mean of a 20 x 20 pixel region placed at the top right corner of the image. Lung masks were created via manual segmentation of the lung FOV, excluding the trachea, major airways and background intensities and separating the left and right lungs. MDCT volume scans were preprocessed via our in house software package PASS (Pulmonary Analysis Software Suite) to generate lung masks excluding the background and major airways and perform left-right splitting.

MDCT based regional ventilation estimates were generated through a mass preserving multi-level BSpline image registration between the 20% and 100% VC datasets (187), minimizing local tissue volume differences between matched lung regions. Image registration-derived estimates of regional ventilation included 1. Jacobian maps (Jaco), reflecting regional expansion and contraction, 2. Specific volume change (sVol), reflecting volume change per unit air volume and 3. Local air volume change (AVC), equivalent to the distribution of inhaled air (52, 129, 186, 187). Among those estimates, specific volume changes (sVol) were generated as a function of the Jacobian of the warping function and fractional tissue content changes based on HU measurements.

To facilitate the correlation between the MRI and MDCT based ventilation estimates, image registration was performed to map the MDCT ventilation estimates into the image space of their MRI equivalents (Figure 49). Given the superior resolution of the MDCT acquisitions with respect to the MRI acquisitions, the xy coverage of the MDCT datasets was down sampled to 128 x 128 pixels, along with down sampling of the z coverage to approximately 50 slices, assisting the image registration in achieving a proper fit and minimizing computation time. Image registration was carried out via an ITK (Insight ToolKit v3.20) based script, performing a Rigid + Affine registration between the MRI (reference image) and MDCT (moving image) datasets (98).

Statistical Analysis. Vertical gradients and profile measurements were generated for all MRI and deformed MDCT datasets through the use of our in house MATLAB GUI (*Mathworks Inc., Natick, MA*), with the option of whole lung and/or left-right lung

analysis (Figure 23). Resultant mean and standard deviation ventilation estimates were then exported in table format to excel to facilitate statistical analysis. Spearman and Pearson correlation coefficients along with slope estimates were achieved through the use of R (CRAN v2.9.2) and Microsoft Excel 2007 (Redmond, WA), on a pixel-by-pixel, gradient and profile basis for each matching pair of images within the matched datasets.

8.2 Results

All imaging was performed without adverse events or unexpected physiological changes of clinical consequence. One subject was excluded due to inability to maintain breathhold for the duration of the maximal inspiration scan, limiting the analysis to eight of the nine subjects (Table 11). Verification of post inspiration lung volumes was achieved through manual segmentation and summation of all voxels within the lung field of view, followed by comparison of these volumes against the originally calculated lung inflation levels. Agreement between the MDCT and MRI inspiration was within 5-7% of desired lung inflation levels. Rigid mapping of the MDCT datasets to their respective MRI counterparts produced satisfactory results in enabling a regional assessment of the underlying ventilation measures, with approximately 85-95% overlap between the datasets (Figure 42).

All subjects illustrated strong positive correlations and linear slopes between the HP ^{3}He and MDCT estimates of regional ventilation (

Table 12), demonstrating the overall agreement and regional sensitivity achievable via the HP ^{3}He static ventilation maps in comparison to their MDCT equivalents. Maximum and minimum observable correlations are presented instead of the overall mean calculated correlations observed the HP ^{3}He and MDCT regional ventilation estimates. Statistical significance of the similarity of means between the two estimates

was determined via paired t-tests of the profile distributions ($P > 0.05$). Correlation differences within a subject are possibly due to differences in airway and vessel threshholding as a result of the different acquisitions, thus introducing slight under or over estimation of the ventilation distribution. Image space matching differences, could also be a culprit in the observed correlation variability within a given subject. Visualization of HP ^{3}He and MDCT profile plot and vertical gradient distribution similarities and differences can be seen in Figure 51, for two subjects and an MDCT equivalent for the latter for the two. A profile plot distribution comparing the two ventilation estimates from a corresponding matched slice can be seen in Figure 52. There exist some discrepancies towards the extremities of the gravitationally dependent and nondependent regions, albeit that the overall distribution is quite similar. Analysis of ventilation distribution along the gravitationally dependent – nondependent profile was divided into thirds to further illustrate the nondependent discrepancies (Figure 53). It can be clearly observed that the dependent and middle sections of the lung had a positive linear relationship and slope between the MRI and MDCT ventilation measures, while the nondependent section illustrated a negative slope and smaller correlation coefficient. Regional (8x8 pixel) coefficient of variation (COV) analysis of the ^{3}He and MDCT ventilation estimates, illustrates a similar distribution, with the exception of increased COV values in the nondependent regions of the ^{3}He maps (Figure 54). This demonstrates the comparable regional heterogeneity assessments achievable via the ^{3}He ventilation maps, albeit the differences in original acquisition and is in agreement with the increased nondependent ventilation observed within.

8.3 Discussion

The ability of HP ^{3}He MRI to assess regional ventilation has been gauged with good positive correlation and linear slope in comparison with MDCT based estimates. Proper multi-modality assessments of regional ventilation are crucial to establishing

and/or extracting the differences and regional sensitivity of a given technique. We believe this work to be complimentary to the literature illustrating the agreements between HP ^{3}He MRI, conventional based HU MDCT and ^{133}Xenon lung scintigraphy assessments of normal and pathological lung function (6, 44, 168). The importance of this work is illustrated in the sensitivity achievable in assessing regional ventilation via the MDCT based estimates and the agreement between these measures and those of Xenon-enhanced MDCT, further strengthening the concept of utilizing HP ^{3}He MRI as a surrogate to some of the current radiation based techniques and its strength as a valid clinical research tool.

Although excellent correlations were achieved, we believe several factors including but not limited to registration, gas density differences and overall image processing to be important factors required to achieve proper multi-modality assessments of any given measurements. Due to the acceptable results of the volume control technique in combination with the lung FOV masks, we deemed the rigid based registration script as an appropriate means of image matching. Initial testing of the registration script incorporated the use of a multi resolution and multi gridded BSpline transform following the implementation of the rigid based transformations. This resulted in extreme deformation of the interior lung regions, producing swirl and wrap around artifacts. Similarly, image registration was performed while swapping the reference and moving images respectively with and without resampling of the MDCT datasets, such that the MRI datasets were the moving images and the MDCT datasets the reference ones. Given the superior resolution and acquisition FOV of the MDCT datasets in comparison with the MRI ones, this resulted in variable convergence points due to the fact that the ^{3}He MRI FOV was encompassed by the MDCT FOV. Improvement of the registration results to eliminate the mismatching of the extremities of the nondependent regions along with the curvature of the apical slices, could be achieved utilizing a regularized single resolution gridded BSpline transform following the rigid transforms (187), similar to the algorithms utilized in generated the MDCT based regional ventilations estimates. This

would limit the deformation of a single BSpline grid node to within acceptable ranges, thus deforming the lung FOV while minimizing possible occurrence of swirl and wrap around artifacts. Additionally, the incorporation of manually defined landmark selections between the MRI and MDCT datasets could possibly be utilized as a ground truth for the overall registration in combination with the regularization of the BSpline transform to further limit the achievable deformations and improve overall goodness of fit between the datasets (49, 76).

Given the density based nature of the MDCT acquisitions, elimination of the vessels from the field of view requires a simple threshholding of the intensities to eliminate any values with the range of -200 HU to +200 HU prior to calculation of the regional ventilation estimates. In the case of the HP ^{3}He MRI acquisitions, similar threshholding is performed to eliminate any outliers including noise, vessels and airways, but the unitless nature of these acquisitions, gives way to the need for a more proper vessel segmentation mask to effectively eliminate the vessel. The incorporation of these settings would provide a twofold improvement in the nature of assessment, not only eliminating the vessels from the field of view, but also creating the opportunity for use of such masks within the registration algorithms.

Analysis of the ventilation distribution based on the profile plots generated and linear regression analysis on a slice per slice basis illustrated a mild discrepancy between the MDCT and MRI based ventilation estimates in the extremities of the gravitationally dependent and nondependent regions (Figure 52). Lin et al. demonstrated the differences in overall gas transport in MDCT based human airway geometries, comparing the distributions of helium and xenon, where the density of the gaseous agent affected the overall resultant distribution (94, 95). We believe this to be an important factor in the overall resultant analysis, illustrated by the increased ventilation observed by the HP ^{3}He measures in the nondependent regions and decreased ventilation in the dependent regions, with respect to the air based ventilation measures of the MDCT maps. Careful

consideration of the density of the exogenous gaseous agents utilized in regional ventilation assessments must be taken to avoid incorrect characterization and classification of the underlying physiological and pathological conditions. Regional heterogeneity assessed as a function of COV values demonstrate a relative agreement between the ventilation estimates, albeit the differences in acquisition resolution differences, further strengthening the surrogacy of the techniques in ventilation assessments. The gas density differences observed throughout the ventilation estimates was clearly observed via increased COV values in the nondependent regions of the ^{3}He estimates, when compared to the MDCT ones.

It was demonstrated and verified that there is excellent agreement between the MDCT based measures of regional ventilation and those achievable via HP ^{3}He MRI. When assessed on a more regional level, both MDCT and MRI based techniques demonstrate some dissimilarities, possibly arising from the gas density differences (helium *0.34 kg/m^3 vs. room air 1.2 kg/m^3*), leading to higher ventilation of ventral lung portions in the HP ^{3}He methods. Similarly, we have demonstrated and implemented a simple yet effective method to facilitate acceptable comparisons between the generated regional ventilation estimates on a multi-modality basis, while providing some insights into possible additions to the overall process to improve the generated results. The importance of proper volume control based on VC measurements, along with appropriate image processing and matching algorithms and proper consideration of the density of the gaseous agents utilized are all crucial aspects to the success of any intra or inter modality assessments of the underlying anatomical structures and physiological phenomenon.

Table 11.Demographic characteristics of imaged normal-never smoker (NVS) population.

Subject	Gender	Age	Weight	Height
1	M	20	55.2	1.63
2	F	44	65.9	1.73
3	F	29	52.1	1.68
4	M	28	88.2	1.76
5	F	27	83.1	1.74
6	F	56	69.4	1.54
7	M	57	86.1	1.79
8	F	41	65.3	153.5

Mean age, weight and height are 35 ± 19.4, 76.5 ± 18.4, 1.727 ± 0.08 and 39.4 ± 11.8, 67.16 ± 11.1, 1.644 ± 0.1 for males and females respectively. No Adverse side effects were observed for any of the imaged population.

Table 12.Correlation and Slope estimates of the HP ^{3}He MRI in comparison with the MDCT based ventilation estimates.

Comparison	Correlation (R^2)	Slope
sVent vs. sVol	0.67 – 0.93	0.95
sVent vs. Jacobian	0.58 – 0.92	0.78
sVent vs. airDiff	0.76 – 0.93	0.91

*Minimum and maximum correlations observed for all slices, along with mean slope of the statistical analysis. Slight differences in pre-processing and elimination of airways and vessels between the matched datasets, along with minimal regional overlap differences, are the main factors influencing the correlation variability within subjects. Paired T-Tests demonstrated a similarity in distribution of means ($P > 0.05$) between the ventilation estimates.

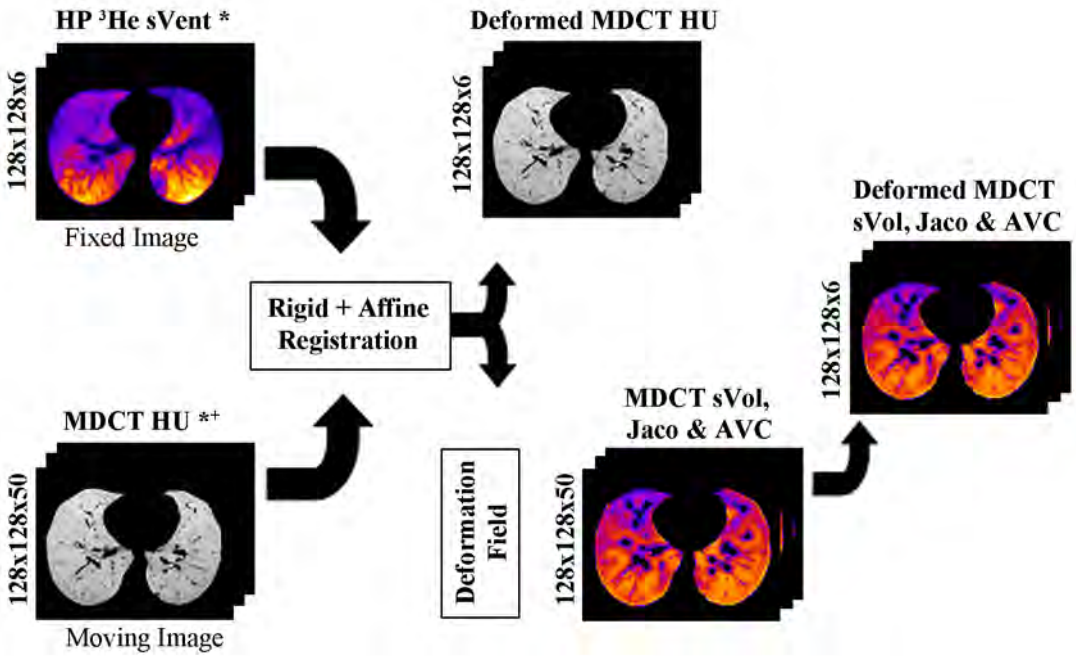

Figure 49.. Image registration flow chart, demonstrating the different steps involved in facilitating an accurate image space matching between the HP ^{3}He MRI and MDCT functional datasets. Fixed (HP ^{3}He MRI) and moving (MDCT) images are pre-preprocessed to remove the background utilizing the generating lung masks (*). To improve image space matching results and computational times, the MDCT HU datasets were downsampled from their original resolutions of ~ 512x512x600 to 128x128x50 (+). The resultant deformation field is then applied to the functional MDCT datasets to place then in the same image space as their MRI equivalents, without the need for additional registration operations. (MDCT HU – conventional MDCT, sVent – HP ^{3}He MRI static ventilation, sVol – specific volume change, Jaco - Jacobian , AVC – air volume change)

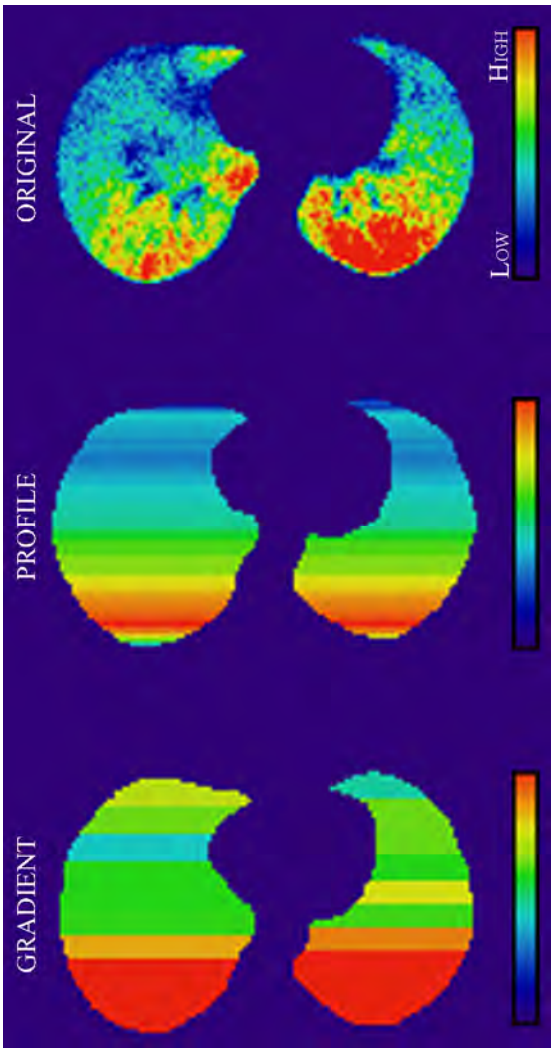

Figure 50. Visual representation of generated profile and vertical gradient distributions of a sample HP ^{3}He MRI static ventilation map utilized in assessing regional agreement of ventilation distribution against the MDCT based estimates.

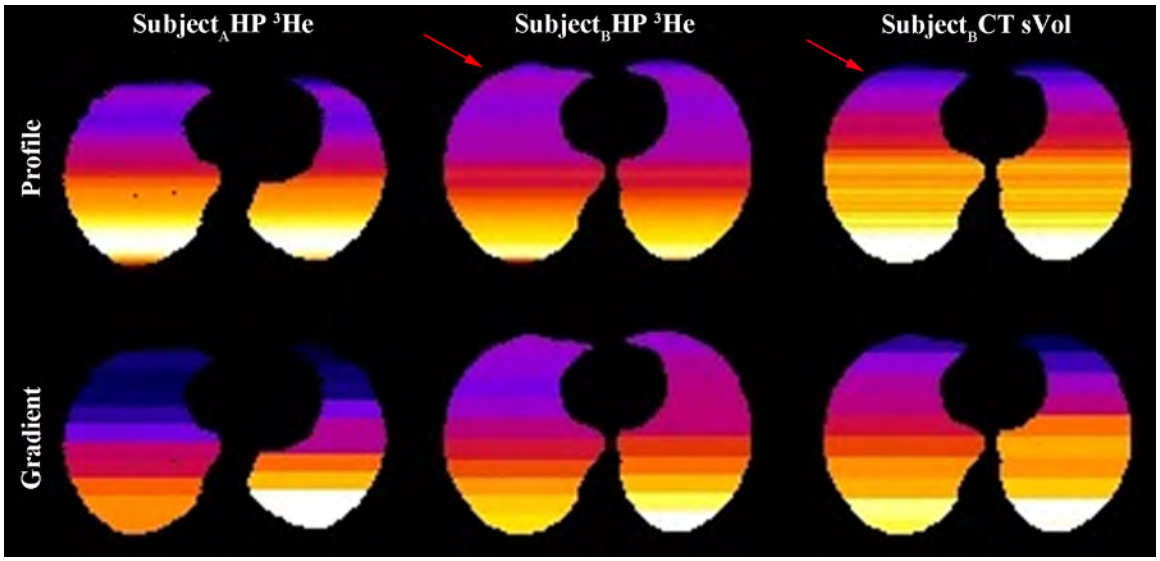

Figure 51. Visualization of Profile and Vertical Gradient differences between the HP ^{3}He MRI ventilation measures and those of the MDCT AVC measurements. Slight discrepancies in ventilation distribution are observed between both modalities in the gravitationally nondependent (ventral) portions, possibly due to gaseous density differences.

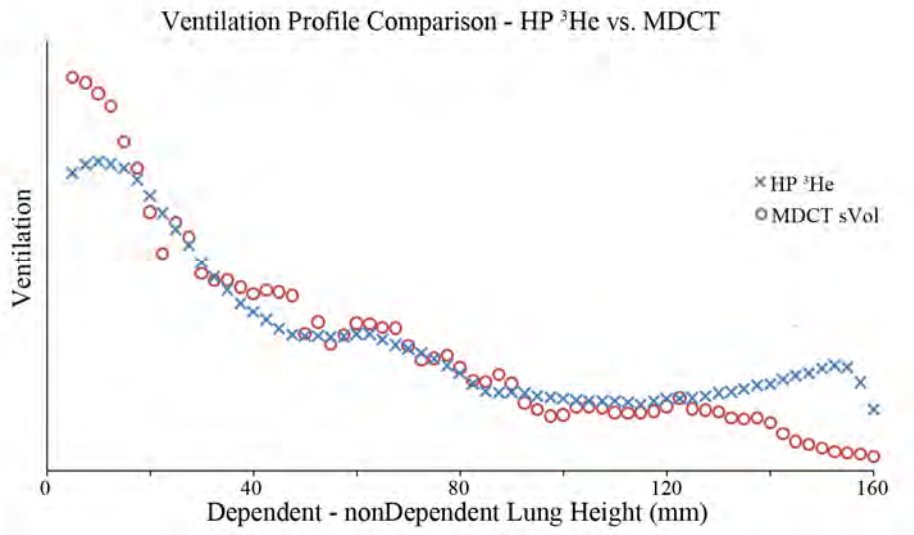

Figure 52. Single slice illustration of regional ventilation profile distribution comparison between the HP ^{3}He MRI and MDCT ventilation estimates. Both profiles follow similar trends, with some mild discrepancies observed in the extremities of the gravitationally dependent and nondependent regions, possibly due to the density differences observed for the exogenous gaseous contrast agents utilized in both modalities (MRI – Helium, MDCT – air).

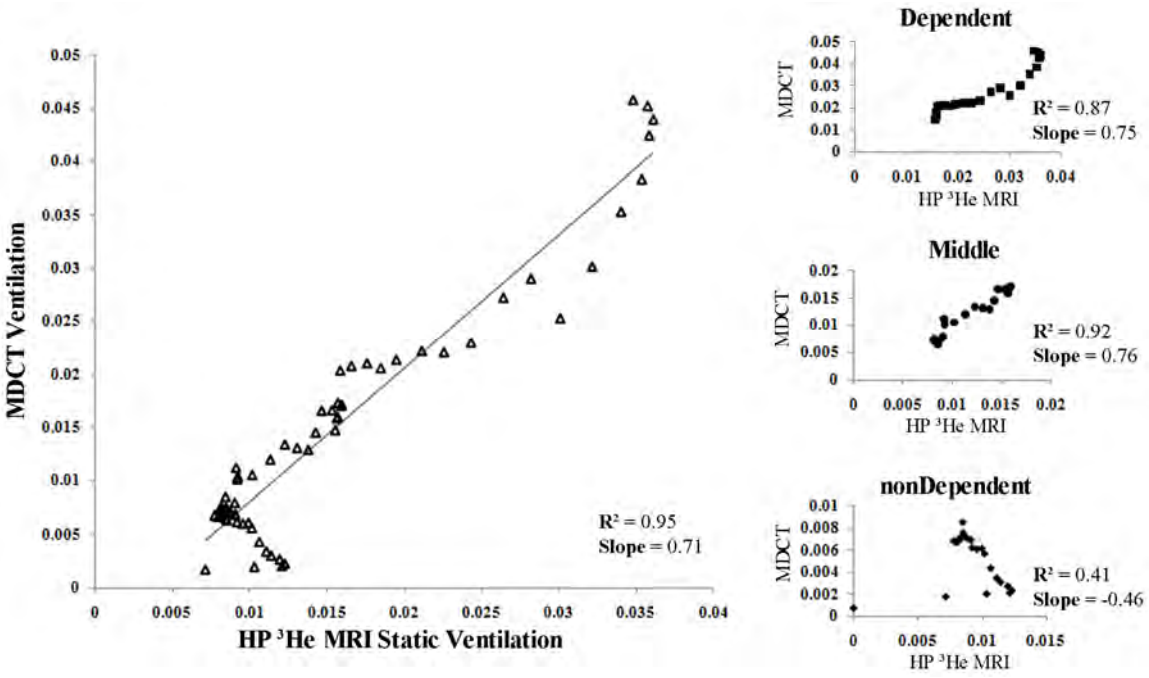

Figure 53. Linear regression analysis of HP ^{3}He MRI and MDCT ventilation estimates along the gravitationally dependent – nondependent profile. Division of profile distribution into thirds (dependent, middle and nondependent), yields a more detailed illustration of the nondependent based differences between the ventilation estimates. Correlation coefficients of the nondependent regions illustrated a lower positive value than the middle and dependent regions, with a negative rather than positive slope.

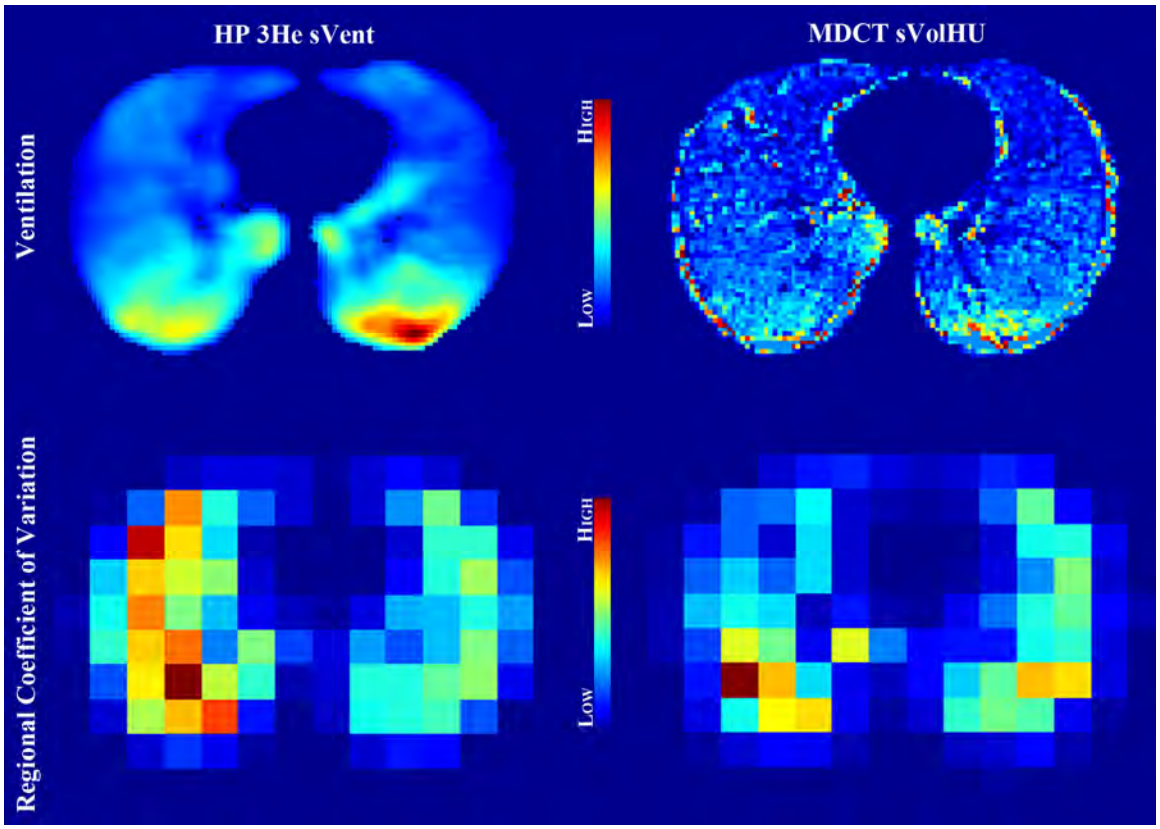

Figure 54. Assessment of regional coefficient of variation (COV) values in 8x8 pixel regions demonstrates similar heterogeneity between the HP ^{3}He and MDCT estimates. Increased COV values in the nondependent regions of the HP ^{3}He maps are observed in relation to their MDCT counterparts.

CHAPTER 9: VOLUME-CONTROLLED HYPERPOLARIZED 3HE ADC: QUALITATIVE AND QUANTITATIVE ASSESSMENT VIA XENON ENHANCED MDCT

Early attempts in evaluating pulmonary ventilation via computed tomography (CT) using non-radioactive xenon gas, relied mainly on analyzing the distribution based on a single-inspiration of a 80% xenon / 20% air mix {Tajik, 2002 #308}. The technique provided satisfactory results in comparing poorly ventilated vs. well ventilated regions throughout the lung, but was limited by long acquisition times and in-accurate lung volume control. The increasing technological advances in CT leading it from single slice acquisitions to multi-slice acquisitions, along with decreased radiation exposures and faster imaging times; have made the technique practical for physiological studies and suitable in a clinical setting. In combination with CT's ability to visualize anatomical details, this technique provides the mean for a minimally invasive, nearly complete functional and structural evaluation.

The applicability of non-radioactive xenon in the visualization of pulmonary ventilation is given in the characteristics of its k-edge, which is similar to that of iodine, deeming it a potent x-ray attenuator. Attenuation throughout the lungs is also affected by concentration of xenon gas used (2.24 HU ↑ / %Xe ↑) and kilovolt (kV) settings, with lower kV settings yielding greater attenuations, when complemented with CT scanning (50, 100). Delivery of 30-60% xenon concentrations has shown enhancements reaching 150 HU. Taking this enhancement into consideration and implementation of a controlled ventilation protocol, during which repeat volumetric CT scans are acquired (constant volume – same location), an exponential function can be fitted to any selected ROI, where the time constant of wash-in is the inverse of the local ventilation of the selected ROI. The selection of spatially varying ROIs throughout the lungs yields a regional spatial analysis of ventilation patterns. The technique is limited by the need for

specialized equipment for the mixing, delivery and control of volumes, high cost and the anesthetic properties of the gas (60, 100, 161). The most crucial of them all being the anesthetic properties of the gas, limiting the maximal amount of contrast achievable in human subjects (85, 188).

Through the implementation of a dual piston ventilator system to control both inspiratory and expiratory volumes, the xenon-enhanced MDCT technique has been assessed in humans and animals alike within our laboratory. Post processing of the generated datasets gives rise to three different assessments of regional ventilation: 1. Xenon wash-in time constant (Tau-τ) distribution, 2. Specific ventilation (sV) distribution based on the inverse of the time constant and 3. Fractional air content, which is based on the HU intensity. Given the minimal invasive nature of the HP ^{3}He MRI technique, we aim to qualitatively and quantitatively validate the sensitivity of ADC maps in assessing regional ventilation against the multi-breath xenon-enhanced MDCT technique, in a cohort of normal never smoking and COPD subjects. We hypothesize that both HP ^{3}He MRI maps will follow similar trends and tendencies as their MDCT based counterparts, but will fail to distinguish between fast and slow ventilating regions of the lungs, mainly due to the nature of acquisitions, where HP ^{3}He MRI is a single breath technique while the xenon-enhanced technique is a multi breath one.

9.1 Materials and Methods

This study was approved by our Institutional Review Board, complied with HIPAA (Health Insurance Portability Accountability Act) policies and informed consent was obtained for all subjects. Administration of ^{3}He and Xe were carried out in accordance with our physicians IND for each gas under the supervision of Dr. Edwin J.R. vanBeek.

Subject Population. Eight normal never-smoking and two COPD subjects between the ages of 20-50 were recruited and imaged. All subjects underwent pulmonary

function testing (PFT) to verify their lung function status as either normal never-smokers or COPD, based on ATS set gold standards (Normal Never-Smoker: FEV_1 and FVC > 80% predicted, FEV_1/FVC > 70% (post bronchodilator), COPD: FEV1>80%, FEV1/FVC < 70% (post bronchodilator)). Given that the PFT was performed in the seated position and imaging in the supine position, all subjects further underwent 3-4 slow vital capacity (sVC) maneuvers in the supine position on the scanner table for proper determination of lung volumes.

HP ^{3}He Imaging. All Imaging was performed on a clinical, broadband capable, Siemens Avanto 1.5T MR scanner (Siemens, Erlangen, Germany). A flexible, vest-like coil specifically tuned to the Larmor frequency of ^{3}He (48.4676 MHz) was utilized to transmit and receive RF pulses for the imaging (Clinical MRI Solutions, Milwaukee, USA). Physiological monitoring consisted of ECG (heart rate), non-invasive blood pressure (NBP) and pulse-oximetry (SPO_2). Imaging breath-holds were conducted at approximately 20%, 60% and 100% of each subjects' respective vital capacity. Volume control was achieved following the protocol presented in Chapter 5, where the desired inflation level was achieved via end expiratory inspiration of the inspiratory Tedlar bag volumes (calculated accordingly based on each subjects' VC). In the case of the proton localizers, the inspiratory volume Tedlar bag was pre-filled with a volume of room air, such that inspiration of aforementioned volumes would allow the subjects to reach the desired percentage of their VC. In the case of the HP ^{3}He scans, datasets acquired at or around 20% VC, were based on either the use of the ^{3}He doses alone to reach the desired volumes or the use of both the inspiratory volume Tedlar bags and the ^{3}He doses. The choice of either technique was purely based on each subjects' lung volume measurements acquired during the PFT sessions. Given the dependence of these measurements upon age, weight, height and lung function, some subjects tend to have very small lung volumes, such that the inspiration of the 1 liter ^{3}He doses would be sufficient to reach 20% of their VC. For the remainder of the required breatholds, the volumes within the

inspiratory Tedlar bags were one liter less than those calculated for the proton localizers, to allow top up with the 1 liter ^{3}He doses.

Polarization and Doses. ^{3}He was polarized through spin exchange optical pumping (SEOP) using a GE Healthcare polarizer (GE Healthcare, Princeton, USA), generating 1 liter at polarization levels between 38-42%. Doses were transported via rapid transfer between the polarizer and MR scanner. The administered doses consisted of approximately 300 ml ^{3}He and 700 ml of medical grade Nitrogen in a 1 liter Tedlar bag fitted with ½" inner diameter (ID) Tygon tubing, allowing for the conduction of three ^{3}He breath-hold maneuvers per subject with minimal resistance.

MDCT Imaging. MDCT imaging was carried out on a Siemens Somatom 64 scanner (Siemens, Erlangen, Germany) (80kV, 150 mA, Axial 0.33 sec scans, 1.2mm slices, 24 mm FOV). A time series acquisition protocol was utilized to acquire end expiratory datasets based on the inspiration of air and xenon for the duration of a 20 breath respiratory cycle. The first 3-5 acquisitions of the time series protocol are based on the inspiration of air, while the remaining acquisitions (up to 17) are of xenon, to depict the baseline and washin of the gas respectively. Through the use of the in-house built dual piston ventilator system, proper volume control of inspiratory and expiratory volumes, along with administration of either air or xenon at the appropriate times was achieved. Respiratory circuit occlusion and scanner triggering at the end of each respiratory cycle during the 20 breath time series acquisition were achieved through the use of a LabVIEW script utilized in monitoring inspiratory and expiratory volumes. Based on the limited axial acquisition FOV of the MDCT scanner (approximately 2.4 cm), xenon-enhanced assessment of lung ventilation was limited to the a similar sized region. In order to maximize the probed lung region and minimize cardiac motion, the imaging FOV was placed in a region directly above the diaphragm and below the base of the heart.

Image Analysis. Reconstruction and generation of the HP ^{3}He MRI static ventilation and ADC maps was achieved through the use of the MATLAB script presented in Chapter 4: Image Processing. Wash-in analysis of the xenon enhanced MDCT datasets was accomplished through the use of PASS, generating maps of the fractional air content, xenon wash-in time constants and regional ventilation. Pre-processing of the MDCT datasets included lung segmentation followed by left-right separation and airway-vessel threshholding to eliminate the influence of both structures on the resultant maps. Post processing of the MDCT datasets was performed to eliminate the influence of noise, through the use of a 3x3 or 5x5 moving average window, applied to the resultant ventilation maps.

MRI-MDCT Comparison. Z-axis averaging was performed on the MDCT slices to generate a single 24mm slab, approximating the z-axis coverage of its 15mm HP ^{3}He MRI equivalent. During MRI acquisitions, placement of the HP ^{3}He MRI FOV directly above the diaphragm meant that the first acquired slab would encompass a range of 15mm staring directly above the diaphragm and ending towards the base of the heart (Figure 55). Based on the limited FOV, slice thickness and spatial resolution differences and underlying assumptions of similar lung volume control and FOV placement, a regional assessment of the underlying similarities and differences was carried out via manual selection of the appropriate HP ^{3}He MRI slabs. Mean and coefficient of variation (COV) values were calculated for each slab, while analysis of distribution heterogeneity and gravitationally dependent and non-dependent trends were evaluated qualitatively.

9.2 Results

Data acquisition for the presented material occurred during the early stages of establishing a repeatable and accurate volume control method, therefore due to improper volume control and subject compliance issues during breathholds, analysis was limited to only six subjects (4 - normal never smokers, 2 - COPD). As mentioned earlier, multi-

modality comparisons were facilitated through the approximate matching of the HP ^{3}He MRI and MDCT slices. All normal never smoking subjects qualitatively exhibited homogenous distributions of both HP ^{3}He ADC values and Xe-MDCT ventilation values, along with similar gravitationally dependent-nondependent gradients throughout (Figure 56). On the other hand, COPD subjects exhibited a heterogeneous distribution of HP ^{3}He ADC and Xe-MDCT values alike, with no distinguishable gravitationally dependent-nondependent gradient. Further analysis of the COPD datasets demonstrated regional similarities in the appearance of ventilation defects/voids, with further indistinguishable variations in the HP ^{3}He ADC maps with respect to slow and or fast ventilating regions as observed in the Xe-MDCT ventilations maps. Inclusion of the volumetric conventional ^{1}H and MDCT HU datasets demonstrated a similar appearance of the ventilation defects within the matching slices as an increase in proton density and HU attenuation in the MRI and MDCT datasets respectively (Figure 57). Areas of disrupted ventilation observed in the Xe-MDCT ventilation maps were not apparent in the HP ^{3}He ADC maps, possibly due to the difference in gas density between helium and xenon.

Correlation (R^2) and COV values were calculated to assess the quantitative similarities between the ADC and Xe-MDCT ventilation measures. The ventilation measurements obtained during the Xe-MDCT acquisitions are representative of ventilation changes during a normal baseline end-inspiratory end-expiratory cycle. To approximate similar anatomical changes in the ADC maps, changes between the 60% and 100% VC maps were calculated. Subjects demonstrated an average R^2 of 0.625 between the calculated ADC changes and sV. Quantitative assessment of the gravitationally dependent (dorsal) to nondependent (ventral) regional gradient changes between the 60% and 100% ADC maps against the sV based gradients, were similar for the normal never smoking population, except for two subjects (Figure 58). Based on the reversed nature of the observed gradients, these subjects were removed from the dependent-nondependent gradient analysis (Figure 58). In the case of the COPD subjects, one subject demonstrated

a similar ventral-dorsal gradient as the normal never smokers, while the gradient in the other subject was nonexistent. COV assessment of ADC and sV values for all six subjects can be observed in Table 13. It can be observed that COV values of the ADC maps for all subjects were significantly smaller than their sV counterparts, possibly due to the differences in z-axis coverage, between the two modalities, where the HP ^{3}He MRI analysis is of a single 15 mm slice, while that of the Xe-MDCT is based on the averaging of approximately thirty 0.75 mm slices. Albeit these differences, COV values followed a similar trend for both measurements in the normal never smoking population. In the COPD subjects, a considerable increase in COV was only observed for the subject demonstrating a lack of gravitationally based dependent-nondependent gradient, while the COV of the subject demonstrating a similar gravitationally based gradient as the normal never smokers was relatively unchanged. COV of the sV measurements in both COPD subjects depicted an increase with respect to normal never smoker population probed.

9.3 Discussion

Initial results of the HP ^{3}He ADC MRI methodology comparisons against the MDCT based xenon enhanced assessment of regional ventilation are in agreement with the previously presented results in Chapter 8, demonstrating similar homogenous distribution and gravitationally dependent-nondependent gradients in the normal never smoking population. Singular use of these ADC maps has been established as a methodology for micro structural assessments of the lungs. The results presented demonstrate the ability of these measurements to coarsely assess regional ventilation based on changes between two different lung inflation levels. Differences in the regional assessment of ventilation between the two methodologies could be partially attributed to one of several factors. The low density and small molecular size of the helium atoms with respect to the xenon atoms, facilitates their distribution to areas otherwise inaccessible to

the latter, thus explaining the lack of signal voids within the HP ^{3}He ADC MRI maps when compared against the Xe-MDCT ventilation maps. In Chapter 10, we illustrated the anatomical dependence of helium distribution in a normal airway model, where nondependent regions received a significantly larger proportion of the delivered helium volumes with respect to dependent regions. Similarly in our laboratory, we have evaluated the anatomical dependence of xenon in the same airway model, demonstrating distinguishable differences in distribution with the helium model, where xenon distribution was skewed towards the dependent regions more than the nondependent ones. These dependencies are in agreement with the computational fluid dynamics simulations presented by Lin et al., based on bolus profile shape assessments and measurements (94, 95).

Similarly, the limited spatial resolution of the MRI based technique with respect to the MDCT maps is a significant determining factor in the overall achievable regional sensitivity within the acquired functional maps. Functional information within the HP ^{3}He ADC maps is representative of regional averaging of a 15mm slab of lung, while the MDCT ventilation measures are acquired as individual 0.75 mm slices, encompassing z-axis coverage of approximately 24mm. Given these differences, the dissimilarity observed with respect to the COV of the estimated functional measures comes as no surprise. Finally a major contributing factor to the overall success of the presented methodology is proper lung volume control. The initial success rate of the utilized protocol for lung volume control in the MRI based imaging sessions was low, but improvements were made along the way to establish a more robust protocol to eliminate the inaccurate control of the desired lung inflation levels. In Chapter 5, the testing and development phase of the lung volume control method utilized, along with the finalized protocol and several lung volume measurements are presented, demonstrating the significant improvements achieved in controlling the desired lung inflation levels.

In some instances, HP ^{3}He ADC MRI appeared to be less sensitive in assessing slow ventilating regions, possibly due to the nature of the acquisitions (single vs. multi breath). Initial results of single breath vs. multi breath Xenon enhanced MDCT assessments of regional ventilation testing within our laboratory has shown great correlations between both techniques, possibly eliminating the difference in acquisitions between the MRI and MDCT assessments as a major contributor to the overall observable differences in ventilation assessment. The current state of the HP ^{3}He MRI methodology and the sensitivity achievable via the MDCT based technique in characterizing slow and fast ventilating regions, makes the latter the more appropriate choice in assessing the early pathological changes induced as a function of reduced time constants occurring with disease onset. On the other hand, the minimally invasive nature and non-radiation based image acquisition of the MRI based technique make it a much more viable solution for longitudinal and pediatric assessments. The existing literature has demonstrated the ability and sensitivity of the HP ^{3}He MRI methodology in assessing regional changes during the early stages of several disease conditions, including asthma, COPD and alpha-1 antitrypsin (41, 43, 83, 167). The complimentary use of the different functional measurements achievable via the methodology (static and dynamic ventilation, ADC and PO_2 measurements), demonstrate the multi-factorial ability to assess normal and pathological conditions on the basis of airway changes, air trapping, micro structural changes, ventilation distribution, dynamics of distribution and efficiency of the oxygen exchange process.

In conclusion we have validated the ability of HP ^{3}He ADC MRI to assess regional ventilation, through a qualitative and quantitative assessment of the underlying similarities in distribution and gravitationally based gradients of lung ventilation. These results are complimentary to the results presented throughout the hypothesis driven aims of the presented material, establishing the validity of the HP ^{3}He MRI methodology in assessing regional ventilation and the differences observed based on acquisition

differences and gaseous densities. Furthermore, we have demonstrated the importance of proper volumetric control of the lung inflation levels if a multi-modality or longitudinal assessment of lung function is a desired end point. Albeit, the preliminary nature of the these results, the development of the desired tools and protocols required for accurate acquisitions and processing of the datasets, is a large step towards facilitating a more regional and quantitative assessment between the two measures for future users.

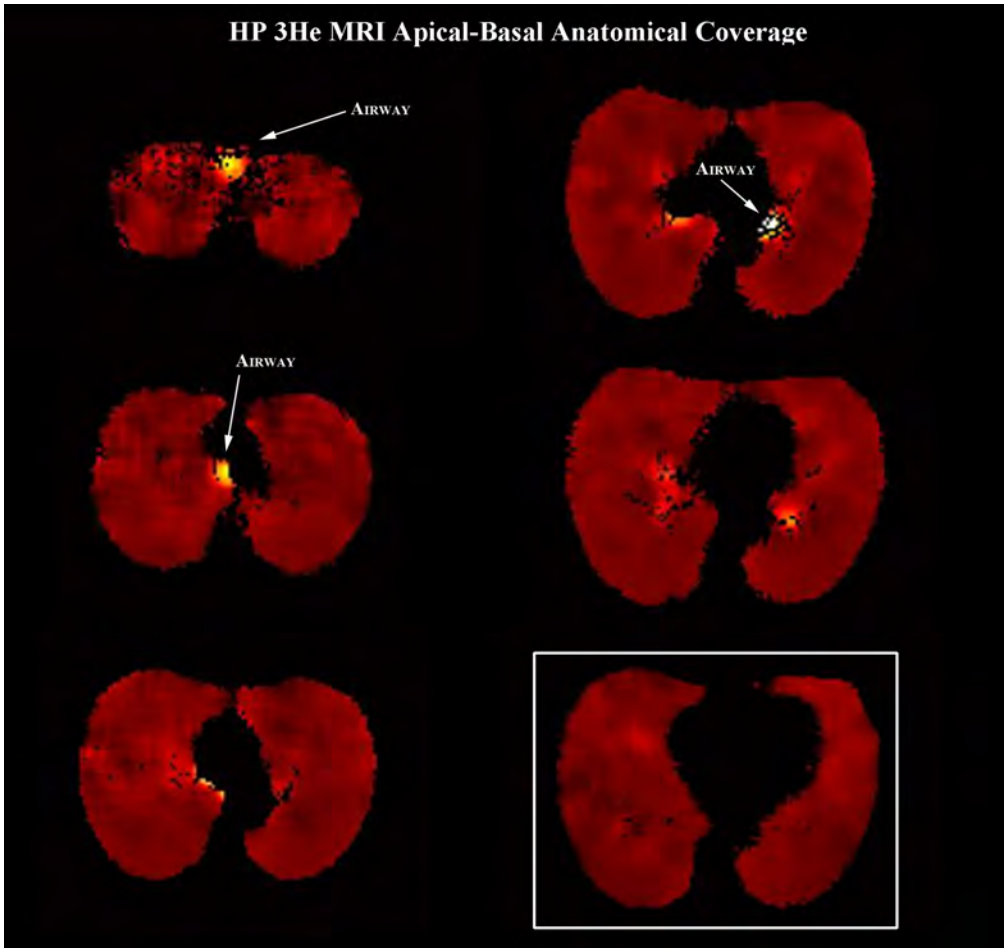

Figure 55. Sample apical-basal anatomical coverage achieved during HP ^{3}He MRI. Placement of imaging field of view was such to encompass the overall apical-basal lung coverage in attempts to provide a comprehensive assessment of the underlying physiological changes. Manual selection of a slice representative of similar coverage as the Xe-MDCT maps was carried out due to the limited nature of the acquisitions (*blue square*). Regions of high ADC (represented by higher intensities) are of the airways and were removed from the overall analysis via manual segmentation.

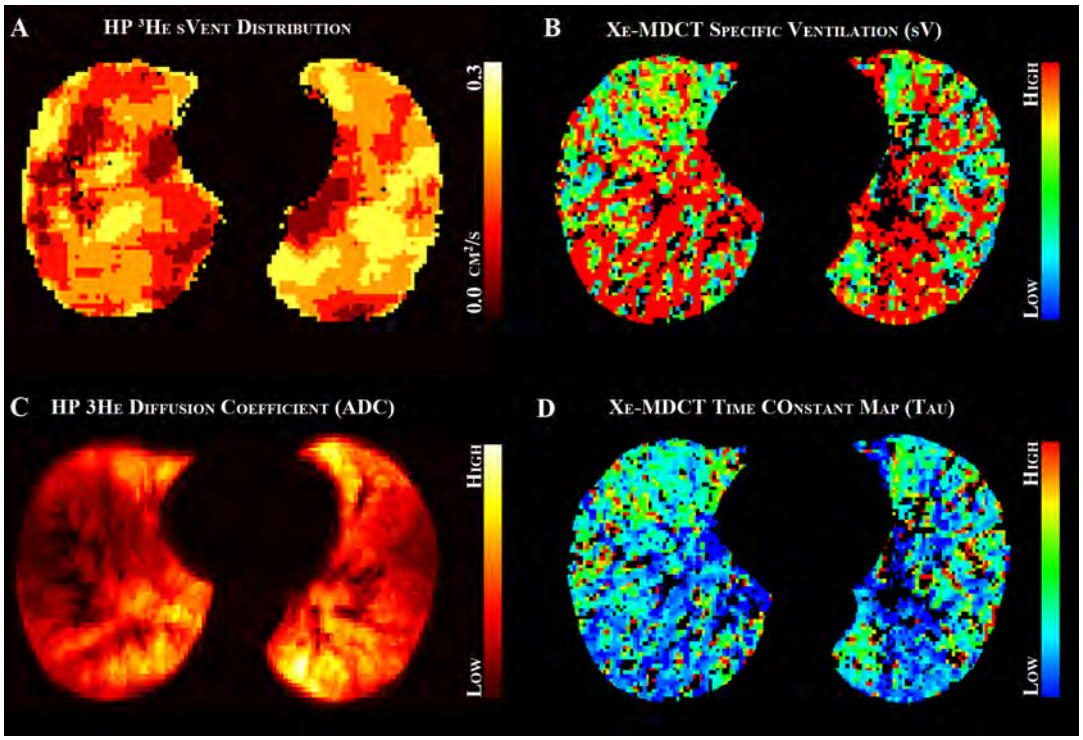

Figure 56. Functional maps of Normal Never-Smoker subject, ^{3}He ADC (A), ^{3}He sVent (airspace ventilation) (C), Xe-MDCT specific ventilation (B), and Xe-MDCT time constant (D). Functional values throughout illustrate a homogenous distribution and dependent-nondependent gradient similarities in the ^{3}He sVent and Xe-MDCT ventilation maps (BandC). The inverse relationship between the time constant (D) and the ventilation metrics (B) of the Xe-MDCT results in a reversed gradient.

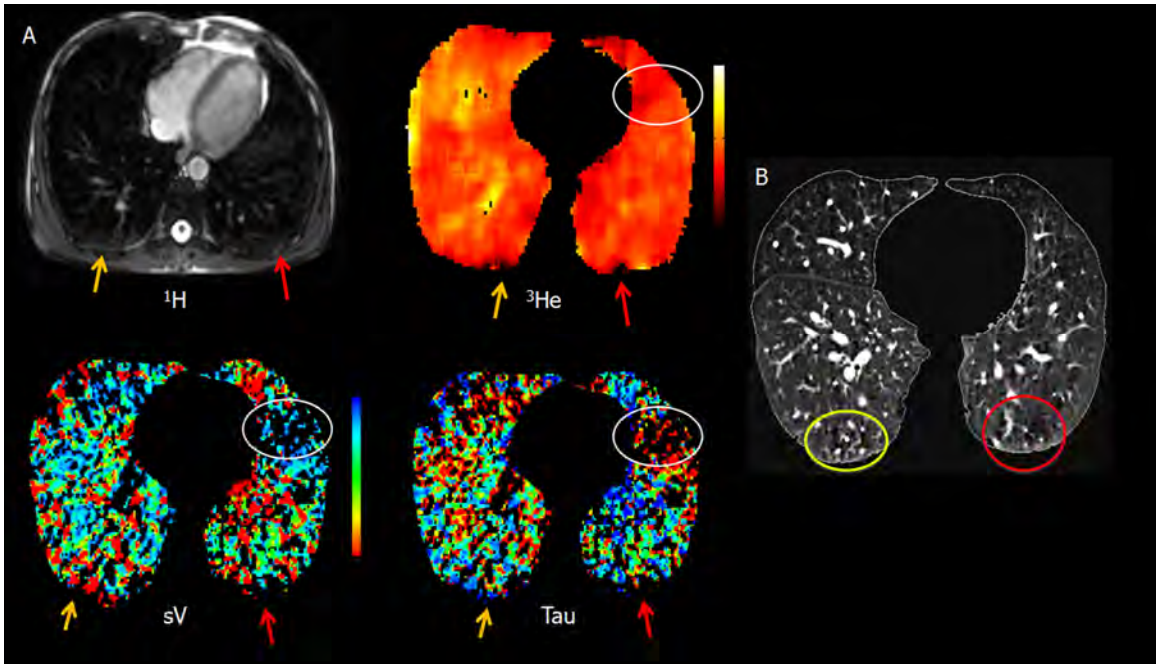

Figure 57. COPD subject ^{1}H MR, ^{3}He ADC, Xe-CT sV and Xe-CT time-constant maps, illustrating heterogeneous distributions. Ventilation defects along with inconsistencies in representing slow and fast ventilating regions are illustrated (A). Ventilation defects were also observed in the MDCT volumetric scan (B).

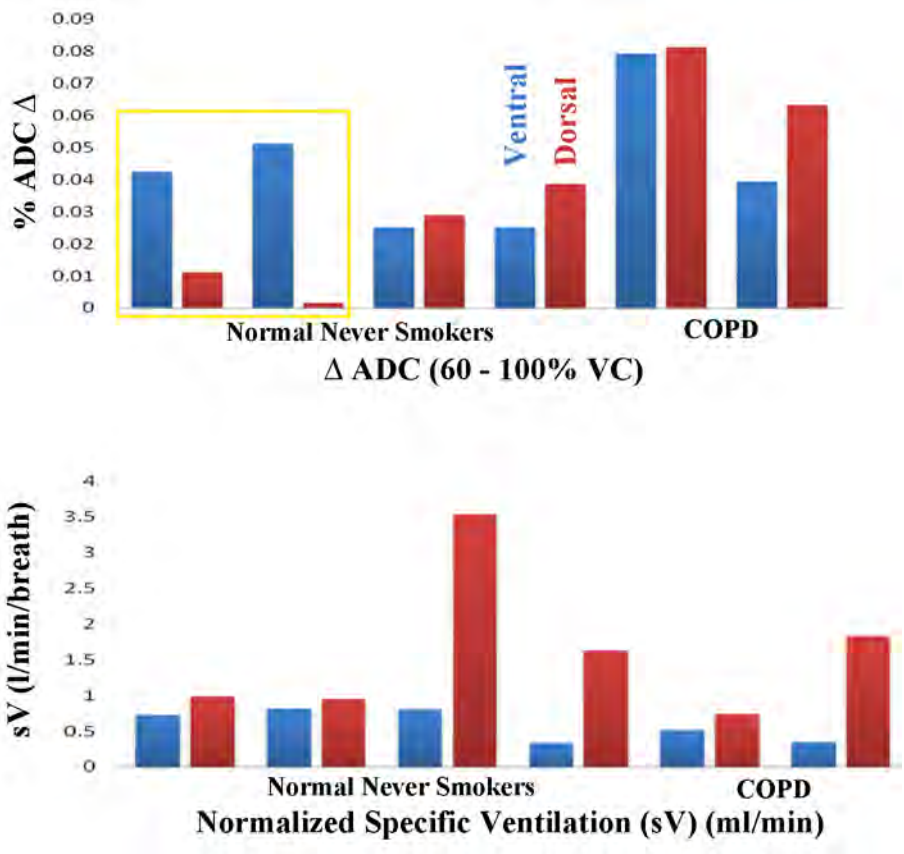

Figure 58. Dorsal-Ventral distribution of ADC changes between 60% and 100% VC and sV Xe-MDCT measurements of regional ventilation. Similarities in the observable gravitationally based gradient are easily distinguishable in the normal never smoking population. The reversed nature of these gradients in the ADC measurements of first two normal never smoking subjects, suggests improper volume control of the subjects and or differences in breathhold initiation, thus were excluded (red square). In the ADC measurements, one COPD subject depicted a similar gradient as the normal never smokers, while the other had an indistinguishable gradient.

Table 13. Coefficient of Variation (COV) of 4 normal-never smokers and 2 COPD subjects.

	COV	
	^{3}He ADC	**Xe-CT sV**
Normal	0.1365	0.5615
Normal	0.1934	0.4899
Normal	0.1545	0.4294
Normal	0.1893	0.574
COPD	0.289	0.657
COPD*	0.1589	0.6209

* One COPD subject (red) exhibited a similar COV of ADC as the normal never smokers, while the Xe-CT sV assessment demonstrated an increased COV.

CHAPTER 10: COMPUTATIONAL FLUID DYNAMICS AND IMAGING BASED ASSESSMENT OF HYPERPOLARIXED 3HELIUM DISTRIBUTION IN A NORMAL AIRWAY MODEL: ANATOMICAL DEPENDENCE AND LUNG IMAGING CONSIDERATIONS

Advancements in medical imaging through the use of exogenous and endogenous contrast mechanisms and agents have enabled a relatively non-invasive assessment of the underlying structure and function of pulmonary ventilation, via the introduction of Magnetic Resonance Imaging (MRI) based techniques, such as Hyperpolarized (HP) ^{3}He (81, 168, 169) and ^{129}Xe (65, 121), Oxygen Enhanced (93, 115, 117), Sulfur Hexafluoride (SF_6) (145, 182) and Fourier Decomposition MRI (17), as well as several MDCT based acquisitions (24, 29, 52, 68). The emergence of HP ^{3}He gas as an exogenous contrast agent to probe normal and pathological pulmonary states has provided a great amount of information with regards to the underlying microstructure and gas dynamics and distribution throughout the lungs in both normal and pathological conditions such as asthma and COPD (42, 83, 160).

Lin et al. (94), demonstrated the intra-bronchial anatomical and posture related differences between xenon and helium gas distributions in an six generation airway model, based on segmented MDCT data. Consistent with the measurements of Weibel et al.(174), both upright and supine positions demonstrated significant differences in the washin and washout of the gases (94). Giesel et al (54) demonstrated the applicability of MDCT based rapid prototype airway geometries in dynamic HP ^{3}He MRI imaging, in assessing gas flow dynamics and airway measurements. The use of these anatomically accurate geometries could potentially serve as non-invasive means of gas flow and intra-operative planning assessments.

Given the underlying differences in density between the aforementioned contrast agents and air, it is crucial to determine the anatomically dependent distribution

differences between them to establish their sensitivity in assessing regional ventilation and appropriateness in multi-modality applications. Complimented with Computational Fluid dynamics (CFD) modeling, HP ^{3}He MRI was utilized to evaluate these regional differences in distribution of helium in a normal airway model generated by rapid prototyping from an in-vivo high-resolution MDCT scan, with the underlying hypothesis that both should follow similar trends and intra-bronchial distributions.

10.1 Materials and Methods

Subject Imaging and Rapid Prototyping. Volume controlled high resolution MDCT imaging of a normal never-smoking male was carried out via a Siemens Somatom 64 scanner (Siemens, Erlangen, Germany), at maximal inspiration. Automatic segmentation and generation of the lung and airway masks were carried out through the use of Pulmonary Workstation (PW2, Vida Diagnostics, Coralville, IA). Based on the airway geometries, a rapid prototype of the segmented airways was generated through the use of a polycarbonate material, to ensure strength and durability (Figure 59).

HP ^{3}He Imaging. All Imaging was performed on a clinical, broadband capable, Siemens Avanto 1.5T MR scanner (Siemens, Erlangen, Germany). A flexible, vest-like coil specifically tuned to the larmor frequency of ^{3}He was utilized to transmit and receive RF pulses for the imaging (Clinical MRI Solutions, Milwaukee, WI). ^{3}He scans were acquired via a 2D Dynamic FLASH sequence, modified to acquire a sagitally oriented slab (2.34x2.34x50 mm) through the airway phantom to include the trachea, bifurcation and branching airways @ 48.4676 MHz, with a 200x200 acquisition matrix, a 7º flip angle and ~ 0.75 second temporal resolution. Airway positioning within the center of the coil was alternated between imaging sessions to represent right lateral and left lateral recumbent positions, such that the right main branch (RMB) and the left main branch (LMB) were alternated between gravitationally dependent and nondependent branching respectively. Imaging of airways in the supine position was also carried out to establish

the distribution of ^{3}He during the most commonly utilized anatomical positioning in medical imaging. Repeatability and accuracy of the measurements was assessed via multiple imaging sessions with identical imaging parameters and flow rates in the right recumbent position.

^{3}He was polarized through spin exchange optical pumping (SEOP) using a GE Healthcare polarizer (GE Healthcare, Princeton, USA), generating 1 liter at polarization levels between 35-42%. The imaging doses consisted of approximately 300 ml ^{3}He diluted with 1200ml of medical grade Nitrogen, administered via a 1500 ml syringe over the course of a 20 second imaging protocol.

Computational Fluid Dynamics Simulations. were carried out following the procedures presented in Lin et al. (95) and Tawhai et al.(162).

10.2 Results

Phantom Imaging. A surface rendering screenshot of the utilized phantom is illustrated in Figure 59. The results of the flow distribution in the airway phantom are shown in Figure 60, representing slow and fast flow rates respectively. It can be observed that independent of flow rate, the nondependent airways receive a larger proportion of the delivered helium, in comparison with its dependent counterpart. Figure 61 represents the average signal intensity plot of ROIs placed in the trachea, RMB and LMB, and several smaller airways further illustrating the preferential distribution of helium to the nondependent airways, throughout the entire duration of the imaging session. Slight increased differences were observed in smaller dependent airways, where the airway branching angle was less dependent. Imaging in the right and left lateral recumbent positions, illustrates a preferentially distribution in the RMB of the airway phantom regardless of dependent – nondependent positioning (Figure 62). The observed increase in helium distribution in the RMB was independent of flow rate. Imaging of the airways

in the supine position, demonstrated an increased helium distribution in the nondependent airways with respect to the depndent ones (Figure 62).

CFD Simulations. Results of the CFD simulations are in agreement with the dynamic imaging results in the supine position (Figure 63). Identical distribution patterns to those observed with the airway phantom are seen, with a larger proportion of the helium in the nondependent airways with respect to the dependent ones. This was further strengthened by modeling the flow in a no gravity environment, leading to elimination of the preferential distribution of the gas and a more evenly distributed flow pattern (Figure 64).

10.3 Discussion

Agreement of the results with our previous knowledge gas flow dynamics in anatomically correct airway geometries, presents itself as a validation tool for assessing the intrinsic properties of these distributions. We have demonstrated the ability to utilize both CFD simulations in combination with dynamic HP ^{3}He MRI imaging to assess these variations. The preferential distribution of the helium gas in the nondependent portions of the airway model is in agreement with gas flow characteristics evaluated by Lin et. al. (94). The incorporation of multi-scale pulmonary gas flow evaluations via CFD simulations in conjunction with the exogenous based contrast enhancements achievable via MRI and/or MDCT functional imaging techniques, provides the means for non-invasive assessments of gas flow characteristics and the interaction between structure and function within the probed organs (95, 162).

The use of HP ^{3}He MRI in probing structural and functional variations intrinsic to normal and pathological conditions has shown great insight into the origin and progression of these metrics (10, 43, 83, 165). Multi-modality assessments have facilitated the validation of these metrics in correlation with either imaging based or computational models of structure and function (32, 39, 103, 159). The apparent

differences observed between the utilized gaseous contrast agents and the foundations of lung physiology based on the distribution and interactions of normal air with the underlying structure and function, necessitates the assessment of these observable characteristic differences to validate their use and extraction of potential viable biomarkers.

In our laboratory, we have evaluated the regional sensitivity achievable via HP ^{3}He MRI in assessing pulmonary ventilation, in correlation with quantitative MDCT based regional ventilation measures. The resultant positive correlations and agreement between the gravitationally dependent – nondependent gradients, showed promise in the use of the technique as a surrogate to the ionizing radiation based modality. Significantly small differences in gas distribution between the two modalities arose, with slight preferential distribution of helium to the nondependent regions. The presented results and validation of this preferential distribution, in conjunction with the aforementioned multi-modality assessment of lung ventilation, illustrates the importance of proper characteristic evaluations of the gas flow dynamics and distributions in the validation of metrics achievable via a given modality.

Figure 59. Surface rendering of the generated airway tree utilized in setting the boundary conditions for the simulations.

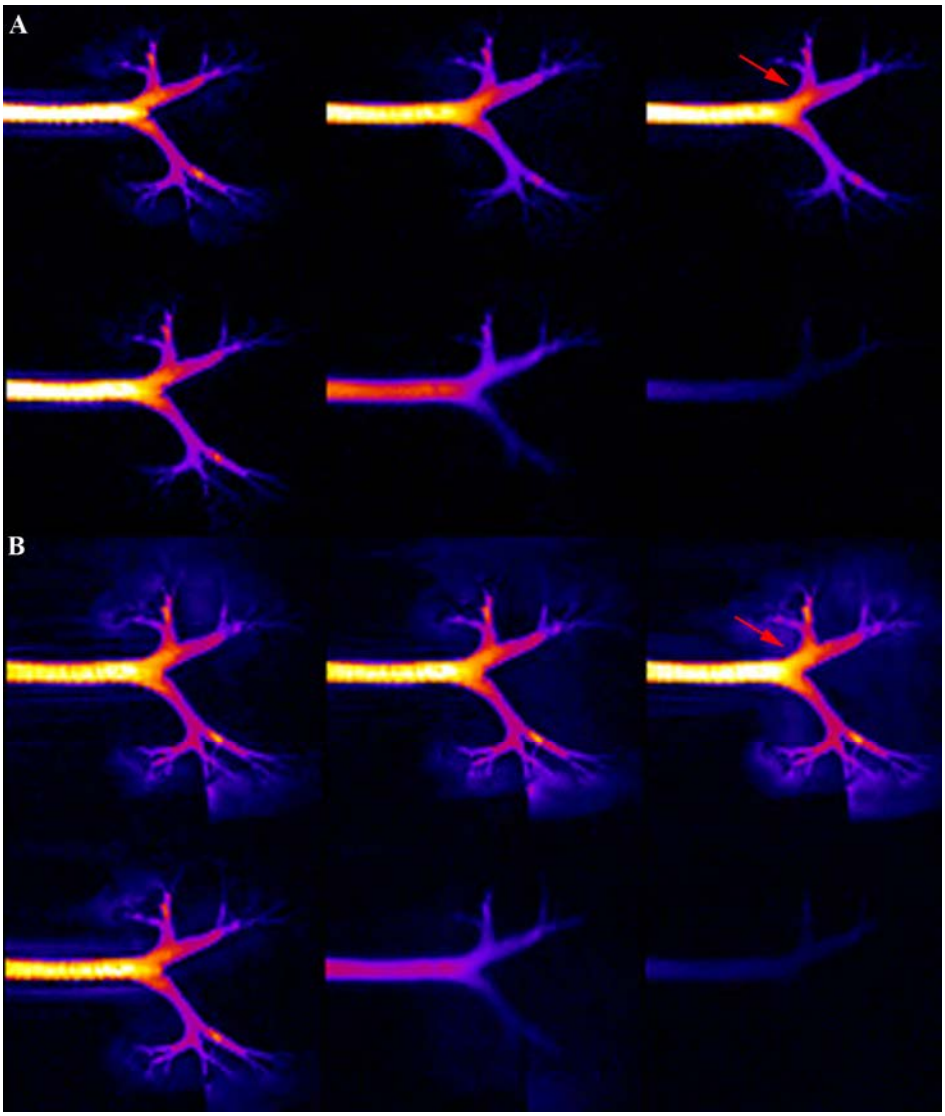

Figure 60. Dynamic HP ^{3}He imaging of gas distribution in normal airway model during slow (A) and fast (B) flow rate infusions, demonstrates a nondependent preferential distribution (*red arrow*). No relationships between flow rate and distribution patterns were observed. (*Airway snapshots presented within the figure approximate similar time points throughout the duration of the imaging*)

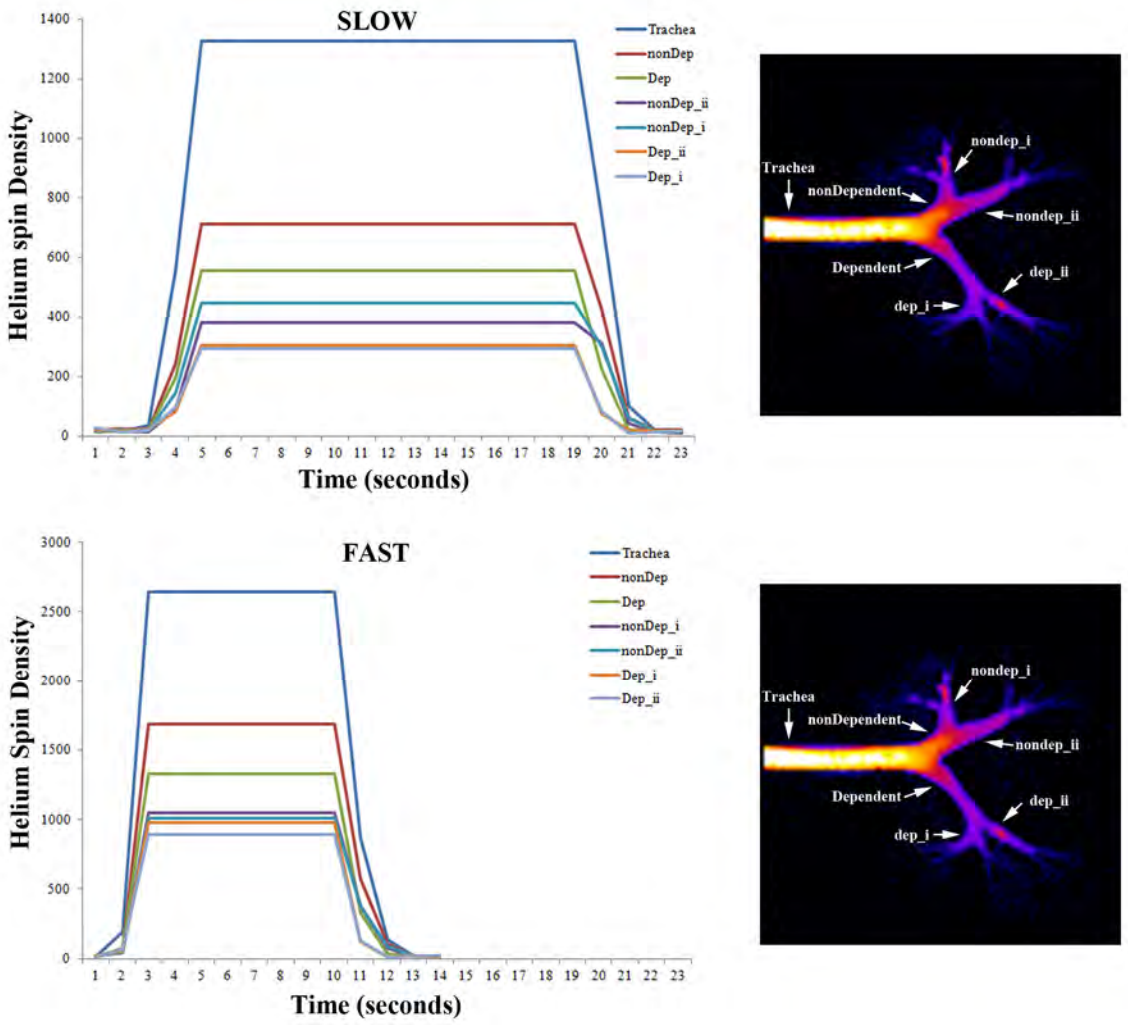

Figure 61. Average intensity plot of ^{3}He spin density throughout various airways within the airway phantom. It can be clearly observed that all nondependent airways receive a larger proportion of the infused ^{3}He gas, regardless of infusion rate. In the dependent regions, slightly increased ^{3}He distributions were observed in the *dep_ii* labeled airways.

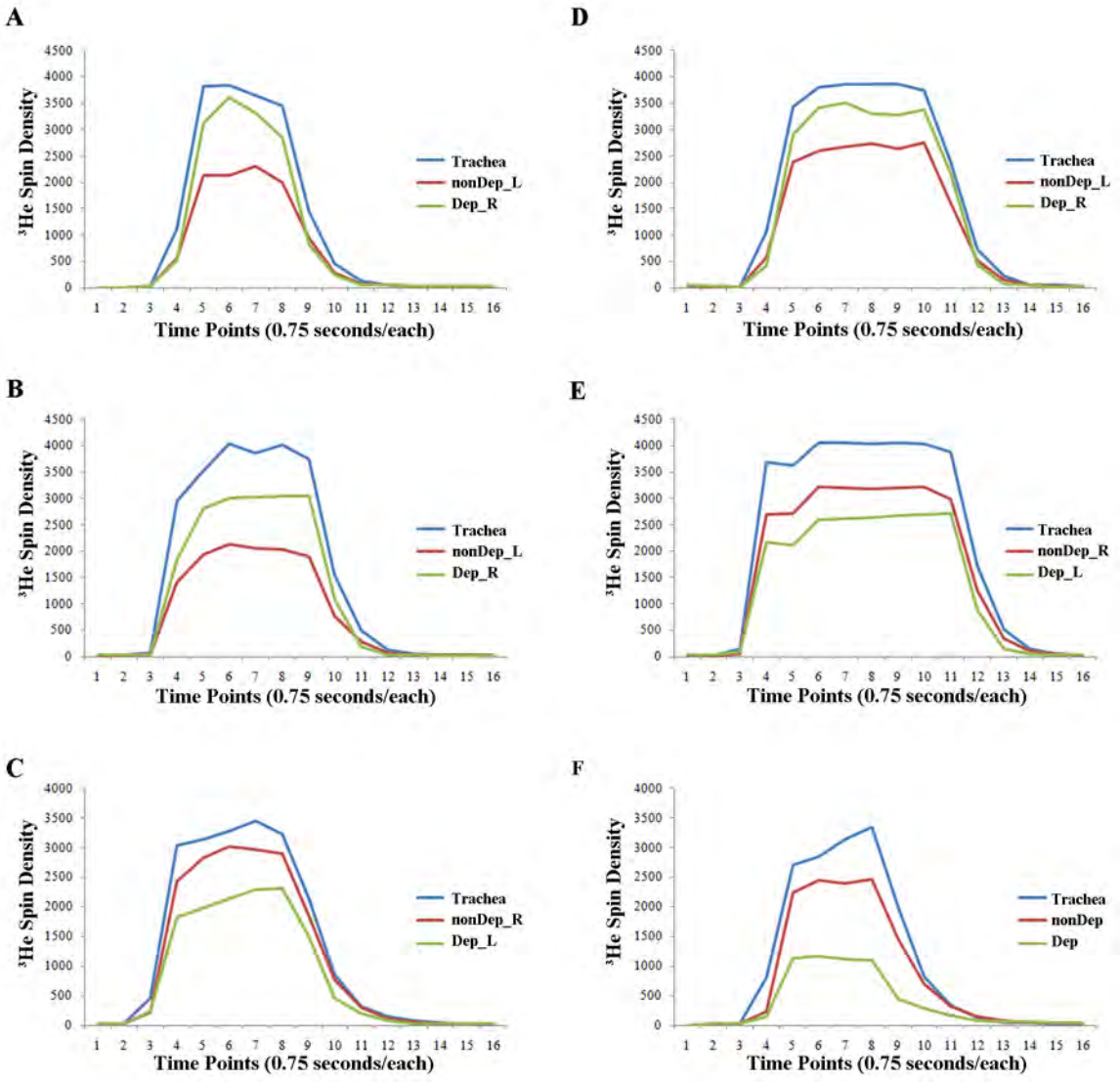

Figure 62. Nondependent and dependent distribution of ^{3}He in right recumbent (A), left recumbent (C) and supine position (F) during normal physiological flow rates (~0.2 L/sec). Plots D and E represent the right and left recumbent positions respectively, during slower flow rates (~0.1 L/second). Preferential distribution of ^{3}He in the right airway is apparent regardless of the right and left recumbent positions. Supine positioning illustrates a significant preferential increase of flow in the nondependent airways with respect to the depndent ones. Plot B demonstrates the repeatability of the technique (right recumbent – fast flow rate).(*nonDep – nondependent, Dep – dependent*)

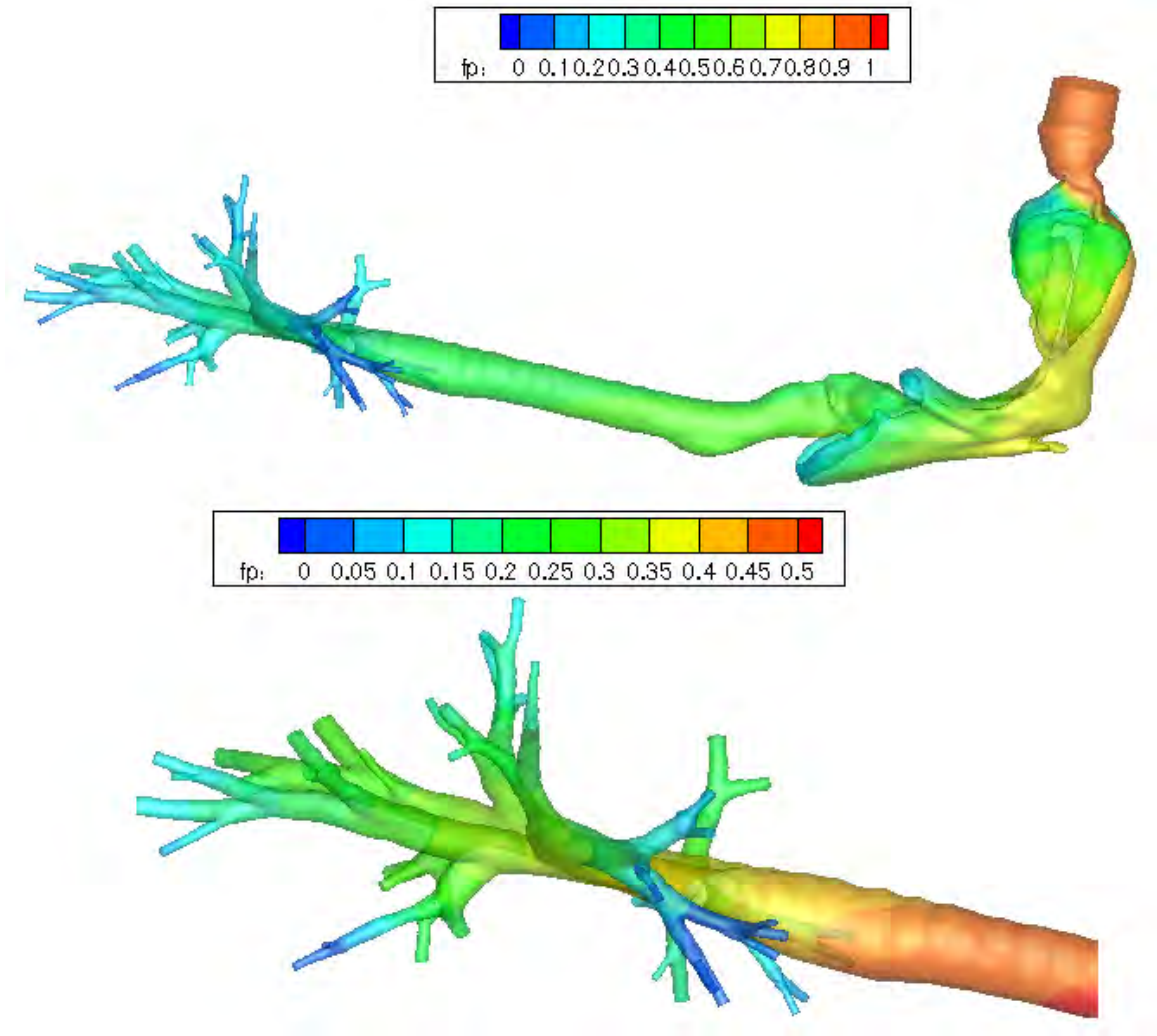

Figure 63. CFD simulation results of dependent – nondependent gas distribution differences under normal gravitational forces. A significant difference is clearly observed between the dependent and nondependent airways, with the latter receiving a larger proportion of the delivered gas. This is in agreement with the dynamic imaging results.

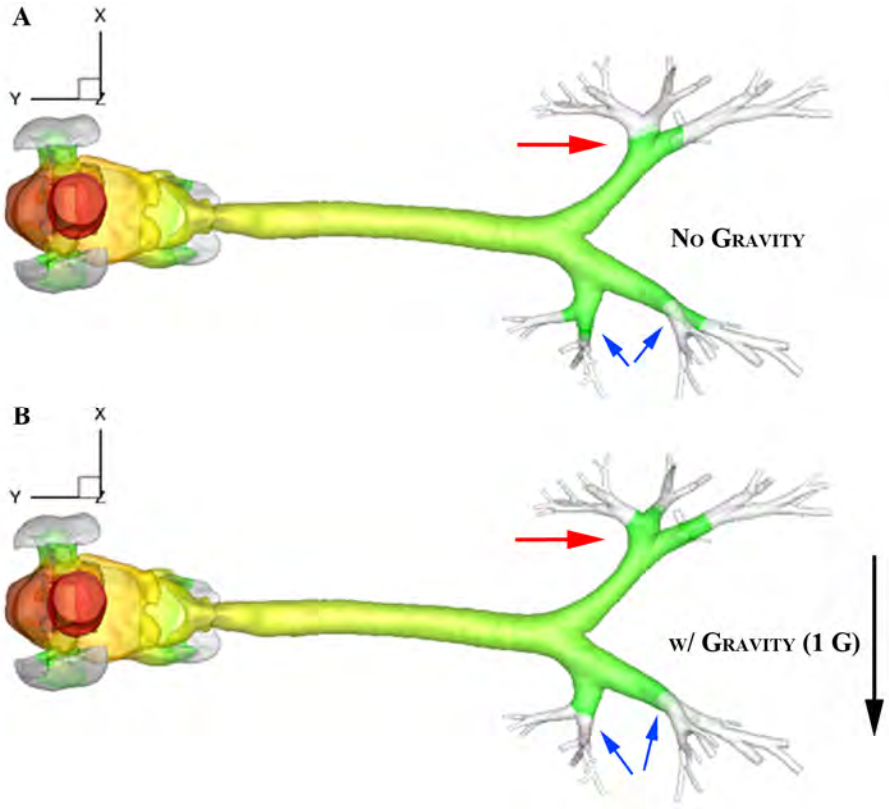

Figure 64. CFD simulation of gravitational effects upon ^{3}He distribution within a normal airway model (A – no gravity, B – 1G gravity). Increased nondependent distribution is observed in the 1G gravity simulation (red arrows), with decreased distributions in the dependent airways (blue arrows), when compared to the zero gravity simulation.

CHAPTER 11: CONCLUSION, FUTURE CONSIDERATIONS AND TRANSLATIONAL PERSPECTIVE

Use of Hyperpolarized ^{3}Helium (HP ^{3}He) Noble Gas Magnetic Resonance Imaging (MRI) to study the properties of the peripheral lung spaces provides a possibility for use in assessing presence and progression of smoking associated emphysema. However, little attention has been paid to the role of lung inflation level and its affects upon the MR based measures of peripheral airspaces.

In this study, the extracted dependency between diffusion weighted HP ^{3}He MRI and lung inflation levels at the time of imaging demonstrated a semi-linear positive relationship between the two and significant changes in expansion on a regional and global basis following well recognized alveolar ventilation patterns. Strengthened by recent literature findings demonstrating the appearance of significantly small changes during longitudinal assessment of COPD conditions, these findings promote the notion of proper volumetric control of lung inflation levels during imaging to facilitate extraction of these changes prior to the onset of early disease conditions and monitor normal structural and functional changes.

Quantitative and qualitative lung ventilation assessments in correlation with established MDCT based ventilation measures were carried out with considerable success, through the incorporation of volumetric control of the lung inflation levels, proper image space matching and profile and vertical gradient based assessments. In conjunction with local air volume changes (AVC), we demonstrated significant correlations between the MDCT AVC ventilation measurements and the spin density distributions of HP ^{3}He MRI static ventilation maps in a cohort of normal never-smoking subjects. Similarly, qualitative and semi-quantitative assessment of the MRI based ventilation measures in relation to multi-breath xenon-enhanced MDCT measures demonstrated an agreement in visualized trends of ventilation. The differences in

acquisitions between the two, have deemed HP ^{3}He MRI ventilation maps insensitive to fast and slow ventilating regions, while the latter is insensitive to ventilation voids. Both evaluations are the first of their kind in establishing the sensitivity and validity of HP ^{3}He MRI in assessing regional ventilation in correlation with quantitative MDCT based measures. The observed agreement with our previous understanding of normal pulmonary physiology and the gravitationally dependent (dorsal) – nondependent (ventral) gradients, further strengthens the surrogacy of the technique in clinical applications.

Computational fluid dynamic simulations in combination with dynamic HP ^{3}He MRI demonstrated a slight but significant favoring of nondependent and right main branch distribution irrespective of flow rates. These results were in agreement with the nondependent discrepancies observed between the MDCT and MRI based ventilation estimates, where the latter demonstrated slight \over-estimation of the underlying ventilation. The importance of this finding is crucial for multi-modality assessments of lung ventilation, where deviations from our normal understanding of pulmonary ventilation based on the distribution of normal air throughout must be approached with caution to prevent over and/or under estimation of the evaluated structures.

The developmental aspects of the presented work are critical elements in establishing the accuracy of the extracted variables and efficiency of longitudinal assessments. The incorporation of a simplistic apparatus for the proper control of lung inflation levels is a must to ensure similar anatomical and physiological conditions during imaging, as demonstrated previously. Similarly, the flexibility of the image registration and pre and post processing scripts, facilitated the ability to extract and generate viable functional data from the MRI and MDCT based datasets, while facilitating proper statistical analysis. The inclusion of proper tools and analysis pipelines is a determining factor of the overall success of any given analysis and proper care and evaluation must be

taken prior to initiating the experimentation/imaging process to ensure accuracy and validity of the generated information.

The ability of MRI to sensitively detect small airspace changes through the use of HP ^{3}He MRI diffusion weighted and spin density distribution metrics has been demonstrated through the aforementioned analysis. These findings in combination with the developmental aspects of the presented research are critical to the efficacy and surrogacy of the technique as a viable lung imaging biomarker. The recent insight into the deleterious effects of excessive radiation exposure and the current reliance upon the global measurements attainable via pulmonary function tests (PFT) within the research and clinical environments, instigates the need for more regionally specific minimally invasive assessments of the underlying anatomical and physiological changes in attempts to detect early changes associated with disease onset. Combined with proper volumetric control of lung inflation levels, the findings within the presented research demonstrate the ability of MRI to assess the underlying airspace changes and its ability to estimate regional ventilation, which are essential biomarkers in establishing MRI as a contender in the lung imaging field for use in conjunction with surgical and pharmaceutical interventions.

REFERENCES

1. Basics of Magnetic Resonance Imaging and Magnetic Resonance Spectroscopy. **http://www.physics.utu.fi/projects/kurssit/UFYS3093/MagneticResonanceTomographyBasics.pdf**

2. **Albert MS, Cates GD, Driehuys B, Happer W, Saam B, Springer CS, Jr., and Wishnia A**. Biological magnetic resonance imaging using laser-polarized 129Xe. *Nature* 370: 199-201, 1994.

3. **Albert RK, and Hubmayr RD**. The prone position eliminates compression of the lungs by the heart. *Am J Respir Crit Care Med* 161: 1660-1665, 2000.

4. **Altes TA, and de Lange EE**. Applications of hyperpolarized helium-3 gas magnetic resonance imaging in pediatric lung disease. *Top Magn Reson Imaging* 14: 231-236, 2003.

5. **Altes Ta, Powers PL, Knight-Scott J, Rakes G, Platts-Mills Ta, de Lange EE, Alford Ba, Mugler JP, and Brookeman JR**. Hyperpolarized 3He MR lung ventilation imaging in asthmatics: preliminary findings. *Journal of magnetic resonance imaging : JMRI* 13: 378-384, 2001.

6. **Altes TA, Rehm PK, Harrell F, Salerno M, Daniel TM, and de Lange EE**. Ventilation imaging of the lung: Comparison of hyperpolarized helium-3 MR imaging with Xe-133 scintigraphy. *Academic Radiology* 11: 729-734, 2004.

7. **Amundsen T, Torheim G, Waage a, Bjermer L, Steen Pa, and Haraldseth O**. Perfusion magnetic resonance imaging of the lung: characterization of pneumonia and chronic obstructive pulmonary disease. A feasibility study. *Journal of magnetic resonance imaging : JMRI* 12: 224-231, 2000.

8. **Ashburner J, and Friston KJ**. Nonlinear spatial normalization using basis functions. *Hum Brain Mapp* 7: 254-266, 1999.

9. **Atalay MK, Poncelet BP, Kantor HL, Brady TJ, and Weisskoff RM**. Cardiac susceptibility artifacts arising from the heart-lung interface. *Magn Reson Med* 45: 341-345, 2001.

10. **Aysola R, de Lange EE, Castro M, and Altes TA**. Demonstration of the heterogeneous distribution of asthma in the lungs using CT and hyperpolarized helium-3 MRI. *J Magn Reson Imaging* 32: 1379-1387, 2010.

11. **Bakker ME, Putter H, Stolk J, Shaker SB, Piitulainen E, Russi EW, and Stoel BC**. Assessment of regional progression of pulmonary emphysema with CT densitometry. *Chest* 134: 931-937, 2008.

12. **Barnes PJ**. Emerging pharmacotherapies for COPD. *Chest* 134: 1278-1286, 2008.

13. **Barnes PJ**. Emerging targets for COPD therapy. *Curr Drug Targets Inflamm Allergy* 4: 675-683, 2005.

14. **Barnes PJ**. Inhaled corticosteroids in COPD: a controversy. *Respiration* 80: 89-95, 2010.

15. **Barnes PJ, and Stockley RA**. COPD: current therapeutic interventions and future approaches. *Eur Respir J* 25: 1084-1106, 2005.

16. **Bartel S-ET, Haywood SE, Woods JC, Chang YV, Menard C, Yablonskiy Da, Gierada DS, and Conradi MS**. Role of collateral paths in long-range diffusion in lungs. *Journal of applied physiology (Bethesda, Md : 1985)* 104: 1495-1503, 2008.

17. **Bauman G, Puderbach M, Deimling M, Jellus V, Chefd'hotel C, Dinkel J, Hintze C, Kauczor HU, and Schad LR**. Non-contrast-enhanced perfusion and ventilation assessment of the human lung by means of fourier decomposition in proton MRI. *Magn Reson Med* 62: 656-664, 2009.

18. **Bink A, Hanisch G, Karg A, Vogel A, Katsaros K, Mayer E, Gast KK, and Kauczor H-U**. Clinical aspects of the apparent diffusion coefficient in 3He MRI: results in healthy volunteers and patients after lung transplantation. *Journal of magnetic resonance imaging : JMRI* 25: 1152-1158, 2007.

19. **Blackall JM, Ahmad S, Miquel ME, McClelland JR, Landau DB, and Hawkes DJ**. MRI-based measurements of respiratory motion variability and assessment of imaging strategies for radiotherapy planning. *Phys Med Biol* 51: 4147-4169, 2006.

20. **Bouchiat MA, Carver TR, and Varnum CR**. Nuclear polarisation in 3He gas induced by optical pumping and dipolar exchange. *Phys Rev Lett* 5: 373-375, 1960.

21. **Butler JP, Mair RW, Hoffmann D, Hrovat MI, Rogers Ra, Topulos GP, Walsworth RL, and Patz S**. Measuring surface-area-to-volume ratios in soft porous materials using laser-polarized xenon interphase exchange nuclear magnetic resonance. *Journal of physics Condensed matter : an Institute of Physics journal* 14: L297-304, 2002.

22. **Cai J, Miller GW, Altes Ta, Read PW, Benedict SH, de Lange EE, Cates GD, Brookeman JR, Mugler JP, and Sheng K**. Direct measurement of lung motion using hyperpolarized helium-3 MR tagging. *International journal of radiation oncology, biology, physics* 68: 650-653, 2007.

23. **Celli BR, and MacNee W**. Standards for the diagnosis and treatment of patients with COPD: a summary of the ATS/ERS position paper. *Eur Respir J* 23: 932-946, 2004.

24. **Chae EJ, Seo JB, Goo HW, Kim N, Song K-S, Lee SD, Hong S-J, and Krauss B**. Xenon ventilation CT with a dual-energy technique of dual-source CT: initial experience. *Radiology* 248: 615-624, 2008.

25. **Chae EJ, Seo JB, Lee J, Kim N, Goo HW, Lee HJ, Lee CW, Ra SW, Oh YM, and Cho YS**. Xenon ventilation imaging using dual-energy computed tomography in asthmatics: initial experience. *Invest Radiol* 45: 354-361, 2010.

26. **Chen Q, Jakob PM, Griswold Ma, Levin DL, Hatabu H, and Edelman RR**. Oxygen enhanced MR ventilation imaging of the lung. *Magma (New York, NY)* 7: 153-161, 1998.

27. **Chen XJ, Moller HE, Chawla MS, Cofer GP, Driehuys B, Hedlund LW, and Johnson GA**. Spatially resolved measurements of hyperpolarized gas properties in the lung in vivo. Part I: diffusion coefficient. *Magn Reson Med* 42: 721-728, 1999.

28. **Chevalier PA, Rodarte JR, and Harris LD**. Regional lung expansion at total lung capacity in intact vs. excised canine lungs. *J Appl Physiol* 45: 363-369, 1978.

29. **Chon D, Simon BA, Beck KC, Shikata H, Saba OI, Won C, and Hoffman EA**. Differences in regional wash-in and wash-out time constants for xenon-CT ventilation studies. *Respir Physiol Neurobiol* 148: 65-83, 2005.

30. **Christensen GE, Carlson B, Chao KS, Yin P, Grigsby PW, Nguyen K, Dempsey JF, Lerma FA, Bae KT, Vannier MW, and Williamson JF**. Image-based dose planning of intracavitary brachytherapy: registration of serial-imaging studies using deformable anatomic templates. *Int J Radiat Oncol Biol Phys* 51: 227-243, 2001.

31. **Comroe JH, Forster RE, Dubois AB, Briscoe WA, and Carlsen E**. *The Lung.* Chicago: The Year Book Publishers, Inc., 1955.

32. **Conradi MS, Yablonskiy DA, Woods JC, Gierada DS, Bartel SET, Haywood SE, and Menard C**. The role of collateral paths in long-range diffusion of 3He in lungs. *Academic radiology* 15: 675, 2008.

33. **Conradi MS, Yablonskiy Da, Woods JC, Gierada DS, Jacob RE, Chang YV, Choong CK, Sukstanskii AL, Tanoli T, Lefrak SS, and Cooper JD**. 3He diffusion MRI of the lung. *Academic radiology* 12: 1406-1413, 2005.

34. **Crum WR, Hartkens T, and Hill DL**. Non-rigid image registration: theory and practice. *Br J Radiol* 77 Spec No 2: S140-153, 2004.

35. **Cullen SC, and Gross EG**. The anesthetic properties of xenon in animals and human beings, with additional observations on krypton. *Science* 113: 580-582, 1951.

36. **Cumming G, and Jones JG**. The construction and repeatability of lung nitrogen clearance curves. *Respir Physiol* 1: 238-248, 1966.

37. **D P**. An Introduction to the Physics Magnetic Imaging of Resonance. *RadioGraphics* 371-383, 1987.

38. **Davis MH, Khotanzad A, Flamig DP, and Harms SE**. A physics-based coordinate transformation for 3-D image matching. *IEEE Trans Med Imaging* 16: 317-328, 1997.

39. **Diaz S, Casselbrant I, Piitulainen E, Magnusson P, Peterson B, Wollmer P, Leander P, Ekberg O, and Akeson P**. Validity of apparent diffusion coefficient hyperpolarized 3He-MRI using MSCT and pulmonary function tests as references. *European journal of radiology* 71: 257-263, 2009.

40. **Diaz S, Casselbrant I, Piitulainen E, Pettersson G, Magnusson P, Peterson B, Wollmer P, Leander P, Ekberg O, and Akeson P**. Hyperpolarized 3He apparent diffusion coefficient MRI of the lung: reproducibility and volume dependency in healthy volunteers and patients with emphysema. *Journal of magnetic resonance imaging : JMRI* 27: 763-770, 2008.

41. **Evans A, McCormack D, Ouriadov A, Etemad-Rezai R, Santyr G, and Parraga G**. Anatomical distribution of 3He apparent diffusion coefficients in severe chronic obstructive pulmonary disease. *Journal of magnetic resonance imaging : JMRI* 26: 1537-1547, 2007.

42. **Evans A, McCormack DG, Santyr G, and Parraga G**. Mapping and quantifying hyperpolarized 3He magnetic resonance imaging apparent diffusion coefficient gradients. *Journal of applied physiology (Bethesda, Md : 1985)* 105: 693-699, 2008.

43. **Fain S, Schiebler ML, McCormack DG, and Parraga G**. Imaging of lung function using hyperpolarized helium-3 magnetic resonance imaging: Review of current and emerging translational methods and applications. *J Magn Reson Imaging* 32: 1398-1408, 2010.

44. **Fain SB, Gonzalez-Fernandez G, Peterson ET, Evans MD, Sorkness RL, Jarjour NN, Busse WW, and Kuhlman JE**. Evaluation of structure-function relationships in asthma using multidetector CT and hyperpolarized He-3 MRI. *Acad Radiol* 15: 753-762, 2008.

45. **Fain SB, Korosec FR, Holmes JH, O'Halloran R, Sorkness RL, and Grist TM**. Functional lung imaging using hyperpolarized gas MRI. *Journal of magnetic resonance imaging : JMRI* 25: 910-923, 2007.

46. **Ferrara A**. Chronic obstructive pulmonary disease. *Radiologic technology* 82: 245-263, 2000.

47. **Fichele S, Paley MNJ, Woodhouse N, Griffiths PD, van Beek EJR, and Wild JM**. Investigating 3He diffusion NMR in the lungs using finite difference simulations and in vivo PGSE experiments. *Journal of magnetic resonance (San Diego, Calif : 1997)* 167: 1-11, 2004.

48. **Fichele S, Woodhouse N, Swift AJ, Said Z, Paley MN, Kasuboski L, Mills GH, van Beek EJ, and Wild JM**. MRI of helium-3 gas in healthy lungs: posture related variations of alveolar size. *J Magn Reson Imaging* 20: 331-335, 2004.

49. **Fischer B, and Modersitzki J**. Combination of automatic non-rigid and landmark based registration: the best of both worlds. *Medical Imaging* 2003.

50. **Foley WD, Haughton VM, Schmidt J, and Wilson CR**. Xenon contrast enhancement in computed body tomography. *Radiology* 129: 219-220, 1978.

51. **Frahm J**. Rapid FLASH NMR imaging. *Naturwissenschaften* 74: 415-422, 1987.

52. **Fuld MK, Easley RB, Saba OI, Chon D, Reinhardt JM, Hoffman Ea, and Simon Ba**. CT-measured regional specific volume change reflects regional ventilation in supine sheep. *Journal of applied physiology (Bethesda, Md : 1985)* 104: 1177-1184, 2008.

53. **Gee J, Sundaram T, Hasegawa I, Uematsu H, and Hatabu H**. Characterization of regional pulmonary mechanics from serial magnetic resonance imaging data. *Acad Radiol* 10: 1147-1152, 2003.

54. **Giesel FL, Mehndiratta A, von Tengg-Kobligk H, Schaeffer A, Teh K, Hoffman EA, Kauczor HU, van Beek EJ, and Wild JM**. Rapid prototyping raw models on the basis of high resolution computed tomography lung data for respiratory flow dynamics. *Acad Radiol* 16: 495-498, 2009.

55. **Golay X, Hendrikse J, and Lim TCC**. Perfusion imaging using arterial spin labeling. *Topics in magnetic resonance imaging : TMRI* 15: 10-27, 2004.

56. **Goo HW, Chae EJ, Seo JB, and Hong SJ**. Xenon ventilation CT using a dual-source dual-energy technique: dynamic ventilation abnormality in a child with bronchial atresia. *Pediatr Radiol* 38: 1113-1116, 2008.

57. **Goo HW, Yang DH, Hong SJ, Yu J, Kim BJ, Seo JB, Chae EJ, Lee J, and Krauss B**. Xenon ventilation CT using dual-source and dual-energy technique in children with bronchiolitis obliterans: correlation of xenon and CT density values with pulmonary function test results. *Pediatr Radiol* 40: 1490-1497, 2010.

58. **Greil GF, Powell AJ, Gildein HP, and Geva T**. pulmonary and systemic venous anomalies Magnetic Resonance Angiography Gadolinium-Enhanced Three-Dimensional Magnetic Resonance Angiography of Pulmonary and Systemic Venous Anomalies. *Journal of the American College of Cardiology* 2008.

59. **Grimby G, and Soderholm B**. Spirometric studies in normal subjects. III. Static lung volumes and maximal voluntary ventilation in adults with a note on physical fitness. *Acta Medica Scandinavica* 173: 199-208, 1964.

60. **Gur D, Shabason L, Borovetz HS, Herbert DL, Reece GJ, Kennedy WH, and Serago C**. Regional pulmonary ventilation measurements by xenon enhanced dynamic computed tomography: an update. *J Comput Assist Tomogr* 5: 678-683, 1981.

61. **Harris RS**. Pressure-volume curves of the respiratory system. *Respiratory care* 50: 78-98; discussion 98-79, 2005.

62. **Hatabu H, Alsop DC, Listerud J, Bonnet M, and Gefter WB**. T2* and proton density measurement of normal human lung parenchyma using submillisecond echo time gradient echo magnetic resonance imaging. *European journal of radiology* 29: 245-252, 1999.

63. **Hatabu H, Chen Q, Stock KW, Gefter WB, and Itoh H**. Fast magnetic resonance imaging of the lung. *European journal of radiology* 29: 114-132, 1999.

64. **Hatabu H, Tadamura E, Chen Q, Stock KW, Li W, Prasad PV, and Edelman RR**. Pulmonary ventilation: dynamic MRI with inhalation of molecular oxygen. *European journal of radiology* 37: 172-178, 2001.

65. **Hersman FW, Ruset IC, Ketel S, Muradian I, Covrig SD, Distelbrink J, Porter W, Watt D, Ketel J, Brackett J, Hope A, and Patz S**. Large production system for hyperpolarized 129Xe for human lung imaging studies. *Acad Radiol* 15: 683-692, 2008.

66. **Hill DL, Batchelor PG, Holden M, and Hawkes DJ**. Medical image registration. *Phys Med Biol* 46: R1-45, 2001.

67. **Hoffman Ea**. Effect of body orientation on regional lung expansion: a computed tomographic approach. *Journal of applied physiology (Bethesda, Md : 1985)* 59: 468-480, 1985.

68. **Hoffman EA, and Chon D**. Computed tomography studies of lung ventilation and perfusion. *Proc Am Thorac Soc* 2: 492-498, 506, 2005.

69. **Hoffman EA, and Olson LE**. Characteristics of Respiratory System Complexity Captured via X-Ray Computed Tomography. In: *Complexity in structure and Function of the Lung*, edited by Hlastala MP, and Robertson HT. New York, NY: Marcel Dekker, 1998.

70. **Hoffman EA, and Ritman EL**. Effect of body orientation on regional lung expansion in dog and sloth. *J Appl Physiol* 59: 481-491, 1985.

71. **http://pacific.mpi-cbg.de/wiki/index.php/Fiji**. Fiji.

72. **http://www.slicer.org**. Slicer 3D.

73. **Hubmayr RD, Walters BJ, Chevalier PA, Rodarte JR, and Olson LE**. Topographical distribution of regional lung volume in anesthetized dogs. *J Appl Physiol* 54: 1048-1056, 1983.

74. **Huettermann J, Koehnlein W, and Teoule R**. *Effects of ionizing radiation of DNA: physical, chemical, and biological aspects*. 1978, p. Medium: X; Size: Pages: 383.

75. **Imhof H, Rand T, Trattnig S, and Kramer J**. [Basics of MRI technique and MRI image interpretation]. *Orthopade* 23: 300-305, 1994.

76. **Johnson HJ, and Christensen GE**. Consistent landmark and intensity-based image registration. *IEEE Transactions on Medical Imaging* 21: 450-461, 2002.

77. **Kallok MJ, Wilson TA, Rodarte JR, Lai-Fook SJ, Chevalier PA, and Harris LD**. Distribution of regional volumes and ventilation in excised canine lobes. *J Appl Physiol* 47: 182-191, 1979.

78. **Kauczor H, Surkau R, and Roberts T**. Chest radiology Original article MRI using hyperpolarized noble gases. *Time* 827: 820-827, 1998.

79. **Kauczor HU**. Helium-3 imaging of pulmonary ventilation. *The British journal of radiology* 71: 701-703, 1998.

80. **Kauczor HU, Chen XJ, van Beek EJ, and Schreiber WG**. Pulmonary ventilation imaged by magnetic resonance: at the doorstep of clinical application. *Eur Respir J* 17: 1008-1023, 2001.

81. **Kauczor HU, Hanke A, and Van Beek EJ**. Assessment of lung ventilation by MR imaging: current status and future perspectives. *Eur Radiol* 12: 1962-1970, 2002.

82. **Keogh BA, and Crystal RG**. Clinical significance of pulmonary function tests. Pulmonary function testing in interstitial pulmonary disease. What does it tell us? *Chest* 78: 856-865, 1980.

83. **Kirby M, Mathew L, Wheatley A, Santyr GE, McCormack DG, and Parraga G**. Chronic obstructive pulmonary disease: longitudinal hyperpolarized (3)He MR imaging. *Radiology* 256: 280-289, 2010.

84. **Kouzes RT**. The 3He Supply Problem 2009.

85. **Lachmann B, Armbruster S, Schairer W, Landstra M, Trouwborst A, Van Daal GJ, Kusuma A, and Erdmann W**. Safety and efficacy of xenon in routine use as an inhalational anaesthetic. *Lancet* 335: 1413-1415, 1990.

86. **Lambert AR, O'shaughnessy PT, Tawhai MH, Hoffman EA, and Lin C-L**. Regional Deposition of Particles in an Image-Based Airway Model: Large-Eddy simulation and Left-Right Lung Ventilation Asymmetry. *Aerosol Science and Technology* 45: 11-25, 2010.

87. **Lancaster JL, Cykowski MD, McKay DR, Kochunov PV, Fox PT, Rogers W, Toga AW, Zilles K, Amunts K, and Mazziotta J**. Anatomical global spatial normalization. *Neuroinformatics* 8: 171-182, 2010.

88. **Lancaster JL, Fox PT, Downs H, Nickerson DS, Hander TA, El Mallah M, Kochunov PV, and Zamarripa F**. Global spatial normalization of human brain using convex hulls. *J Nucl Med* 40: 942-955, 1999.

89. **Laukemper-Ostendorf S, and Scholz A**. 19F-MRI of perflubron for measurement of oxygen partial pressure in porcine lungs during partial liquid ventilation. *Magnetic* 8: 2191-2191, 2002.

90. **Leawoods JC, Yablonskiy DA, Gierada DS, Conradi MS, and Saam B**. Production and MR Imaging of the Lung. 2001.

91. **Levitzky MG**. *Pulmonary Physiology*. McGraw Hill, 2003.

92. **Levitzky MG**. Teaching the effects of gravity and intravascular and alveolar pressures on the distribution of pulmonary blood flow using a classic paper by West et al. *Advances in physiology education* 30: 5-8, 2006.

93. **Ley-Zaporozhan J, and van Beek EJ**. Imaging phenotypes of chronic obstructive pulmonary disease. *J Magn Reson Imaging* 32: 1340-1352, 2010.

94. **Lin C-L, and Hoffman EA**. A numerical study of gas transport in human lung models. *SPIE Medical Imaging* 5746: 92-100, 2005.

95. **Lin CL, Tawhai MH, McLennan G, and Hoffman EA**. Computational Fluid Dynamics Multiscale Simulation of Gas Flow in Subject-Specific Models of the Human Lung. *Ieee Eng Med Biol* 28: 25-33, 2009.

96. **Loken MK**. Studies of pulmonary function and regional blood flow using xenon 133. *Lahey Clin Found Bull* 16: 337-343, 1967.

97. **Loken MK, Medina JR, Lillehei JP, L'Heureux P, Kush GS, and Ebert RV**. Regional pulmonary function evaluation using xenon 133, a scintillation camera, and computer. *Radiology* 93: 1261-1266, 1969.

98. **Luis Ibanez WS, Lydia Ng, Josh Cates**. The ITK Software Guide - Second Edition. *Insight ToolKit, Clifton Park, NY* 836.

99. **MacFall JR, Charles HC, Black RD, Middleton H, Swartz JC, Saam B, Driehuys B, Erickson C, Happer W, Cates GD, Johnson GA, and Ravin CE**. Human lung air spaces: potential for MR imaging with hyperpolarized He-3. *Radiology* 200: 553-558, 1996.

100. **Marcucci C, Nyhan D, and Simon BA**. Distribution of pulmonary ventilation using Xe-enhanced computed tomography in prone and supine dogs. *J Appl Physiol* 90: 421-430, 2001.

101. **Matsuoka S, Patz S, Albert MS, Sun Y, Rizi RR, Gefter WB, and Hatabu H**. Hyperpolarized gas MR Imaging of the lung: current status as a research tool. *J Thorac Imaging* 24: 181-188, 2009.

102. **McGee KP, Hubmayr RD, and Ehman RL**. MR elastography of the lung with hyperpolarized 3He. *Magnetic resonance in medicine : official journal of the Society of Magnetic Resonance in Medicine / Society of Magnetic Resonance in Medicine* 59: 14-18, 2008.

103. **McMahon CJ, Dodd JD, Hill C, Woodhouse N, Wild JM, Fichele S, Gallagher CG, Skehan SJ, van Beek EJ, and Masterson JB**. Hyperpolarized 3helium magnetic resonance ventilation imaging of the lung in cystic fibrosis: comparison with high resolution CT and spirometry. *Eur Radiol* 16: 2483-2490, 2006.

104. **Mettler FAJ, and Upton AC**. *Medical effects of ionizing radiation*. 1995, p. Medium: X; Size: 430 p.

105. **Middleton H, Black RD, Saam B, Cates GD, Cofer GP, Guenther R, Happer W, Hedlund LW, Johnson GA, Juvan K, and et al.** MR imaging with hyperpolarized 3He gas. *Magn Reson Med* 33: 271-275, 1995.

106. **Milic-Emili J**. Regional distribution of gas in the lung. *Can Respir J* 7: 71-76, 2000.

107. **Milic-Emili J, Henderson Ja, Dolovich MB, Trop D, and Kaneko K**. Regional distribution of inspired gas in the lung. *Journal of applied physiology* 21: 749-759, 1966.

108. **Miller MR, Hankinson J, Brusasco V, Burgos F, Casaburi R, Coates A, Crapo R, Enright P, van der Grinten CP, Gustafsson P, Jensen R, Johnson DC, MacIntyre N, McKay R, Navajas D, Pedersen OF, Pellegrino R, Viegi G, and Wanger J**. Standardisation of spirometry. *Eur Respir J* 26: 319-338, 2005.

109. **Moller HE, Chen XJ, Saam B, Hagspiel KD, Johnson GA, Altes Ta, de Lange EE, and Kauczor H-U**. MRI of the lungs using hyperpolarized noble gases. *Magnetic resonance in medicine : official journal of the Society of Magnetic Resonance in Medicine / Society of Magnetic Resonance in Medicine* 47: 1029-1051, 2002.

110. **Morbach AE, Gast KK, Schmiedeskamp J, Dahmen A, Herweling A, Heussel CP, Kauczor H-U, and Schreiber WG**. Diffusion-weighted MRI of the lung with hyperpolarized helium-3: a study of reproducibility. *Journal of magnetic resonance imaging : JMRI* 21: 765-774, 2005.

111. **Morbach AE, Gast KK, Schmiedeskamp J, Herweling A, Windirsch M, Dahmen A, Ley S, Heussel CP, Heil W, Kauczor HU, and Schreiber WG**. [Microstructure of the lung: diffusion measurement of hyperpolarized 3Helium]. *Z Med Phys* 16: 114-122, 2006.

112. **Mugler JP, Driehuys B, Brookeman JR, Cates GD, Berr SS, Bryant RG, Daniel TM, de Lange EE, Downs JH, Erickson CJ, Happer W, Hinton DP, Kassel NF, Maier T, Phillips CD, Saam BT, Sauer KL, and Wagshul ME**. MR imaging and spectroscopy using hyperpolarized 129Xe gas: preliminary human results. *Magnetic Resonance in Medicine* 37: 809-815, 1997.

113. **Musch G, Layfield JD, Harris RS, Melo MF, Winkler T, Callahan RJ, Fischman AJ, and Venegas JG**. Topographical distribution of pulmonary perfusion and ventilation, assessed by PET in supine and prone humans. *J Appl Physiol* 93: 1841-1851, 2002.

114. **Nicolson R, DeVito TJ, Vidal CN, Sui Y, Hayashi KM, Drost DJ, Williamson PC, Rajakumar N, Toga AW, and Thompson PM**. Detection and mapping of hippocampal abnormalities in autism. *Psychiatry Res* 148: 11-21, 2006.

115. **Ohno Y, Hatabu H, Murase K, Higashino T, Kawamitsu H, Watanabe H, Takenaka D, Fujii M, and Sugimura K**. Quantitative assessment of regional pulmonary perfusion in the entire lung using three-dimensional ultrafast dynamic contrast-enhanced magnetic resonance imaging: Preliminary experience in 40 subjects. *Journal of magnetic resonance imaging : JMRI* 20: 353-365, 2004.

116. **Ohno Y, Hatabu H, Takenaka D, Van Cauteren M, Fujii M, and Sugimura K**. Dynamic oxygen-enhanced MRI reflects diffusing capacity of the lung. *Magnetic Resonance in Medicine* 47: 1139-1144, 2002.

117. **Ohno Y, Koyama H, Nogami M, Takenaka D, Matsumoto S, Obara M, and Sugimura K**. Dynamic oxygen-enhanced MRI versus quantitative CT: pulmonary functional loss assessment and clinical stage classification of smoking-related COPD. *AJR Am J Roentgenol* 190: W93-99, 2008.

118. **Ohno Y, Oshio K, Uematsu H, Nakatsu M, Gefter WB, and Hatabu H**. Single-shot half-Fourier RARE sequence with ultra-short inter-echo spacing for lung imaging. *Journal of magnetic resonance imaging : JMRI* 20: 336-339, 2004.

119. **Oros A-M, and Shah NJ**. Hyperpolarized xenon in NMR and MRI. *Physics in Medicine and Biology* 49: R105-R153, 2004.

120. **Palmer J, Bitzen U, Jonson B, and Bajc M**. Comprehensive ventilation/perfusion SPECT. *J Nucl Med* 42: 1288-1294, 2001.

121. **Patz S, Hersman FW, Muradian I, Hrovat MI, Ruset IC, Ketel S, Jacobson F, Topulos GP, Hatabu H, and Butler JP**. Hyperpolarized (129)Xe MRI: a viable functional lung imaging modality? *European journal of radiology* 64: 335-344, 2007.

122. **Patz S, Muradian I, Hrovat MI, Ruset IC, Topulos G, Covrig SD, Frederick E, Hatabu H, Hersman FW, and Butler JP**. Human pulmonary imaging and spectroscopy with hyperpolarized 129Xe at 0.2T. *Acad Radiol* 15: 713-727, 2008.

123. **Pérez-Sánchez JM, Pérez de Alejo R, Rodríguez I, Cortijo M, Peces-Barba G, and Ruiz-Cabello J**. In vivo diffusion weighted 19F MRI using SF6. *Magnetic resonance in medicine : official journal of the Society of Magnetic Resonance in Medicine / Society of Magnetic Resonance in Medicine* 54: 460-463, 2005.

124. **Pieper S, Lorensen B, Schroeder W, and Kikinis R**. The NA-MIC Kit: ITK, VTK, Pipelines, Grids and 3D Slicer as an Open Platform for the Medical Image Computing Community. *Proceedings of the 3rd IEEE International Symposium on Biomedical Imaging: From Nano to Macro* 1: 698-701, 2006.

125. **Plathow C, Fink C, Ley S, Puderbach M, Eichinger M, Schmahl A, and Kauczor HU**. Measurement of diaphragmatic length during the breathing cycle by dynamic MRI: comparison between healthy adults and patients with an intrathoracic tumor. *Eur Radiol* 14: 1392-1399, 2004.

126. **Plathow C, Hof H, Kuhn S, Puderbach M, Ley S, Biederer J, Claussen CD, Huber PE, Schaefer J, Tuengerthal S, and Kauczor HU**. Therapy monitoring using dynamic MRI: analysis of lung motion and intrathoracic tumor mobility before and after radiotherapy. *Eur Radiol* 16: 1942-1950, 2006.

127. **Plathow C, Ley S, Fink C, Puderbach M, Hosch W, Schmahl A, Debus J, and Kauczor HU**. Analysis of intrathoracic tumor mobility during whole breathing cycle by dynamic MRI. *Int J Radiat Oncol Biol Phys* 59: 952-959, 2004.

128. **Qaseem A, Wilt TJ, Weinberger SE, Hanania NA, Criner G, van der Molen T, Marciniuk DD, Denberg T, Schunemann H, Wedzicha W, MacDonald R, and Shekelle P**. Diagnosis and management of stable chronic obstructive pulmonary disease: a clinical practice guideline update from the American College of Physicians, American College of Chest Physicians, American Thoracic Society, and European Respiratory Society. *Ann Intern Med* 155: 179-191, 2011.

129. **Reinhardt JM, Ding K, Cao K, Christensen GE, Hoffman Ea, and Bodas SV**. Registration-based estimates of local lung tissue expansion compared to xenon CT measures of specific ventilation. *Medical image analysis* 12: 752-763, 2008.

130. **Reinhardt JM, and Hoffman EA**. Quantitative pulmonary imaging: spatial and temporal considerations in high-resolution CT. *Acad Radiol* 5: 539-546, 1998.

131. **Rhodes CG, Valind SO, Brudin LH, Wollmer PE, Jones T, Buckingham PD, and Hughes JM**. Quantification of regional V/Q ratios in humans by use of PET. II. Procedure and normal values. *J Appl Physiol* 66: 1905-1913, 1989.

132. **Rhodes CG, Valind SO, Brudin LH, Wollmer PE, Jones T, and Hughes JM**. Quantification of regional V/Q ratios in humans by use of PET. I. Theory. *J Appl Physiol* 66: 1896-1904, 1989.

133. **Robertson HT, Glenny RW, Stanford D, McInnes LM, Luchtel DL, and Covert D**. High-resolution maps of regional ventilation utilizing inhaled fluorescent microspheres. *J Appl Physiol* 82: 943-953, 1997.

134. **Robertson HT, and Hlastala MP**. Microsphere maps of regional blood flow and regional ventilation. *J Appl Physiol* 102: 1265-1272, 2007.

135. **Ronchetti R, Ewan PW, Jones T, and Hughes JM**. Proceedings: Use of 13N for regional clearance curves compared with 133Xe. *Bull Physiopathol Respir (Nancy)* 11: 124P-125P, 1975.

136. **Ronchetti R, Stocks J, Freedman N, Glass H, and Godfrey S**. Clinical application of regional lung function studies in infants and small children using 13N. *Arch Dis Child* 50: 595-603, 1975.

137. **Rueckert D, Sonoda LI, Hayes C, Hill DL, Leach MO, and Hawkes DJ**. Nonrigid registration using free-form deformations: application to breast MR images. *IEEE Trans Med Imaging* 18: 712-721, 1999.

138. **Ruppert K, Brookeman JR, Hagspiel KD, and Mugler JP**. Probing lung physiology with xenon polarization transfer contrast (XTC). *Magnetic resonance in medicine : official journal of the Society of Magnetic Resonance in Medicine / Society of Magnetic Resonance in Medicine* 44: 349-357, 2000.

139. **Ruppert K, Mata JF, Brookeman JR, Hagspiel KD, and Mugler JP**. Exploring lung function with hyperpolarized (129)Xe nuclear magnetic resonance. *Magnetic Resonance in Medicine* 51: 676-687, 2004.

140. **Russakoff DB, Rohlfing T, Adler JR, Jr., and Maurer CR, Jr.** Intensity-based 2D-3D spine image registration incorporating a single fiducial marker. *Acad Radiol* 12: 37-50, 2005.

141. **Saam BT, Yablonskiy Da, Kodibagkar VD, Leawoods JC, Gierada DS, Cooper JD, Lefrak SS, and Conradi MS**. MR imaging of diffusion of (3)He gas in healthy and diseased lungs. *Magnetic resonance in medicine : official journal of the Society of Magnetic Resonance in Medicine / Society of Magnetic Resonance in Medicine* 44: 174-179, 2000.

142. **Salerno M, Altes Ta, Mugler JP, Nakatsu M, Hatabu H, and de Lange EE**. Hyperpolarized noble gas MR imaging of the lung: potential clinical applications. *European journal of radiology* 40: 33-44, 2001.

143. **Salerno M, de Lange EE, Altes Ta, Truwit JD, Brookeman JR, and Mugler JP**. Emphysema: hyperpolarized helium 3 diffusion MR imaging of the lungs compared with spirometric indexes-initial experience. *Radiology* 222: 252-260, 2002.

144. **Schoene RB, Giboney K, Schimmel C, Hagen J, Robinson J, Sato W, and Sullivan KN**. Spirometry and airway reactivity in elite track and field athletes. *Clin J Sport Med* 7: 257-261, 1997.

145. **Schreiber WG, Eberle B, Laukemper-Ostendorf S, Markstaller K, Weiler N, Scholz a, Bürger K, Heussel CP, Thelen M, and Kauczor HU**. Dynamic (19)F-MRI of pulmonary ventilation using sulfur hexafluoride (SF(6)) gas. *Magnetic resonance in medicine : official journal of the Society of Magnetic Resonance in Medicine / Society of Magnetic Resonance in Medicine* 45: 605-613, 2001.

146. **Schreiber WG, Morbach AE, Stavngaard T, Gast KK, Herweling A, Søgaard LV, Windirsch M, Schmiedeskamp J, Heussel CP, and Kauczor H-U**. Assessment of lung microstructure with magnetic resonance imaging of hyperpolarized Helium-3. *Respiratory physiology and neurobiology* 148: 23-42, 2005.

147. **Shibel EM, Landis GA, and Moser KM**. Inhalation lung scanning evaluation--radioaerosol versus radioxenon techniques. *Dis Chest* 56: 284-289, 1969.

148. **Slutsky AS**. Mechanical ventilation. American College of Chest Physicians' Consensus Conference. *Chest* 104: 1833-1859, 1993.

149. **Slutsky AS, and Ranieri VM**. Mechanical ventilation: lessons from the ARDSNet trial. *Respir Res* 1: 73-77, 2000.

150. **Stancil DD, and Prabhakar A**. *Spin Waves: Theory and Applications*. New York: Springer, 2009.

151. **Stavngaard T, Sogaard LV, Batz M, Schreiber LM, and Dirksen A**. Progression of emphysema evaluated by MRI using hyperpolarized (3)He (HP (3)He) measurements in patients with alpha-1-antitrypsin (A1AT) deficiency compared with CT and lung function tests. *Acta Radiol* 50: 1019-1026, 2009.

152. **Stock K, Chen Q, and Hatabu H**. Magnetic resonance T2* measurements of the normal human lung in vivo with ultra-short echo times. *Magnetic resonance imaging* 17: 997-1000, 1999.

153. **Stock KW, Chen Q, Morrin M, Hatabu H, and Edelman RR**. Oxygen-enhanced magnetic resonance ventilation imaging of the human lung at 0.2 and 1.5 T. *Journal of magnetic resonance imaging : JMRI* 9: 838-841, 1999.

154. **Stolk J, Putter H, Bakker EM, Shaker SB, Parr DG, Piitulainen E, Russi EW, Grebski E, Dirksen A, Stockley RA, Reiber JH, and Stoel BC**. Progression parameters for emphysema: a clinical investigation. *Respir Med* 101: 1924-1930, 2007.

155. **Subsol G, Roberts N, Doran M, Thirion JP, and Whitehouse GH**. Automatic analysis of cerebral atrophy. *Magn Reson Imaging* 15: 917-927, 1997.

156. **Suga K**. Technical and analytical advances in pulmonary ventilation SPECT with xenon-133 gas and Tc-99m-Technegas. *Ann Nucl Med* 16: 303-310, 2002.

157. **Suga K, Kawakami Y, Yamashita T, Zaki M, and Matsunaga N**. Characterization of 133Xe gas washout in pulmonary emphysema with dynamic 133Xe SPECT functional images. *Nucl Med Commun* 27: 71-80, 2006.

158. **Suga K, Nishigauchi K, Kume N, Takano K, Koike S, Shimizu K, and Matsunaga N**. Ventilation abnormalities in obstructive airways disorder: detection with pulmonary dynamic densitometry by means of spiral CT versus dynamic Xe-133 SPECT. *Radiology* 202: 855-862, 1997.

159. **Sukstanskii aL, and Yablonskiy Da**. In vivo lung morphometry with hyperpolarized 3He diffusion MRI: theoretical background. *Journal of magnetic resonance (San Diego, Calif : 1997)* 190: 200-210, 2008.

160. **Swift AJ, Wild JM, Fichele S, Woodhouse N, Fleming S, Waterhouse J, Lawson Ra, Paley MNJ, and Van Beek EJR**. Emphysematous changes and normal variation in smokers and COPD patients using diffusion 3He MRI. *European journal of radiology* 54: 352-358, 2005.

161. **Tajik JK, Chon D, Won C, Tran BQ, and Hoffman EA**. Subsecond multisection CT of regional pulmonary ventilation. *Acad Radiol* 9: 130-146, 2002.

162. **Tawhai MH, and Lin CL**. Image-based modeling of lung structure and function. *J Magn Reson Imaging* 32: 1421-1431, 2010.

163. **Thompson PM, MacDonald D, Mega MS, Holmes CJ, Evans AC, and Toga AW**. Detection and mapping of abnormal brain structure with a probabilistic atlas of cortical surfaces. *J Comput Assist Tomogr* 21: 567-581, 1997.

164. **Tsuda A, Butler JP, and Fredberg JJ**. Effects of alveolated duct structure on aerosol kinetics. II. Gravitational sedimentation and inertial impaction. *J Appl Physiol* 76: 2510-2516, 1994.

165. **Tzeng Y-S, Lutchen K, and Albert M**. The difference in ventilation heterogeneity between asthmatic and healthy subjects quantified using hyperpolarized 3He MRI. *Journal of applied physiology (Bethesda, Md : 1985)* 106: 813-822, 2009.

166. **Valind SO, Rhodes CG, and Jonson B**. Quantification of regional ventilation in humans using a short-lived radiotracer--theoretical evaluation of the steady-state model. *J Nucl Med* 28: 1144-1154, 1987.

167. **van Beek EJ, Dahmen AM, Stavngaard T, Gast KK, Heussel CP, Krummenauer F, Schmiedeskamp J, Wild JM, Sogaard LV, Morbach AE, Schreiber LM, and Kauczor HU**. Hyperpolarised 3He MRI versus HRCT in COPD and normal volunteers: PHIL trial. *Eur Respir J* 34: 1311-1321, 2009.

168. **van Beek EJ, and Hoffman EA**. Functional imaging: CT and MRI. *Clin Chest Med* 29: 195-216, vii, 2008.

169. **van Beek EJ, and Wild JM**. Hyperpolarized 3-helium magnetic resonance imaging to probe lung function. *Proc Am Thorac Soc* 2: 528-532, 510, 2005.

170. **van Beek EJ, Wild JM, Kauczor HU, Schreiber W, Mugler JP, 3rd, and de Lange EE**. Functional MRI of the lung using hyperpolarized 3-helium gas. *J Magn Reson Imaging* 20: 540-554, 2004.

171. **Walker T, Thywissen J, and Happer W**. Spin-rotation interaction of alkali-metal–He-atom pairs. *Physical Review A* 56: 2090-2094, 1997.

172. **Walker TG, and Happer W**. RMP Colloquia Spin-exchange optical pumping of noble-gas nuclei. 69: 629-642, 1997.

173. **Wanger J, Clausen JL, Coates A, Pedersen OF, Brusasco V, Burgos F, Casaburi R, Crapo R, Enright P, van der Grinten CP, Gustafsson P, Hankinson J, Jensen R, Johnson D, Macintyre N, McKay R, Miller MR, Navajas D, Pellegrino R, and Viegi G**. Standardisation of the measurement of lung volumes. *Eur Respir J* 26: 511-522, 2005.

174. **Weibel ER**. Morphometry of the Human Lung. *Biometrische Zeitschrift* 8: 143-144, 1966.

175. **Weibel ER**. Morphometry of the human lung: the state of the art after two decades. *Bull Eur Physiopathol Respir* 15: 999-1013, 1979.

176. **Weibel ER**. What makes a good lung? *Swiss medical weekly : official journal of the Swiss Society of Infectious Diseases, the Swiss Society of Internal Medicine, the Swiss Society of Pneumology* 139: 375-386, 2009.

177. **Weibel R**. Morphological Basis of Gas Exchange. 53: 1973.

178. **Weishaupt D, and Köchli VD**. How does MRI work? An introduction to the physics and function of Magnetic Resonance Imaging. 2003. D. Weishaupt, V.D. K�chli, B. *European Journal of Nuclear Medicine and Molecular Imaging* 32: 338-338, 2005.

179. **West JB**. *Respiratory Phsyiology: The Essentials*. Baltimore, MD: Lippincott Williams and Wilkins, 2008.

180. **West JB**. Understanding pulmonary gas exchange: ventilation-perfusion relationships. *American journal of physiology Lung cellular and molecular physiology* 287: L1071-1072, 2004.

181. **West JB, Dollery CT, and Naimark a**. Distribution of Blood Flow in Isolated Lung; Relation To Vascular and Alveolar Pressures. *Journal of applied physiology* 19: 713-724, 1964.

182. **Wolf U, Scholz A, Heussel CP, Markstaller K, and Schreiber WG**. Subsecond fluorine-19 MRI of the lung. *Magnetic resonance in medicine : official journal of the Society of Magnetic Resonance in Medicine / Society of Magnetic Resonance in Medicine* 55: 948-951, 2006.

183. **Woolcock AJ, and Read J**. Lung volumes in exacerbations of asthma. *Am J Med* 41: 259-273, 1966.

184. **Woolcock AJ, Rebuck AS, Cade JF, and Read J**. Lung volume changes in asthma measured concurrently by two methods. *Am Rev Respir Dis* 104: 703-709, 1971.

185. **Woolf CR**. Pulmonary function tests and their clinical application. *Can Med Assoc J* 75: 1007-1015, 1956.

186. **Yin Y, Choi J, Hoffman EA, Tawhai MH, and Lin CL**. Simulation of pulmonary air flow with a subject-specific boundary condition. *J Biomech* 43: 2159-2163, 2010.

187. **Yin Y, Hoffman EA, and Lin CL**. Mass preserving nonrigid registration of CT lung images using cubic B-spline. *Med Phys* 36: 4213-4222, 2009.

188. **Yonas H, Grundy B, Gur D, Shabason L, Wolfson SK, Jr., and Cook EE**. Side effects of xenon inhalation. *J Comput Assist Tomogr* 5: 591-592, 1981.

189. **Yushkevich PA, Piven J, Hazlett HC, Smith RG, Ho S, Gee JC, and Gerig G**. User-guided 3D active contour segmentation of anatomical structures: significantly improved efficiency and reliability. *Neuroimage* 31: 1116-1128, 2006.